Adsorption Science & Technology

Fourth Industrial Revolution of Wastewater Treatment with Adsorption

Lead Guest Editor: Mahmoud Nasr
Guest Editors: Nadeem Khan and Mika Erik Tapio Sillanpää

Fourth Industrial Revolution of Wastewater Treatment with Adsorption

Adsorption Science & Technology

Fourth Industrial Revolution of Wastewater Treatment with Adsorption

Guest Editors: and

Contents

Hindawi
Adsorption Science & Technology
Volume 2023, Article ID 9897865, 3 pages
https://doi.org/10.1155/2023/9897865

Editorial

Fourth Industrial Revolution of Wastewater Treatment with Adsorption

Mahmoud Nasr[1,2] **Nadeem Khan**[3] **and Mika Sillanpää**[4]

[1]*Environmental Engineering Department, Egypt-Japan University of Science and Technology (E-JUST), New Borg El-Arab City, Alexandria 21934, Egypt*
[2]*Sanitary Engineering Department, Faculty of Engineering, Alexandria University, P.O. Box 21544, Alexandria 21526, Egypt*
[3]*Department of Civil Engineering, Mewat Engineering College, 122107, Nuh, Haryana, India*
[4]*Department of Biological and Chemical Engineering, Aarhus University, Nørrebrogade 44, 8000 Aarhus, Denmark*

Correspondence should be addressed to Mahmoud Nasr; mahmoud.nasr@ejust.edu.eg

Received 3 March 2023; Accepted 3 March 2023; Published 3 October 2023

1. Background

The fourth industrial revolution of the water sector complies with the objectives of Water 4.0 by employing digital technology for flexible, reliable, and competitive water management [1, 2]. Digitization and automation are used to promote and strengthen the water-human-data nexus, especially to maintain efficient wastewater treatment technologies [3, 4]. The digital support systems allow for collecting a sufficient amount of data with nonexcessive field sampling and monitoring [5, 6]. This advantage would further save time and effort, viz., avoiding workers' exposure to dust, airborne bacteria, and endotoxins, for data collection and assessment [7, 8]. Because the adsorption process has been widely used for removing heavy metals, dyes, turbidity, and organic compounds in wastewater treatment, its performance optimization and prediction by advanced modeling techniques should be comprehensively investigated [9, 10]. Hence, this Special Issue represents the utilization of the adsorption technique to remove various pollutants from wastewater, focusing on the application of artificial intelligence techniques to simulate and forecast the pollutants' removal efficiencies. This Special Issue also attempts to show that applying the advanced and innovative computational tools in various adsorption-based wastewater treatment systems would overcome the drawbacks of conventional modeling and statistical methods.

2. Summaries of Accepted Articles

Reynel-Ávila et al. [11] represented a review of the artificial neural network (ANNs) applications for modeling, simulation, and optimization of the adsorption process for organic and inorganic pollutant reduction. The study demonstrated that ANN had been widely used in more than 250 papers reported in the Web of Science® database to predict the adsorption performance and the related isotherm and kinetic parameters for either batch or dynamic operation. The review concluded that the ANN-based modeling of adsorption systems was efficient for resolving complex engineering problems due to achieving both technical and economic advantages.

Yadav et al. [12] used incense stick ash to prepare Ca-rich zeolite, which was characterized in terms of gismondine ($Ca_2Al_4Si_4O_{16}{\cdot}9H_2O$). A computational model was used to estimate the electronic properties and density of states of gismondine ($Ca_2Al_4Si_4O_{16}{\cdot}9H_2O$), indicating the successful synthesis of Ca-based zeolites. The Ca-exchanged zeolite was further employed to remove heavy metals and alkali metals from fly ash aqueous phases. The removal efficiencies of these metals were about 27.6% for Cu, 64.1% for Cd, 80.0% for Cr, 20.5% for Co, 23.4% for Ni, 48.8% for Zn, 73.5% for Ba, 27.6% for Ca, 64.1% for Mg, 32.5% for Mn, and 62.6% for Al within 120 min adsorption time.

Kumi et al. [13] represented the application of the pyrolysis process to convert sewage sludge into biochar. The biochar elemental composition was modified by adding eggshell waste, generating an adsorbent suitable for toluene and xylene (TX) removals. The removal efficiencies of T and X reached 79.1% and 86.6%, respectively, at pH = 10, biochar dosage = 2 g/L, and initial TX of 40 mg/L for 1 h adsorption time. The economic feasibility of the proposed adsorption system was estimated, equivalent to a 6.9 yr payback period. Isotherm and kinetic models were used for fitting the adsorption data and suggesting the removal mechanisms.

Alhothali et al. [14] represented the application of artificial intelligence prediction models and statistical methods to simulate and optimize the removals of chemical oxygen demand (COD) and total organic carbon (TOC) via biochar adsorbent. Biochar was prepared from the pyrolysis of tea leaves at 700°C for 2 h under an inert atmosphere (N_2 gas). Each modeling method was composed of 3 inputs (pH, dosage, and adsorption time) and 2 outputs (COD and TOC removals). The highest removal efficiencies of 83.0% for COD and 98.3% for TOC were achieved at biochar dosage = 25 mg/L and pH = 10 within 35 min. The study demonstrated that the highest predictive accuracy was maintained by adaptive neuro-fuzzy interference (ANFIS), followed by artificial neural network (ANN) and response surface methodology (RSM).

Suditu et al. [15] investigated the application of artificial intelligence-related models to optimize and predict the color removal efficiency by adsorption onto activated carbon. The adsorbent material showed a decolorization efficiency of 39.92%, using the RSM method with optimum factors of bromocresol green color = 5.135 mg/L and adsorbent dosage = 1.58 g/L within 62.74 min. An ANN model with 2 hidden layers was employed to optimize the adsorption process, improving the decolorization performance to more than 99%.

Mostafa et al. [16] used the adsorption process to remove organic pollutants (expressed by biochemical oxygen demand; BOD) from wastewater. For this purpose, zerovalent iron nanoparticles were prepared and encapsulated into cellulose acetate, giving CA/nZVI adsorbent. The adsorbent material was characterized for surface morphology, elemental composition, and surface functional groups and used for BOD uptake. The highest BOD removal efficiency was 96.4% at initial concentration = 100 mg/L, 200 rpm agitation, and 3 g/L CA/nZVI dosage. The adsorption system should also be operated at a wastewater pH of around 7 within 30 min. Further, the factors affecting the adsorbent performance toward pollution reduction were optimized by quadratic regression model and ANN. The highest predictive performance (R^2: 0.972 and Adj-R^2: 0.971) was achieved by the ANN model using 10 neurons in the hidden layer and "trainlm" learning algorithm as a back-propagation training function. The proposed models also demonstrated that the highest influential factor was solution pH followed by adsorbent dosage.

We hope that this Special Issue can assist relevant academic and industry researchers in meeting the requirements of the Internet of Things (IoT) and the fourth industrial revolution for wastewater treatment by adsorption.

Conflicts of Interest

The guest editors declare that they have no conflicts of interest regarding the publication of this editorial.

Acknowledgments

The lead editor would like to thank all the authors who submitted their valuable contributions and anonymous reviewers who carefully scrutinized and evaluated the articles submitted. He would also like to thank the chief editor of Adsorption Science & Technology, Prof. Ashleigh Fletcher, for providing this opportunity and lots of guidance throughout the process. The lead editor also would like to acknowledge Nasr Academy for Sustainable Environment (NASE).

Mahmoud Nasr
Nadeem Khan
Mika Sillanpää

References

[1] H. Efendic, L. Becirovic, A. Deumic, and L. Pokvic, "Biosensors in monitoring public health: industry 4.0 applications - a review," *IFAC-PapersOnLine*, vol. 55, no. 4, pp. 38–44, 2022.

[2] L. David, N. Nwulu, C. Aigbavboa, and O. Adepoju, "Integrating fourth industrial revolution (4IR) technologies into the water, energy & food nexus for sustainable security: a bibliometric analysis," *Journal of Cleaner Production*, vol. 363, article 132522, 2022.

[3] M. Nasr, K. Mohamed, M. Attia, and M. Ibrahim, "Sustainable management of wastewater treatment plants using artificial intelligence techniques," in *Soft Computing Techniques in Solid Waste and Wastewater Management*, pp. 171–185, Elsevier, 2021.

[4] V. Hernández-Chover, L. Castellet-Viciano, A. Bellver-Domingo, and F. Hernández-Sancho, "The potential of digitalization to promote a circular economy in the water sector," *Water*, vol. 14, no. 22, p. 3722, 2022.

[5] L. Heijnen, G. Elsinga, M. de Graaf, R. Molenkamp, M. Koopmans, and G. Medema, "Droplet digital RT-PCR to detect SARS-CoV-2 signature mutations of variants of concern in wastewater," *Science of the Total Environment*, vol. 799, article 149456, 2021.

[6] K. Nam, S. Heo, S. Kim, and C. Yoo, "A multi-agent AI reinforcement-based digital multi-solution for optimal operation of a full-scale wastewater treatment plant under various influent conditions," *Journal of Water Process Engineering*, vol. 52, article 103533, 2023.

[7] H. Kwon, H.-J. Kang, Y. Park, and J. Bae, "Optimization of a sequencing batch reactor with the application of the Internet of Things," *Water Research*, vol. 229, article 119511, 2023.

[8] M. Bahramian, R. Dereli, W. Zhao, M. Giberti, and E. Casey, "Data to intelligence: the role of data-driven models in wastewater treatment," *Expert Systems with Applications*, vol. 217, article 119453, 2023.

[9] C. Li, Y. Lin, X. Li, J. Cheng, and C. Yang, "Cupric ions inducing dynamic hormesis in duckweed systems for swine wastewater treatment: quantification, modelling and mechanisms," *Science of the Total Environment*, vol. 866, article 161411, 2023.

[10] D. Vaghela, A. Pawar, N. Panwar, and D. Sharma, "Modelling and optimization of biochar-based adsorbent derived from wheat straw using response surface methodology on adsorption of Pb^{2+}," *International Journal of Environmental Research*, vol. 17, no. 1, p. 9, 2023.

[11] H. Reynel-Ávila, I. Aguayo-Villarreal, L. Diaz-Muñoz et al., "A review of the modeling of adsorption of organic and inorganic pollutants from water using artificial neural networks," *Adsorption Science & Technology*, vol. 2022, article 9384871, pp. 1–51, 2022.

[12] V. Yadav, N. Choudhary, D. Ali et al., "Experimental and computational approaches for the structural study of novel Ca-rich zeolites from incense stick ash and their application for wastewater treatment," *Adsorption Science and Technology*, vol. 2021, article 6066906, pp. 1–12, 2021.

[13] A. Kumi, M. Ibrahim, M. Fujii, and M. Nasr, "Petrochemical wastewater treatment by eggshell modified biochar as adsorbent: atechno-economic and sustainable approach," *Adsorption Science and Technology*, vol. 2022, article 2323836, pp. 1–13, 2022.

[14] A. Alhothali, H. Khurshid, M. Mustafa, K. Moria, U. Rashid, and O. Bamasag, "Evaluation of contemporary computational techniques to optimize adsorption process for simultaneous removal of COD and TOC in wastewater," *Adsorption Science and Technology*, vol. 2022, article 7874826, pp. 1–16, 2022.

[15] G. Suditu, E. Drăgoi, A. Apostică et al., "Artificial intelligence-based tools for process optimization: case study—bromocresol green decolorization with active carbon," *Adsorption Science and Technology*, vol. 2022, article 8110436, pp. 1–15, 2022.

[16] M. Mostafa, A. Mahmoud, M. Mahmoud, and M. Nasr, "Computational-based approaches for predicting biochemical oxygen demand (BOD) removal in adsorption process," *Adsorption Science and Technology*, vol. 2022, article 9739915, pp. 1–15, 2022.

Hindawi
Adsorption Science & Technology
Volume 2022, Article ID 8110436, 15 pages
https://doi.org/10.1155/2022/8110436

Research Article

Artificial Intelligence-Based Tools for Process Optimization: Case Study—Bromocresol Green Decolorization with Active Carbon

Gabriel Dan Suditu,[1] **Elena Niculina Drăgoi**,[1,2] **Alexandra Georgiana Apostică**,[1] **Andra Maria Mănăilă**,[1] **Veronica Mădălina Radu**,[1] **Adrian Cătălin Puițel**,[1] **and Mircea Teodor Nechita**[1]

[1]*Faculty of Chemical Engineering and Environmental Protection "Cristofor Simionescu", "Gheorghe Asachi" Technical University of Iași, Bd. Prof. Dimitrie Mangeron, No. 73, 700050 Iași, Romania*
[2]*Faculty of Automatic Control and Computer Engineering, "Gheorghe Asachi" Technical University of Iași, Bd. Prof. Dimitrie Mangeron, No. 73, 700050 Iași, Romania*

Correspondence should be addressed to Mircea Teodor Nechita; mircea-teodor.nechita@academic.tuiasi.ro

Received 10 March 2022; Accepted 14 July 2022; Published 30 July 2022

Academic Editor: Mahmoud Nasr

This study highlights the benefits of optimizing the decolorization of bromocresol green (a colorant/pH indicator widely used in the industry, whose degradation produces toxic byproducts) by adsorption on active carbon. A set of experiments were planned and performed based on the design of experiments methodology for the following parameters: the colorant concentration (0.009-0.045 g/L), the amount of adsorbent (0.5-3 g/L), and the contact time (60-240 min). Modeling and optimization strategies were employed to determine the working conditions leading to efficiency maximization. Using the response surface methodology, the optimum values of the primary process parameters were established. In addition, a modified bacterial foraging optimization algorithm was applied as an alternative optimizer in combination with artificial neural networks in order to determine multiple combinations of parameters that can lead to maximum process efficiency. Different solutions were obtained with the considered strategies, and the maximum efficiency obtained was >99%. The study emphasizes that adsorption on active carbon is an effective method for bromocresol green decolorization in wastewater that can be further improved using advanced optimization methods.

1. Introduction

For thousands of years, the dyes and the pigments used were derived from natural sources. Only in the middle of the 19th century, when the natural resources were insufficient to fulfill the increasing demand, did the genuine industry of synthetic dyes and pigments start to grow [1–6]. Nowadays, the production of dyes and pigments has reached millions of tons per year [7], and almost every industry is a consumer. On a global scale and in a relatively short time, such tremendous growth generated massive amounts of air, water, and soil pollutants [8–11].

Many manufacturing branches generate colored industrial wastewaters such as dye industries, Kraft bleaching, tannery, textiles, pulp and paper, food processing, cosmetics, and pharmaceuticals [12, 13]. Consequently, over the years, numerous physicochemical treatments and decolorization methods have been proposed [14, 15]: coagulation and flocculation [16], electrocoagulation [17], adsorption [18–21], wet oxidation [22], ozonation [23], photochemical degradation [24], biodegradation [25], and other advanced oxidation processes [22], with each method having its own advantages and drawbacks [26]. To be competitive, all these methods must evolve with the technical progress and the continuous tightening of the environmental standards and regulations [27]. In this view, there are a series of directions that focus on (i) finding new, more effective technologies [28, 29], (ii) combining existing methods to increase their effectiveness

[30–33], and (iii) optimizing existing technologies to increase the efficiency and decrease the operation costs [34, 35].

One of the classical approaches with multiple applications in the optimization of industrial wastewater treatments [23, 24, 36–38] is the response surface method (RSM) based on central composite design (CCD), proposed in the '60s by Box and Hunter [39]. RSM is based on a collection of statistical and mathematical techniques (helpful in developing, improving, and optimizing processes) that is widely used to design an experiment, explain the main interaction effects of the independent variables, and determine the optimal conditions using a limited number of experiments [40–42]. On the other hand, artificial neural networks (ANNs), although proposed roughly during the same period as RSM, has recorded in the latest years a series of breakthroughs that demonstrated their extraordinary potential to model complex systems with highly nonlinear interactions. Therefore, ANNs have a large area of applicability, being applied to many fields. Examples in the adsorption area include (i) ultrasonic-assisted adsorption [43], (ii) dye adsorption [44], and (iii) heavy metal biosorption [45]. However, despite their advantages and capabilities, ANNs suffer from several drawbacks related to the model type and hyperparameter tuning [46, 47], which depend on the problem's characteristics. In this context, neuroevolution (combining ANNs with evolutionary-based algorithms) is a strategy that can be used to overcome these problems, with the hyperparameter optimization being performed by the optimization strategy.

For the optimization step of this study, a population-based algorithm represented by bacterial foraging optimization (BFO) was used. BFO [48] is a bioinspired metaheuristic that mimics the foraging behavior of *E. coli*. Among the multitude of nature-inspired algorithms [49], BFO distinguished itself as an efficient approach. Its simplicity, ease of use, and efficiency in solving a wide range of problems represent the main reasons for selecting BFO from the multitude of algorithms from its class [34] and applying it as an alternative approach to RSM for optimizing the considered process. Furthermore, it was successfully applied to various synthetic [50, 51] and real-world problems [52].

Various types of adsorbents: conventional [53, 54], nonconventional [55], ion-exchange [56], and biosorbents [57], were employed in decolorization of dye-polluted wastewaters [58]. Although rather costly, activated carbon is generally recognized as one of the most efficient adsorbents that can be successfully used for various colored or noncolored pollutants [26].

Typically, the chemicals that generate the effluent's color absorb light, directly impacting photosynthesis. They also reduce visibility, making it more difficult for microorganisms to eat or reproduce [59]. Bromocresol green (BCG) is a member of the triphenylmethane (anionic) family and has a variety of applications as a pH indicator, DNA tracer, and tracking dye in the weaving industry (cotton, flax) [60, 61]. However, the three benzene rings' molecular structure makes it difficult to degrade once released into wastewater naturally. As a result, there are numerous studies related to its complete removal and/or decolorization using various methods [62–66]. Among these, two strategies attract much attention: advanced oxidation processes (AOPs) and adsorption on activated carbons (AC) or other materials such as chitin [61] or polymers [67]. The AOPs usually involve chemically assisted UV irradiation [68, 69] and/or heterogeneous photocatalysis [70, 71]. As for the active carbon-based materials, the focus is on preparing activated carbon from various low-value natural materials [72, 73] using pyrolysis and, in some cases, additional chemical activation [34]. Although this method is one of the most cost-effective, the properties of the resulting AC are highly dependent upon the conditions under which the raw material is produced (soil quality, precipitation, temperature, etc.).

As a result, this research focuses on commercial AC with controlled and repeatable properties. This research is aimed at evaluating the AC's capacity for BCG decolorization and underlining that process optimization using artificial intelligence-based strategies can improve process efficacy. In this context, the interaction among three parameters (the BCG concentration, the amount of adsorbent, and the contact time) and their influence on the process yield was analyzed, modeled, and optimized using RSM, ANNs, and a BFO-based approach. The variant of BFO used in this work is a modified, improved version. In order to distinguish between the two versions, the standard algorithm will be referred to as BFO, while the modified version will be denoted as iBFO. Graphical response surface and contour plots were used to identify the best operating conditions. This work's novelty consists of applying classic (RSM) and newer modeling and optimization methods (ANNs, iBFO) for improving the bromocresol green decolorization using active carbon. Moreover, to the author's knowledge, iBFO has never been applied to such a process.

2. Materials and Methods

2.1. Work Plan. This study is aimed at showing that even classical and well-known processes (e.g., colorant adsorption on active carbon) can be improved by using a combination of (i) standard approaches for planning, modeling, and optimization and (ii) artificial intelligence techniques that combine ANNs with bioinspired metaheuristic optimizers. Consequently, the knowledge about the considered process was gathered through experimental analysis and planned using a design of experiment (DOE) approach. Then, the process was modeled using two approaches (RSM and ANNs). Finally, the process optimization was performed by two distinct strategies (RSM and iBFO). Figure 1 presents the main workflow of data and the interconnection between all the applied strategies.

2.2. Materials. BCG powder (analytical purity, supplied by S. C. ChimReactiv Ltd.) and bidistilled water were used to prepare the dye solutions. Irregular-shape particles of active carbon, supplied by Romcarbon S.A., were used to perform the experiments. Before performing the experiments, the particles were washed several times with bidistilled water to remove surface impurities, dried at 120°C for 24 h, and

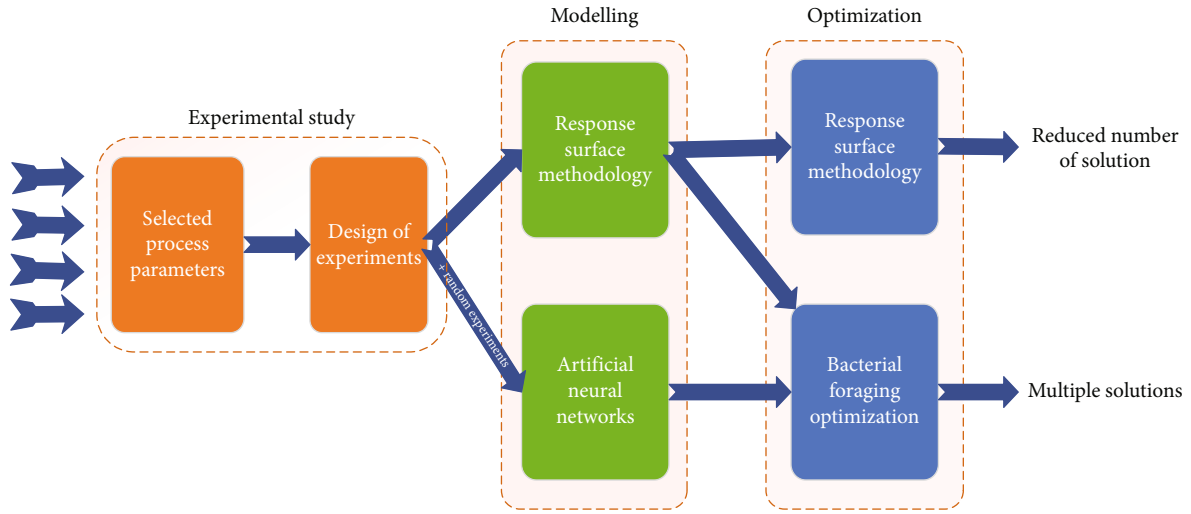

Figure 1: Workflow for the application of the different strategies used in this work.

Table 1: The specific surface areas and porous characteristics of commercial activated carbon.

Physical properties	Characteristics	Value
Surface	BET surface	1403 m^2/g
	External surface	38 m^2/g
	Total surface	631 m^2/g
	Mean pore size	1.62 nm
Volume	Specific microporous volume	0.48 cm^3/g
	Total microporous volume	0.66 cm^3/g

classified by sieving; the average diameter ranges between 2.5 and 3.15 mm.

The main characteristics of the commercial active carbon (Table 1) were investigated by Secula et al. [74]. In addition, for this study, SEM images were registered (Figure 2). The captured images emphasized the parallel arrangement of the pores and their size similarity (Figure 2(b)). In addition, the micropores are perpendicularly placed on the macropores (Figure 2(a)).

2.3. Experimental Design. In order to determine the optimal parameters for BCG decolorization, three independent variables were considered based on the experience of our previous studies [34, 75]. Table 2 presents the considered variables, their unit of measure, and the considered range used in the experimental phase based on DOE.

The UV-Vis spectra and the absorbance values were recorded using a JASCO V-550 UV-Vis spectrophotometer. Disposable disc filters of 0.45 μm were used for particle separation during solution sampling. The morphologies of the AC particles were observed using a Vega-Tescan scanning electron microscope.

Following the DOE procedure proposed by Box and Hunter [39], a minimum number of relevant experiments were statistically identified (Table 3) and further used in the experimental analysis.

2.4. Experimental Procedure. Batch adsorption experiments were performed using 100 mL solution samples with the required BCG concentration without additional pH adjustments. The solutions were mixed with an adequate amount of active carbon for a well-defined time, according to the data presented in Table 3. In order to avoid settling, the slurry was constantly stirred during all the experiments.

The AC performances were characterized by measuring the rate of BCG decolorization by adsorption.

Since one of its typical applications is the pH indicator, the BCG is highly sensitive to pH deviations. The pH increase from being acidic to basic leads to a color variation ranging from yellow to green and blue. The UV-Vis spectrum of BCG also varies with the pH change. BCG's acid and basic forms display an isosbestic point in their UV-Vis spectrum, around 515 nm [68, 76]. Zaggout [76] and Fassi et al. [68] show that at acidic and natural pH, the most intense band is at around 614 nm, while at basic pH, the most intense band is shifted to around 444 nm. The pH sensitivity of BCG, certified by the spectroscopic versatility, is highlighted in various literature reports. Many authors working with BCG reported different values of the reference band (Table 4). Some followed the band at 440 nm, while others tracked it at 614 nm.

During this study, the absorbance values at 412 nm (Figure 3(a)) were used to analyze the process course. BCG concentration was calculated from an absorbance versus concentration calibration curve with an R^2 value of 0.99677 (Figure 3(b)). It is worth mentioning that the calibration curve failed from linearity when parallel measurements were done at 617 nm (results not shown).

The efficiency of BCG decolorization η (%) was calculated using the following equation:

$$\eta\,[\%] = \frac{\mathrm{BCG}^0 - \mathrm{BCG}^t}{\mathrm{BCG}^0}, \quad (1)$$

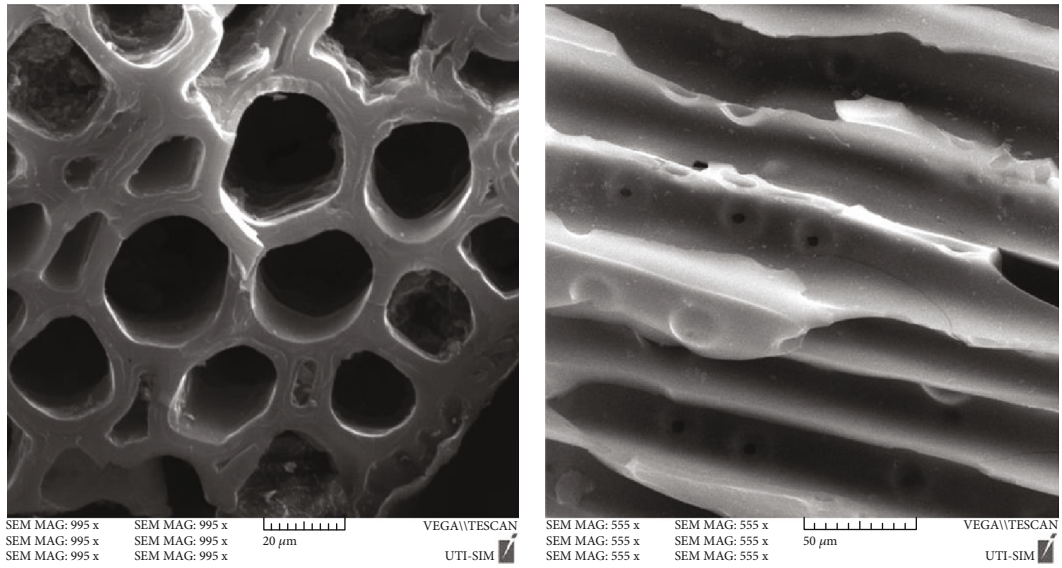

(a) (b)

Figure 2: SEM images of the commercial AC: pore size, shape, and alignment.

Table 2: Designated variables and their variation range for BCG decolorization with active carbon.

Independent variables	Measure units	Range		Symbol
		From	To	
BCG concentration	g/L	0.009	0.045	BCG
Adsorbent amount	g/L	0.5	3	AA
Contact time	min	60	240	CT

where BCG^0 and BCG^t are the BCG (g/L) concentrations at the time $t = 0$ and at the time $t = t$.

2.5. Bacterial Foraging Optimization. BFO is an optimization technique inspired by the foraging behavior of *E. coli* bacteria. In order to provide solutions to a specific problem, it simulates the evolution of a series of potential solutions using a set of specific mechanisms that include chemotaxis, reproduction, elimination, and dispersal (Figure 4).

All these steps are repeated until a stop criterion is reached. For the standard BFO, this stop criterion is represented by the number of dispersal steps (N_{ed}). In this work, the stop criterion combines two criteria, and the algorithm stops when one of them becomes true. These criteria are (i) the number of dispersal steps and (ii) the number of function evaluations (FEs). The reason for this modification relies on the fact that FEs can be relatively easily set as a stop criterion for almost all bioinspired metaheuristics and can be further used for comparison purposes, while the number of internal repetitions an algorithm performs does not correctly show the computational resources consumed versus the efficiency of the solution provided.

As can be observed from Figure 3, there is a close interconnection between the steps of the algorithm. The most iterated step is chemotaxis, which represents the movement of bacteria from food-scarce areas to affluent areas through swimming and tumbling. This is done by all bacteria (which, for the sake of simplicity, will be further referred to as individuals, and the colony of bacteria will be referred to as population) several times indicated by the N_c parameter. In the BFO algorithm, the mechanism used for food searching is associated with the repellent-attraction biological principle [79].

In the reproduction step, the individuals are sorted based on their fitness (a function that measures the individual's fitting to the environment). After that, the best individuals reproduce, while the worst ones are removed. This is performed N_{re} times, during which the population will be centered on several clusters and the overall diversity reduced. Therefore, to simulate the migration of bacteria into a new environment, with a probability indicated by a parameter (p_{ed}), some individuals are randomly replaced with new ones (the elimination-dispersal step).

In the initial BFO, p_{ed} has a fixed value; therefore, as the population evolves, the probability of replacing good individuals is the same as replacing worse individuals. As a result, individuals located in the vicinity of the global optimum can be replaced with individuals far from the optimum. Thus, potentially good solutions to the problem at hand can be lost. In order to avoid this aspect, in this work, p_{ed} is modified adaptively (equation (2)). This modification represents the main idea of the iBFO variant used in this work.

$$p_{ed} = \begin{cases} \dfrac{\text{fit}_{min} + \text{fit}_{avg}}{\text{fit}_{max} + \text{fit}_{min}}, & \text{if the objective is fitness minimization,} \\ \dfrac{\text{fit}_{max} - \text{fit}_{avg}}{\text{fit}_{max} - \text{fit}_{min}}, & \text{if the objective is fitness maximization,} \end{cases} \quad (2)$$

Table 3: Designated variables and their variation range for BCG decolorization with active carbon.

No.	Type[1]	Input variables						Response η (%)
		BCG (g/L)		AA (g/L)		CT (min)		
		Real	Coded[2]	Real	Coded[2]	Real	Coded[2]	
1	O1	0.045	1	3.006	1	240	1	27.96
2	O2	0.009	1	3.004	−1	240	1	31.94
3	O3	0.045	1	3.002	1	60	−1	21.54
4	O4	0.009	1	3.002	−1	60	−1	28.95
5	O5	0.045	−1	0.506	1	240	1	13.37
6	O6	0.009	−1	0.506	−1	240	1	23.77
7	O7	0.045	−1	0.5	1	60	−1	9.23
8	O8	0.009	−1	0.501	−1	60	−1	32.21
9	S1	0.049	0	1.754	α	150	0	18.27
10	S2	0.0051	0	1.752	$-\alpha$	150	0	44.60
11	S3	0.027	0	1.753	0	259.35	α	28.31
12	S4	0.027	0	1.757	0	40.65	$-\alpha$	16.33
13	S5	0.027	α	3.27	0	150	0	21.23
14	S6	0.027	$-\alpha$	0.23	0	150	0	12.16
15	C1	0.027	0	1.752	0	150	0	21.50
16	C2	0.027	0	1.752	0	150	0	21.59
17	C3	0.027	0	1.75	0	150	0	22.50
18	C4	0.027	0	1.754	0	150	0	24.32

[1]O = orthogonal design points; S = axial or star points; C = center points. [2]-1 = low value, 1 = high value, 0 = center value, and $-\alpha$, α = star point value.

Table 4: Literature reported BCG reference bands.

Authors	Tracked band (nm)	Ref.
Ghaedi et al.; this work	412	[62]; this work
Özdemir et al.	424	[63]
Salmalian et al.	430	[65]
Khan et al.	438	[73]
Bhanuprakash and Belagali; Murmu et al.; Shokrollahi et al.	442	[60, 64, 77]
Fassi et al.; Fassi et al.	444	[68, 69]
Palazzolo et al.	404 and 617	[78]
Bai et al.	613	[66]
Liu et al.	614	[61]
Chaleshtori et al.	616	[70]
Palazzolo et al.	617	[78]
Ying et al.	620	[71]
Torğut and Demirelli	623	[67]

where fit_{min}, fit_{max}, and fit_{avg} are the minimum, maximum, and average of the fitness of all individuals in the population.

In order to determine the optimal conditions for the considered process, two models were considered: (i) the regression equations determined using the RSM-based approach and (ii) ANNs. In the second case, the ANNs, on their own, required a series of optimization to determine their best parameters. Thus, in this work, iBFO is applied to perform two optimization types: process and model optimization.

Regarding process optimization, the process parameters are evolved and then fed into the considered model to generate the necessary predictions. On the other hand, in the case of ANN optimization, the necessary ANN parameters are directly encoded into a vector containing real numbers and then fed into the iBFO. This encoding is necessary because iBFO cannot directly work with ANN structures. Even though in neuroevolution, both topology (structure and organization of the neurons) and training can be performed by the optimizer, in this work, iBFO performs only

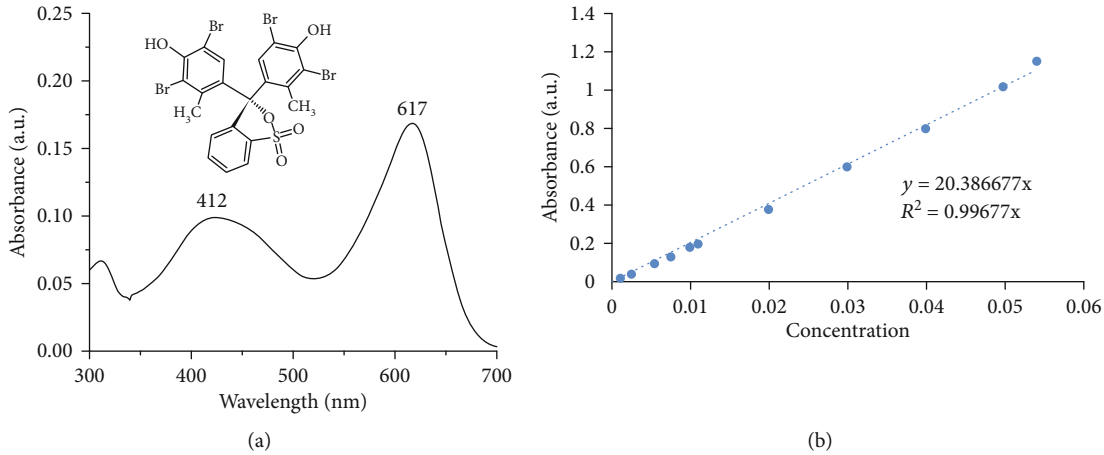

Figure 3: Chemical structure of BCG: (a) UV-Vis spectra and absorbance; (b) concentration calibration curve.

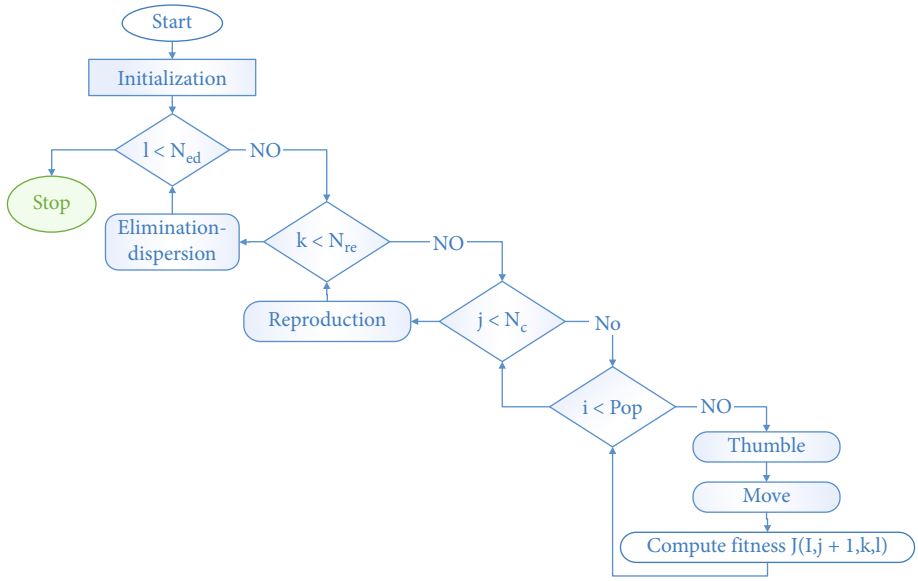

Figure 4: Schema of the BFO algorithm.

a topology determination. The training procedure is the standard approach used in the Keras framework for the ANN model implementation in combination with Adam, a stochastic optimizer based on scaled gradient updates. The type of model considered is sequential. The entire software implementation (iBFO and ANNs) was performed in Python.

3. Results and Discussions

3.1. Response Surface Method. The parameters that directly affect the efficiency of the decolorization process are BCG, AA, and CT, as presented in Table 2. In order to study the combined outcome of these three factors, experiments were performed, varying their values in carefully chosen intervals (Table 2), following a statistically designed experimental routine (Table 3). The experimental results were analyzed and interpreted using the MINITAB 17.1.0 software package. The full quadratic model obtained (equation (3)) had an R^2 of 90.34% and an adjusted R^2 of 79.47%.

$$\eta\,[\%] = 42.85 - 1741 \cdot \mathrm{BCG} - 0.0236 \cdot \mathrm{CT} + 7.04 \cdot \mathrm{AA} + 17631 \cdot \mathrm{BCG}^2 - 0.000056 \cdot \mathrm{CT}^2 - 2.72 \cdot \mathrm{AA}^2 + 1.231 \cdot \mathrm{BCG} \cdot \mathrm{CT} + 122.1 \cdot \mathrm{BCG} \cdot \mathrm{AA} + 0.0154 \cdot \mathrm{CT} \cdot \mathrm{AA}. \quad (3)$$

By setting one parameter at a constant value, preferable to the value in the middle of the designated interval of variation, three-dimensional plots (surface plots) were drawn as presented in Figures 5(a)–5(c).

Such exposure of the parameter variation allows the visualization of maximum and/or minimum points, which leads to accurate identification of the optimal values, highlighting the impact of the selected parameters on the decolorization efficiency.

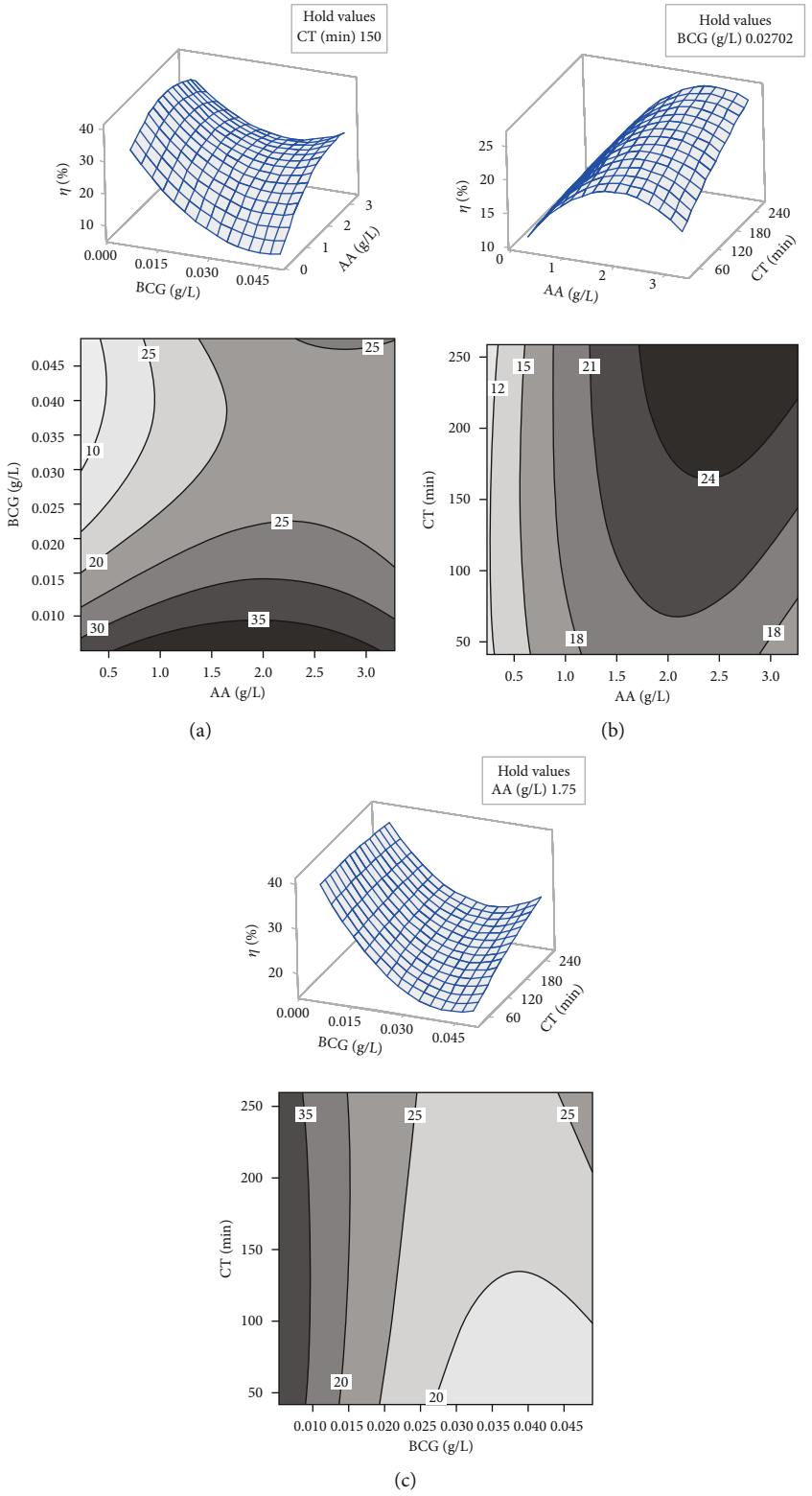

Figure 5: Surface and contour plots: (a) efficiency vs. BCG (g/L) and AA (g/L) at CT = 150 min; (b) efficiency vs. AA (g/L) and CT (min) at BCG = 0.02702 g/L; (c) efficiency vs. BCG (g/L) and CT (min) at AA = 1.75 g/L.

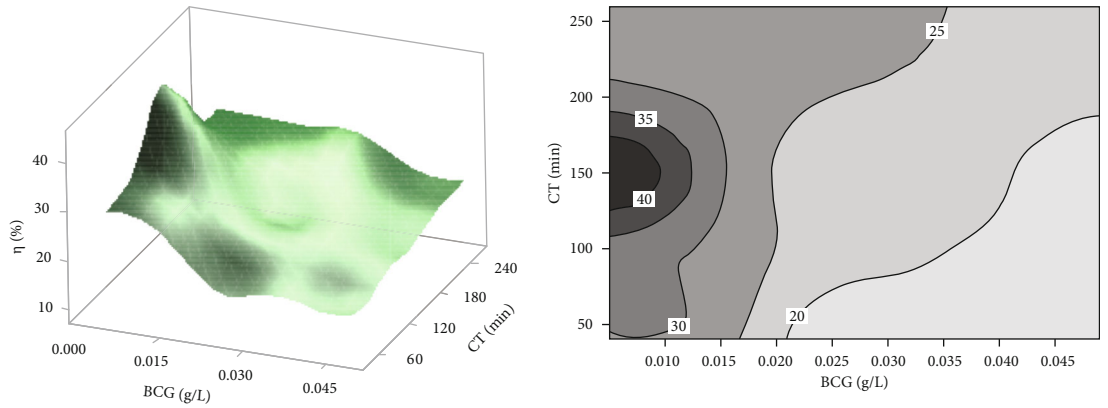

(a) (b)

Figure 6: (a) Three-dimensional response surface displaying the effects of BCG and CT on the process efficiency. (b) Two-dimensional contour plot showing the effects of BCG and CT on the process efficiency.

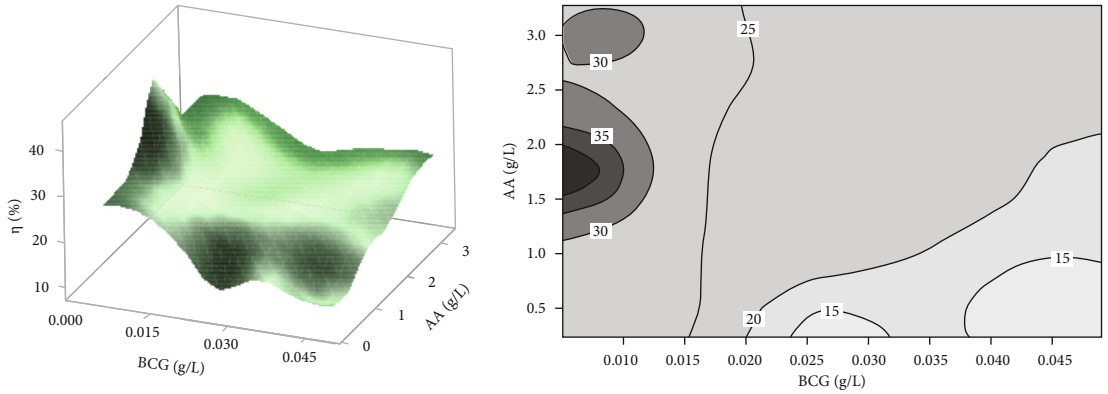

(a) (b)

Figure 7: (a) Three-dimensional response surface displaying the effects of BCG and AA on the process efficiency. (b) Two-dimensional contour plot showing the effects of BCG and AA on the process efficiency.

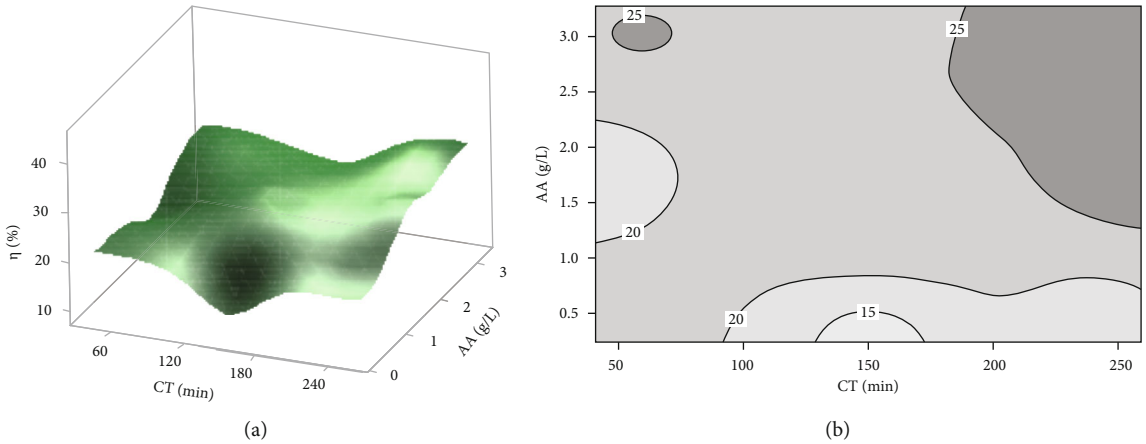

(a) (b)

Figure 8: (a) Three-dimensional response surface displaying the effects of CT and AA on the process efficiency. (b) Two-dimensional contour plot showing the effects of CT and AA on the process efficiency.

Table 5: Optimization results obtained with BFO and RSM for typical and extrapolation cases.

Case	Sol. no.	AA (g/L)	CT (min)	BCG (g/L)	η (%)
(i) Typical (-1,1 from DOE)*	1	1.683	81	0.010000	34.2
	2	1.830	235	0.010086	34.0
	3	1.632	122	0.010413	33.9
	4	1.819	151	0.010711	33.8
	5	1.948	216	0.011115	33.4
(ii) Extrapolation ($-\alpha$, α from DOE)*	6	1.844	197	0.005111	39.3
	7	2.112	212	0.005184	39.1
	8	2.018	99	0.007150	37.3
	9	1.485	123	0.007219	37.1
	10	1.162	79	0.007698	36.0

* $-\alpha$, -1, 0, 1, and α are the coding levels for the values from Table 3.

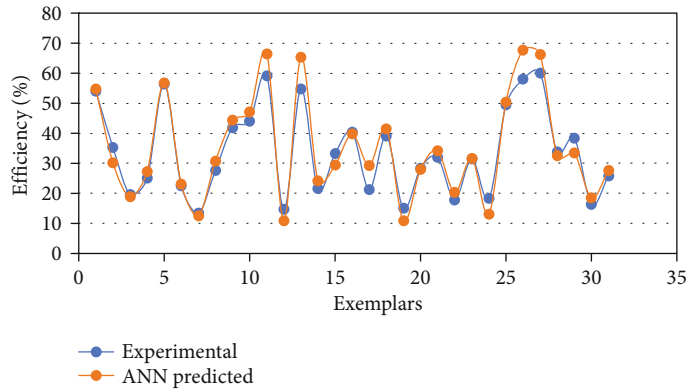

Figure 9: Evolution of the MSE in the training and validation phases for the best model obtained.

Table 6: Optimization results based on the ANN model.

Case	Sol. no.	AA (g/L)	CT (min)	BCG (g/L)	η (%)
(i) Model limits	1	0.110	4080	0.001730	99.9
	2	1.012	3862	0.001490	95.8
	3	1.188	1813	0.000330	93.0
	4	0.188	1737	0.000330	92.5
	5	2.771	3551	0.043100	92.3
(ii) (-1,1) from DOE*	6	1.777	237	0.009000	45.6
	7	1.685	235	0.009800	43.9
	8	1.687	227	0.011010	43.9
	9	1.795	238	0.009070	43.8
	10	1.353	155	0.027460	37.1
(iii) ($-\alpha$, α) from DOE*	11	1.844	197	0.005111	39.3
	12	2.112	212	0.005184	39.1
	13	2.243	202	0.006830	37.4
	14	1.485	123	0.007219	37.1
	15	1.162	79	0.007698	36.0

* $-\alpha$, -1, 0, 1, and α are the coding levels for the values from Table 3.

The 3D (three-dimensional) surface plots and contour plots were used to graphically describe decolorization efficiency at different values of the main process parameters. The interactive effect of bromocresol concentration and contact time for an adsorbent concentration of 1.75 g/L is illustrated in Figures 6(a) and 6(b). The active carbon performs better at lower BCG concentrations. The prolongation of contact time after reaching the equilibrium does not have positive outcomes towards decolorization efficiency.

The combined effect of AA and BCG after 150 min CT on the efficiency is depicted in Figures 7(a) and 7(b). It can be observed that the percentage of adsorbed BCG is increased with raising the adsorbent dosage especially at lower BCG values. The growing of the adsorbent amount besides a 2.5 g/L threshold does not improve the adsorption yield.

Finally, the evolution of the decolorization efficiency as a function of the contact time and the adsorbent amount is presented in Figure 8, where the interactive effect of these two parameters is studied at fixed values of BCG. As expected, raising the adsorbent amount and the contact time leads to an increase in BCG retention percentage.

According to the RSM method, the optimal values of the considered variables are BCG = 5.135 E − 03 g/L, AA = 1.58

Table 7: Comparison of several adsorbents' efficiency in decolorizing BCG.

Adsorbent	Considered process parameters	Optimization method	η (%)	Ref.
Acid-treated charcoal (ACT)	UV irradiation time, catalyst dosage, recycled catalyst dosage.	—	16.85	[73]
Co-adsorbed ACT			40.5	
AC derived from rice husk	Contact time, temperature, adsorbent dosage, pH, and initial concentration	—	93	[72]
Chitin nanofibers	Contact time, temperature, adsorbent dosage, pH, and initial concentration	IBM SPSS statistics; one-way ANOVA	92.75	[65]
Zeolitic imidazolate framework (ZIF-11)	pH, stirring speed, contact time, temperature	—	89	[80]
Almond husk	pH, adsorbent dosage, contact time, and initial and final concentration	—	97.5	[77]
Rice straw biochar	Biochar, pyrolysis temperature, solution pH, biochar dosage, initial dye concentration, and contact time	—	80	[81]
Rice husk biochar			50	
Activated biosorbent Phragmites karka	pH, agitation speed, contact time, biosorbent dosage, initial dye concentration, temperature	—	99.99	[64]
Fe_3O_4/MIL-88A nanocomposite	Contact time, adsorbent dosage, initial concentration	—	70	[82]
Commercial active carbon	Contact time, adsorbent dosage, initial concentration	Differential evolution	99.83	[75]
		RSM	97.77	
		Differential search	99.99	
Commercial active carbon	Contact time, adsorbent dosage, initial concentration	RSM	39.3	This work
		iBFO	>99	

g/L, and CT = 62.74 min that lead to 39.92% process efficiency.

As observed, there is a complex interdependency between the process parameters. Therefore, the standard analysis of the variation of efficiency considering two parameters at once does not provide a complete picture regarding the output parameters' lowest or highest surface points. Furthermore, since the RSM performs the optimization by setting some parameters fixed and varying only a few (usually just one parameter), the search space is not efficiently explored, and there is the possibility that other solutions can be found. Thus, iBFO was applied to perform an exhaustive search and identify promising high-efficiency regions.

The optimal results attained with this method (39.92%) are comparable to those reported in other studies focusing on the decolorization of bromocresol green with different types of active carbon. For example, in [73], the maximum efficiency of active charcoal from pine cones doped with Co was 41.86%.

3.2. Bacterial Foraging Optimization. Two cases were considered for process optimization using bacterial foraging optimization: (i) the statistical model determined using RSM and (ii) an ANN model. However, the determination of the ANN model is, in its turn, an optimization problem, and thus, iBFO was also applied for model optimization. In both the model and process optimization, the settings for the iBFO parameters were the same: $N_c = 20$, $N_s = 5$, $N_{re} = 8$, $N_{ed} = 20$, and the initial value for $p_{ed} = 0.25$.

3.2.1. RSM-Based Optimization. Using the regression model determined by the RMS approach (equation (3)), iBFO was applied to determine if additional optimal points could be found by thoroughly searching the search space indicated by the process parameters. To this means, the maximum process efficiency was identified based on AA, CT, and BCG.

As iBFO is flexible and permits an easy alteration of the intervals for the process parameters, multiple optimization cases were considered: (i) typical (when the minimum and maximum values for the independent variables are identical to the experiments, coded -1 and 1 from the DOE planning) and (ii) extrapolation (where the limits are set to $-\alpha$ and α from the DOE planning). Thus, in each considered case, ten runs were performed. From the multitude of solutions (from the vicinity of the optimum) provided by iBFO, for each case, Table 5 presents the best five combinations of parameters that optimize the process.

As observed in Table 5, the iBFO algorithm provided various solutions indicating a high capability of exploring the search space and finding promising areas. Depending on the specific requirements at a given time, the end user or the process manager can select a different optimization solution. Compared to the RSM approach, the iBFO, in combination with the statistical model, provided results similar in terms of efficiency. However, iBFO generated multiple solutions in the vicinity of the optimum, indicating that the interaction between parameters is complex and that different combinations of parameters lead to the same efficiency.

3.2.2. ANN-Based Optimization. In this case, the iBFO role is to determine the optimal topology that best fits the

considered process. The sequential ANNs considered in this work are trained using a supervised approach, and thus, the experimental data describing the process is used for hyperparameter tuning. However, as the number of experiments resulting from the standard DOE planning is relatively small, a series of random experiments were performed to increase the number of points that can be included in the training/testing phase. As a result, the efficiency was measured for a more extended period compared with the DOE plan. Thus, compared with the RSM strategy, the ANN model can predict without extrapolating a higher number of parameter combinations.

In order to perform the model determination, the standard data processing techniques used in the machine learning area were applied: (i) data normalization, (ii) data randomization, and (ii) data splitting. For data normalization, all the experimental points were normalized in the [-1,1] interval to ensure that no specific process parameter significantly influences the model based on the order of magnitude for its values. After that, to ensure that training is not performed on a subgroup of points, the data is randomly assigned to one of the phases: training/testing. The percentage of training data is 75%, and 25% is for testing.

After data processing, iBFO was applied to determine the best-suited model. This suitability is measured by the fitness function, which in the case of ANN determination is represented by the Mean Squared Error (MSE) in the training phase. The elements evolved by iBFO are strictly related to topology (hidden layers and neurons in each hidden layer). As the current iBFO version works with a population of fixed dimension, which for the current case corresponds to a limit on the number of hidden layers, based on a series of preliminary analyses, it was set to 5. Furthermore, the activation function for each neuron from the hidden layer is set to ReLU, while the activation function for the output layer is linear. Finally, in order to train each identified topology, the Adam optimizer was considered.

The best model obtained had two hidden layers with 33 and 22 neurons, respectively. The MSE was 16.14 in the training phase and 26.7 in the testing phase. The average absolute error and the correlation were 9.14% and 0.962 for training and 10.73% and 0.961 for testing. A comparison between the experimental and predicted values for the testing data is presented in Figure 9. As it can be observed, for most exemplars, the differences are relatively small, indicating the model's capability to capture the process efficiently.

iBFO and the determined ANN were then utilized to optimize the process. Table 6 presents the best five solutions provided by the model. In this case, two situations were considered: (i) when the limits for the search are the ones obtained through the supplementary experiments performed to expand the dataset, (ii) when the limits are set as in the DOE approach (-1,1), and (iii) when the limits are set to $(-\alpha, \alpha)$.

As seen in Table 6, the results considering the extended limits allow the identification of conditions that lead to ~100% efficiency. Regarding cases where the (-1,1) interval was considered, the solutions provided with the ANN-based model have a higher efficiency than those obtained with the RSM-based model. On the other hand, for the $(-\alpha, \alpha)$, the solutions provided had a similar efficiency. Therefore, the results obtained in this case are similar to those presented in the literature. For example, in [72], for an active carbon produced from rice husks, the maximum efficiency was 93%.

Overall, the results obtained with iBFO when using both the RSM and the ANN-based models indicate that the optimizer can explore the search space and identify distinct solutions in the vicinity of the optimum. Furthermore, this variety can support a large area of use cases where a specific parameter can be limited within the desired interval (considering a maximum efficiency and a minimization of consumed resources).

3.3. Comparison with Other Adsorbents. Several adsorbents have been used for BCG decolorization/removal from wastewater. Most of them are active carbons/charcoals prepared from various lignocellulosic biomass. Chitins, polymers, and various nanocomposites were also used, as presented in Table 7.

Most authors report the direct influence of individual process parameters on decolorization efficacy, such as adsorbent dosage, contact time, initial BCG concentration, pH, and temperature. However, only a few show optimization studies that report the conjugate influence of the process parameters and classify them in order of their significance for the process.

4. Conclusions

This study applied various modeling and optimization strategies to BCG decolorization on commercial activated carbon with the scope of demonstrating that the application of new approaches from the artificial intelligence area can provide optimal solutions. The methodologies included conventional (RSM) and nonconventional artificial intelligence methodologies (ANNs and a modified version of bacterial foraging optimization). iBFO was utilized as an optimizer for the model and process, with its adaptability and capabilities substantiating the favorable results obtained.

First, in order to consume the minimum resources (time, chemicals, etc.), the DOE methodology was applied to program a minimal number of statistically relevant experiments. Then, the most used strategy encountered in literature (RSM) was applied. Using the MINITAB 17.1.0 software suite, the findings were analyzed and interpreted and a statistical model was determined and then used for process optimization, with the maximum efficiency obtained being 39.92% at BCG = $5.135E-03$ g/L, AA = 1.58 g/L, and CT = 62.74 min. Compared with the experimental data obtained for the $[-\alpha, \alpha]$ DOE limits, this optimal value is close, but lower. This can be explained by the RSM-based model error ($R^2 = 90.34\%$). These results point out that this approach is not able to find better solutions.

To further test if the issue of not finding better solutions than the experimental data is related to the optimization strategy or to the model, the statistical model was applied in combination with iBFO. While the maximum efficiency

obtained was similar when using the same statistic model, iBFO could find multiple distinct combinations of parameters that lead to the same efficiency. This proved the capability of the optimizer to explore the search space efficiently and identify the regions with promising potential (local and global minima). These results also pointed out that within the considered DOE limits of $[-\alpha, \alpha]$, a higher efficiency could not be obtained.

Thus, a series of additional random experiments were performed and, together with the DOE plan, were used to determine an ANN model. First, its optimized topology (2 hidden layers with 33 neurons in the first one and 22 neurons in the second one) was identified using the iBFO approach. Then, it is applied to optimize the process considering different limitations for parameters. In this case, conditions that lead to >99% efficiency were identified, proving that even the classical processes can be further improved when good strategies are applied.

The strategy of starting with standard approaches and then when they fail to provide improved solutions to replace them with novel strategies from the area of artificial intelligence demonstrated that process modeling and optimization are not a straightforward fit-all approach and that there are cases where multiple variants must be tested before reaching an acceptable solution. The good results of the current case study pave the way for the advanced optimization of other types of processes, with a significant economic and industrial impact.

Data Availability

The data supporting the reported results is presented in the manuscript.

Conflicts of Interest

The authors highlight that they have no known competing financial interests or personal relationships that could have appeared to influence the work reported in this study.

Authors' Contributions

The authors are responsible for correctness of the statements provided in the manuscript.

Acknowledgments

This work was supported by "Program 4: Fundamental and frontier research—Exploratory research projects" financed by UEFISCDI (project no. PCE 58/2021).

References

[1] A. Abel, *The history of dyes and pigments: from natural dyes to high performance pigments, in Colour Design*, J. Best, Ed., Woodhead Publishing, 2nd edition, 2012.

[2] A. Gürses, M. Açıkyıldız, K. Güneş et al., "Classification of dye and pigments," in *Dyes and Pigments*, pp. 31–45, Springer International Publishing, Cham, 2016.

[3] L. P. Lingamdinne, S. Lee, J. S. Choi, V. R. Lebaka, V. R. P. Durbaka, and J. R. Koduru, "Potential of the magnetic hollow sphere nanocomposite (graphene oxide-gadolinium oxide) for arsenic removal from real field water and antimicrobial applications," *Journal of Hazardous Materials*, vol. 402, article 123882, 2021.

[4] R. I. Alsantali, Q. A. Raja, A. Y. A. Alzahrani et al., "Miscellaneous azo dyes: a comprehensive review on recent advancements in biological and industrial applications," *Dyes and Pigments*, vol. 199, article 110050, 2022.

[5] L. D. Ardila-Leal, R. A. Poutou-Piñales, A. M. Pedroza-Rodríguez, and B. E. Quevedo-Hidalgo, "A brief history of colour, the environmental impact of synthetic dyes and removal by using laccases," *Molecules*, vol. 26, no. 13, p. 3813, 2021.

[6] R. M. El-Shishtawy, "Functional dyes, and some hi-tech applications," *International Journal of Photoenergy*, vol. 2009, Article ID 434897, 21 pages, 2009.

[7] S. Benkhaya, S. M'rabet, and A. El Harfi, "A review on classifications, recent synthesis and applications of textile dyes," *Inorganic Chemistry Communications*, vol. 115, article 107891, 2020.

[8] S. Benkhaya, S. M'rabet, H. Lgaz, A. el Bachiri, and A. el Harfi, "Dyes: classification, pollution, and environmental effects," in *Dye Biodegradation, Mechanisms and Techniques: Recent Advances*, S. S. Muthu and A. Khadir, Eds., pp. 1–50, Springer, Singapore, 2022.

[9] S. H. Hashemi and M. Kaykhaii, "Azo dyes: sources, occurrence, toxicity, sampling, analysis, and their removal methods," in *Emerging Freshwater Pollutants*, T. Dalu and N. T. Tavengwa, Eds., pp. 267–287, Elsevier, 2022.

[10] A. Gürses, K. Güneş, and E. Şahin, "Removal of dyes and pigments from industrial effluents," in *Green Chemistry and Water Remediation: Research and Applications*, S. K. Sharma, Ed., pp. 135–187, Elsevier, 2021.

[11] R. Al-Tohamy, S. S. Ali, F. Li et al., "A critical review on the treatment of dye-containing wastewater: ecotoxicological and health concerns of textile dyes and possible remediation approaches for environmental safety," *Ecotoxicology and Environmental Safety*, vol. 231, article 113160, 2022.

[12] O. J. Hao, H. Kim, and P.-C. Chiang, "Decolorization of wastewater," *Critical Reviews in Environmental Science and Technology*, vol. 30, no. 4, pp. 449–505, 2000.

[13] Y. Anjaneyulu, N. Sreedhara Chary, and D. Samuel Suman Raj, "Decolourization of industrial effluents – available methods and emerging technologies – a review," *Reviews in Environmental Science and Bio/Technology*, vol. 4, no. 4, pp. 245–273, 2005.

[14] S. Samsami, M. Mohamadizaniani, M. H. Sarrafzadeh, E. R. Rene, and M. Firoozbahr, "Recent advances in the treatment of dye-containing wastewater from textile industries: overview and perspectives," *Process Safety and Environmental Protection*, vol. 143, pp. 138–163, 2020.

[15] M. C. Collivignarelli, A. Abbà, M. Carnevale Miino, and S. Damiani, "Treatments for color removal from wastewater: state of the art," *Journal of Environmental Management*, vol. 236, pp. 727–745, 2019.

[16] A. K. Verma, R. R. Dash, and P. Bhunia, "A review on chemical coagulation/flocculation technologies for removal of colour from textile wastewaters," *Journal of Environmental Management*, vol. 93, no. 1, pp. 154–168, 2012.

[17] J. Behin, N. Farhadian, M. Ahmadi, and M. Parvizi, "Ozone assisted electrocoagulation in a rectangular internal-loop airlift reactor: application to decolorization of acid dye," *Journal of Water Process Engineering*, vol. 8, pp. 171–178, 2015.

[18] A. H. Konsowa, M. E. Ossman, Y. Chen, and J. C. Crittenden, "Decolorization of industrial wastewater by ozonation followed by adsorption on activated carbon," *Journal of Hazardous Materials*, vol. 176, no. 1-3, pp. 181–185, 2010.

[19] D. Shahbazi, S. A. Mousavi, and D. Nayeri, "Low-cost activated carbon: characterization, decolorization, modeling, optimization and kinetics," *International Journal of Environmental Science and Technology*, vol. 17, no. 9, pp. 3935–3946, 2020.

[20] B. Beigzadeh, M. Bahrami, M. J. Amiri, and M. R. Mahmoudi, "A new approach in adsorption modeling using random forest regression, Bayesian multiple linear regression, and multiple linear regression: 2,4-D adsorption by a green adsorbent," *Water Science and Technology*, vol. 82, no. 8, pp. 1586–1602, 2020.

[21] M. Bahrami, M. J. Amiri, and F. Bagheri, "Optimization of the lead removal from aqueous solution using two starch based adsorbents: design of experiments using response surface methodology (RSM)," *Journal of Environmental Chemical Engineering*, vol. 7, no. 1, article 102793, 2019.

[22] J. L. Wang and L. J. Xu, "Advanced oxidation processes for wastewater treatment: formation of hydroxyl radical and application," *Critical Reviews in Environmental Science and Technology*, vol. 42, no. 3, pp. 251–325, 2012.

[23] A. S. Powar, A. Perwuelz, N. Behary, L. Hoang, and T. Aussenac, "Application of ozone treatment for the decolorization of the reactive-dyed fabrics in a pilot-scale process—optimization through response surface methodology," *Sustainability*, vol. 12, no. 2, pp. 471–485, 2020.

[24] S. Khameneh Asl, B. Mohammadi, and A. Khataee, "Optimization of anodizing parameters on photo decolorization of textile dye solution using N-doped titanium nanotubes with response surface methodology," *Asian Journal of Green Chemistry*, vol. 4, pp. 258–275, 2020.

[25] R. G. Saratale, G. D. Saratale, J. S. Chang, and S. P. Govindwar, "Decolorization and biodegradation of reactive dyes and dye wastewater by a developed bacterial consortium," *Biodegradation*, vol. 21, no. 6, pp. 999–1015, 2010.

[26] T. Arfin, N. Varshney, and B. Singh, "Ionic liquid modified activated carbon for the treatment of textile wastewater," in *Green Materials for Wastewater Treatment*, pp. 257–275, Springer, 2020.

[27] D. M. Lewis, "Coloration in the next century," *Review of Progress in Coloration and Related Topics*, vol. 29, no. 1, pp. 23–28, 1999.

[28] A. Venkataraman, L. Babu, and K. Aravamudan, "Unified, simple and decentralized treatment process for synthetic and real-time dye contaminated wastewaters," *Journal of Hazardous Materials*, vol. 423, no. Part B, article 127059, 2022.

[29] A. Singh, D. B. Pal, A. Mohammad et al., "Biological remediation technologies for dyes and heavy metals in wastewater treatment: new insight," *Bioresource Technology*, vol. 343, article 126154, 2022.

[30] C. Zampeta, K. Bertaki, I. E. Triantaphyllidou, Z. Frontistis, P. G. Koutsoukos, and D. V. Vayenas, "Pilot-scale hybrid system combining hydrodynamic cavitation and sedimentation for the decolorization of industrial inks and printing ink wastewater," *Journal of Environmental Management*, vol. 302, article 114108, 2022.

[31] V. S. Hakke, M. M. Seepana, S. H. Sonawane, A. K. Kola, and R. Vooradi, "Hybrid treatment technologies for the treatment of industrial wastewater," in *Water Pollution and Remediation: Heavy Metals, Inamuddin*, M. I. Ahamed and E. Lichtfouse, Eds., pp. 211–241, Springer International Publishing, Cham, 2021.

[32] A. Dulov, N. Dulova, and M. Trapido, "Combined physicochemical treatment of textile and mixed industrial wastewater," *Ozone: Science & Engineering*, vol. 33, no. 4, pp. 285–293, 2011.

[33] X.-J. Ma and H.-L. Xia, "Treatment of water-based printing ink wastewater by Fenton process combined with coagulation," *Journal of Hazardous Materials*, vol. 162, no. 1, pp. 386–390, 2009.

[34] M. T. Nechita, G. D. Suditu, A. C. Puițel, and E. N. Drăgoi, "Differential evolution-based optimization of corn stalks black liquor decolorization using active carbon and TiO_2/UV," *Scientific Reports*, vol. 11, no. 1, pp. 1–12, 2021.

[35] G. Alam, I. Ihsanullah, M. Naushad, and M. Sillanpää, "Applications of artificial intelligence in water treatment for optimization and automation of adsorption processes: recent advances and prospects," *Chemical Engineering Journal*, vol. 427, article 130011, 2022.

[36] M. S. Secula, G. D. Suditu, I. Poulios, C. Cojocaru, and I. Cretescu, "Response surface optimization of the photocatalytic decolorization of a simulated dyestuff effluent," *Chemical Engineering Journal*, vol. 141, no. 1-3, pp. 18–26, 2008.

[37] A. I. Atomi, G. D. Suditu, A. C. Puițel, and M. T. Nechita, "Experimental study on TiO_2 promoted photo-degradation of methylene blue," *Bulletin of Romanian Chemical Engineering Society*, vol. 5, no. 1, pp. 68–74, 2018.

[38] A. Azari, M. Yeganeh, M. Gholami, and M. Salari, "The superior adsorption capacity of 2,4-dinitrophenol under ultrasound-assisted magnetic adsorption system: modeling and process optimization by central composite design," *Journal of Hazardous Materials*, vol. 418, article 126348, 2021.

[39] G. E. Box and J. S. Hunter, "Multi-factor experimental designs for exploring response surfaces," *The Annals of Mathematical Statistics*, vol. 28, no. 1, pp. 195–241, 1957.

[40] R. H. Myers, D. C. Montgomery, and C. M. Anderson-Cook, *Response surface methodology: process and product optimization using designed experiments*, John Wiley & Sons, 2016.

[41] A. I. Khuri and S. Mukhopadhyay, "Response surface methodology," *WIREs Computational Statistics*, vol. 2, no. 2, pp. 128–149, 2010.

[42] M. Y. Badi, A. Esrafili, H. Pasalari et al., "Degradation of dimethyl phthalate using persulfate activated by UV and ferrous ions: optimizing operational parameters mechanism and pathway," *Journal of Environmental Health Science and Engineering*, vol. 17, no. 2, pp. 685–700, 2019.

[43] A. Azari, M. H. Mahmoudian, M. H. Niari et al., "Rapid and efficient ultrasonic assisted adsorption of diethyl phthalate onto $Fe^{II}Fe_2{}^{III}O_4$@GO: ANN-GA and RSM-DF modeling, isotherm, kinetic and mechanism study," *Microchemical Journal*, vol. 150, article 104144, 2019.

[44] A. M. Ghaedi and A. Vafaei, "Applications of artificial neural networks for adsorption removal of dyes from aqueous solution: a review," *Advances in Colloid and Interface Science*, vol. 245, pp. 20–39, 2017.

[45] D. I. Fertu, E. N. Dragoi, L. Bulgariu, S. Curteanu, and M. Gavrilescu, "Modeling the biosorption process of heavy

metal ions on soybean-based low-cost biosorbents using artificial neural networks," *Processes*, vol. 10, no. 3, 2022.

[46] H. Faris, S. Mirjalili, and I. Aljarah, "Automatic selection of hidden neurons and weights in neural networks using grey wolf optimizer based on a hybrid encoding scheme," *International Journal of Machine Learning and Cybernetics*, vol. 10, no. 10, pp. 2901–2920, 2019.

[47] A. Tealab, "Time series forecasting using artificial neural networks methodologies: a systematic review," *Future Computing and Informatics Journal*, vol. 3, no. 2, pp. 334–340, 2018.

[48] K. M. Passino, "Biomimicry of bacterial foraging for distributed optimization and control," *IEEE Control Systems Magazine*, vol. 22, no. 3, pp. 52–67, 2002.

[49] E. N. Dragoi and V. Dafinescu, "Review of metaheuristics inspired from the animal kingdom," *Mathematics*, vol. 9, no. 18, p. 2335, 2021.

[50] B. Hernández-Ocana, E. Mezura-Montes, and P. Pozos-Parra, "A review of the bacterial foraging algorithm in constrained numerical optimization," in *2013 IEEE Congress on Evolutionary Computation*, pp. 2695–2702, Cancun, Mexico, 2013.

[51] C. Yang, J. Ji, J. Liu, and B. Yin, "Bacterial foraging optimization using novel chemotaxis and conjugation strategies," *Information Sciences*, vol. 363, pp. 72–95, 2016.

[52] C. Luo, X. Yin, and C. Ni, "A novel discrete bacterial foraging algorithm and its application," *The Journal of Communication*, vol. 10, no. 4, pp. 238–244, 2015.

[53] V. K. Gupta, "Application of low-cost adsorbents for dye removal - a review," *Journal of Environmental Management*, vol. 90, no. 8, pp. 2313–2342, 2009.

[54] D. Taylor, *Adsorbents, in Bleaching and Purifying Fats and Oils*, G. R. List, Ed., AOCS Press, 2nd edition, 2009.

[55] G. Crini, "Non-conventional low-cost adsorbents for dye removal: a review," *Bioresource Technology*, vol. 97, no. 9, pp. 1061–1085, 2006.

[56] M. M. Hassan and C. M. Carr, "A critical review on recent advancements of the removal of reactive dyes from dyehouse effluent by ion-exchange adsorbents," *Chemosphere*, vol. 209, pp. 201–219, 2018.

[57] A. Srinivasan and T. Viraraghavan, "Decolorization of dye wastewaters by biosorbents: a review," *Journal of Environmental Management*, vol. 91, no. 10, pp. 1915–1929, 2010.

[58] S. De Gisi, G. Lofrano, M. Grassi, and M. Notarnicola, "Characteristics and adsorption capacities of low-cost sorbents for wastewater treatment: a review," *Sustainable Materials and Technologies*, vol. 9, pp. 10–40, 2016.

[59] I. Haq, A. S. Kalamdhad, and A. Pandey, "Genotoxicity evaluation of paper industry wastewater prior and post-treatment with laccase producing Pseudomonas putida MTCC 7525," *Journal of Cleaner Production*, vol. 342, article 130981, 2022.

[60] A. Shokrollahi, A. Alizadeh, Z. Malekhosseini, and M. Ranjbar, "Removal of Bromocresol green from aqueous solution via adsorption on Ziziphus nummularia as a new, natural, and low-cost adsorbent: kinetic and thermodynamic study of removal process," *Journal of Chemical & Engineering Data*, vol. 56, no. 10, pp. 3738–3746, 2011.

[61] D. Liu, J. Yuan, J. Li, and G. Zhang, "Preparation of chitosan poly(methacrylate) composites for adsorption of Bromocresol green," *ACS Omega*, vol. 4, no. 7, pp. 12680–12686, 2019.

[62] M. Ghaedi, H. Khajesharifi, A. Hemmati Yadkuri, M. Roosta, R. Sahraei, and A. Daneshfar, "Cadmium hydroxide nanowire loaded on activated carbon as efficient adsorbent for removal of Bromocresol green," *Spectrochimica Acta Part A: Molecular and Biomolecular Spectroscopy*, vol. 86, pp. 62–68, 2012.

[63] M. Özdemir, Ö. Durmuş, Ö. Şahin, and C. Saka, "Removal of methylene blue, methyl violet, rhodamine B, alizarin red, and bromocresol green dyes from aqueous solutions on activated cotton stalks," *Desalination and Water Treatment*, vol. 57, no. 38, pp. 18038–18048, 2016.

[64] B. M. Murmu, S. S. Behera, S. Das, R. K. Mohapatra, B. K. Bindhani, and P. K. Parhi, "Extensive investigation on the study for the adsorption of Bromocresol green (BCG) dye using activated Phragmites karka," *Indian Journal of Chemical Technology*, vol. 25, pp. 409–420, 2018.

[65] E. Salmalian, H. Rezaei, and A. Shahbazi, "Removal of bromocresol green from aqueous solutions using chitin nanofibers," *Environmental Resources Research*, vol. 7, no. 2, pp. 79–86, 2019.

[66] H. Bai, P. He, J. Chen et al., "Electrocatalytic degradation of bromocresol green wastewater on Ti/SnO_2-RuO_2 electrode," *Water Science and Technology*, vol. 75, no. 1, pp. 220–227, 2017.

[67] G. Torğut and K. Demirelli, "Comparative adsorption of different dyes from aqueous solutions onto polymer prepared by ROP: kinetic, equilibrium and thermodynamic studies," *Arabian Journal for Science and Engineering*, vol. 43, no. 7, pp. 3503–3514, 2018.

[68] S. Fassi, I. Bousnoubra, T. Sehili, and K. Djebbar, "Degradation of "bromocresol green"by direct UV photolysis, acetone/UV and advanced oxidation processes (AOP's) in homogeneous solution (H2O2/UV, S2O8 2-/UV). Comparative study," *Journal of Materials and Environmental Science*, vol. 3, no. 4, pp. 732–743, 2012.

[69] S. Fassi, K. Djebbar, I. Bousnoubra, H. Chenini, and T. Sehili, "Oxidation of bromocresol green by different advanced oxidation processes: Fenton, Fenton-like, photo-Fenton, photo-Fenton-like and solar light. Comparative study," *Desalination and Water Treatment*, vol. 52, no. 25-27, pp. 4982–4989, 2014.

[70] M. Z. Chaleshtori, M. Hosseini, R. Edalatpour, S. M. S. Masud, and R. R. Chianelli, "New porous titanium-niobium oxide for photocatalytic degradation of bromocresol green dye in aqueous solution," *Materials Research Bulletin*, vol. 48, no. 10, pp. 3961–3967, 2013.

[71] Y. L. Ying, S. Y. Pung, M. T. Ong, and Y. F. Pung, "A comparison study between ZnO nanorods and WO_3/ZnO nanorods in bromocresol green dye removal," *Solid State Phenomena*, vol. 264, pp. 87–90, 2017.

[72] O. C. Elijah, O. N. Collins, O. C. Obumneme, and N. B. Jessica, "Application of modified agricultural waste in the adsorption of bromocresol green dye," *Asian Journal of Chemical Science*, vol. 7, no. 1, pp. 15–24, 2020.

[73] I. Khan, N. U. Rahman, A. Ali, and K. Saeed, "Adsorption of cobalt onto activated charcoal and its utilization for decolorization of bromocresol green dye," *Bulgarian Chemical Communications*, vol. 51, no. 4, pp. 488–493, 2019.

[74] M. S. Secula, B. Cagnon, I. Cretescu, M. Diaconu, and S. Petrescu, "Removal of an acid dye from aqueous solutions by adsorption on a commercial granular activated carbon: equilibrium, kinetic and thermodynamic study," *Scientific Study & Research. Chemistry & Chemical Engineering, Biotechnology, Food Industry*, vol. 12, no. 4, pp. 307–322, 2011.

[75] E. N. Dragoi, M. T. Nechita, and G. D. Suditu, "Bromocresol green adsorption optimization using bio-inspired

metaheuristic optimizers," in *Achievements and Perspectives of Modern Chemistry*, pp. 154–154, Chişinău, Moldova, 2019.

[76] F. R. Zaggout, "Encapsulation of bromocresol green pH indicator into a sol-gel matrix," *Journal of Dispersion Science and Technology*, vol. 26, no. 6, pp. 757–761, 2005.

[77] M. Bhanuprakash and S. Belagali, "Study of adsorption phenomena by using almond husk for removal of aqueous dyes," *Current World Environment*, vol. 12, no. 1, pp. 80–88, 2017.

[78] M. A. Palazzolo, P. D. Postemsky, and M. Kurina-Sanz, "From agro-waste to tool: biotechnological characterization and application of Ganoderma lucidum E47 laccase in dye decolorization. 3," *Biotech*, vol. 9, no. 6, p. 213, 2019.

[79] X. Feng, Y. He, H. Yang, and Y. Juan, "Self-adaptive bacterial foraging optimization algorithm based on evolution strategies," *Revista Tecnica de la Facultad de Ingenieria Universidad del Zulia*, vol. 39, no. 8, pp. 350–358, 2016.

[80] R. Lamaria, B. Benotmanea, and S. Mezalib, "Zeolite imidazolate framework-11 for efficient removal of bromocresol green in aqueous solution, isotherm kinetics, and thermodynamic studies," *Desalination and Water Treatment*, vol. 224, pp. 407–420, 2021.

[81] D. Phuong, N. Loc, and T. Miyanishi, "Efficiency of dye adsorption by biochars produced from residues of two rice varieties, Japanese Koshihikari and Vietnamese IR50404," *Desalination and Water Treatment*, vol. 165, pp. 333–351, 2019.

[82] Y. Liu, Y. Huang, A. Xiao, H. Qiu, and L. Liu, "Preparation of magnetic Fe_3O_4/MIL-88A nanocomposite and its adsorption properties for bromophenol blue dye in aqueous solution," *Nanomaterials*, vol. 9, no. 1, p. 51, 2019.

Hindawi
Adsorption Science & Technology
Volume 2022, Article ID 9739915, 15 pages
https://doi.org/10.1155/2022/9739915

Research Article

Computational-Based Approaches for Predicting Biochemical Oxygen Demand (BOD) Removal in Adsorption Process

Mohamed K. Mostafa,[1] **Ahmed S. Mahmoud**,[2] **Mohamed S. Mahmoud**,[3] **and Mahmoud Nasr**[4,5]

[1]*Faculty of Engineering and Technology, Badr University in Cairo (BUC), Cairo, Egypt*
[2]*Scientific Research Development Unit, Egyptian Russian University (ERU), Badr, Egypt*
[3]*Sanitary and Environmental Engineering Institute (SEI), Housing and Building National Research Center (HBRC), Egypt*
[4]*Environmental Engineering Department, Egypt-Japan University of Science and Technology (E-JUST), New Borg El-Arab City Alexandria 21934, Egypt*
[5]*Sanitary Engineering Department, Faculty of Engineering, Alexandria University, P.O. Box 21544, Alexandria 21526, Egypt*

Correspondence should be addressed to Mahmoud Nasr; mahmoud.nasr@ejust.edu.eg

Received 8 March 2022; Revised 22 April 2022; Accepted 27 April 2022; Published 10 May 2022

Academic Editor: Stefano Salvestrini

Predicting the adsorption performance to remove organic pollutants from wastewater is an essential environmental-related topic, requiring knowledge of various statistical tools and artificial intelligence techniques. Hence, this study is the first to develop a quadratic regression model and artificial neural network (ANN) for predicting biochemical oxygen demand (BOD) removal under different adsorption conditions. Nanozero-valent iron encapsulated into cellulose acetate (CA/nZVI) was synthesized, characterized by XRD, SEM, and EDS, and used as an efficient adsorbent for BOD reduction. Results indicated that the medium pH and adsorption time should be adjusted around 7 and 30 min, respectively, to maintain the highest BOD removal efficiency of 96.4% at initial BOD concentration $(C_o) = 100$ mg/L, mixing rate = 200 rpm, and adsorbent dosage of 3 g/L. An optimized ANN structure of 5–10–1, with the "*trainlm*" back-propagation learning algorithm, achieved the highest predictive performance for BOD removal (R^2: 0.972, Adj-R^2: 0.971, RMSE: 1.449, and SSE: 56.680). Based on the ANN sensitivity analysis, the relative importance of the adsorption factors could be arranged as pH > adsorbent dosage > time ≈ stirring speed > C_o. A quadratic regression model was developed to visualize the impacts of adsorption factors on the BOD removal efficiency, optimizing pH at 7.3 and time at 46.2 min. The accuracy of the quadratic regression and ANN models in predicting BOD removal was approximately comparable. Hence, these computational-based methods could further maximize the performance of CA/nZVI material for removing BOD from wastewater under different adsorption conditions. The applicability of these modeling techniques would guide the stakeholders and industrial sector to overcome the nonlinearity and complexity issues related to the adsorption process.

1. Introduction

Recently, adsorption has been employed in several types of research as an efficient and reliable process for wastewater treatment [1–3]. The adsorption systems neither consume a lot of electricity nor generate large amounts of sludge [4, 5]. Moreover, the adsorbent material could be appropriately synthesized to provide effective adsorption sites to capture the pollutants from wastewater [6, 7]. However, the adsorption process is highly influenced by several operational factors such as time, pH, and mixing speed [8]. The correlation between these environmental factors and pollutant removal efficiency could be described by nonlinear and complex modeling methods [9]. Hence, more studies are required to investigate the applicability of various statistical tools and artificial intelligence techniques for predicting adsorption performance.

Artificial neural network (ANN) models have been used in recently published studies as a proper method to describe the adsorption performance in relation to operational conditions [10–12]. The architecture of ANN is composed of multiple processing elements (or units) arranged in layers. These units, known as neurons, are highly interconnected and work in parallel to solve complex problems and get relevant relationships among the input attributes. For instance, Mahmoud et al. [13] found that an ANN model could simulate and predict phosphate removal in adsorption experimentation, showing a predictive accuracy of R^2: 0.976. Several operational factors such as solution pH, adsorbent dosage, and mixing speed were used in the adsorption process, showing that pH was the most influential attribute [13]. Hamdy et al. [14] also demonstrated that the removal efficiency of methylene blue (MB) dye from wastewater could be explained by several adsorption factors incorporated into an ANN model (R^2: 0.931). These input attributes included medium pH, initial MB level, and adsorption time; among them, time was the most influential factor [14].

Several researchers have also used regression models and a combination of statistical tools to predict the treatment performance under different operational factors. For example, Fawzy et al. [15] used a quadratic regression model to predict the Ni(II) removal efficiency via adsorption onto plant biomass. The quadratic equation described the correlation between Ni(II) and several inputs (e.g., pH, biomass dosage, and adsorption time) with high predictive accuracy of R^2 = 0.837 [15]. Their study demonstrated that the statistical model could appropriately illustrate the interaction among the input parameters and the shape of the input-output curve [15]. In another study, Fawzy et al. [16] employed a quadratic model to predict the Cd(II) removal efficiency via adsorption onto *Gossypium barbadense* waste. Total Cd(II) removal was achieved under the optimized condition of pH = 7.61, biosorbent diameter = 0.125–0.25 mm, and biosorbent dosage = 24.74 g/L within 109.77 min at initial Cd(II) = 50 mg/L [16].

Given the aforementioned aspects, the application of the computational approaches to describe the adsorption process is an essential point of research. However, further investigations are required to verify the implementation of ANN and quadratic models to predict organic matter removal. This objective would offer a feasible and sustainable approach to domestic wastewater treatment.

Hence, this research focused on predicting and optimizing the BOD removal performance in adsorption experimentation by a computational-based approach (quadratic regression and ANN models). In particular, the study objectives are fourfold: (1) characterization of adsorbent material synthesized by the entrapment of nanozero-valent iron into cellulose acetate polymer (CA-nZVI), i.e., this material has been widely used in the adsorption system due to its proper mechanical strength, thermal stability, and accessibility; (2) use of the CA-nZVI adsorbent to reduce organic matter from wastewater, expressed by BOD, i.e., BOD is considered the standard criterion for assessing the organic pollution of domestic wastewater; (3) describe the influence of various adsorption factors, i.e., pH, adsorbent dosage, time, mixing rate, and initial BOD concentration (C_o), on BOD removal efficiency; and (4) employ computational techniques, i.e., ANN and polynomial regression models, to predict and optimize the adsorption process.

2. Materials and Methods

2.1. Preparation of Adsorbent Material. For preparing an iron solution, around 0.0037 M of ferric chloride hexahydrate ($FeCl_3{\cdot}6H_2O$; 98.5% pure, Arabic lab.) was dissolved in 60 mL of a mixture of 4 (ethanol; C_2H_6O, 95% pure, World Co.) : 1 (deionized water). In parallel, 0.7564 g of reducing sodium borohydride ($NaBH_4$; 99% pure, Win lab.) was dissolved in 200 mL of deionized water to prepare the $NaBH_4$ solution. Further, the reducing $NaBH_4$ solution was placed in a burette and added drop by drop into the prepared iron solution. Black iron nanoparticles precipitate as a result of the direct reaction (Equation ((1)). The iron nanoparticles, known as nZVI, were then washed with distilled water and dried at 75°C for 5 h:

$$2FeCl_3(aq) + 6NaBH_4(aq) + 18H_2O \longrightarrow 2Fe^0(s) + 21H_2(g) + 6B(OH)_3(aq) + 6NaCl(aq). \quad (1)$$

Further, the prepared nZVI was capsulated into cellulose acetate (CA; 99%, Oxford) polymer, using the phase inversion approach [17]. Briefly, at room temperature, 4 g of CA was dissolved in 25 mL dimethylformamide (DMF; 99.99%, Fisher Chemical) solution and then mixed at 300 rpm until complete dissolution (within approximately 60 min). About 0.4 g of nZVI was mixed into the dissolved CA solution for 10 min before being cast into a gelation bath. The preparation of the gelation bath included 2 L of nonsolvent distilled water, 2 wt% DMF, and 0.2 wt% sodium lauryl sulphate (SLS). The prepared CA/nZVI beads (around 3–4 mm in diameter) were collected and washed with distilled water and then used for the adsorption experimentation.

2.2. Preparation of BOD Containing Solution (Adsorbate). Raw wastewater samples were collected from a sewage treatment plant located in New Cairo, Egypt. The samples were analyzed for BOD and subjected to different dilution regimes with ultrapure water. Working stock solutions with BOD concentrations of about 100, 200, 300, 400, and 500 mg/L were prepared and used for the individual experiments.

2.3. Batch Studies on Adsorption. Batch experiments were conducted to determine the effects of adsorption factors on the BOD removal efficiency. For this objective, a one-factor-at-a-time approach was used to prepare the batch assays statistically (Table 1). The factors (pH, CA/nZVI dosage, time, stirring rate, and C_o) and the associated range values were selected following the approaches of previous studies [18–20]. After each experimental run, the percentage of BOD removal (R) and the quantity of sorbed BOD were calculated by Equations (2) and (3). All tests were performed in triplicate, and the average values were recorded:

Table 1: Operating conditions of batch adsorption experiments for BOD removal.

Experimental assay	pH	Dosage (g/L)	Time (min)	Stirring rate (rpm)	C_o (mg/L)
Effect of pH	3–11	3	25	200	300
Effect of adsorbent dose	7	1–5	25	200	300
Effect of contact time	7	3	5–60	200	300
Effect of stirring rate	7	3	25	100–500	300
Effect of BOD concentration	7	3	25	200	100–500

$$R\,(\%) = \left(\frac{C_0 - C_e}{C_0}\right) \times 100, \tag{2}$$

$$q_e\,(\mathrm{mg/g}) = \frac{(C_0 - C_e)V}{M}, \tag{3}$$

where C_o and C_e refer to the initial and equilibrium BOD concentrations (in mg/L), respectively, q_e represents the equilibrium adsorption capacity (mg/g), V is aqueous phase volume (L), and M represents the adsorbent's dry mass (mg).

2.4. Analytical Analysis. The concentrations of BOD in the aqueous solutions were determined using the procedures of *Standard Methods for the Examination of Water and Wastewater* [21]. An X-ray diffractometer (PANalytical's, X'Pert PRO MRD, Netherlands) was used to determine the X-ray diffraction (XRD) patterns of the synthesized nZVI. The XRD equipment was operated with current and voltage levels of 30 mA and 40 kV, respectively. A copper (Cu) K-alpha radiation with a wavelength $(\lambda) = 1.5406$ Å was used to record the XRD patterns in a 40–90° range (step size of 0.02°) [14]. The XRD spectra were used to estimate the crystallite size of the prepared nanoparticles, following Scherrer's formula:

$$D = \frac{K \quad \lambda}{\beta \quad \cos}, \tag{4}$$

where D is the average crystal size, K is the nanoparticle shape factor, θ is the peak diffraction angle, β is pure diffraction broadening, and λ is the X-ray wavelength.

The nanoparticles' surface morphology was measured by a scanning electron microscope (Philips SEM, Quanta 250 field emission gun (FEG), USA). The elemental composition of nZVI was analyzed using energy-dispersive spectroscopy (EDS) in conjunction with SEM at a high magnification of 16kx. For determining the pH at the point of zero charge (pH_{PZC}), the solution pH was incrementally adjusted from 2 to 12 using either 1 N H_2SO_4 or 1 N NaOH (pH_i) in a 100 mL Erlenmeyer flask. About 0.1 g of nZVI was added to the flasks and kept at 23°C for 24 h, and then, the final pH readings were recorded (pH_f).

2.5. Computational-Based Studies

2.5.1. Artificial Intelligence Neural Networks. Figure 1 shows the ANN architecture used to predict BOD removal from a given dataset of five input variables (pH, adsorbent dose, time, stirring rate, and C_o), forming 25 experimental runs. The ANN model is composed of three subsequent layers, i.e., an input layer with 5 neurons, a hidden layer with multiple neurons (m), and the last layer with a single neuron. Each node in the hidden layer is interconnected with a number of weighted signals from the neurons of the 5-length input vector ($P_{5\times1}$). In particular, the inputs were weighted using a $m \times 5$ weight matrix ($W_{m\times5}$) and summed up, giving the formula of $\Sigma W_{m\times5} \cdot P_{5\times1}$. This expression was added to a m-length bias ($b_{m\times1}$), and then, a tangent sigmoid (tansig) transfer function was employed to generate an output; $a_{m\times1} = \mathrm{tansig}(\Sigma W_{m\times5} \cdot P_{5\times1} + b_{m\times1})$. This output was weighted using a $1 \times m$ weight matrix ($W_{1\times m}$), and then, a 1-length bias ($b_{1\times1}$) was added. Finally, a linear (purlin) transfer function was used to generate a single neuron in the output layer using the formula of $a_{1\times1} = \mathrm{purlin}(\Sigma W_{1\times m} \cdot a_{m\times1} + b_{1\times1})$. The "tansig" transfer function limits the output between −1 and +1, whereas the "purlin" function generates outputs in the $-\infty$ to $+\infty$ range [22]. The ANN output was compared with the actual BOD removal efficiencies, and the network weights and biases were adapted until reaching the best predictive performance. The total data describing the inputs-target correlations were randomly separated into three subgroups: training (70%), validation (15%), and testing (15%).

During the ANN learning phase with a back-propagation technique, the weights and biases were adjusted using several epochs (trials). The mean squared error (MSE) between the ANN output and measured BOD removal reached its minimum value at the best network performance. This feed-forward ANN model was used for its simplicity (no cycles or loops) to describe complex input-output relationships and to cope with the weighting adjustment issues [23]. In this study, the number of neurons (m) and the training algorithms were optimized to develop the most suitable ANN architecture. The MATLAB (R2015a) software was used to perform all the ANN computations.

2.5.2. Regression Analysis. A quadratic regression model (Equation (5)) was developed to predict BOD removal and estimate the optimum adsorption condition. Moreover, the results of the polynomial model were used to visualize the correlation between BOD removal and the adsorption factors. The model parameters were estimated based on the least square method [24] to fit the BOD removal data. The goodness-of-fit criteria (R^2 and Adj-R^2) were used to assess the predictive accuracy of the quadratic model [25]. The t-test was used to verify the significance level ($\alpha = 0.05$) among the adsorption variables [26]. The MATLAB (R2015a) software was used to conduct all the statistical calculations:

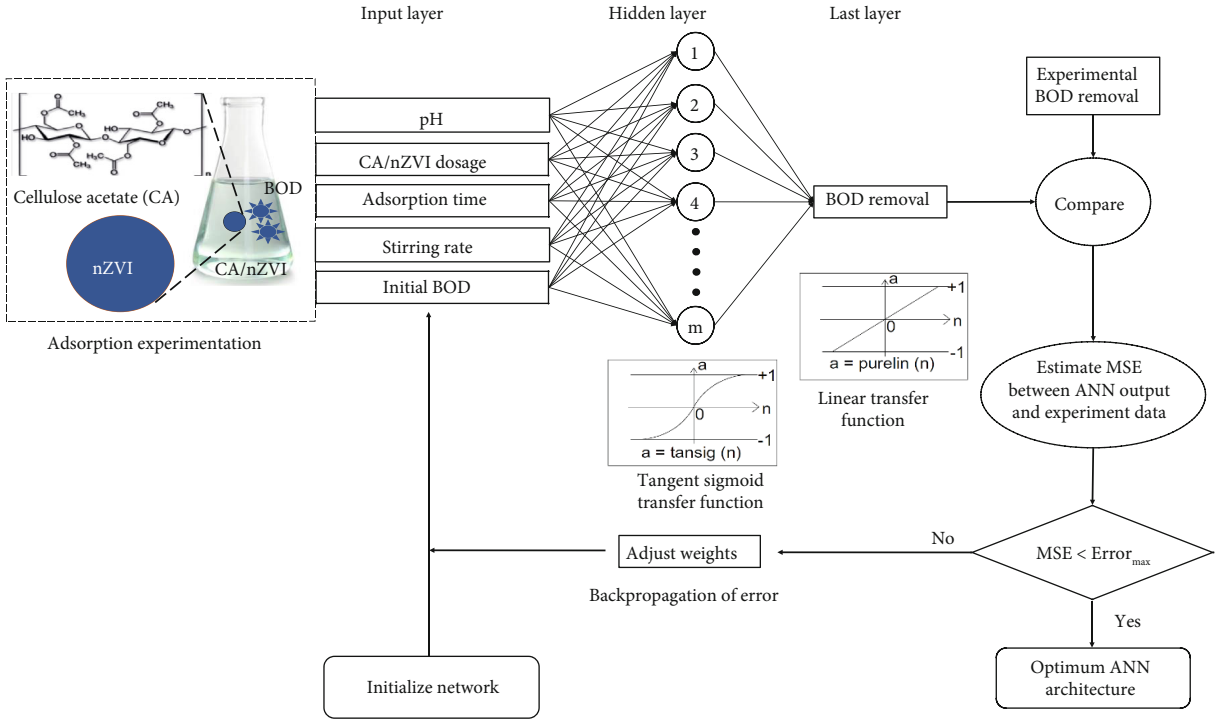

Figure 1: Flowchart of feed-forward back-propagation ANN model for predicting BOD removal efficiency using five adsorption factors, i.e., solution pH, CA/nZVI dosage, time, stirring speed, and initial BOD concentration.

$$Y = \beta_0 + \beta_i(x_i) + \beta_{ii}(x_i)^2, \quad (5)$$

where Y is the BOD removal efficiency predicted using the inputs (x_i), β_0 is the model intercept, and β_i and β_{ii} represent the constants associated with the linear and squared forms of the inputs, respectively.

3. Results and Discussion

3.1. Characterization of nZVI. Figure 2(a) shows the XRD pattern in the 2θ range of 40–90° for the prepared nZVI. Two peaks were recorded at $2\theta \approx 44.6$ and 64.9° for planes Fe (110) and Fe (200), respectively. The results of XRD demonstrated the dominance of zero-valent iron (Fe^0) in the prepared nanoparticles. Comparable XRD peaks related to nZVI characterization have been reported elsewhere [13, 27]. Based on Scherrer's equation, the particle size of the prepared nZVI adsorbent ranged from 23 to 59 nm, obeying the results provided by the SEM morphological study (Figure 2(b)). In particular, the SEM image of the synthesized nZVI showed a heterogeneous and irregular pore structure with particle sizes ranging from 33 to 56 nm. Additionally, many pores were observed in the prepared nanoparticles, facilitating the diffusion and mass transfer of molecules inside the nanomaterial [28]. The SEM image also showed the presence of larger nanoclusters (agglomerated particles), which could be assigned to the magnetic forces existing between the iron nanoparticles. Similar chainlike aggregates and surface tension properties have also been reported while preparing the nZVI material [29]. The EDS analysis observed the presence of iron, gold, and oxygen with an elemental weight content of 51.49%, 34.53%, and 13.98, respectively (Figure 2(c)). The oxygen element could be generated from the oxidation reaction with air and/or water in the outer layer of nZVI. The oxide formation on the nanoparticles' surface layer has also been reported [30]. Moreover, the detection of the Au signal in EDS could assign to the sample coating with a gold layer, following the laboratory analytical procedure [31]. The plot of ΔpH versus pH_i indicated that the pH_{PZC} of nZVI could be determined around 7.5 (Figure 2(d)). At this pH_{PZC}, the net surface charge of nZVI became zero, where the nZVI surface would be positively charged at $pH < pH_{PZC}$ and negatively charged at $pH > pH_{PZC}$ [32]. Moreover, at $pH > pH_{PZC}$, the nZVI particles could partially disaggregate because of surface charge repulsion [33].

3.2. Effect of Operating Conditions on BOD Removal. The BOD removal efficiency varied considerably in response to the change in the adsorption factors (Figure 3). For instance, adapting the solution pH to 7–8 would provide a suitable condition for BOD reduction (Figure 3(a)). This pH range complied with the pH_{PZC}, supporting the involvement of strong attractive and binding forces to remove organic impurities. Moreover, the optimum pH condition would facilitate the generation of hydroxyl radicals (·OH) to degrade and oxidize a series of organic compounds [29]. However, decreasing the pH level below pH_{PZC} was associated with unsatisfactory BOD removal, probably due to the dissolution and/or separation of Fe from nZVI [34]. The BOD removal efficiency was also maximized (above 90%) at pH of 7 in an adsorption process using mixed adsorbent

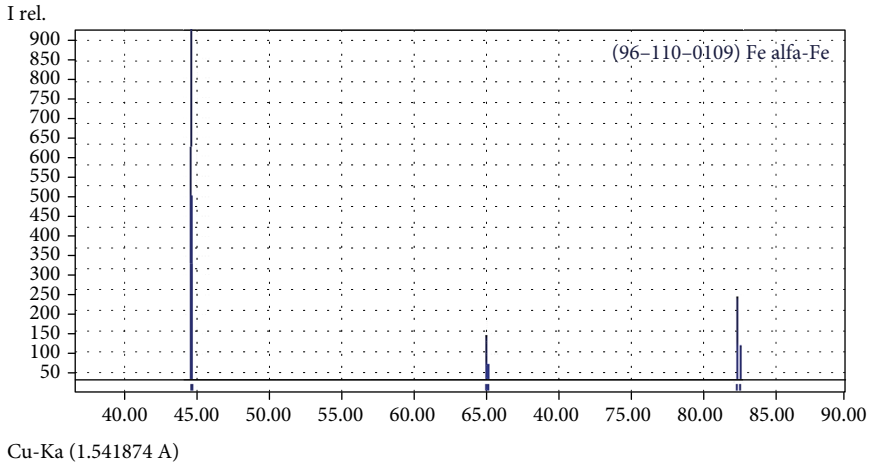

(a)

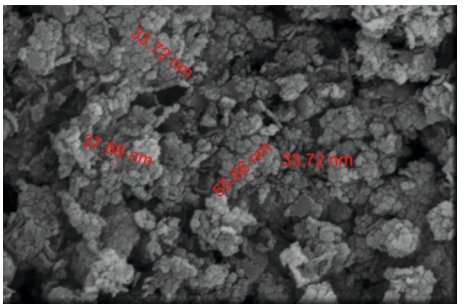

(b)

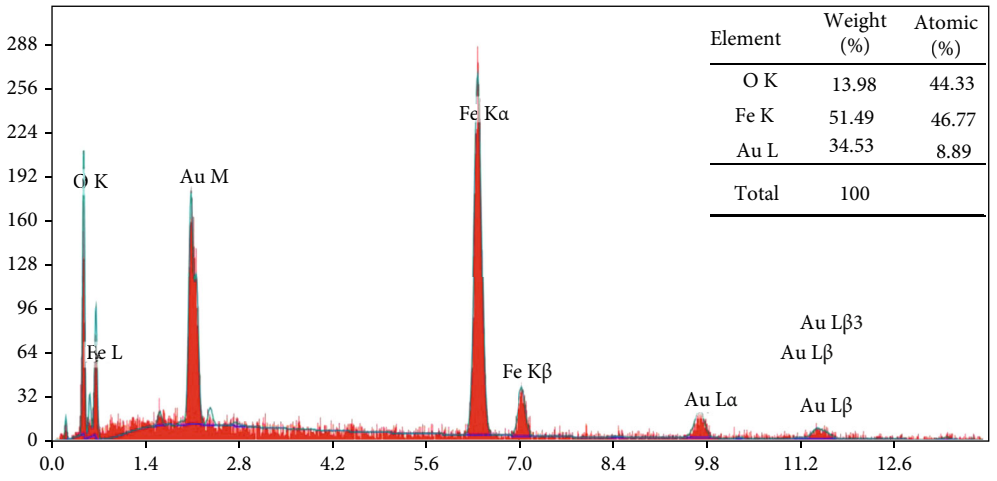

(c)

Figure 2: Continued.

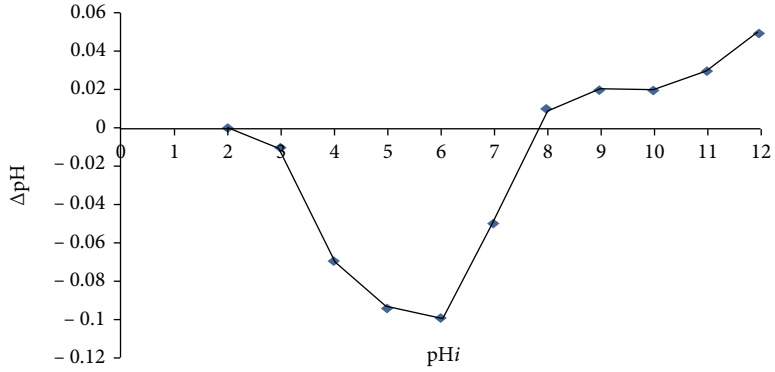

(d)

Figure 2: Characterization of the prepared CA/nZVI adsorbent (a) XRD, (b) SEM, (c) EDS, and (d) pH_{PZC}.

carbon [35]. Their study also demonstrated that the alkaline condition ($pH > pH_{PZC}$) would promote the abundance of OH^- ions to hinder the diffusion of organic ions [35].

The BOD removal efficiency was also enhanced by increasing the CA/nZVI dosage for the 1–5 g/L range (Figure 3(b)). For instance, the BOD removal efficiency improved from 66.3% to 83.2% when the CA/nZVI dosage increased from 1.0 g/L to 5.0 g/L, respectively. Increasing the adsorbent dosage provided more vacant sites to capture large amounts of organic ions. Similar behavior was observed for organic matter removal via an adsorption system with wood fly ash (adsorbent), showing an increase in BOD removal from 4 to 24% with elevating the dosage from 20 to 160 g/L, respectively [36]. Their study demonstrated that raising the adsorbent dosage was accompanied by greater surface area and carbon content, finally promoting higher sorption of organic pollutants [36].

The adsorption time within the range of 5–60 min also influenced the BOD removal efficiency (Figure 3(c)). A high BOD reduction (61.5%) occurred rapidly within the first 10 min, assigning to the availability of a large number of vacant sites at the initial stage. This BOD removal reached 76.8% after 25 min and then slightly increased to 81.2% after 60 min (Figure 3(c)). It could be observed that the adsorption process started to reach the equilibrium state after 25 min due to nZVI saturation. This time was shorter than 60 min used to remove BOD with an efficiency of 91.3% via adsorption onto green synthesized nanomaterials [37].

The BOD removal efficiency also varied according to the rate of mixing nZVI particles in the aqueous solutions (Figure 3(d)). The mixing speed of about 200–300 rpm was suitable to improve BOD removal due to facilitating the transfer and diffusion of organic ions through the nZVI pores. However, increasing the mixing speed over 300 rpm would not be recommended in the adsorption process, probably due to further desorption of the captured contaminants under fast agitation. Moreover, the operational cost of the adsorption system would be expensive due to the surplus electricity input to reach 500 rpm.

The results in Figure 3(e) depict that increasing C_o in the 100–500 mg/L range was associated with a drop in BOD removal from 96.4% to 61.5%. Most vacant adsorption sites are available for entrapping organic ions at low C_o, in agreement with previous results [27, 37, 38]. Increasing C_o tends to provide a driving force to overcome the mass transfer resistance of solute onto nZVI. However, at a high C_o condition, the adsorption capacity of nZVI would suffer from increased competition among organic ions and blockage of the available active sites [10]. This finding verifies the slight reduction in the adsorption performance at an excessive C_o.

3.3. BOD Removal by Different Adsorbents Reported in the Literature. Table 2 includes the removal efficiencies of BOD using various adsorbent materials reported in the literature compared to CA/nZVI applied in this study. For example, Mahmoud et al. [37] used soft black tea to prepare nZVI, which removed 91.3% of BOD at pH 8, stirring rate 200 rpm, and adsorbent dosage 3.2 g/L within 60 min. To avoid the unmanaged disposal of wood residues, Laohaprapanon et al. [36] used wood fly ash to remove BOD via batch sorption experiments. Their study achieved BOD removal of 24% using an ash dosage of 160 g/L within 20 min. Due to its high carbon content and quite accessibility, date palm waste was used to prepare activated carbon, which is further employed for organic matter adsorption [39]. Their study showed that 1 g/L of this activated carbon could eliminate 92.8% of BOD at pH = 6.0, agitation rate = 400 rpm, and 25°C within 150 min [39]. It could be noticed that nZVI exhibited higher BOD reduction than the application of agricultural wastes. This finding could be assigned to the dual effects of adsorption and degradation caused by nZVI.

3.4. Isotherm and Kinetic Studies. Three isotherm models were used to describe the adsorption equilibrium between organic pollutants and CA/nZVI (Figure 4(a)). These models were Langmuir [40] (Equation (6)), Freundlich [41] (Equation (7)), and Tempkin and Pyzhev [42] (Equation (8)):

$$\frac{C_e}{q_e} = \left(\frac{1}{Q_m}\right) C_e + \frac{1}{K_L \cdot Q_m}, \quad (6)$$

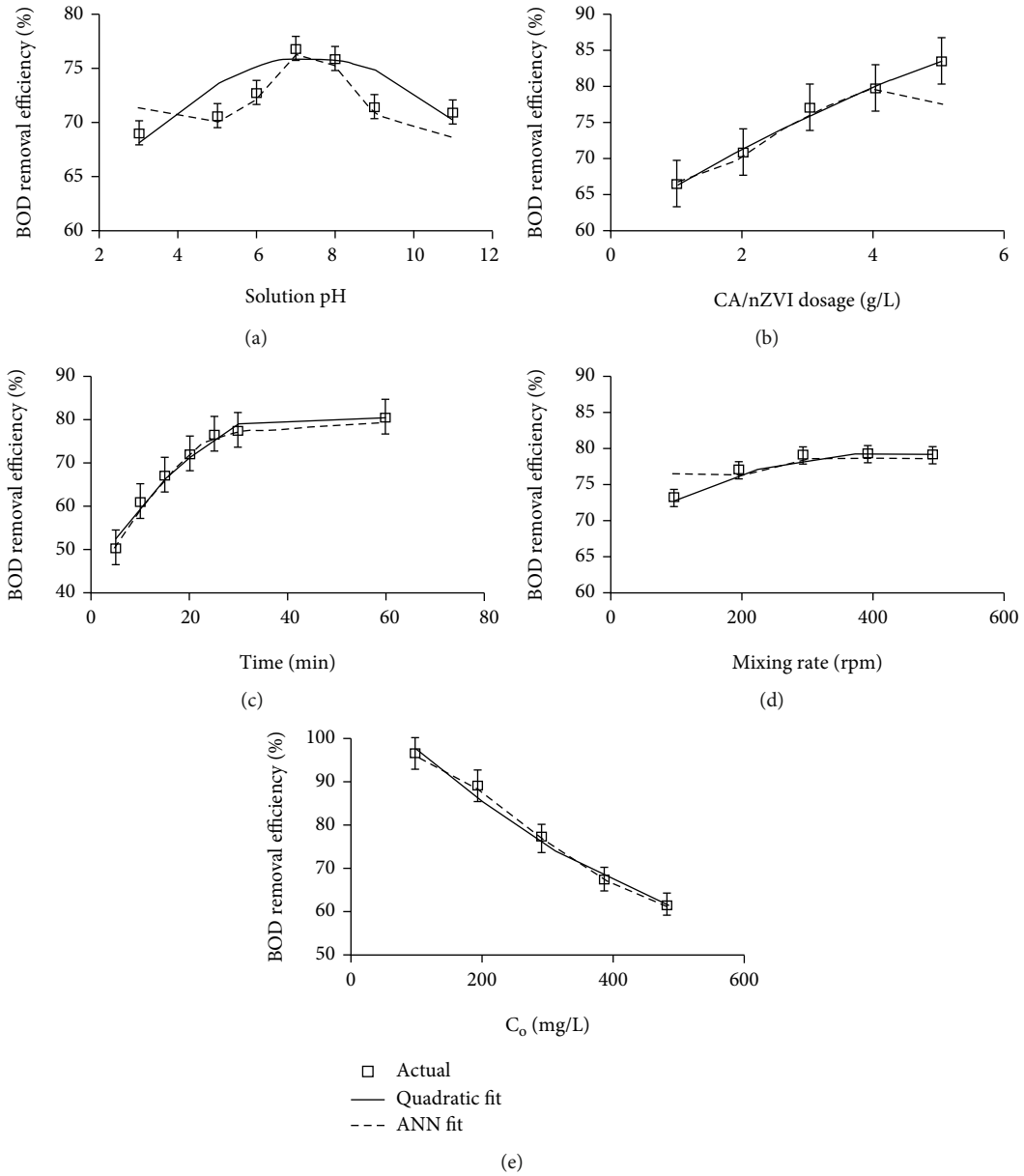

Figure 3: Influences of adsorption factors on BOD removal efficiency: (a) solution pH, (b) adsorbent dosage, (c) contact time, (d) stirring rate, and (e) initial adsorbate concentration.

$$\log(q_e) = \left(\frac{1}{n}\right) \log(C_e) + \log(K_F), \quad (7)$$

$$q_e = B_T \ln(A_T) + B_T \ln(C_e), \quad (8)$$

where q_e is the number of biological pollutants adsorbed in the form of BOD at equilibrium per gram of CA/nZVI (mg/g) corresponding to the equilibrium BOD concentration (C_e, in mg/L), Q_m (mg/g), and K_L (L/mg) which are the Langmuir model parameters, $1/n$ and K_F ((mg/g) $(\text{L/mg})^{1/n}$) are the Freundlich model parameters, and B_T (J/mol) and A_T (L/g) are the Tempkin and Pyzhev model parameters.

Table 3 lists the values of isotherm parameters and the corresponding fitting accuracies (R^2 values). A low R^2 of 0.881 obtained by fitting the adsorption data to the Langmuir model suggested that BOD removal by nZVI could not follow the monolayer adsorption hypothesis [43]. The Freundlich model achieved a sufficient fitting accuracy ($R^2 = 0.994$) to describe the adsorption isotherm. This goodness-of-fit indicates that multilayer adsorption and heterogeneous sites could facilitate BOD removal by CA/nZVI [44]. The $1/n$ and K_F values were 0.285 and 23.014 (mg/g) $(\text{L/mg})^{1/n}$, indicating that the adsorption of organic ions onto CA/nZVI was preferable under the experimental conditions. A high R^2 value (0.985) was also observed using

Table 2: Removal efficiencies of BOD using various adsorbent materials reported in literature.

Adsorbent	Experimental factor					Removal efficiency (%)	Reference
	Adsorbent dosage (g/L)	pH	C_o (mg/L)	Time (min)	Stirring rate (rpm)		
Wood fly ash	160	1.4	15001	20	600	24	Laohaprapanon et al. [36]
$FeSO_4{\cdot}7H_2O$ coagulant	2.0	5	25500	30	200/50	78	Hossain et al. [46]
nZVI from black tea extract	3.2	8.0	365	60	200	91.3	Mahmoud et al. [37]
Activated carbon prepared from date palm waste	1.0	6.0	14	150	400	92.8	Nayl et al. [39]
CA/nZVI	3.0	7.0	100	30	200	96.4	This study
Mixed adsorbent carbon	35	7	505	150	600	99.1	Devi and Dahiya [35]
Commercial activated carbon	40	2	505	180	600	99.5	Devi and Dahiya [35]

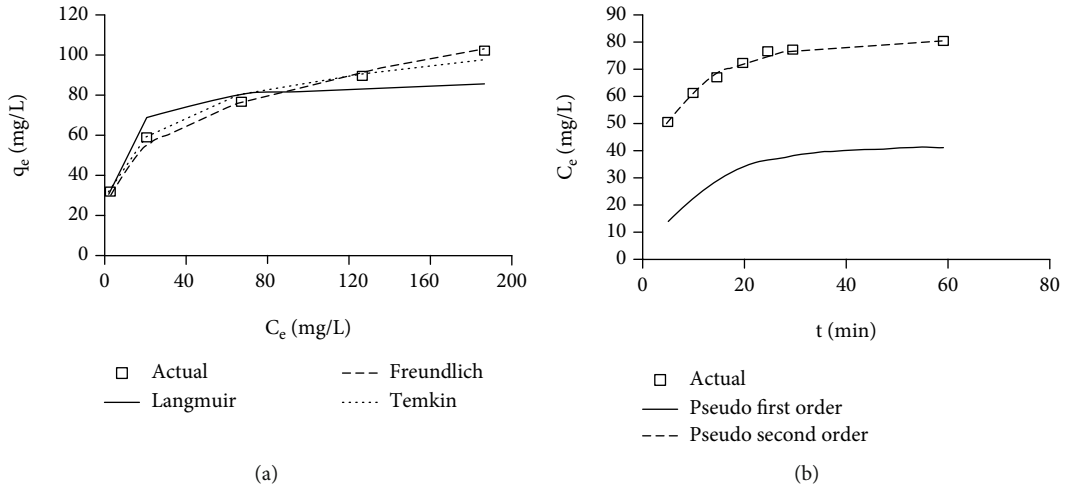

Figure 4: Fitting of adsorption data to (a) isotherm models and (b) kinetic models.

Table 3: Results of isotherm and kinetic studies for BOD removal by CA/nZVI adsorbent.

Model	Parameter	Fitting formula	Fitting accuracy (R^2)
Langmuir isotherm	$Q_m = 88.496$ mg/g $K_L = 0.155$ L/mg $R_L = 0.013$–0.060	$Q_e = 13.755C_e/(1 + 0.155C_e)$	0.881
Freundlich isotherm	$1/n = 0.285$ $K_F = 23.014$ (mg/g) (L/mg)$^{1/n}$	$Q_e = 23.014C_e^{0.285}$	0.994
Tempkin and Pyzhev isotherm	$B_T = 17.009$ J/mol $A_T = 1.630$ L/g	$Q_e = 17.009\ln(1.630C_e)$	0.985
Pseudo-first-order kinetic	$Q_e = 42.442$ mg/g $k_1 = 0.0791$/min	$Q_t = 42.442[1 - \exp(-0.079t)]$	0.997
Pseudo-second-order kinetic	$Q_e = 86.207$ mg/g $k_2 = 0.003$ g/mg/min	$Q_t = 23.202t/(1 + 0.269t)$	0.984

Table 4: Determining the best ANN predictive performance by adapting the number of hidden layer neurons and the back-propagation learning algorithm.

ANN structure	Back-propagation learning algorithm	Coefficient of determination (R^2)			Goodness of fit			
		Training	Validation	Testing	R^2	Adj-R^2	RMSE	SSE
5–3–1	*trainlm*	0.992	0.579	0.931	0.740	0.730	3.067	254.000
5–5–1	*trainlm*	0.174	0.980	0.830	0.198	0.168	3.088	257.500
5–8–1	*trainlm*	0.908	0.955	0.910	0.914	0.911	2.207	131.500
5–10–1	*trainlm*	0.975	0.926	0.998	0.972	0.971	1.449	56.680
5–15–1	*trainlm*	0.752	0.430	0.819	0.741	0.731	4.103	454.500
5–20–1	*trainlm*	0.992	0.994	0.684	0.910	0.908	2.831	216.400
5–10–1	*trainbfg*	0.960	0.992	0.924	0.960	0.949	1.729	80.690
5–10–1	*traingdm*	0.228	0.598	0.399	0.246	0.218	2.359	150.200
5–10–1	*traingda*	0.823	0.740	0.968	0.824	0.819	3.175	272.300
5–10–1	*traincgb*	0.169	0.441	0.027	0.127	0.095	10.940	3234.000
5–10–1	*traincgf*	0.835	0.918	0.507	0.815	0.809	3.762	382.100
5–10–1	*trainoss*	0.904	0.891	0.982	0.906	0.903	2.696	196.200
5–10–1	*trainscg*	0.000	0.005	0.264	0.000	-0.037	10.290	2860.000

the Tempkin and Pyzhevisotherm model, signifying a good fit with the experimental data. The estimated Tempkin and Pyzhev parameters ($B_T = 17.009$ J/mol ; $A_T = 1.630$ L/g) were assigned to the occurrence of physical adsorption and uniform distribution of bounding energies for BOD removal.

The pseudo-first-order (PFO) (Equation (9)) and pseudo-second-order (PSO) (Equation (10))) kinetic models [45] were used to quantitatively describe the kinetic adsorption of organic impurities onto CA/nZVI:

$$\log(q_e - q_t) = \log(q_e) - \frac{k_1}{2.303}t, \tag{9}$$

$$\frac{t}{q_t} = \frac{1}{k_2 \times q_e^2} + \frac{1}{q_e}t, \tag{10}$$

where k_1 (1/min) and k_2 (g/mg/min) are the PFO and PSO constants, respectively, and q_t (mg/g) and q_e (mg/g) represent the amount of adsorbed molecules at time t and equilibrium, respectively.

The plot of q_e vs. t shows the applicability of the adsorption kinetic models for fitting the experimental data (Figure 4(b)). This fitting reveals that the interaction between organic pollutants and CA/nZVI for BOD removal is influenced by the physisorption and chemisorption pathways. In another kinetic adsorption study [39], a chemisorption reaction was dominant for removing BOD by activated carbon. Hossain et al. [46] also demonstrated that the removal of BOD from palm oil mill effluent by coagulation/adsorption using $FeSO_4{\cdot}7H_2O$ followed the PSO kinetic modeling.

3.5. Artificial Neural Network (ANN) for Adsorption Computation

3.5.1. ANN Optimization. Table 4 lists the predictive performances of several ANN structures derived by altering the number of hidden layer neurons and the back-propagation learning algorithm. The input layer (with 5 neurons) received data from the five adsorption factors. Only one hidden layer was used in these ANNs to avoid an overcomplex network's architecture and obey the optimality criterion (e.g., save computational cost, minimize MSE, and fasten the learning speed). The output layer included a single node, and hence, the ANN configuration could be expressed as 5 – m – 1. The network performance was unsatisfactory for small m, probably due to a lower learning capability caused by the insufficient computational neurons. It was also found that 10 neurons yielded the highest R^2 values, where a further increase in the number of neurons would cause more fitted functions and prolong the computation time. Hence, local minima or overfitting might affect the ANN training process by either elevating or lowering the number (m) beyond 10 neurons, finally leading to an imprecise fit. Moreover, Levenberg-Marquardt (*trainlm*) yielded the best goodness-of-fit statistics compared with other learning algorithms. The "*trainlm*" training function is one of the fastest back-propagation algorithms to adapt the weight and bias values [22]. Although some functions such as "*trainbfg*" showed high R^2 values for the training dataset, R^2 of the validation and testing procedures were unsatisfactory. Accordingly, the "*trainlm*" training function with $m = 10$ neurons was selected for the optimized network configuration.

3.5.2. ANN Training, Validation, and Test. During network optimization, the predictive accuracies for the training, validation, and testing processes were recorded (Figure 5(a)). In these figures, the theoretical and best regression fittings are given by the dashed and solid lines, respectively. These processes showed R^2 values of 0.975, 0.926, and 0.998 for the optimum ANN structure (5–10–1), respectively. The overall R^2 value was 0.972, in which the ANN model would explain 97.2% of variability within the BOD removal efficiencies via a linear regression model. Figure 5(b) shows the validation checks during training that stopped at epoch number 6. This epoch corresponded to a validation check of 6, in which the

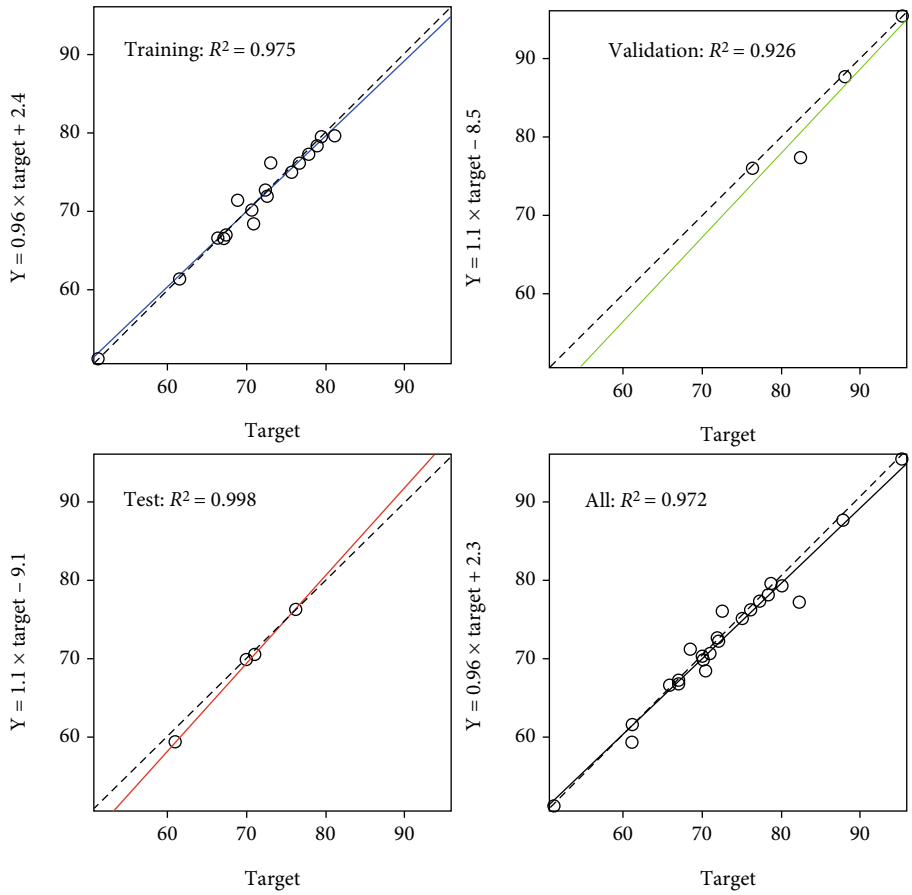

(a)

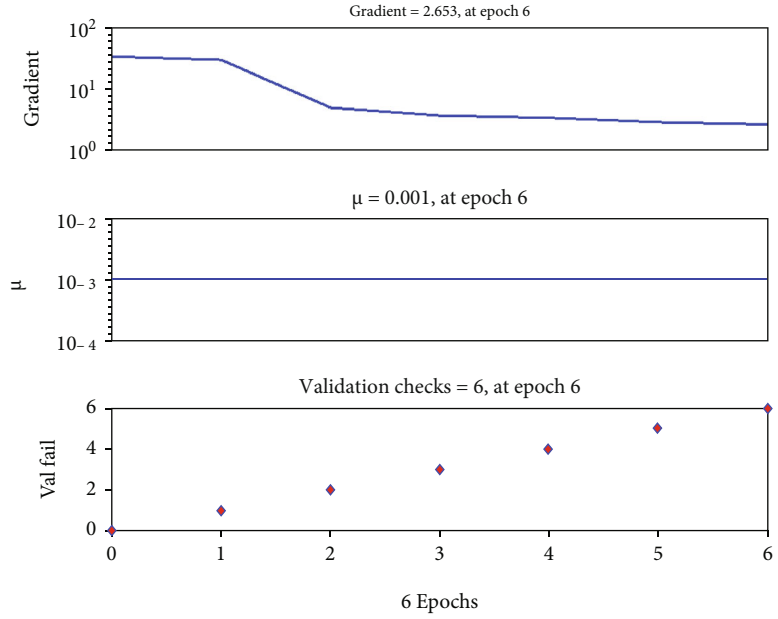

(b)

Figure 5: Continued.

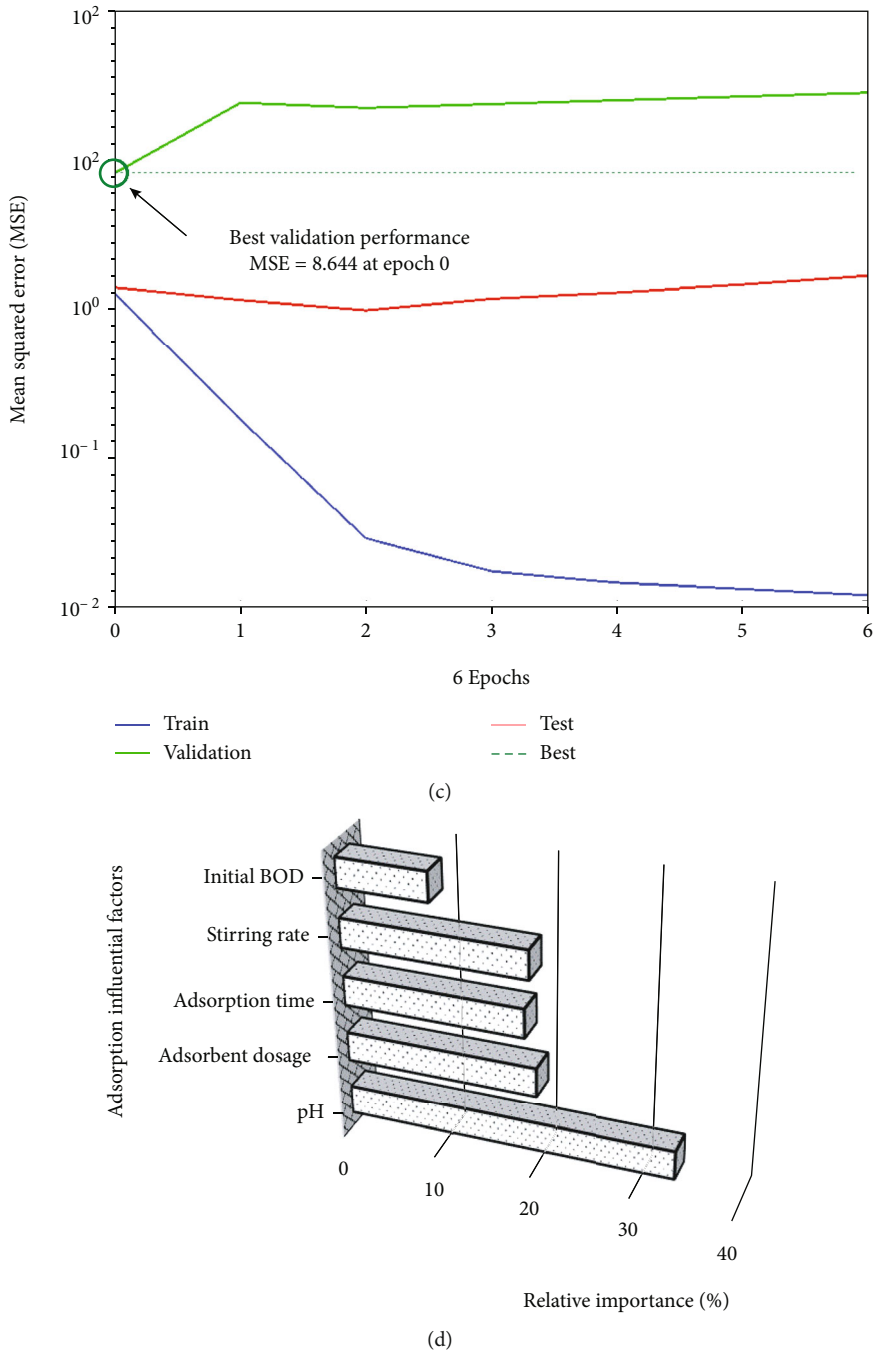

Figure 5: Performance of ANN model for predicting BOD removal efficiency: (a) regression plot, (b) validation checks, (c) best validation, and (d) relative importance. The number of data points in the training, cross-validating, and testing sets had 70%, 15%, and 15% proportions, respectively.

errors were repeated six times before the process termination. During the 6 error repetitions (Figure 5(c)), the MSE of the training dataset dropped due to the fact that "*trainlm*" is an efficient algorithm to improve the learning of ANN subjected to complex relationships [47]. For instance, the ANN parameters (weights and biases) were appropriately adjusted during training. The validation curve initiated to rise after epoch 0, giving the best validation performance at the minimum MSE of 8.644. Based on the validation plot, the ANN model would overfit the data after epoch 0, giving unsatisfactory generalization power. The testing curve gradually declined until epoch 2, followed by a slight rise; where the MSE between the predicted and target outputs increased. The MSE of the testing dataset implied that the ANN model could predict BOD removal using new input records not seen during training and validation. Based on the network performance during training, validation, and test, the optimum weights and biases were determined at epoch 0 to give precise results when importing new input data.

Table 5: t statistics and p values for coefficients of the quadratic regression model to predict BOD removal efficiency. Significant level at $p < 0.05$. Goodness-of-fit indices are $R^2 = 0.973$ and Adj-$R^2 = 0.959$, with MSE = 3.096 and DFE = 18.

Variable	Beta	SE	t ratio	Prob > $\lvert t \rvert$	Effect
Constant	β_0: 33.0635	9.049	3.654	0.002	Significant
pH	β_1: 6.2763	1.202	5.222	0.000	Significant
Dosage	β_2: 6.2479	2.070	3.019	0.007	Significant
Time	β_3: 1.7217	0.123	14.022	0.000	Significant
Rate	β_4: 0.0496	0.027	1.805	0.088	Insignificant
C_o	β_5: -0.1421	0.021	-6.866	0.000	Significant
pH × pH	β_{11}: -0.4274	0.084	-5.110	0.000	Significant
Dosage × dosage	β_{22}: -0.3297	0.332	-0.992	0.334	Insignificant
Time × time	β_{33}: -0.0186	0.002	-10.551	0.000	Significant
Mixing × mixing	β_{44}: -0.0001	0.000	-1.286	0.215	Insignificant
$C_o \times C_o$	β_{55}: 0.0001	0.000	2.549	0.020	Significant

3.5.3. ANN Applicability for Adsorption Studies. In this study, a three-layer feed-forward back-propagation ANN with a "*trainlm*" training algorithm and 5–10–1 architecture was the optimized artificial intelligence model. This model would be beneficial in predicting the adsorption performance to remove BOD under varying environmental conditions. Moreover, the obtained weights ($W_{10\times5}$ and $W_{1\times10}$) and thresholds ($b_{10\times1}$ and $b_{1\times1}$) would be used to determine the relative importance of the input factors. This step was achieved by partitioning the network's connection weights, as reported elsewhere [47, 48].

Figure 5(d) shows each experimental factor's relative importance, where the solution pH experienced the most influence on the BOD removal efficiency. Accordingly, the medium pH should be adjusted to around 7.5 for maintaining the highest adsorption performance. Controlling and adjusting the medium pH would be essentially considered to design and scale up the adsorption system. The relative importance of adsorbent dosage, time, and mixing speed was almost comparable at around 18%. Lower relative importance for C_o could be assigned to the efficient adsorption process for the investigated range of BOD (100–500 mg/L). Moreover, all the relative importance percentages were satisfactory, implying that no input factor could be excluded during the adsorption experimentation.

3.6. Quadratic Regression Model for Adsorption Computation. Table 5 lists the statistical results generalized from the t-test analysis for predicting BOD removal (response variable). The model's performance showed a reliable goodness-of-fit with R^2 of 0.973 and Adj-R^2 of 0.959. Adj-R^2 was approximately comparable to R^2, which could be assigned to the importance of the selected parameters in describing the adsorption process. Moreover, significant ($p < 0.05$) results were observed for the linear correlations of x_1, x_2, x_3, and x_5, suggesting that the BOD removal efficiency would be improved with incrementing pH, dosage, and time. Moreover, an increase in C_o tended to reduce the BOD removal significantly ($p < 0.05$) because the vacant adsorbent sites would be exhausted by increasing the BOD concentration. The model output also showed significant correlations with the quadratic forms of x_1, x_3, and x_5. Hence, a quadratic linear concave up curve would be visualized for the plot of BOD removal against each pH and time. This curve indicated that the improvement of BOD removal after certain values of pH and time would be insignificant ($p > 0.05$). The optimum values of these parameters were numerically assigned as 7.3 and 46.2 min, respectively. Moreover, a quadratic linear convex down shape would be noticed for the plot of BOD removal versus C_o because increasing the BOD concentration would deteriorate the adsorption performance of CA/nZVI. The plot of the BOD removal vs. mixing rate showed a "flat" curve, assigning to the insignificant ($p > 0.05$) influence of the input "x_4" on the model response. This "flat" pattern could be attributed to the narrow range of stirring rate during the investigation, making it imprecise to demonstrate a considerable relationship. Accordingly, the mixing rate was selected as 100 rpm to reduce the cost of the adsorption process.

3.7. Model Verification. The accuracy of the developed computational models to predict BOD removal under new conditions was estimated. In particular, additional 25 experimental runs were performed by varying the adsorption factors, followed by the analysis of BOD concentrations. In parallel, these inputs were incorporated into the quadratic and ANN models to predict the corresponding BOD removal efficiencies. The average of the absolute differences between the experimental results and model outputs was used to estimate the mean absolute error (MAE). The results in Table 6 demonstrate that the MAE values for the ANN and quadratic regression models were 0.73% and 1.91%, respectively. Apparently, both models showed a promising ability to predict the BOD removal efficiencies remarkably close to experimental values. However, the ANN model was more reliable and robust than the quadratic regression method in providing the predictions closer to the measured data. Each of the modeling techniques has advantages, regarding the prediction, optimization, and recognition applications in wastewater treatment processes.

Table 6: Verification of quadratic regression and ANN models for predicting BOD removal using additional experimental runs.

Run	Experimental parameters*					BOD removal efficiency (%)			Absolute error (%)	
	x_1	x_2	x_3	x_4	x_5	Actual	ANN	Quadratic regression model	ANN	Quadratic regression model
1	3	3	25	200	300	69.0	69.0	67.5	0.0	1.5
2	5	3	25	200	300	70.6	70.6	73.2	0.0	2.6
3	6	3	25	200	300	72.7	75.4	74.8	2.7	2.1
4	7	3	25	200	300	76.8	76.8	75.5	0.0	1.3
5	8	3	25	200	300	75.8	74.4	75.4	1.4	0.4
6	9	3	25	200	300	71.4	71.4	74.4	0.0	3.0
7	11	3	25	200	300	70.9	70.9	69.9	0.0	1.0
8	7	1	25	200	300	66.3	66.3	65.7	0.0	0.6
9	7	2	25	200	300	70.5	70.5	70.9	0.0	0.4
10	7	4	25	200	300	79.4	79.4	79.5	0.0	0.1
11	7	5	25	200	300	83.2	83.2	82.8	0.0	0.4
12	7	3	5	200	300	50.7	54.5	52.3	3.8	1.6
13	7	3	10	200	300	61.5	61.5	59.5	0.0	2.0
14	7	3	15	200	300	67.3	67.3	65.8	0.0	1.5
15	7	3	20	200	300	72.4	72.2	71.1	0.2	1.3
16	7	3	30	200	300	77.9	81.0	79.0	3.1	1.1
17	7	3	60	200	300	81.0	81.0	80.5	0.0	0.5
18	7	3	25	100	300	73.0	73.0	73.6	0.0	0.6
19	7	3	25	300	300	78.9	78.9	75.5	0.0	3.4
20	7	3	25	400	300	79.1	79.1	73.5	0.0	5.6
21	7	3	25	500	300	79.0	76.7	69.4	2.3	9.6
22	7	3	25	200	100	96.4	96.4	96.0	0.0	0.4
23	7	3	25	200	200	88.9	93.2	84.7	4.3	4.2
24	7	3	25	200	400	67.4	66.9	68.3	0.5	0.9
25	7	3	25	200	500	61.5	61.5	63.1	0.0	1.6
Mean absolute error (MAE) (%)									0.73	1.91

*x_1 is pH; x_2 is adsorbent dose (g/L); x_3 is contact time (min); x_4 is stirring rate (rpm); x_5 is initial concentration (mg/L).

However, ANN is able to overcome some shortages that could arise during regression analysis implementation. In particular, the input factors do not require a statistical experimental design to train the ANN model (compared to the regression analysis that only provides first- or second-order polynomial models). ANN as a soft computing technique and a black-box model depends on the analysis of available data to simulate any form of nonlinearity. In parallel, the regression models utilize a small number of experiments to generate manifold information, provide graphical illustrations for input-output relationships, and establish significance analysis. Hence, the authorities are encouraged to develop and scale up these modeling approaches in real-scale wastewater adsorption systems.

4. Conclusions

This study focused on the application of computational-based techniques to predict BOD removal in an adsorption process. The adsorbent material was characterized by XRD, SEM, and EDS, showing a successful preparation of Fe nanoparticles in the zero-valent state. The highest BOD removal efficiency (96.4%) was observed at pH = 7, adsorbent dosage = 3 g/L, mixing rate = 200 rpm, and C_o = 100 mg/L within 25 min. A quadratic regression model was developed to enhance BOD reduction, showing optimum pH of 7.3 and time of 46.2 min, equivalent to a BOD removal efficiency of over 99%. Moreover, an ANN structure was properly optimized as 5–10–1 with the "*trainlm*" back-propagation learning algorithm to predict BOD removal (R^2: 0.972, Adj-R^2: 0.971). The results of the computational-based studies revealed that the adjustment of medium pH at the 7–8 range would be essentially considered to design and scale up the adsorption system. The results also showed that the ANN model (MAE 0.73%) was more reliable than the quadratic regression model (MAE 1.91%) in predicting the BOD removal efficiency; however, both models maintained acceptable predictive accuracies. Hence, both modeling approaches would be employed to guide the stakeholders and industrial sector to overcome the nonlinearity and complexity issues associated with the adsorption process. Further studies are required to apply these ANN and quadratic models to enhance organic pollution reduction at a large scale.

Nomenclature

ANN: Artificial neural network
BOD: Biochemical oxygen demand
CA: Cellulose acetate
CA/nZVI: Nanozero-valent iron encapsulated into cellulose acetate
DMF: Dimethylformamide
EDS: Energy-dispersive spectroscopy
$FeCl_3 \cdot 6H_2O$: Ferric chloride hexahydrate
MAE: Mean absolute error
MSE: Mean squared error
$NaBH_4$: Sodium borohydride
PFO: Pseudo-first-order
PSO: Pseudo-second-order
SEM: Scanning electron microscope
SLS: Sodium lauryl sulphate
XRD: X-ray diffraction.

Data Availability

The article includes all data generated or analyzed during the investigation.

Conflicts of Interest

No known competing financial interests or personal relationships could have appeared to influence the study.

Authors' Contributions

All authors contributed to conceptualization, methodology, formal analysis, and writing—review and editing.

Acknowledgments

The authors would like to thank Badr University in Cairo (BUC), Egyptian Russian University (ERU), and Housing and Building National Research Center (HBRC) for supporting this research. The last author acknowledges Nasr Academy for Sustainable Environment (NASE). This work was supported by The Academy of Scientific Research and Technology (ASRT)/the Bibliotheca Alexandrina (BA) Research Grants (grant number 1469) awarded to the first author of this paper (Associate Professor Mohamed K. Mostafa, BUC).

References

[1] Z. Berizi, S. Y. Hashemi, M. Hadi, A. Azari, and A. H. Mahvi, "The study of non-linear kinetics and adsorption isotherm models for Acid Red 18 from aqueous solutions by magnetite nanoparticles and magnetite nanoparticles modified by sodium alginate," *Water Science and Technology*, vol. 74, no. 5, pp. 1235–1242, 2016.

[2] E. Ahmadi, B. Kakavandi, A. Azari et al., "The performance of mesoporous magnetite zeolite nanocomposite in removing dimethyl phthalate from aquatic environments," *Desalination and Water Treatment*, vol. 57, no. 57, pp. 1–15, 2016.

[3] A. G. Kumi, M. G. Ibrahim, M. Fujii, and M. Nasr, "Synthesis of sludge-derived biochar modified with eggshell waste for monoethylene glycol removal from aqueous solutions," *SN Applied Sciences*, vol. 2, no. 10, pp. 1–12, 2020.

[4] M. K. Mostafa, A. S. Mahmoud, R. A. Saryel-Deen, and R. W. Peters, "Application of entrapped nano zero valent iron into cellulose acetate membranes for domestic wastewater treatment," in *Environmental aspects, applications and implications of nanomaterials and nanotechnology 2017–Topical conference at the 2017 AIChE annual meeting* 27–34, Minneapolis, MN, United States, 2017.

[5] Z. Othman, H. R. Mackey, and K. A. Mahmoud, "A critical overview of MXenes adsorption behavior toward heavy metals," *Chemosphere*, vol. 295, p. 133849, 2022.

[6] R. A. Saryel-Deen, A. S. Mahmoud, M. Mahmoud, M. K. Mostafa, and R. W. Peters, "Adsorption and kinetic studies of using entrapped sewage sludge ash in the removal of chemical oxygen demand from domestic wastewater, with artificial intelligence approach," *AIChE Annual Meeting*, vol. 3, pp. 1587–1594, 2017.

[7] M. Nasr, "Modeling applications in environmental bioremediation studies," in *Phytobiont and Ecosystem Restitution*, pp. 143–160, Springer, Singapore, 2018.

[8] Z. Iqbal, M. S. Tanweer, and M. Alam, "Recent advances in adsorptive removal of wastewater pollutants by chemically modified metal oxides: a review," *Journal of Water Process Engineering*, vol. 46, p. 102641, 2022.

[9] M. Nasr, "Modeling applications in bioremediation of hydrocarbon pollutants," in *Microbial Action on Hydrocarbons*, pp. 181–197, Springer, Singapore, 2018.

[10] A. S. Mahmoud, R. A. Saryel-Deen, M. K. Mostafa, and R. W. Peters, "Artificial intelligence for organochlorine pesticides removal from aqueous solutions using entrapped nzvi in alginate biopolymer," in *Annual AIChE Meeting. Minneapolis*, pp. 420–427, Minneapolis, MN, United States, October 2017.

[11] A. S. Mahmoud, R. S. Farag, M. M. Elshfai, L. A. Mohamed, and S. M. Ragheb, "Nano zero-valent aluminum (nZVAl) preparation, characterization, and application for the removal of soluble organic matter with artificial intelligence, isotherm study, and kinetic analysis," *Air, Soil and Water Research*, vol. 12, p. 117862211987870, 2019.

[12] G. Wang, Q. S. Jia, M. Zhou, J. Bi, J. Qiao, and A. Abusorrah, "Artificial neural networks for water quality soft-sensing in wastewater treatment: a review," *Artificial Intelligence Review*, vol. 55, no. 1, pp. 565–587, 2022.

[13] A. S. Mahmoud, M. K. Mostafa, and M. Nasr, "Regression model, artificial intelligence, and cost estimation for phosphate adsorption using encapsulated nanoscale zero-valent iron," *Separation Science and Technology (Philadelphia)*, vol. 54, no. 1, pp. 13–26, 2019.

[14] A. Hamdy, M. K. Mostafa, and M. Nasr, "Regression analysis and artificial intelligence for removal of methylene blue from aqueous solutions using nanoscale zero-valent iron," *International Journal of Environmental Science and Technology*, vol. 16, no. 1, pp. 357–372, 2019.

[15] M. Fawzy, M. Nasr, S. Adel, and S. Helmi, "Regression model, artificial neural network, and cost estimation for biosorption of Ni(II)-ions from aqueous solutions by Potamogeton pectinatus," *International Journal of Phytoremediation*, vol. 20, no. 4, pp. 321–329, 2018.

[16] M. Fawzy, M. Nasr, H. Nagy, and S. Helmi, "Artificial intelligence and regression analysis for Cd(II) ion biosorption from aqueous solution by Gossypium barbadense waste,"

Environmental Science and Pollution Research, vol. 25, no. 6, pp. 5875–5888, 2018.

[17] P. J. D. P. van de Witte, P. J. Dijkstra, J. W. A. Van den Berg, and J. Feijen, "Phase separation processes in polymer solutions in relation to membrane formation," *Journal of Membrane Science*, vol. 117, no. 1-2, pp. 1–31, 1996.

[18] M. El-Shafei, A. Mahmoud, M. Mostafa, and R. Peters, "Effects of entrapped nZVI in alginate polymer on BTEX removal," in *AIChE Annual Meeting*, pp. 15–22, San Francisco, CA, 2016.

[19] M. S. Mahmoud, M. K. Mostafa, S. A. Mohamed, N. A. Sobhy, and M. Nasr, "Bioremediation of red azo dye from aqueous solutions by _A_ spergillus niger strain isolated from textile wastewater," *Journal of Environmental Chemical Engineering*, vol. 5, no. 1, pp. 547–554, 2017.

[20] A. S. Mahmoud, M. K. Mostafa, and S. A. Abdel-Gawad, "Artificial intelligence for the removal of benzene, toluene, ethyl benzene and xylene (BTEX) from aqueous solutions using iron nanoparticles," *Water Supply*, vol. 18, no. 5, pp. 1650–1663, 2018.

[21] W. E. F. Apha Awwa, *Standard Methods for Examinations of Water and Wastewater*, Apha Wef Awwa, Washington, DC,, 21st ed edition, 2005.

[22] M. H. Beale, M. T. Hagan, and H. B. Demuth, *Neural Network Toolbox User Guide*, The Math Works Inc, Natick, 2004.

[23] O. I. Abiodun, A. Jantan, A. E. Omolara, K. V. Dada, N. A. Mohamed, and H. Arshad, "State-of-the-art in artificial neural network applications: a survey," *Heliyon*, vol. 4, no. 11, p. e00938, 2018.

[24] O. Axelsson, "A generalized conjugate gradient, least square method," *Numerische Mathematik*, vol. 51, pp. 209–227, 1987.

[25] I. Helland, "On the interpretation and use of R2 in regression analysis," *Biometrics*, vol. 43, no. 1, pp. 61–69, 1987.

[26] T. Kim, "T test as a parametric statistic," *Korean Journal of Anesthesiology*, vol. 68, no. 6, pp. 540–546, 2015.

[27] A. Hamdy, M. K. Mostafa, and M. Nasr, "Techno-economic estimation of electroplating wastewater treatment using zero-valent iron nanoparticles: batch optimization, continuous feed, and scaling up studies," *Environmental Science and Pollution Research*, vol. 26, no. 24, pp. 25372–25385, 2019.

[28] Y. H. Shih, C. Y. Hsu, and Y. F. Su, "Reduction of hexachlorobenzene by nanoscale zero-valent iron: kinetics, pH effect, and degradation mechanism," *Separation and Purification Technology*, vol. 76, no. 3, pp. 268–274, 2011.

[29] A. Ishag, Y. Li, N. Zhang et al., "Environmental application of emerging zero-valent iron-based materials on removal of radionuclides from the wastewater: a review," *Environmental Research*, vol. 188, p. 109855, 2020.

[30] M. Stefaniuk, P. Oleszczuk, and Y. S. Ok, "Review on nano zerovalent iron (nZVI): from synthesis to environmental applications," *Chemical Engineering Journal*, vol. 287, pp. 618–632, 2016.

[31] Q. Li, Z. Chen, H. Wang et al., "Removal of organic compounds by nanoscale zero-valent iron and its composites," *Science of the Total Environment*, vol. 792, p. 148546, 2021.

[32] F. M. Omar, H. A. Aziz, and S. Stoll, "Aggregation and disaggregation of ZnO nanoparticles: influence of pH and adsorption of Suwannee River humic acid," *The Science of the Total Environment*, vol. 468, pp. 195–201, 2014.

[33] S. Bae and K. Hanna, "Reactivity of nanoscale zero-valent iron in unbuffered systems: effect of pH and Fe (II) dissolution," *Environmental science & technology*, vol. 49, no. 17, pp. 10536–10543, 2015.

[34] Y. Zhao, F. Liu, and X. Qin, "Adsorption of diclofenac onto goethite: adsorption kinetics and effects of pH," *Chemosphere*, vol. 180, pp. 373–378, 2017.

[35] R. Devi and R. P. Dahiya, "COD and BOD removal from domestic wastewater generated in decentralised sectors," *Bioresource Technology*, vol. 99, no. 2, pp. 344–349, 2008.

[36] S. Laohaprapanon, M. Marques, and W. Hogland, "Removal of organic pollutants from wastewater using wood fly ash as a low-cost sorbent," *Clean - Soil, Air, Water*, vol. 38, no. 11, pp. 1055–1061, 2010.

[37] A. S. Mahmoud, R. S. Farag, and M. M. Elshfai, "Reduction of organic matter from municipal wastewater at low cost using green synthesis nano iron extracted from black tea: artificial intelligence with regression analysis," *Egyptian Journal of Petroleum*, vol. 29, no. 1, pp. 9–20, 2020.

[38] M. A. Fulazzaky, M. H. Khamidun, and R. Omar, "Understanding of mass transfer resistance for the adsorption of solute onto porous material from the modified mass transfer factor models," *Chemical Engineering Journal*, vol. 228, pp. 1023–1029, 2013.

[39] A. E. A. Nayl, R. A. Elkhashab, T. El Malah et al., "Adsorption studies on the removal of COD and BOD from treated sewage using activated carbon prepared from date palm waste," *Environmental Science and Pollution Research*, vol. 24, no. 28, pp. 22284–22293, 2017.

[40] I. Langmuir, "The constitution and fundamental properties of solids and LIQUIDS. PART I. SOLIDS," *Journal of the American Chemical Society*, vol. 38, no. 11, pp. 2221–2295, 1916.

[41] H. Freundlich, "Over the adsorption in solution," *Journal of Physical Chemistry*, vol. 57, pp. 385–471, 1906.

[42] M. I. Tempkin and V. J. A. P. C. Pyzhev, "Kinetics of ammonia synthesis on promoted iron catalyst," *Acta Physicochim USSR*, vol. 12, pp. 327–356, 1940.

[43] B. Boulinguiez, P. Le Cloirec, and D. Wolbert, "Revisiting the determination of Langmuir parameters application to tetrahydrothiophene adsorption onto activated carbon," *Langmuir*, vol. 24, no. 13, pp. 6420–6424, 2008.

[44] K. Y. Foo and B. H. Hameed, "Insights into the modeling of adsorption isotherm systems," *Chemical Engineering Journal*, vol. 156, no. 1, pp. 2–10, 2010.

[45] Y.-S. Ho, "Second-order kinetic model for the sorption of cadmium onto tree fern: a comparison of linear and non-linear methods," *Water Research*, vol. 40, no. 1, pp. 119–125, 2006.

[46] M. S. Hossain, F. Omar, A. J. Asis, R. T. Bachmann, M. Z. I. Sarker, and M. O. Ab Kadir, "Effective treatment of palm oil mill effluent using $FeSO_4.7H_2O$ waste from titanium oxide industry: Coagulation adsorption isotherm and kinetics studies," *Journal of Cleaner Production*, vol. 219, pp. 86–98, 2019.

[47] M. H. Bakr, M. Nasr, M. Ashmawy, and A. Tawfik, "Predictive performance of auto-aerated immobilized biomass reactor treating anaerobic effluent of cardboard wastewater enriched with bronopol (2-bromo-2-nitropropan-1,3-diol) via artificial neural network," *Environmental Technology and Innovation*, vol. 21, p. 101327, 2021.

[48] F. A. Ansari, M. Nasr, I. Rawat, and F. Bux, "Artificial neural network and techno-economic estimation with algae-based tertiary wastewater treatment," *Journal of Water Process Engineering*, vol. 40, p. 101761, 2021.

Hindawi
Adsorption Science & Technology
Volume 2022, Article ID 7874826, 16 pages
https://doi.org/10.1155/2022/7874826

Research Article

Evaluation of Contemporary Computational Techniques to Optimize Adsorption Process for Simultaneous Removal of COD and TOC in Wastewater

Areej Alhothali,[1] **Hifsa Khurshid**,[2] **Muhammad Raza Ul Mustafa**,[2,3] **Kawthar Mostafa Moria**,[1] **Umer Rashid**,[4] **and Omaimah Omar Bamasag**[5]

[1]*Department of Computer Sciences, Faculty of Computing and Information Technology, King Abdulaziz University, Jeddah, Saudi Arabia*
[2]*Department of Civil & Environmental Engineering, Universiti Teknologi PETRONAS 32610 Seri Iskandar, Perak Darul Ridzuan, Malaysia*
[3]*Centre for Urban Resource Sustainability, Institute of Self-Sustainable Building, Universiti Teknologi PETRONAS, Seri Iskandar, 32610 Perak, Malaysia*
[4]*Institute of Nanoscience and Nanotechnology (ION2), Universiti Putra Malaysia, 43400 UPM Serdang, Selangor, Malaysia*
[5]*Center of Excellence in Smart Environment Research, King Abdulaziz University, Jeddah, Saudi Arabia*

Correspondence should be addressed to Hifsa Khurshid; hifsa_18002187@utp.edu.my

Received 31 October 2021; Revised 3 January 2022; Accepted 30 March 2022; Published 27 April 2022

Academic Editor: George Kyzas

This study was aimed at evaluating the artificial neural network (ANN), genetic algorithm (GA), adaptive neurofuzzy interference (ANFIS), and the response surface methodology (RSM) approaches for modeling and optimizing the simultaneous adsorptive removal of chemical oxygen demand (COD) and total organic carbon (TOC) in produced water (PW) using tea waste biochar (TWBC). Comparative analysis of RSM, ANN, and ANFIS models showed mean square error (MSE) as 5.29809, 1.49937, and 0.24164 for adsorption of COD and MSE of 0.11726, 0.10241, and 0.08747 for prediction of TOC adsorption, respectively. The study showed that ANFIS outperformed the ANN and RSM in terms of fast convergence, minimum MSE, and sum of square error for prediction of adsorption data. The adsorption parameters were optimized using ANFIS-surface plots, ANN-GA hybrid, RSM-GA hybrid, and RSM optimization tool in design expert (DE) software. Maximum COD (88.9%) and TOC (98.8%) removal were predicted at pH of 7, a dosage of 300 mg/L, and contact time of 60 mins using ANFIS-surface plots. The optimization approaches showed the performance in the following order: ANFIS-surface plots>ANN-GA>RSM-GA>RSM.

1. Introduction

With an increase in the world population, industrialization, and urbanization, the evaluation of water resources and monitoring of their quality have become a significant concern in hydroenvironmental science. Various contaminants are being released continuously into water resources and causing the degradation of aquatic animals' habitat and freshwater quality up to a greater extent [1, 2]. Attempts have been made to establish strategies for the safe removal of contaminants in wastewaters, e.g., coagulation-flocculation, photocatalytic treatment, electrocoagulation, adsorption, and oxidation [3, 4]. However, in comparison to other methods, adsorption has gained prominence due to its high operating speed, design stability, cost-effectiveness, and robustness [5, 6].

The adsorption process is influenced by various operating variables, including contact time between adsorbent and adsorbate, adsorbent particle size, pollutant concentration, and pH of the solution. It has been noted that building an automated and optimized adsorption treatment process is complex in wastewater treatment plants (WWTP) due to the

following reasons: (i) complex nature of adsorption process, (ii) nonlinear interactions between the operating variables, and (iii) drastic changes in pollutant's concentrations [7]. Therefore, mathematical models are needed to understand, optimize, and quantify the interactions between the operating variables. Modeling and simulation can save time, reagents, and delayed analysis by avoiding multiple time-consuming experimental runs of the process. Classical and linear mathematical models can not completely model and simulate the adsorption results. Recently, response surface methodology (RSM) has been used to model a wide variety of adsorption processes, but it has been found to have limited application when the data is minimum. Therefore, to interrelate the adsorption operating variables with output removal efficiencies of the pollutants and automate the WWTP, advanced computer-simulated models are necessary. Automation and optimization of the adsorption process can help in saving workforce, cost, and resources [8].

Artificial Intelligence (AI) is an advanced computer-based simulation technology. It was first implemented in the mid-1950s in the world of computer science. After that, many more robust and realistic AI-based techniques were developed in engineering to solve challenging problems and provide real-world implementations, whereas traditional or conventional methods were inadequate or unsuccessful [7, 9]. The application of AI techniques in the water treatment sector and optimization process has recently gained attention [10]. AI-based methods, such as knowledge-based structures and fuzzy logics (FIS), including adaptive neurofuzzy interface systems (ANFIS) [11], particle swarm optimization (PSO) [12, 13], genetic algorithm (GA) [14, 15], and artificial neural network (ANN) [16, 17], have been applied recently in water treatment and adsorption optimization systems. Such as optimization of the adsorption process of various dyes [18–24], metals [8, 14, 25, 26], and organic matter [27] has been reported in the literature using ANN, ANFIS, and RSM methods. However, limited studies have been found for the application of ANN, GA, and ANFIS for modeling and optimization of chemical oxygen demand (COD) and total organic carbon (TOC) adsorptive removal in produced water (PW).

The PW is one of the largest wastewater streams obtained during oil and gas exploration. Contaminants in PW change significantly depending on the source of their disposal. However, recently organic contaminants in PW have become the highest priority pollutants and need to be treated on a priority basis [28]. The COD and TOC are significant parameters for analyzing organic contaminants in PW and have been commonly used to represent the effluent water quality (WQ) [29, 30]. Hence, for the safe disposal of PW, these parameters need to be reduced significantly.

Most of the studies in the literature are performed on synthetic waters, which cannot be used efficiently for automation of oil and gas reservoirs' effluent treatment plants. Hence, there is a gap in the literature regarding the application of ANN, GA, and ANFIS in the adsorption field utilising PW. This research work was aimed at designing, implementing, comparing, and evaluating the ANN, GA, and ANFIS approach to remove COD and TOC in PW. Tea waste biochar (TWBC) had been used as an adsorbent in batch studies under the control of three factors, i.e., pH, adsorbent dosage, and contact time. The ANN and ANFIS results were compared with RSM results. It is expected that this study would help to scale up the industrial application of the adsorption process for COD and TOC removal in PW.

2. Materials and Methods

2.1. Materials. Tea leaves waste was used for the preparation of biochar (BC). The waste was collected from local Malaysian restaurants. High range (HR) COD vials were obtained from Avanti's laboratory items supplier in Malaysia. The water sample was taken from a South-East Asian oil and gas company.

2.2. Characterization of PW. The PW was filtered to remove suspended solids using a suction filtration unit. The filtered water was characterized for initial COD and TOC concentration. COD was measured using the USEPA reactor digestion method. Briefly, 2 mL of filtered PW sample was added to the high range COD vial. The vial was capped, mixed, and kept in a preheated digester at 150°C for 2 hrs. An empty vial prepared using 2 mL pure water was also observed in the digester. After 2 hrs, the concentration of COD (mg/L) was measured using USEPA method 800 under program 430, using HACH DR 2800 spectrophotometer. TOC in PW was measured using the Shimadzu TOC-L/SSM-5000A analyzer. The pH value of PW was found out using the OHAUS pH meter, and it was about 8 ± 0.2.

2.3. Preparation and Characterization of Biochar. The TWBC was prepared using our previously reported method [31]. Briefly, the tea leaves were washed and all impurities were removed. Before pyrolysis, the leaves were soaked overnight in phosphoric acid. The soaked leaves were dried and pyrolyzed at 700°C for 2 hrs in the presence of N_2 gas. The obtained TWBC was washed, dried in an oven for 24 hrs, and stored in a desiccator. The surface characteristics of the TWBC were determined using a ZEISS scanning electron microscope with energy-dispersive X-ray spectroscopy (SEM-EDX) mapping and a 15 kV accelerating voltage.

2.4. Design of Experiments Using RSM. The RSM-based polynomial Box–Behnken Design (BBD) in design expert (DE) software (Stat-Ease, version 12) was used for the design of adsorption batch experiments. Three independent variables were taken as inputs, including initial pH of PW, contact time, and dosage of TWBC. Adsorptive removal efficiencies of COD and TOC were taken as outputs. The design was chosen at three stages of low (-1), center (0), and high (1) points (Table 1), giving a total of 13 experimental runs.

2.5. Adsorption Batch Experiments. According to the design of experiments obtained through BBD, 13 batch experiments were conducted to investigate the effects of initial solution pH, adsorbent dosage, and contact time on COD and TOC removal in PW. The adsorbent was applied in varying amounts (25–300 mg/L) for 100 mL of PW at varying initial

Table 1: Ranges of variables for the design of experiments.

Factor	Variables	Level		
		-1	0	1
A	pH	3	6	10
B	Adsorbent dosage (mg/L)	25	162.5	300
C	Contact time (min)	10	35	60

pH (3 – 10) and contact times (10–60 mins). The water was stirred at 220 rpm at a temperature of 20 ± 5°C using a magnetic stirrer. The initial and final COD and TOC concentrations were measured before and after each experiment. All data were measured in three replicates, and the average value was recorded. The removal efficiencies were determined using the formula given as follows:

$$\text{Removal efficiency}\,(\%) = \frac{\text{Initial concentration} - \text{Final concentration}}{\text{Initial concentration}} \times 100, \quad (1)$$

where initial and final concentrations refer to COD and TOC amounts in mg/L before and after the adsorption experiment, respectively.

2.6. Modelling of Artificial Neural Network (ANN). Artificial neural networks (ANNs) are well known for their ability to research and organize large amounts of data. It is influenced by the brain, neurological system, neuronal learning, and reaction mechanism [18].

MATLAB R2021a was used to create a three-layer feed-forward neural network (FFNN). A FFNN network has no loops or cycles because all data is solely delivered forward [32]. For training the network, three inputs in the input layer, 2–20 neurons in the hidden layer, and two outputs in the output layer were taken. The input layer was given pH, TWBC dosage (mg/L), and contact time (min) as independent variables. The output layer had two dependent variables showing the removal efficiency of COD (%) and TOC (%), as shown in Figure 1. The neurons in the hidden layer were connected to the inputs and outputs through weights (w) and biases (b). In Figure 1, the symbol i represents the i^{th} input in the input layer ($1 \le i \le 3$), j represents the j^{th} neuron in the hidden layer ($1 \le j \le n$), and k represents the k^{th} output in the output layer ($1 \le k \le 2$). $w_{i,j}$ represents the weights from the input layer to the hidden layer, and $w_{j,k}$ represents the hidden layer to output layer weights, where n represents the total number of neurons in the hidden layer.

Training a network aims to reduce the error between the network's outputs and the target values. The training procedure reduces the error by modifying the weights and biases of the network. The ANN architecture was repeatedly trained to select the best suitable number of neurons, training algorithm, weights, and biases to predict COD and TOC removal efficiencies. A total of 13 data sets were taken through batch experiments for COD and TOC removal efficiencies, respectively. 70% data was used to train the model and 15% for validation and testing, respectively. For all data sets in ANN, the symmetric sigmoid transfer function (tansig) was used in the hidden layer. The linear transfer function (purelin) was used at the output node for the simulation and prediction of COD and TOC elimination.

The suitable number of neurons in the hidden layer was selected based on the hit and trial method using 2–20 neurons. As for performance criteria, minimum mean square error (MSE) and simulation time were taken.

After selecting the no. of neurons, the network was evaluated for various algorithms. The backpropagation (BP) algorithms were chosen for the network's training. It is a first-order gradient descent technique to model the experimental data [33]. The three BP algorithms named Elman BP (EBP), Cascade Forward BP (CFBP), and Levenberg Marquardt BP (LMBP) were evaluated for their performance, and the best algorithm was taken for the training purpose.

In order to train the ANN model, input values are multiplied by connection weights, followed by bias addition. The same procedure is used for the output layer, with the hidden layer's output acting as the input. After training the ANN model, it was tested and validated. The goal was to achieve an overall correlation coefficient (R) of nearly 1. The relationship between inputs and outputs can be expressed through Equation (2) [34].

$$y = f(x) = \left(\left(\sum_{j=1}^{n} w_{j,k} \left(\sum_{i=1}^{m} w_{i,j}.x + b_j \right) \right) + b_k \right), \quad (2)$$

where y shows the output variable and x denotes the input variable, and n represents the number of neurons in the hidden layer and m is the number of input variables. w and b are the weights and biases between the layers. i, j, and k represent the input order number, hidden neuron order number, and output order number, respectively.

2.7. Modelling of Adaptive Neurofuzzy Interference System (ANFIS). Fuzzy systems have some advantages over traditional approaches, particularly where ambiguous data is involved. Recently, fuzzy systems have gained popularity as alternative methods for information processing [35].

As illustrated in Figure 2, the fuzzy inference system (FIS) used in ANFIS was created in MATLAB R2021a using a neurofuzzy designer. The Sugeno-type ANFIS design consisted of four hidden layers: fuzzification layer, inference layer, defuzzification layer, and output layer [36]. For each output, a total of 13 data sets were used to train the model. Data were randomly divided into training (70%), testing, and checking data (30%). Three variables (pH, TWBC dosage, and contact time) were selected as inputs and removal efficiency of COD, and TOC were taken as targets. Minimum numbers of membership functions (mf) were selected based on minimum MSE. Optimization of the model was done based on backpropagation and least square estimation. FIS and optimization methods were selected based on error minimization.

2.8. Modelling of Response Surface Methodology (RSM). The experimental data collected through batch tests were

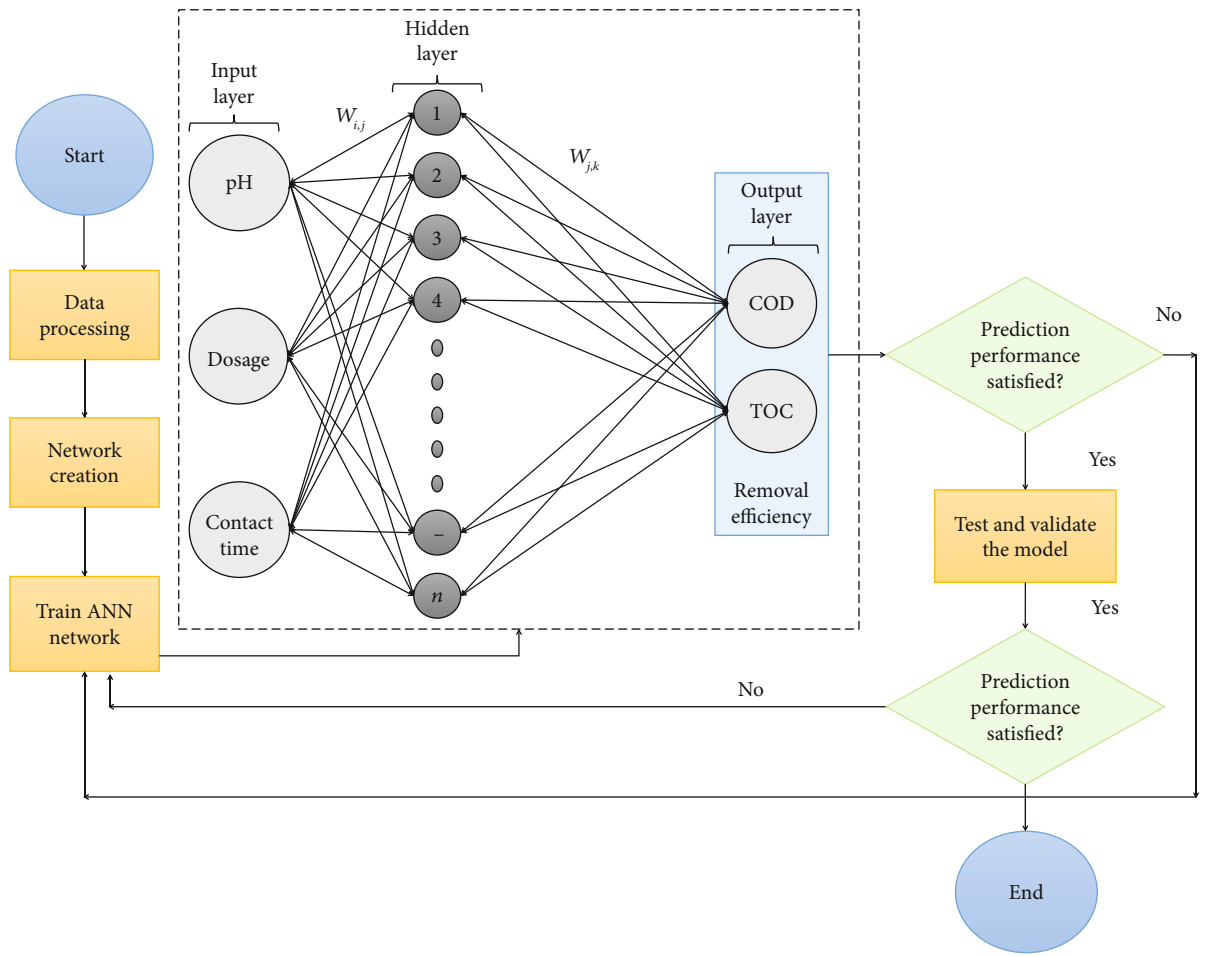

Figure 1: Schematic diagram of ANN model.

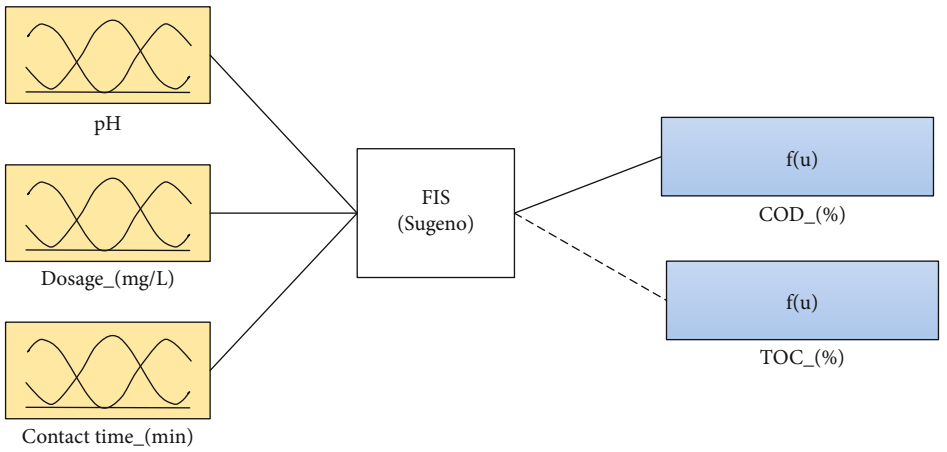

Figure 2: Schematic diagram of FIS.

subjected to the second-order polynomial regression model. As a polynomial model based on the quadratic equation, the response Y can be connected to the independent variables. At the middle of the pattern, one center point was used to approximate the total error. The quadratic regression equation used to extract the expected response results is given as follows:

$$Y = \beta_0 + \sum_{p=1}^{m} \beta_p + \sum_{p=1}^{m} \beta_{pp} x_p^2 + \sum_{q=1} \sum_{p=1} \beta_{qp} x_q x_p + \varepsilon. \quad (3)$$

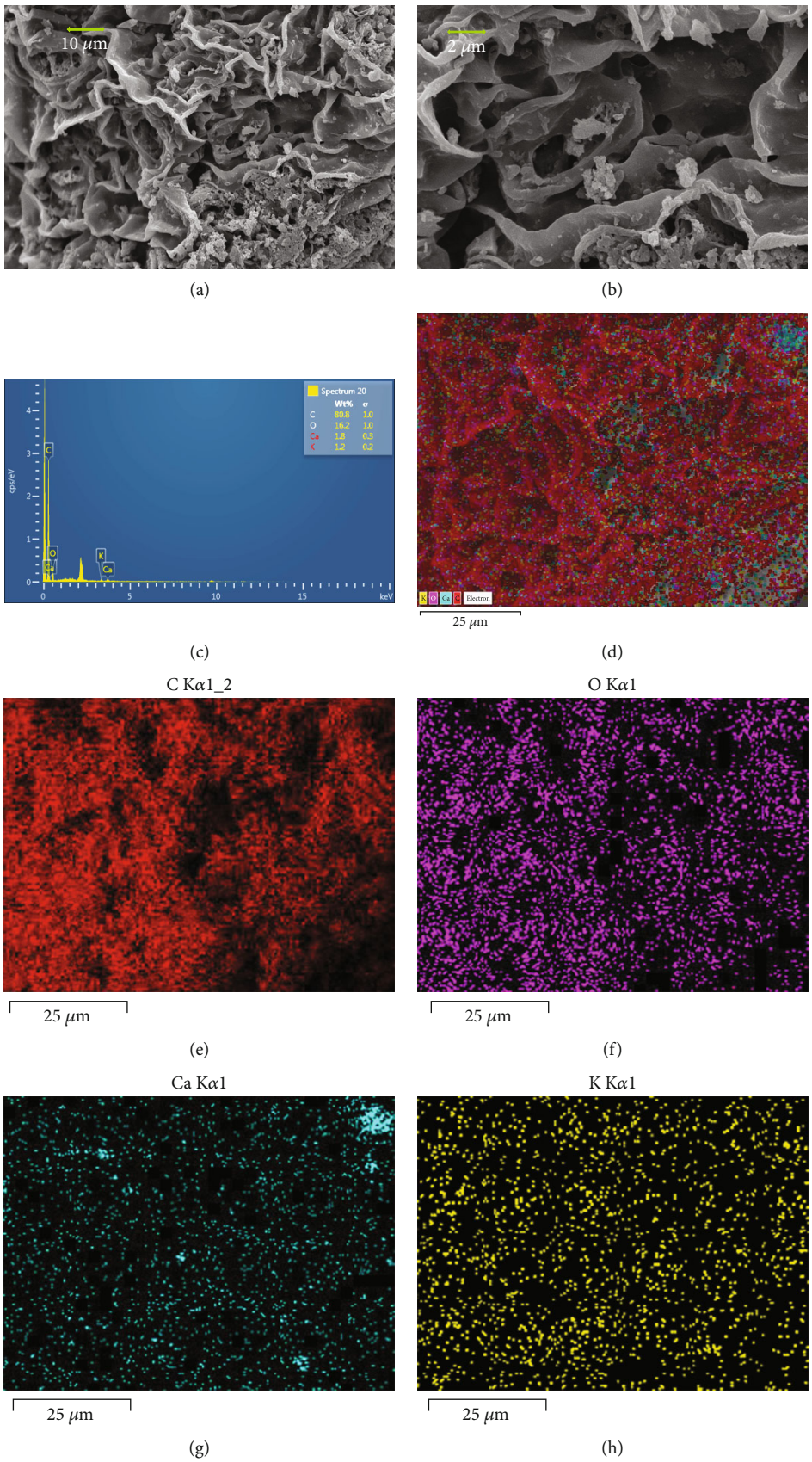

Figure 3: SEM-EDX images.

The output is expressed here by Y, while variables are written in the form of x_q and x_p. m shows the number of variables examined. B_0, β_p, β_{pp}, and β_{qp}, are classified as a constant coefficient, linear coefficient of interaction, coefficient of quadratic interaction, and the interaction coefficient of the 2nd order terms, respectively. Furthermore, the F-test and p values were used to determine the validity of each element.

To determine the adequacy of the established model and the statistical importance of the constant regression coefficients, the analysis of variance (ANOVA) was applied [37]. ANOVA analyzed the interactive, individual, and quadratic effects of input variables using TWBC on the removal efficiency of COD and TOC. Using the p value with a 95% trust rating, the model terms were evaluated. The F-value was used to analyze the sensitivity of the coefficients in regression. Also, to verify the adequacy of the formula, the coefficient of determination (R^2) value was compared to the adjusted R^2 value.

2.9. Performance Evaluation of the Models. The performance of the AI techniques (ANN and ANFIS) and RSM for prediction of adsorption data were evaluated using statistical equations, i.e., (i) the coefficient of determination (R^2) Equation (4), (ii) the sum of squared error (SSE) Equation (5), and (iii) mean squared error (MSE) Equation (6) [32, 38]. The value of R^2 should lie between 0 and 1. A value near 1 shows a good correlation between the experimental and model-simulated data sets. The SSE has values ranging from 0 to 1, while the best value is closer to 0 [39]. The minimum value of MSE is taken as the best value [40]. Following equations were used to measure the errors:

$$R^2 = 1 - \frac{\sum_{l=1}^{r}\left(y_{\text{pred},l} - y_{\text{exp},l}\right)^2}{\sum_{l=1}^{r}\left(y_{\text{pred},l} - y_m\right)^2}, \tag{4}$$

$$\text{SSE} = \sqrt{\frac{1}{r}\sum_{l=1}^{r}\left(y_{\text{pred},l} - y_{\text{exp},l}\right)^2}, \tag{5}$$

$$\text{MSE} = \frac{1}{r}\sum_{l=1}^{r}\left(y_{\text{pred},l} - y_{\text{exp},l}\right)^2, \tag{6}$$

where Y_{pred} and Y_{exp} denote the predicted and experimental values, respectively. r denotes the total number of values in data. The mean value of the response is denoted by y_m.

2.10. Optimization of the Adsorption Process

2.10.1. Development of ANN-GA. ANN and genetic algorithm (GA) hybrid were used for the optimization purpose using MATLAB optimization tool. Multiobjective optimization using GA (gamultobj) was taken as solver, and the ANN output equation (Equation (2)) was taken as an objective function. The algorithm had the following attributes: (i) population type of double vector; (ii) population size of 50; (iii) creation and mutation functions were constraint dependent; and (iv) crossover fraction of 0.8. The algorithm was run for optimization further. The goal was to maximize the COD and TOC removal efficiency.

2.10.2. Development of ANFIS Surface Plots. For the optimization of adsorption data through ANFIS, 2D surface plots were generated for pH range 3–10, dosage 25–300 mg/L, and contact time 10–60 min. Optimal values of the input variables were obtained through the surface plots.

Table 2: Experimental design matrix using the RSM technique with the experimental values for COD and TOC removal efficiency.

Run order	pH	Dosage (mg/L)	Contact time (min)	COD removal efficiency (%)	TOC removal efficiency (%)
1	10	162.5	60	30.61 ± 3	83.13 ± 3
2	3	162.5	60	75.27 ± 3	91.52 ± 3
3	6.5	25	60	58.94 ± 3	89.34 ± 3
4	6.5	300	60	89.87 ± 3	96.87 ± 3
5	6.5	162.5	35	70.57 ± 3	88.35 ± 3
6	10	25	35	83.04 ± 3	98.39 ± 3
7	6.5	25	10	68.83 ± 1	88.75 ± 3
8	3	162.5	10	52.12 ± 3	93.13 ± 3
9	3	25	35	60.96 ± 3	88.78 ± 3
10	10	162.5	10	78.3 ± 3	94.6 ± 3
11	3	300	35	55.89 ± 3	90.07 ± 3
12	10	300	35	62.92 ± 3	92.19 ± 3
13	6.5	300	10	57.12 ± 2	88.32 ± 3
13	6.5	300	10	57.12 ± 2	88.32 ± 3

Table 3: Performance evaluation of ANN based on number of neurons and algorithms.

Parameters	MSE	R^2
No. of neurons		
1	0.01	0.789
2	0.004	0.872
3	0.006	0.842
4	0.008	0.812
5	0.0002	0.998
6	0.0009	0.891
7	0.0005	0.997
8	0.0006	0.994
9	0.0008	0.991
10	0.0001	0.999
Algorithm		
Cascade-forward backpropagation (CFBP)	0.4	0.7
Levenberg-Marquardt backpropagation (LMBP)	0.0001	0.99
Bayesian regularization (BR)	0.04	0.85
Scaled conjugate gradient (SCG)	0.001	0.91

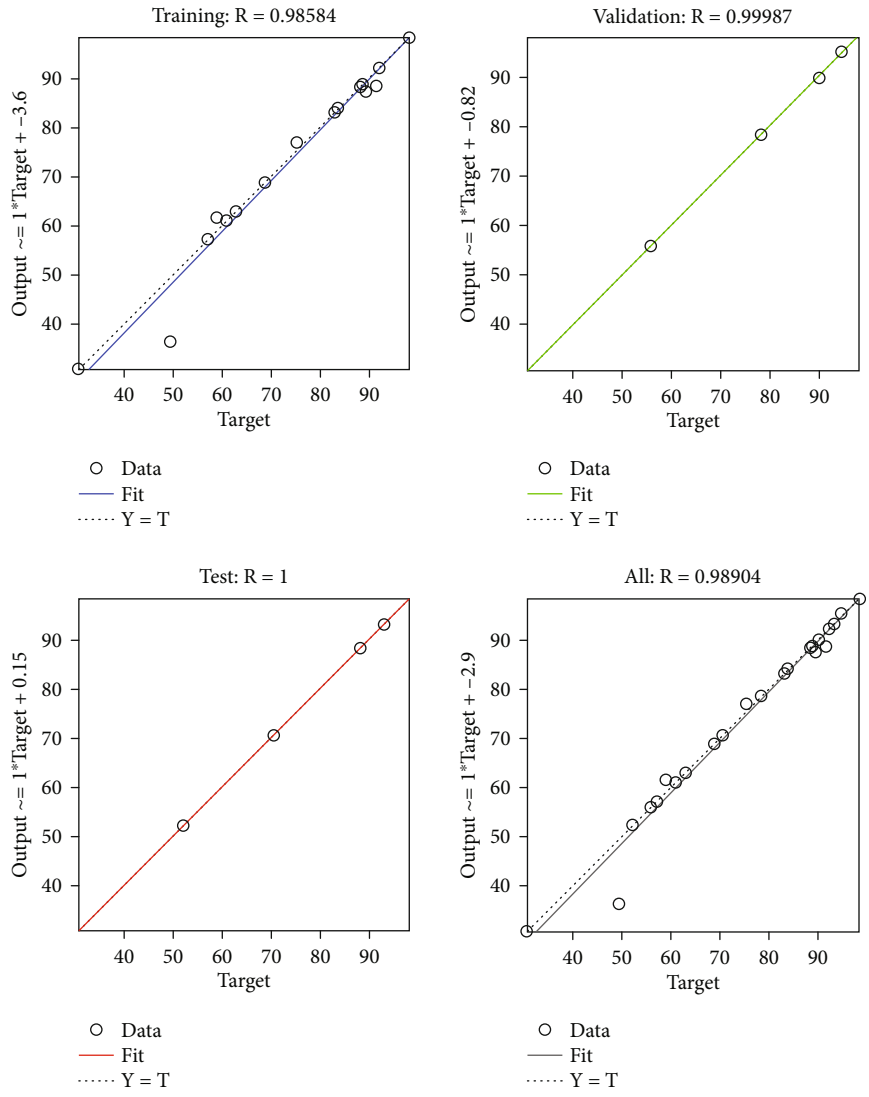

Figure 4: Training of ANN model.

Table 4: Weights and biases for ANN model.

Weights from input 1 to hidden layer $w_{i,j}$	Weights from input 2 to hidden layer $w_{i,j}$	Weights from input 3 to hidden layer $w_{i,j}$	Weights from hidden layer to output 1 $w_{j,k}$	Weights from hidden layer to output 2 $w_{j,k}$	Biases for hidden layer b_j	Biases for output layer b_k
$w_{1,1} = -1.157$	$w_{2,1} = 2.0135$	$w_{3,1} = 0.9782$	$w_{1,1} = 1.5125$	$w_{1,2} = -0.6018$	3.7538	
$w_{1,2} = -1.8344$	$w_{2,1} = 1.4641$	$w_{3,1} = -2.2931$	$w_{2,1} = 0.24355$	$w_{2,2} = 0.5023$	2.5117	
$w_{1,3} = 0.72447$	$w_{2,1} = 1.0304$	$w_{3,1} = 2.8132$	$w_{3,1} = 0.98934$	$w_{3,2} = 0.6861$	-2.9508	
$w_{1,4} = 0.74183$	$w_{2,1} = -3.2745$	$w_{3\,1} = -0.0515$	$w_{4,1} = 1.2401$	$w_{4,2} = 0.6152$	-1.3429	
$w_{1,5} = -2.8229$	$w_{2,1} = -0.6843$	$w_{3,1} = 1.5581$	$w_{5,1} = -0.01233$	$w_{5,2} = 0.7447$	0.67837	
$w_{1,6} = 2.3265$	$w_{2,1} = -1.6772$	$w_{3\,1} = -1.1571$	$w_{6,1} = -0.57107$	$w_{6,2} = 0.2616$	-0.0693	-1.4341
$w_{1,7} = 1.5054$	$w_{2,1} = -2.3961$	$w_{3,1} = -0.7552$	$w_{7,1} = -0.58306$	$w_{7,2} = -0.8805$	1.26	0.042027
$w_{1,8} = 0.65708$	$w_{2,1} = 2.5639$	$w_{3,1} = -2.1007$	$w_{8,1} = 0.46212$	$w_{8,2} = 0.1041$	0.51291	
$w_{1,9} = -2.4848$	$w_{2,1} = -1.169$	$w_{3,1} = -1.1492$	$w_{9,1} = -0.9444$	$w_{9,2} = -0.6083$	-2.1602	
$w_{1,10} = 3.1325$	$w_{2,1} = -0.5409$	$w_{3,1} = 0.4161$	$w_{10,1} = 1.0595$	$w_{10,2} = 0.8042$	2.2443	
$w_{1,11} = 3.5646$	$w_{2,1} = -1.3943$	$w_{3\,1} = -0.0107$	$w_{11,1} = -0.2883$	$w_{11,2} = 0.2258$	1.9193	
$w_{1,12} = 2.0214$	$w_{2,1} = -0.1438$	$w_{3,1} = 2.2269$	$w_{12,1} = 0.5544$	$w_{12,2} = 0.1560$	2.8432	

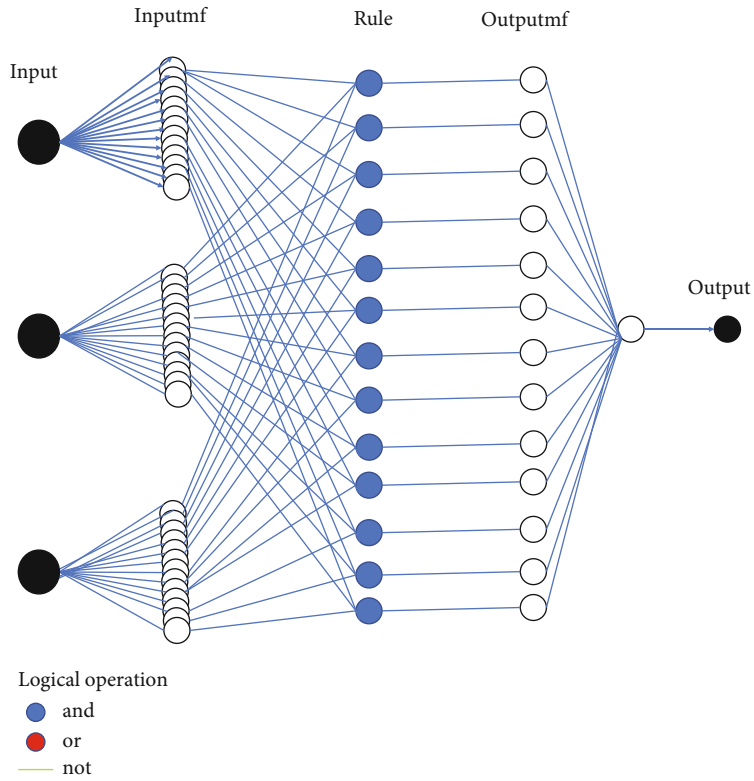

Figure 5: Schematic diagram of optimized ANFIS.

2.10.3. Development of RSM Surface Plots and RSM-GA. Using the DE software, three-dimensional surface and two-dimensional contour plots were created to visualize the relationship between the process factors and their corresponding effect on the output response. Optimal conditions were calculated after the model was completely analyzed. The numerical method was used under the optimization option in the Design Export software. For all independent variables "in range" options were chosen (e.g., pH 3–10, biochar dosage 25–300 mg/L, and contact time 10–60 min) while the "maximize" alternative was chosen for COD and TOC elimination.

RSM was also hybridized with GA in MATLAB R2021a using the response equations as the objective function. Response equation was obtained through the RSM model. GA parameters were the same as stated above. The optimized input values were obtained.

3. Results and Discussion

3.1. Characteristics of BC. The SEM-EDX images of TWBC are presented in Figure 3. Figures 3(a) and 3(b) showed that TWBC had many open pores available for adsorption of COD and TOC. The activating agent (phosphoric acid) seems to create an etched texture, as well as volatile matter decomposition [41]. The AC surfaces are uneven due to the etching, with significant porosity and roughness, indicating a desirable textural property of AC [42]. The mesopores available at the surface seem to cause capillary condensation as well as transferring adsorptive into the micropores, hence increasing the AC's adsorption capacity. The elemental composition in Figure 3(c) showed that TWBC had 80.8% of carbon and 16.2% oxygen content. The high carbon content showed good carbonization of TWBC. Small impurities of Ca and K were also observed in the TWBC.

Table 5: Modeling performance of ANFIS.

Output	Training MSE	Testing MSE	Checking MSE
COD	0.3626	0.49414	0.00000001
TOC	0.33281	0.69148	0.00001

3.2. Characterization of PW. The concentration of COD in the PW was about 1400 mg/L, which was much higher than the safe discharge limit of COD in effluents reported as 150 mg/L. The initial concentration of TOC in PW was 433.9 mg/L. It was also higher than the safe discharge limit of TOC in effluents, e.g., 30 mg/L. The COD>TOC indicated that the PW sample contained a substantial amount of chemically oxidizable organic and inorganic molecules. Oil and grease content can be found to attribute to the higher COD and TOC in PW, followed by suspended solids, organic acids, aromatic compounds, carbonyl compounds, anions, phenols, and metals [43].

3.3. Experimental Results. The experimental results of removal efficiencies for COD and TOC are presented in Table 2. A total of 13 batch experiments were conducted, and 26 data points were obtained. The results were used for the modeling of ANN, ANFIS, and RSM models.

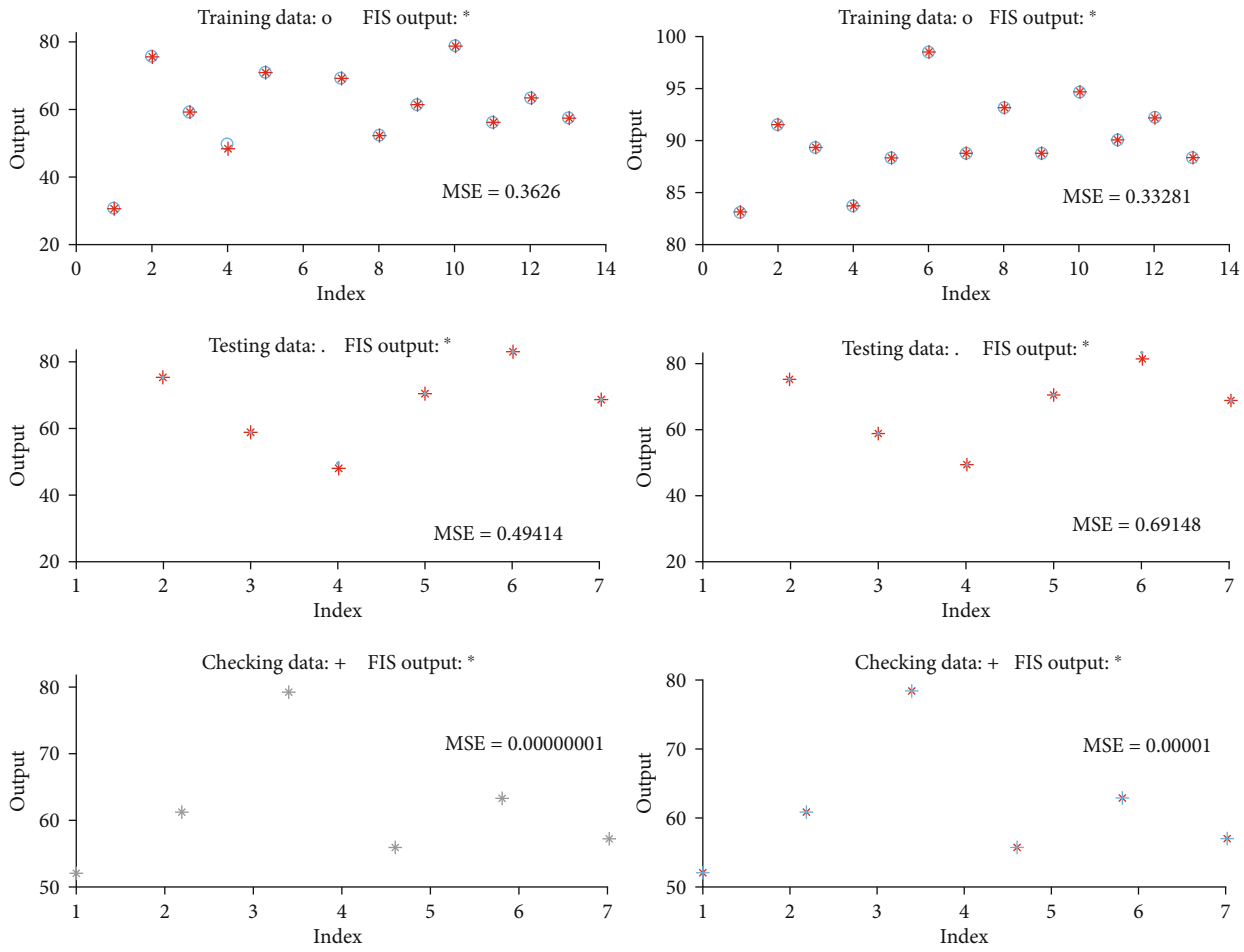

Figure 6: Modeling results using ANFIS for (a) CD removal efficiency and (b) TOC removal efficiency.

3.4. Modelling and Training of ANN. The neural network tool (nntool) was used in MATLAB R2021a for training of the ANN model. Among 26 data points collected from batch experiments, 18 points were selected for the training purpose and the remaining points were used for the testing and validation of the model.

12 no. of neurons, LMBP algorithm with trainlm training function, and tan sigmoid (tansig) transfer function were found most suitable to fit the experimental data. The no. of neurons and algorithm were selected based on the best performance measured as minimum MSE and highest regression analysis coefficient (R^2) as shown in Table 3.

After the selection of ANN architecture parameters, the model was applied for experimental data prediction. The trained model had a correlation coefficient of 0.985 with the experimental data as shown in Figure 4. The MSE value was 0.0001 which showed that the model had a minimum error and was significant. For the validation of the model, the remaining 15% points were tested and removal efficiency was found out, which had an R-value of 0.999. It showed that the model was well trained and could be used effectively for the prediction of COD and TOC adsorption on biochar. The model was further applied for the 15% data set for the prediction of COD and TOC adsorption, and an R-value of 1 was obtained for the predicted data. The overall efficiency of ANN model was 0.989 (Figure 4).

The weights and biases of the trained ANN model at 12 neurons and LMBP algorithm are given in Table 4. $w_{i,j}$ represents the weights from the input layer to hidden layer, $w_{j,k}$ represents the weights from hidden layer to the output layer, b_j represents the biases added at hidden layer, and b_k represents the biases added at the output layer of ANN model.

3.5. Modelling and Training of ANFIS. Sugeno-type subclustering FIS was generated for three inputs (26 data points) and two outputs (COD and TOC removal efficiency). 70% data was used for the training of the model. Membership functions were taken as 13 in numbers for each input variable and guassmf type. The range of influence was tested from 0 to 1 value. A minimum error was obtained at the value of 0.00001. Whereas, squash factor, accept ratio, and rejection ratio were 1.25, 0.5, and 0.15, respectively. The backpropagation method was taken as the optimization method due to the minimum RMSE of training data as compared to the backpropagation method. The optimized schematic diagram of ANFIS generated is shown in Figure 5.

Table 6: ANOVA for removal efficiencies using RSM.

(a) COD removal efficiency

Source	Sum of squares	df	Mean square	F-value	p value	
Model	2248.685	9	249.8539	10.87023	0.037405	Significant
A-pH	548.6328	1	548.6328	23.86902	0.016399	
B-dosage	235.9878	1	235.9878	10.26697	0.049173	
C-contact time	627.6425	1	627.6425	27.30644	0.013633	
AB	0.0081	1	0.0081	0.000352	0.020142	
AC	46.58063	1	46.58063	2.026554	0.024975	
BC	84.73203	1	84.73203	3.686383	0.015064	
A^2	276.9487	1	276.9487	12.04903	0.040312	
B^2	117.588	1	117.588	5.115827	0.108743	
C^2	9.984229	1	9.984229	0.434378	0.556921	
Residual	68.95543	3	22.98514			
Cor Total	2317.64	12				

(b) TOC removal efficiency

Source	Sum of squares	df	Mean square	F-value	p value	
Model	202.2155	9	22.46839	44.11838	0.004961	Significant
A-pH	12.37531	1	12.37531	24.29986	0.016003	
B-dosage	5.6448	1	5.6448	11.08399	0.044744	
C-contact time	25.52551	1	25.52551	50.12128	0.005796	
AB	5.29	1	5.29	10.38732	0.048476	
AC	15.72123	1	15.72123	30.86981	0.0115	
BC	7.29	1	7.29	14.31447	0.032367	
A^2	75.276	1	75.276	147.8101	0.001198	
B^2	2.057432	1	2.057432	4.039924	0.137989	
C^2	3.693889	1	3.693889	7.253231	0.074214	
Residual	1.527825	3	0.509275			
Cor Total	203.7433	12				

A total of 1000 no. of epochs were taken, and the model was trained several times for each output. The ANFIS training parameters were as follows: (i) number of nodes = 110; (ii) number of linear parameters = 52; (iii) number of nonlinear parameters = 78; (iv) total number of parameters = 130; (v) number of training data pairs: 13; (vi) number of checking data pairs: 6; and (vii) number of fuzzy rules = 13. The model was well trained after 10000 epochs for COD and 5000 epochs for TOC output. The minimum MSEs obtained for COD and TOC are given in Table 5. The model was tested and checked for the remaining 30% of experimental data.

Minimum MSE was obtained for both COD and TOC removal efficiencies after repeated training (Figure 6). It showed that model was well trained and could be used for prediction or optimization of adsorption data. The performance of the model was better in understanding the behavior of TOC removal as compared to COD removal. The reason can be low variance in TOC data as compared to COD.

3.6. Modelling of RSM Using BBD and Statistical Analysis. In the BBD design, three variables (pH, dosage, and contact time) were given as inputs. COD and TOC removal efficiencies were given as a response for analyzing the experimental data in design expert software. The generated runs and their experimental outputs are given in Table 2. The results of analysis of variance (ANOVA) are given in Table 6. It predicts the reliability of the applied design and correlation between various variables and their significance. A p value shows the significance of the results if it is less than 0.05. A higher p value shows that the data is insignificant to predict the behavior of variables. It can be seen in Table 6 that the overall model was significant for the removal of COD and TOC using biochar. The model F-values of 10.87 and 44.12 for COD and TOC removal efficiencies, respectively, implied that the model was significant, and there were only 3.74% and 0.50% chances that an F-value this large could occur due to noise. Adequate precision measures the signal to noise ratio. A ratio greater than 4 is desirable. Here, the ratio of 11.51 and 25.046 indicated an adequate signal and indicated that the model could be used to navigate the design space. The terms A, B, C, AB, AC, BC, and A^2 were significant model terms. The results of COD and TOC were fitted

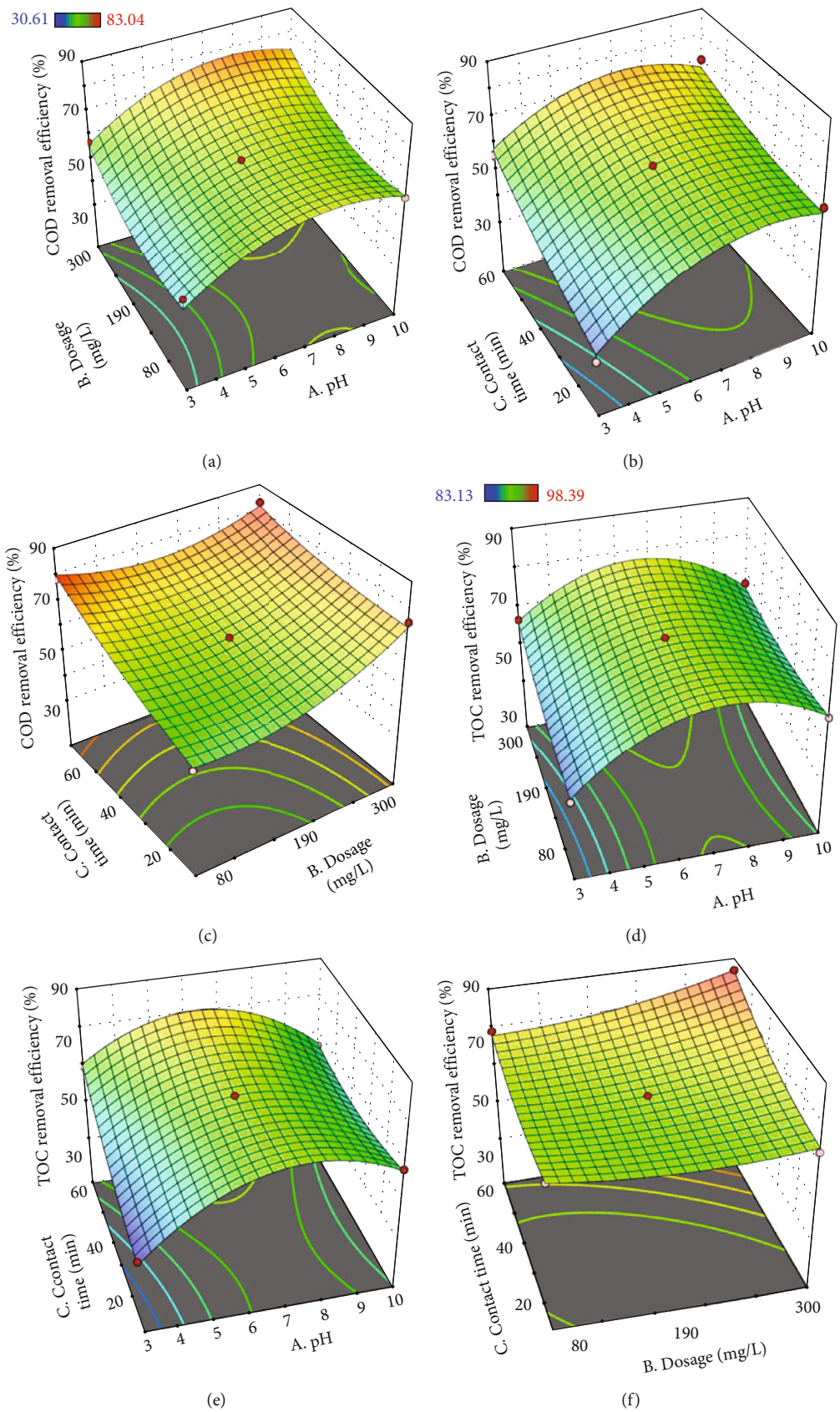

Figure 7: Surface plots for COD and TOC removal efficiencies using RSM (a) pH~dosage~COD removal efficiency (b) pH~contact time~COD removal efficiency (c) dosage~contact time~COD removal efficiency (d) pH~dosage~TOC removal efficiency (b) pH~contact time~TOC removal efficiency (c) dosage~contact time~TOC removal efficiency.

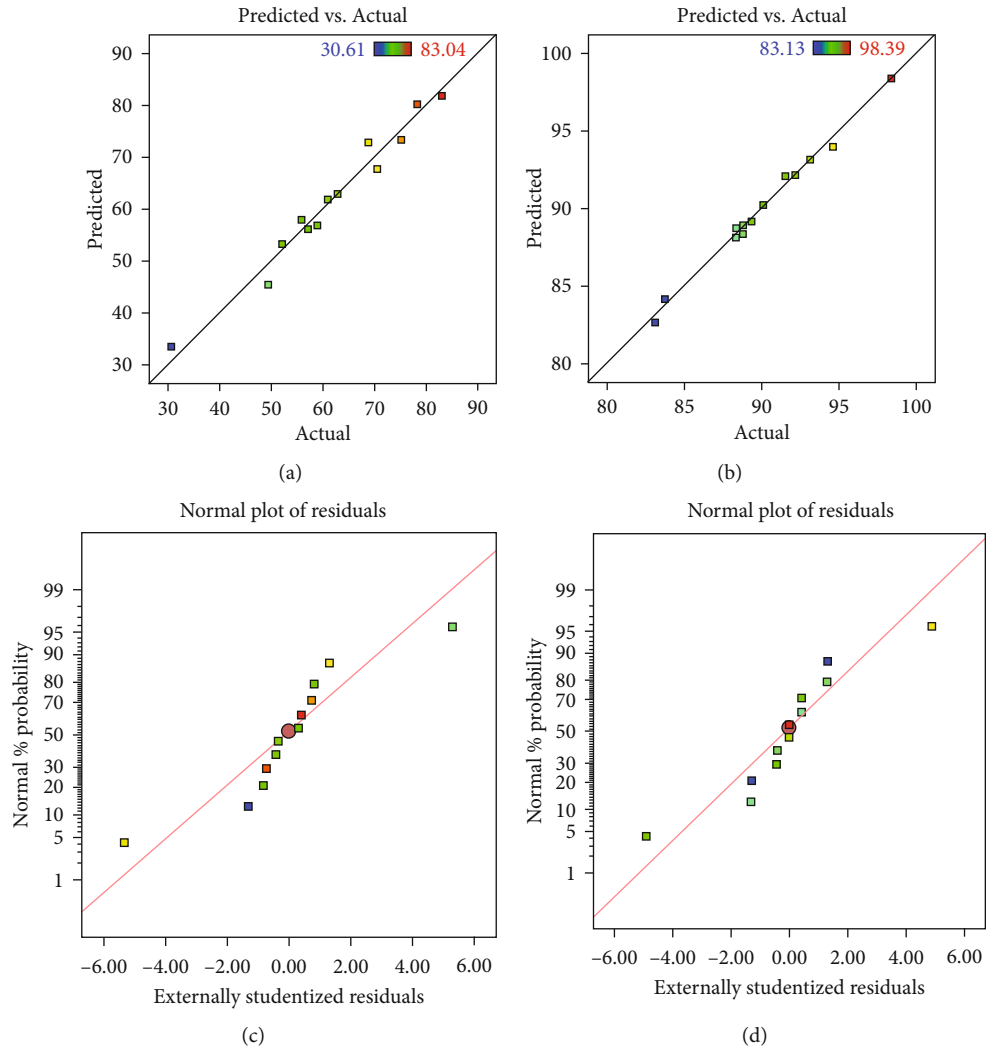

Figure 8: RSM model predicted vs actual data plots and normal residual plots. (a) Predicted and experimental values for COD removal efficiency. (b) Predicted and experimental values for TOC removal efficiency. (c) Normal percentage probability with respect to standardized residuals for COD removal efficiency. (d) Normal percentage probability with respect to standardized residuals for COD removal efficiency.

by a quadratic equation given in Equations (7) and (8), respectively:

$$\mathrm{COD} = +62.92 + 8.28A + 5.43B + 8.86C - 0.00450AB - 3.41AC - 4.60BC - 11.01A^2 + 7.17B^2 + 2.09C^2. \quad (7)$$

$$\mathrm{TOC} = +92.19 + 1.24A + 0.84B + 1.79C - 1.15AB - 1.98AC + 1.35BC - 5.74A^2 + 0.9488B^2 + 1.27C^2. \quad (8)$$

In terms of coded factors, Equations (7) and (8) can be used to predict responses for various ranges of each factor.

The three-dimensional surface plots of variables and their interaction are shown in Figure 7. Figure 7(a) shows that higher removal of COD can be achieved at higher values of dosages and pH within the selected range of parameters. Whereas for TOC adsorption, the removal efficiency decreased after pH 7 (Figure 7(d)). A similar trend has been observed in Figures 7(b) and 7(e) that higher contact times and higher pH was suitable to achieve the maximum removal of COD whereas TOC removal was maximum at middle points of the data range. The interaction plots of dosage and contact time (Figures 7(c) and 7(f)) suggested that higher dosage and contact time were suitable for the maximum removal of COD and TOC onto TWBC.

The correlation between COD and TOC removal efficiencies predicted and real values using RSM was quite strong. The R^2 values of the COD and TOC correlation plots were 0.999 and 0.999, respectively. Figures 8(a) and 8(b) represent the correlation plots of predicted and actual data whereas normal plots of residuals are represented in Figures 8(c) and 8(d). It showed that the model could be used satisfactorily for the prediction and optimization of the actual data set.

Table 7: Experimental and predicted results of COD and TOC adsorption using RSM, ANN, and ANFIS and statistical analysis of predicted results.

Sr. no.	pH	Dosage (mg/L)	Contact time (min)	COD removal efficiency (%)				TOC removal efficiency (%)			
				Actual	Predicted RSM	Predicted ANN	Predicted ANFIS	Actual	Predicted RSM	Predicted ANN	Predicted ANFIS
1	10	162.5	60	30.6	33.45	30.694	30.6	83.1	82.71	83.192	83.1
2	3	162.5	60	75.2	73.36	76.937	75.3	91.5	92.11	88.589	91.5
3	6.5	25	60	58.9	56.84	61.511	58.9	89.3	89.16	87.386	89.3
4	6.5	300	60	89.9	89.86	89.260	90.2	96.9	98.39	96.061	96.8
5	6.5	162.5	35	70.5	67.73	70.546	70.6	88.3	88.77	88.340	88.3
6	10	25	35	83.0	81.87	83.002	83	98.3	98.39	98.331	98.4
7	6.5	25	10	68.8	72.84	68.770	68.8	88.7	88.33	88.728	88.8
8	3	162.5	10	52.1	53.29	52.206	52.1	93.1	93.13	93.146	93.1
9	3	25	35	60.9	61.89	60.936	61	88.7	88.95	88.783	88.8
10	10	162.5	10	78.3	80.21	78.469	78.3	94.6	94.01	95.313	94
11	3	300	35	55.8	57.99	55.832	55.9	90.0	90.25	90.043	89.4
12	10	300	35	62.9	62.92	62.893	62.9	92.1	92.19	92.183	93.2
13	6.5	300	10	57.1	56.19	57.157	57.12	88.3	88.15	88.342	88.3
R^2					0.969	0.9920	0.9986		0.9924	0.9932	0.9943
SSE					2.3017	1.2244	0.4915		0.3424	0.3200	0.2957
MSE					5.2980	1.4993	0.2416		0.1172	0.1024	0.0874

3.7. Optimization of Adsorption Process Using Trained ANN, ANFIS, and RSM. For optimizing process parameters, the GA approach was combined with the ANN model to maximize COD and TOC removal efficiency. The optimum conditions for the COD and TOC removal process were as follows: 6.5 pH, 298.5 mg/L dosage of biochar, and 60 min contact time. The relationship between removal efficiency and iteration showed that the removal efficiency achieved the maximal value after 121 iterations and remained constant. The COD and TOC removal performance obtained under optimum conditions was 89.80% and 98.9%. The values were confirmed in the lab and obtained as $89.3 \pm 3\%$ and $97.95 \pm 3\%$.

For the prediction of adsorption data through ANFIS, surface plots were generated. Optimized value was obtained at pH value of 7, the dosage of 300 mg/L, and contact time 60 mins. The removal achieved at the optimized parameters was 88.9% and 98.8% for COD and TOC, respectively. The experimental value for the found variables was $89.3 \pm 3\%$ and $97.95 \pm 1.5\%$. It shows that the model well predicted the optimized value.

Optimal conditions using RSM were found after the model was completely analyzed. Optimized values were obtained at pH 6.5, dosage 300 mg/L, and contact time 60 min, with COD and TOC elimination of maximum as 89.859% and 98.390%, respectively. The viability of the model and the existence of ideal conditions were confirmed by a strong agreement between the experimental COD ($89.87 \pm 2\%$) and the predicted COD (89.859%) performance. The model predicted value was also confirmed for TOC removal efficiency as $96.87 \pm 3\%$ (experimental) and 98.390% (predicted) values.

The RSM-GA optimization was performed using Equations (7) and (8) as an objective function in GA using MATLAB. GA quickly trained and found the optimum values as pH of 6.6, TWBC dosage as 300 mg/L, and contact time of 60 min with removal efficiencies of COD and TOC as 89.86% and 97.2%, respectively.

3.8. Comparison of ANN, ANFIS, and RSM for Prediction of COD and TOC Adsorption Data. All three models applied for the adsorption data were well trained for COD and TOC removal efficiencies using pH, the dosage of TWBC, and contact time as input variables and COD and TOC as output variables. All models well fitted the adsorption data and were further applied for the prediction of experimental data. It was observed that the model's predicted values were near to the experimental data (Table 7). Further performance of the models was analyzed using Equations (4)–(6) for error analysis of predicted data. The analysis is given in Table 7. Analysis showed that RSM, ANN, and ANFIS had error values of 2.301, 1.2249, and 0.49157 for SSE and 5.29809, 1.49937, and 0.24164 for MSE, respectively, for the adsorption of COD onto biochar. For prediction of TOC adsorption using three models, the error values were as follows: 0.34243, 0.32001, and 0.29576 for SSE and 0.11726, 0.10241, and 0.08747 for MSE. The run time of ANFIS was only 100 seconds for 100 epochs whereas ANN took 120 seconds for 100 epochs. ANFIS proved to be a highly efficient tool in MATLAB for the modeling and prediction and optimization of adsorption data. The error analysis and coefficient of determination of three models determined that ANFIS>ANN>RSM in performance for the prediction of COD and TOC adsorption on the biochar.

Whereas for the optimization of adsorption data, ANN and ANFIS performed better as there were no specific limits for the input and output variables like RSM. Also, for both AI methods, no specific design of experiments was needed. It helped the models to analyze the correlation between inputs and outputs in a broader range. Enhanced efficiency of RSM may be obtained using larger data points. However, AI methods are innovative and include a variety of parameters to understand the nonlinear adsorption data.

4. Conclusions

To obtain the optimized results for COD and TOC adsorption using ANFIS, surface plots were generated. The BC was used in this study to model and optimize the adsorption process using computational techniques. COD and TOC removal efficiencies were taken as the representation of reduction in organic pollutants in the wastewater. Batch tests were performed using pH, dosage, and contact time as input variables. The experimental results were modeled and optimized using RSM, ANN, and ANFIS models. BBD was used for the RSM model, and ANOVA was used to predict the model significance. ANN model was modeled using 3 layered, feed-forward Levenberg-Marquardt backpropagation (LMBP) algorithm and 12 no. of neurons. ANFIS was generated of Sugeno type using subclustering FIS type. The experimental data was successfully optimized using the three models. For optimization of adsorption data, ANN and RSM models were hybridized with GA. Optimized values were well matched with the experimental results. ANFIS showed minimum run time and highest performance as compared to other models. Error analysis and coefficient of determination of three models determine the ANFIS>ANN>RSM in performance for the prediction of COD and TOC adsorption onto the biochar. However, AI methods predicted the optimized values at a broader range of input data which was not possible with RSM. No specific design of experiments was needed for AI methods and once trained can be used for prediction at any range of data. Hence, it can be stated that the AI methods can be used more effectively for the automation of the COD and TOC adsorption process for wastewater treatment.

Data Availability

All the required data are available in the manuscript itself.

Conflicts of Interest

The authors declare that there is no conflict of interest regarding the publication of this article.

Acknowledgments

The authors extend their appreciation to the Deputyship for Reseach & Innovation, Ministry of Education in Saudi Arabia for funding this research work through the project number IFPRC-031-612-2020 and King Abdulaziz University, DSR, Jeddah, Saudi Arabia.

References

[1] G. Elkiran, V. Nourani, and S. I. Abba, "Multi-step ahead modelling of river water quality parameters using ensemble artificial intelligence-based approach," *Journal of Hydrology*, vol. 577, article 123962, 2019.

[2] X. Nong, D. Shao, H. Zhong, and J. Liang, "Evaluation of water quality in the south-to-north water diversion project of China using the water quality index (WQI) method," *Water Research*, vol. 178, article 115781, 2020.

[3] M. M. Parsa, H. Pourfakhar, and M. Baghdadi, "Application of graphene oxide nanosheets in the coagulation-flocculation process for removal of total organic carbon (TOC) from surface water," *Journal of Water Process Engineering*, vol. 37, article 101367, 2020.

[4] U. A. Toor, T. T. Duong, S. Y. Ko, F. Hussain, and S. E. Oh, "Optimization of Fenton process for removing TOC and color from swine wastewater using response surface method (RSM)," *Journal of Environmental Management*, vol. 279, p. 111625, 2021.

[5] A. Bazan-Wozniak and R. Pietrzak, "Adsorption of organic and inorganic pollutants on activated bio-carbons prepared by chemical activation of residues of supercritical extraction of raw plants," *Chemical Engineering Journal*, vol. 393, article 124785, 2020.

[6] F. Masood, M. Ahmad, M. A. Ansari, and A. Malik, "Prediction of biosorption of total chromium by bacillus sp. using artificial neural network," *Bulletin of Environmental Contamination and Toxicology*, vol. 88, no. 4, pp. 563–570, 2012.

[7] S. Al Aani, T. Bonny, S. W. Hasan, and N. Hilal, "Can machine language and artificial intelligence revolutionize process automation for water treatment and desalination?," *Desalination*, vol. 458, pp. 84–96, 2019.

[8] T. Khan, M. R. U. Mustafa, M. H. Isa et al., "Artificial neural network (ANN) for modelling adsorption of lead (Pb (II)) from aqueous solution," *Water, Air, and Soil Pollution*, vol. 228, no. 11, 2017.

[9] N. Prakash, S. A. Manikandan, L. Govindarajan, and V. Vijayagopal, "Prediction of biosorption efficiency for the removal of copper(II) using artificial neural networks," *Journal of Hazardous Materials*, vol. 152, no. 3, pp. 1268–1275, 2008.

[10] T. MacKo, R. Brüll, C. Brinkmann, and H. Pasch, "Automated monitoring of the establishment of the adsorption equilibrium: adsorption of polyethylene from 1,2,4-trichlorobenzene onto a zeolite at temperature 140°C," *Journal of Automated Methods & Management in Chemistry*, vol. 2009, pp. 1–6, 2009.

[11] M. Dolatabadi, M. Mehrabpour, M. Esfandyari, H. Alidadi, and M. Davoudi, "Modeling of simultaneous adsorption of dye and metal ion by sawdust from aqueous solution using of ANN and ANFIS," *Chemometrics and Intelligent Laboratory Systems*, vol. 181, pp. 72–78, 2018.

[12] M. Fan, J. Hu, R. Cao, K. Xiong, and X. Wei, "Modeling and prediction of copper removal from aqueous solutions by nZVI/rGO magnetic nanocomposites using ANN-GA and ANN-PSO," *Scientific Reports*, vol. 7, no. 1, article 18040, 2017.

[13] N. Mahmoodi-Babolan, A. Heydari, and A. Nematollahzadeh, "Removal of methylene blue via bioinspired catecholamine/starch superadsorbent and the efficiency prediction by response surface methodology and artificial neural network-

particle swarm optimization," *Bioresource Technology*, vol. 294, article 122084, 2019.

[14] M. S. Bhatti, D. Kapoor, R. K. Kalia, A. S. Reddy, and A. K. Thukral, "RSM and ANN modeling for electrocoagulation of copper from simulated wastewater: multi objective optimization using genetic algorithm approach," *Desalination*, vol. 274, no. 1-3, pp. 74–80, 2011.

[15] A. S. Dawood and Y. Li, "Modeling and optimization of new flocculant dosage and pH for flocculation: removal of pollutants from wastewater," *Water*, vol. 5, no. 2, pp. 342–355, 2013.

[16] M. Mortula, J. Abdalla, and A. Ghadban, *Modeling Phosphorus Removal Process using Artificial Neural Network Modeling approach, Conference: BALWOIS 2010 At: Ohrid, Republic of Macedonia*, pp. 1–7, 2010, https://www.researchgate.net/publication/324562867.

[17] M. Khayet, C. Cojocaru, and M. Essalhi, "Artificial neural network modeling and response surface methodology of desalination by reverse osmosis," *Journal of Membrane Science*, vol. 368, no. 1-2, pp. 202–214, 2011.

[18] C. A. Igwegbe, L. Mohmmadi, S. Ahmadi et al., "Modeling of adsorption of methylene blue dye on Ho-CaWO4 nanoparticles using response surface methodology (RSM) and artificial neural network (ANN) techniques," *MethodsX*, vol. 6, pp. 1779–1797, 2019.

[19] A. Deb, A. Debnath, and B. Saha, "Ultrasound-aided rapid and enhanced adsorption of anionic dyes from binary dye matrix onto novel hematite/polyaniline nanocomposite: response surface methodology optimization," *Applied Organometallic Chemistry*, vol. 34, no. 2, pp. 1–20, 2020.

[20] A. Deb, A. Debnath, and B. Saha, "Sono-assisted enhanced adsorption of eriochrome black-T dye onto a novel polymeric nanocomposite: kinetic, isotherm, and response surface methodology optimization," *Journal of Dispersion Science and Technology*, vol. 42, no. 11, pp. 1579–1592, 2021.

[21] A. Deb, A. Debnath, N. Bhattacharjee, and B. Saha, "Ultrasonically enhanced dye removal using conducting polymer functionalised ZnO nanocomposite at near neutral pH: kinetic study, isotherm modelling and adsorbent cost analysis," *International Journal of Environmental Analytical Chemistry*, pp. 1–20, 2020.

[22] A. Deb, M. Kanmani, A. Debnath, K. L. Bhowmik, and B. Saha, "Preparation and characterization of magnetic CaFe2O4 nanoparticles for efficient adsorption of toxic Congo red dye from aqueous solution: predictive modelling by artificial neural network," *Desalination and Water Treatment*, vol. 89, pp. 197–209, 2017.

[23] A. Deb, A. Debnath, K. L. Bhowmik, S. Rudra Paul, and B. Saha, "Application of polyaniline impregnated mixed phase Fe2O3, MnFe2O4and ZrO2nanocomposite for rapid abatement of binary dyes from aqua matrix: response surface optimisation," *International Journal of Environmental Analytical Chemistry*, pp. 1–19, 2021.

[24] A. Deb, M. Kanmani, A. Debnath, K. L. Bhowmik, and B. Saha, "Ultrasonic assisted enhanced adsorption of methyl orange dye onto polyaniline impregnated zinc oxide nanoparticles: kinetic, isotherm and optimization of process parameters," *Ultrasonics Sonochemistry*, vol. 54, pp. 290–301, 2019.

[25] A. Ghosh, P. Das, and K. Sinha, "Modeling of biosorption of Cu(II) by alkali-modified spent tea leaves using response surface methodology (RSM) and artificial neural network (ANN)," *Applied Water Science*, vol. 5, no. 2, pp. 191–199, 2015.

[26] T. Shojaeimehr, F. Rahimpour, M. A. Khadivi, and M. Sadeghi, "A modeling study by response surface methodology (RSM) and artificial neural network (ANN) on Cu^{2+} adsorption optimization using light expended clay aggregate (*LECA*)," *Journal of Industrial and Engineering Chemistry*, vol. 20, no. 3, pp. 870–880, 2014.

[27] A. S. Mahmoud, R. S. Farag, and M. M. Elshfai, "Reduction of organic matter from municipal wastewater at low cost using green synthesis nano iron extracted from black tea: artificial intelligence with regression analysis," *Egyptian Journal of Petroleum*, vol. 29, no. 1, pp. 9–20, 2020.

[28] E. Nasher, L. Y. Heng, Z. Zakaria, and S. Surif, "Concentrations and sources of polycyclic aromatic hydrocarbons in the seawater around Langkawi Island, Malaysia," *Journal of Chemistry*, vol. 2013, 10 pages, 2013.

[29] Z. Ma, H. Li, Z. Ye, J. Wen, Y. Hu, and Y. Liu, "Application of modified water quality index (WQI) in the assessment of coastal water quality in main aquaculture areas of Dalian, China," *Marine Pollution Bulletin*, vol. 157, p. 111285, 2020.

[30] S. Palani, S. Y. Liong, and P. Tkalich, "An ANN application for water quality forecasting," *Marine Pollution Bulletin*, vol. 56, no. 9, pp. 1586–1597, 2008.

[31] H. Khurshid, M. R. U. Mustafa, U. Rashid, M. H. Isa, H. Y. Chia, and M. M. Shah, "Adsorptive removal of COD from produced water using tea waste biochar," *Environmental Technology and Innovation*, vol. 23, article 101563, 2021.

[32] M. R. Mustafa, R. B. Rezaur, S. Saiedi, and M. H. Isa, "River suspended sediment prediction using various multilayer perceptron neural network training algorithms-a case study in Malaysia," *Water Resources Management*, vol. 26, no. 7, pp. 1879–1897, 2012.

[33] R. Olawoyin, "Application of backpropagation artificial neural network prediction model for the PAH bioremediation of polluted soil," *Chemosphere*, vol. 161, pp. 145–150, 2016.

[34] P. S. Pauletto, S. F. Lütke, G. L. Dotto, and N. P. G. Salau, "Forecasting the multicomponent adsorption of nimesulide and paracetamol through artificial neural network," *Chemical Engineering Journal*, vol. 412, article 127527, 2021.

[35] J. Sargolzaei, M. H. Asl, and A. H. Moghaddam, "Membrane permeate flux and rejection factor prediction using intelligent systems," *Desalination*, vol. 284, pp. 92–99, 2012.

[36] D. S. P. Franco, F. A. Duarte, N. P. G. Salau, and G. L. Dotto, "Analysis of indium (III) adsorption from leachates of LCD screens using artificial neural networks (ANN) and adaptive neuro-fuzzy inference systems (ANIFS)," *Journal of Hazardous Materials*, vol. 384, article 121137, 2020.

[37] M. Ghaedi, F. N. Azad, K. Dashtian, S. Hajati, A. Goudarzi, and M. Soylak, "Central composite design and genetic algorithm applied for the optimization of ultrasonic-assisted removal of malachite green by ZnO nanorod-loaded activated carbon," *Spectrochimica Acta Part A: Molecular and Biomolecular Spectroscopy*, vol. 167, pp. 157–164, 2016.

[38] M. Dutta and J. K. Basu, "Application of artificial neural network for prediction of Pb(II) adsorption characteristics," *Environmental Science and Pollution Research*, vol. 20, no. 5, pp. 3322–3330, 2013.

[39] S. Dutta, S. A. Parsons, C. Bhattacharjee, S. Bandhyopadhyay, and S. Datta, "Development of an artificial neural network model for adsorption and photocatalysis of reactive dye on TiO_2 surface," *Expert Systems with Applications*, vol. 37, no. 12, pp. 8634–8638, 2010.

[40] E. A. Dil, M. Ghaedi, A. Ghaedi, A. Asfaram, M. Jamshidi, and M. K. Purkait, "Application of artificial neural network and response surface methodology for the removal of crystal violet by zinc oxide nanorods loaded on activate carbon: kinetics and equilibrium study," *Journal of the Taiwan Institute of Chemical Engineers*, vol. 59, pp. 210–220, 2016.

[41] A. A. Adetokun, S. Uba, and Z. N. Garba, "Optimization of adsorption of metal ions from a ternary aqueous solution with activated carbon from *Acacia senegal* (L.) *Willd* pods using central composite design," *Journal of King Saud University-Science*, vol. 31, no. 4, pp. 1452–1462, 2019.

[42] Ö. Çelebican, İ. İnci, and N. Baylan, "Modeling and optimization of formic acid adsorption by multiwall carbon nanotube using response surface methodology," *Journal of Molecular Structure*, vol. 1203, p. 127312, 2020.

[43] J. Lu, X. Wang, B. Shan, X. Li, and W. Wang, "Analysis of chemical compositions contributable to chemical oxygen demand (COD) of oilfield produced water," *Chemosphere*, vol. 62, no. 2, pp. 322–331, 2006.

Hindawi
Adsorption Science & Technology
Volume 2022, Article ID 9384871, 51 pages
https://doi.org/10.1155/2022/9384871

Review Article

A Review of the Modeling of Adsorption of Organic and Inorganic Pollutants from Water Using Artificial Neural Networks

Hilda Elizabeth Reynel-Ávila,[1,2] Ismael Alejandro Aguayo-Villarreal,[3] Lizbeth Liliana Diaz-Muñoz,[1] Jaime Moreno-Pérez,[1] Francisco Javier Sánchez-Ruiz,[4] Cintia Karina Rojas-Mayorga,[3] Didilia Ileana Mendoza-Castillo,[1,2] and Adrián Bonilla-Petriciolet[1]

[1]*Instituto Tecnológico de Aguascalientes, Aguascalientes 20256, Mexico*
[2]*CONACYT, Ciudad de México 03940, Mexico*
[3]*Universidad de Colima, Colima 28400, Mexico*
[4]*Universidad Popular Autónoma del Estado de Puebla, Puebla 72410, Mexico*

Correspondence should be addressed to Adrián Bonilla-Petriciolet; petriciolet@hotmail.com

Received 31 December 2021; Accepted 28 January 2022; Published 27 February 2022

Academic Editor: Nadeem A khan

The application of artificial neural networks on adsorption modeling has significantly increased during the last decades. These artificial intelligence models have been utilized to correlate and predict kinetics, isotherms, and breakthrough curves of a wide spectrum of adsorbents and adsorbates in the context of water purification. Artificial neural networks allow to overcome some drawbacks of traditional adsorption models especially in terms of providing better predictions at different operating conditions. However, these surrogate models have been applied mainly in adsorption systems with only one pollutant thus indicating the importance of extending their application for the prediction and simulation of adsorption systems with several adsorbates (i.e., multicomponent adsorption). This review analyzes and describes the data modeling of adsorption of organic and inorganic pollutants from water with artificial neural networks. The main developments and contributions on this topic have been discussed considering the results of a detailed search and interpretation of more than 250 papers published on Web of Science ® database. Therefore, a general overview of the training methods, input and output data, and numerical performance of artificial neural networks and related models utilized for adsorption data simulation is provided in this document. Some remarks for the reliable application and implementation of artificial neural networks on the adsorption modeling are also discussed. Overall, the studies on adsorption modeling with artificial neural networks have focused mainly on the analysis of batch processes (87%) in comparison to dynamic systems (13%) like packed bed columns. Multicomponent adsorption has not been extensively analyzed with artificial neural network models where this literature review indicated that 87% of references published on this topic covered adsorption systems with only one adsorbate. Results reported in several studies indicated that this artificial intelligence tool has a significant potential to develop reliable models for multicomponent adsorption systems where antagonistic, synergistic, and noninteraction adsorption behaviors can occur simultaneously. The development of reliable artificial neural networks for the modeling of multicomponent adsorption in batch and dynamic systems is fundamental to improve the process engineering in water treatment and purification.

1. Introduction

The removal of pollutants from industrial process streams, groundwater, and wastewaters has an undoubtedly importance in terms of sustainability and human health protection [1, 2]. Adsorption is a key treatment method for facing the current challenges of water depollution. In particular, it is a proven and well-known technology for water purification due to its both technical and economic advantages [3–7]. The recent advances on adsorption for water treatment have

mainly focused on the preparation and evaluation of new materials with outstanding adsorption capacities for the removal of different pollutants like dyes, heavy metals, geogenic compounds, pharmaceuticals, and other emerging toxic chemicals [8–20]. Actually, there is a wide spectrum of adsorbents that have been prepared and assessed to remove inorganic and organic compounds from aqueous solutions. Adsorption properties of these novel adsorbents have been determined experimentally using batch adsorbers and/or packed bed columns, which are the typical operating modes of this purification method.

Experimental studies with batch adsorbers allow to quantify the adsorption kinetics and isotherms as well as other important thermodynamic parameters associated to the adsorbent performance. Batch adsorbers are useful for establishing the maximum adsorption capacities for the adsorbate(s)-adsorbent system under ideal and controlled conditions since the experimental data are obtained at the thermodynamic equilibrium where the mass transfer resistances are reduced [21, 22]. Note that the adsorption processes in batch condition are not commonly employed for the treatment of real fluids at large scale since equipment with significant dimensions and long operating times is required. The packed bed adsorption columns are the most appropriate option for treating real fluids at industrial scale operation including the adsorbent regeneration [23]. Breakthrough curves obtained in packed-bed columns are fundamental to determine the maximum adsorption capacities at dynamic operating conditions and the analysis of mass transfer phenomena on the adsorbent performance.

Process systems engineering of adsorption for water treatment requires the development of reliable models to predict the corresponding kinetic, thermodynamics, and mass transfer parameters of the system at hand. The adsorption modeling offers valuable data for the operation, control, optimization, and design of water purification equipment. For instance, the modeling of adsorption processes is fundamental to estimate the adsorbent performance at both dynamic and batch operating conditions, to optimize the adsorption process variables, to perform a sensitivity analysis of process conditions on the adsorption performance, and to analyze other design issues that are required to improve the operating costs and removal efficacy in water treatment [24–27]. Herein, it is necessary to highlight that the adsorption processes in liquid phase are highly dependent on the type, variety, and concentration of adsorbate(s) contained in the fluid, the fluid physicochemical characteristics (e.g., ionic strength, temperature, and pH), the operational conditions of adsorber (e.g., stirring rate, adsorbent dosage, bed height, flow rate, and residence time), and the adsorbent physicochemical properties (e.g., particle size, surface chemistry, and textural parameters). Therefore, the modeling of adsorption process is a multivariable problem that involves nonlinear relationships between the input and output variable(s). These mathematical characteristics imply that the reliable correlation and prediction of adsorption processes are challenging, especially for multicomponent systems [28–30].

Overall, the available adsorption models can be classified in theoretical, semitheoretical, and empirical, and they can be also in the form of analytical and differential equations. Some reviews have analyzed specific adsorption equations [31–34], and results reported in a number of studies have also illustrated their limitations and advantages [28, 29, 33, 35–38]. In particular, the drawbacks of adsorption models are magnified when they are applied in multicomponent solutions. The simultaneous presence of several compounds to be adsorbed from the fluid can affect the adsorbent behavior due to their antagonic, synergic, and noninteraction effects [39–41]. These adsorption effects depend significantly on the properties of the adsorbates dissolved in the fluid and their concentrations. Multicomponent adsorption models derived from the traditional equations of Langmuir, Freundlich, or Sips are regarded as empirical approaches that can fail to simulate adsorption systems with several adsorbates. Consequently, it is important to develop and improve the available modeling tools for analyzing the multicomponent adsorption involved in the treatment and purification of real-life fluids.

Artificial intelligence-based models are an alternative to improve the simulation of adsorption processes for water treatment. Several authors have recognized the contribution of this type of models to obtain better correlations and estimations of the adsorption of inorganic and organic adsorbates in single and multicomponent solutions [42–47]. The artificial neural networks (ANN) have been introduced as an effective and reliable approach to overcome the problems associated to the simulation of adsorption systems especially those corresponding to fluids with more than one adsorbate at different operating conditions [43, 46, 48, 49]. ANN are based on human brain structures and capable to represent the nonlinear interactions between a set of input and output variable(s) of a given system without considering a sophisticated theory [50]. They have been employed to resolve engineering problems such as fault detection, prediction of materials properties, soil degradation analysis, water treatment modeling, data reconciliation, process modeling, and control [50–54]. The advantages of ANN (e.g., reliable correlation, simplicity, versatility, and prediction capabilities) to handle multivariable problems with nonlinear behavior have justified their application in the analysis and simulation of adsorption processes [50, 52, 55–58].

In this direction, this review covers the ANN-based modeling of adsorption processes in dynamic and batch operating schemes. The objective of this review was to provide the readers a general perspective of the developments, contributions, and opportunities on the modeling of adsorption data with artificial neural networks. A brief description of the theory and basis of ANN is provided in the first section of this review. The modeling of kinetic, isotherms, and breakthrough curves with ANN is analyzed and discussed. Some important guidelines concerning the parameter estimation problem to be resolved for ANN training, the selection of the input and output variables to be modeled with ANN, the details of its numerical implementation in terms of adsorption data correlation and prediction, and some challenges to be faced and resolved besides perspectives on this topic are also covered in this manuscript.

2. Brief Introduction of Artificial Neural Networks

ANN were initially developed using the concept for artificial intelligence with the aim of simulating the activities and functions of nervous system and human brain in terms of memorizing and learning [48, 59]. They came from the analogy made between the human brain and computer processing. Basically, ANN are a computational system that replicates the function of the brain to carry out a specific task [60]. Input value(s) (i.e., independent variables of the system under study) are provided to the network and are manipulated via internal mathematical operations to produce an output value(s) (i.e., dependent variables of the system under study) [60]. ANN are considered as black-box models useful when a mathematical relationship between the output and input variables is not available to describe the phenomenon to be analyzed and/or where the traditional models may fail [61, 62]. ANN contain multiple interconnected nonlinear processing elements that "learn" to represent and extrapolate the nonlinear relationships between the dependent and independent variables of the case of study [48].

Mathematically, ANN are composed of simple elements to perform the calculations where these elements are interconnected with a certain topology or structure. The perceptron (neuron) is the simplest elements of a network. The basic model of a neuron is illustrated in Figure 1(a) and is integrated by the next components [63, 64]: (1) a set of synapses, which are the inputs of a neuron given by a weighted vector; (2) an adder that simulates the neuron body and gets the level of arousal; and (3) an activation function that generates the output if it reaches the level of excitement and restricts the output level, thus, avoiding the network congestion. Formally, the neuron output (y) in ANN is given by the expression

$$y_i = \left(\sum_{j=1}^{n} w_{ij} s_j + w_{i0} \right), \tag{1}$$

where n indicates the number of inputs to the neuron i, and φ denotes the excitation or activation function [65, 66]. The argument of the activation function is the linear combination of the neuron inputs. Considering the set of entries s and weights W of the neuron i as a vector of dimension $n + 1$, Equation (1) can be defined as follows

$$\begin{aligned} y_i &= \varphi\left[W_i^T s\right], \\ s &= \left[-1, s_1, s_2, \cdots, s_n\right]^T, \\ w_i &= \left[w_{i0}, w_{i1}, \cdots, w_{\text{in}}\right]^T. \end{aligned} \tag{2}$$

ANN can be classified into static and dynamic networks where the first one has a broad range of application mainly due to its characteristic of not change with respect to time. Dynamic networks are applied for those problems that have changes with respect of time [67, 68]. Multilayer ANN are widely utilized because they resemble the structures of human brain and can be spread with forward and backward configurations where the selection depends on the case of study [69, 70]. Particularly, the multilayer ANN with forward spread has been successfully applied in the correlation and prediction of batch and dynamic adsorption processes [6, 11, 27, 41, 57, 71–80].

A multilayer ANN structure includes an input layer, one or more hidden layers, and an output layer, see Figure 1(b). Input layer contains the independent variables of the case of study, while the output layer corresponds to the corresponding dependent variables. The structure definition of a multilayer ANN seeks to reduce the problems associated to the prediction of nonlinear behavior of a multivariable system. Therefore, an important issue is to establish the suitable ANN architecture (i.e., the number of hidden layers and their neurons). This task is commonly based on a trial-error approach. In this sense, the theorem of Kolmogorov [81] indicates that "the number of neurons in the hidden layer need not be larger than twice the number of entries." Hecht-Nielsen et al. [82] proposed the next equation to estimate the number of neurons in the hidden layers of ANN [83]:

$$h - \left(\frac{2}{3}\right)(n + m), \tag{3}$$

where h is the number of hidden layer neurons, n is the number of entries, and m is the number of hidden layers used in the ANN, respectively. Equation (3) suggests that the number of neurons required in the hidden layer should be $h < 2n$. For the case of a multilayer structure with a single hidden layer, it has been recommended that the number of neurons should be 2/3 of the corresponding number of entries [84, 85].

The next step for building an ANN model is the application of excitation or activation function(s). These functions are required to spread the information and used for ANN training (i.e., the adjustment of the corresponding synaptic weights to model the system at hand) [86, 87]. There are different excitation/activation functions where the most common ones are the tangential sigmoidal (Equation (4)), logarithmic (Equation (5)), and radial basis (Equation (6))

$$\varphi = \frac{e^{-w_i} + e^{w_i}}{e^{-w_i} + e^{w_i}}, \tag{4}$$

$$\varphi = \frac{1}{1 + e^{-w_i}}, \tag{5}$$

$$\varphi = \sum_{i=1}^{N} w_i \Phi(\|w - w_{ci}\|). \tag{6}$$

The radial basis function is commonly used for dynamic systems and can be utilized in nondynamic processes but at the expense of increasing the computation

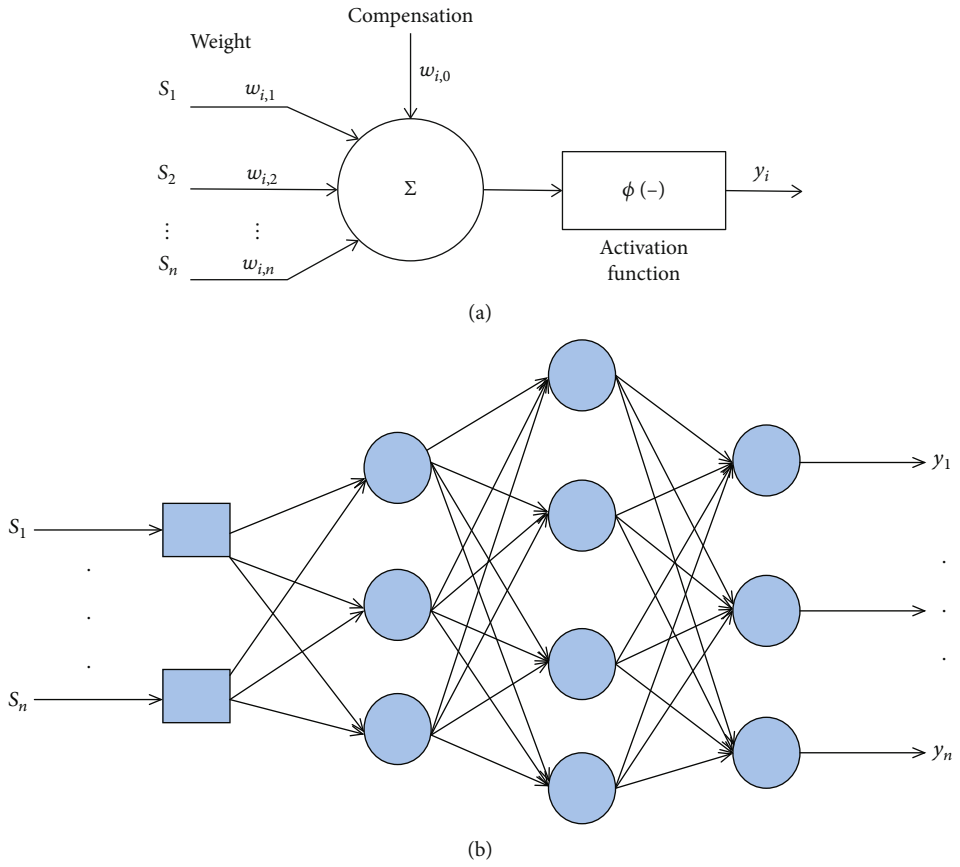

Figure 1: Illustration of (a) neuron element and (b) structure of a multilayer artificial neural network (ANN).

and data processing time [88–91]. Note that there are different radial functions, for example:

Gaussian

$$\Phi(w) = e^{w_i^2}. \tag{7}$$

Multiquadratic

$$\Phi(w) = \sqrt{1 + w_i^2}. \tag{8}$$

Inverse multiquadratic

$$\Phi(w) = \frac{1}{\sqrt{1 + w_i^2}}. \tag{9}$$

Polyharmonic

$$\begin{aligned} \Phi(w) &= w_i^k \quad k = 1, 3, 5, \cdots, \\ \Phi(w) &= w_i^k \ln(w_i) \quad k = 2, 4, 6, \cdots. \end{aligned} \tag{10}$$

After selecting the excitation/activation function(s), it is necessary to train the ANN model. This training can be performed with different approaches but the most common one is the training of back-propagation (BP), which has been the basis to apply other numerical methods like Levenberg-Maquart (LM) and Broyden-Fletcher-Goldfarb-Shannon (BFGS) [92–95], or even more sophisticated optimization algorithms like the metaheuristics also known as stochastic optimizers [96, 97]. BP algorithm is used to define the parameters of a multilayer ANN with a fixed architecture with the aim of "learning" the system behavior. An optimization algorithm is required to minimize the sum of errors between the ANN output values and the given target values of the system to be modeled. Interested readers on advance topics of ANN, its characteristics and developments are encouraged to consult the reviews of Basheer and Hajmeer [73], Abraham [66], Poznyak et al. [98], Alam et al. [99], Gopinath et al. [29], Chong et al. [97], and Aani et al. [100].

Finally, ANN have been combined and/or hybridized with other numerical approaches to resolve complex engineering problems. Stochastic global optimization methods (e.g., particle swarm optimization, genetic algorithm, cuckoo search, and ant colony optimization), fuzzy logic, and principal component analysis have been employed to improve the performance of ANN modeling in several fields including adsorption [29, 96–102].

3. Applications of ANNs to Model the Adsorption of Water Pollutants

A wide variety of theoretical and empirical models have been proposed to analyze, correlate, and predict adsorption

processes. However, these models are generally based on restrictive assumptions and theories, which can limit significantly their application [7]. For instance, the traditional adsorption isotherms like Langmuir and Freundlich have adjustable parameters that neglect the impact of solution temperature or pH on the adsorption capacities at equilibrium. These traditional models have been extended to handle the multicomponent adsorption but their errors are significant for those systems with the simultaneous presence of antagonistic and synergistic adsorption effects [31, 34, 38, 103, 104]. Other examples corresponded to statistical physics models that are theoretical equations utilized to estimate physicochemical parameters of adsorption processes but with the limitation of neglecting the role of solution pH or other fluid characteristics. Similar remarks can be formulated for the conventional kinetic equations (e.g., pseudofirst and pseudosecond order models) or even mass transfer models. Therefore, ANN are an alternative to overcome these disadvantages and also to develop improved versions with better correlation and prediction capabilities. However, it is convenient to remark that ANN can be considered as black-box (i.e., empirical) models that are effective for correlation and prediction but without providing an additional theoretical understanding of the system under analysis. This drawback of ANN can be partially resolved via its hybridization with theoretical adsorption models [105, 106].

Mathematically, the performance of an adsorption system is a nonlinear function depended on the adsorbent properties, chemistry of adsorbate(s), operating conditions, fluid properties, and equipment configuration. This nonlinear functionality can be modeled using ANN based on the fact that there is no a limitation to incorporate all the independent variables affecting the adsorption system, see Figure 2. ANN can also predict the performance of multicomponent adsorption systems where the adsorption capacities or other performance metrics, like the concentration profiles of breakthrough curves, of all adsorbates are incorporated as output variables.

For the preparation of the current manuscript, a literature review was performed in Web of Science® database using the keywords "adsorption," "water," and "artificial neural network(s)." All articles found with these keywords were scrutinized to identify papers out of the scope of this review. Several references were identified with a significant lack of information in terms of type of characteristics of ANN, input and output data, and other relevant points, which were discarded for the analysis and discussion. This review covers more than 250 papers related to ANN modeling of adsorption data. For illustration, Figure 3 provides an overview of paper published on ANN and adsorption of water pollutants since 1999 to 2021 (July) according to Web of Science® database using the keywords. It is clear that the number of publications about this topic has continuously increasing where a diversity of adsorption systems (i.e., adsorbents, adsorbates, process configurations, and operating conditions) has been analyzed via ANN with different topologies, activation functions, and training methods including hybrid approaches. This set of publications has briefly described and discussed to provide an overview of

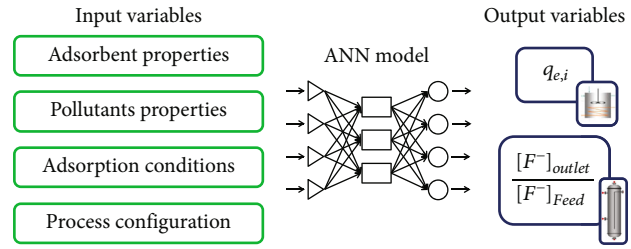

Figure 2: Input and output variables of an adsorption process that can be incorporated in ANN modeling.

the advantages, limitations, and current challenges on the adsorption modeling using ANN. Consequently, this section summarizes the main findings on the application of ANN for the modeling of kinetics, isotherms, and breakthrough curves obtained in the adsorption of different water pollutants.

3.1. Kinetic and Isotherms. Batch adsorption tests are required to quantify kinetics and isotherms thus characterizing the performance of adsorption processes. First applications of ANN in adsorption modeling were associated to the correlation and prediction of kinetics and isotherms. Tables 1 and 2 summarize the ANN modeling of kinetic and equilibrium studies for the adsorption of several pollutants from water. For instance, the adsorption data of arsenic, dyes, fluorides, heavy metals, pesticides, and organic compounds using activated carbons, bone char, lignocellulosic biomasses, clays, nanocomposites, hydrogels, and metal-organic frameworks have been modeled with ANN. These experimental studies have covered different operating conditions (e.g., 20–60 °C and pH 1–11) and a broad spectrum of adsorption capacities (3-270 mg/g). Several input variables have been considered in the ANN modeling such as pH, temperature, adsorbent dosage, contact time, initial concentration, physicochemical properties of the pollutant(s), and adsorbent, among others. Adsorption systems with one pollutant (i.e., adsorbate) dominate in the literature (~87%), and a limited number of multicomponent adsorption studies with two or more pollutants have been reported although the recognized capabilities of ANN to handle multiresponse processes. A brief description of representative studies on ANN modeling of kinetics and isotherms for different water pollutants is provided below.

Brasquet and Le Cloirec [107] were pioneers in the modeling of batch adsorption data with ANN. These authors formulated the question "why use neural networks in adsorption processes?" thus determining that ANN can be excellent predictors for this separation process if properly implemented. They studied the adsorption of 368 organic compounds on three activated carbons and used an ANN with four input variables: molecular size and flexibility with the variable ^{3}Xp (0–10.33), molecular volume and topology of insaturation and heteroatoms with the variable ^{2}X^{v}p (0–9.58), the critical dimension with the variable ^{6}X^{v}p (0–5.06), and a dummy variable "D" (-1.15–1.08). ANN with three neurons in the hidden layer were applied considering $\log(q_e/C_e)$ as the output variable where q_e is the equilibrium

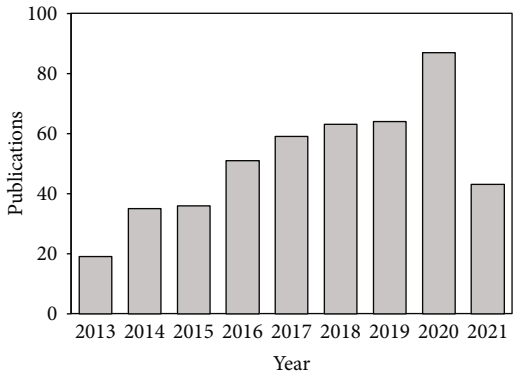

Figure 3: Survey of papers published on the ANN modeling of the adsorption of inorganic and organic pollutants from water. Source: Web of Science (July 2021).

adsorption capacity and C_e is the adsorbate equilibrium concentration [108]. These authors used 333 quantitative structure-activity relationship (QSAR) data for learning and 35 for testing of ANN from Blum et al. [109]. They used a classical neural network with BP algorithm as a training method and hyperbolic tangent sigmoid as activation function. This study concluded that an excessive number of neurons in the hidden layer was not necessary to achieve satisfactory modeling results with $R^2 = 0.875$. It was also analyzed the impact of the number of neurons on the ANN overtraining.

Chu and Kim [110] compared the modified Langmuir model and feed-forward ANN for the prediction of competitive adsorption of cadmium and copper by a plant biomass. Equilibrium adsorption data at pH 4-5 and 25 °C were taken from Pagnanelli et al. [111] where a mutual suppression of the adsorption of both metals occurred in the binary metallic system due to the competition for the binding sites of this adsorbent. Input variables for ANN modeling were the copper and cadmium equilibrium concentrations (0.124–2.243 mmol/L) and pH, while the ANN outputs were the copper and cadmium adsorption capacities (0.006–0.165 mmol/g). ANN training was performed with 83.3% of data set, while the remaining 16.7% was utilized for testing. The logistic sigmoid function was applied in neuron activation. The best ANN configuration consisted of 1 hidden layer with 10 neurons and BP training. These models were compared using the relative errors where the best values were obtained for the ANN thus outperforming the data correlation with the modified Langmuir model.

Singh et al. [112] employed an adapted neural fuzzy model and a BP-ANN for the prediction of cadmium adsorption by hematite. Specifically, a 3-layered feed-forward BP-ANN was employed where the input variables were the cadmium concentration (44.48–88.96 μmol/L), agitation rate (50–125 rpm), pH (9.2), temperature (20.5–40.5 °C), and contact time (29–222 min), while the output variable was the final cadmium concentration (43–103 μmol/L). The training database consisted of 15 datasets. The activation functions were the logistic sigmoid and symmetric Gaussian for classical ANN model and hybrid neural fuzzy model, respectively. Results showed that the cadmium adsorption depended on the five input variables. The hybrid neuro-fuzzy model ($R^2 = 0.96$) provided better predictions of the cadmium adsorption than BP-ANN ($R^2 = 0.88$).

ANN were used by Aber et al. [113] for modeling the kinetic adsorption data of the acid orange 7 dye using powdered activated carbon. In the kinetics experiments, the effect of initial concentration (150-350 mg/L) and pH (2.8-10.5) was evaluated. Input variables were the initial concentration (150–350 mg/L), pH (2.8–10.5), and contact time (75-600 min), while the final concentration after adsorption (5.48–178 mg/L) was the output variable to obtain the ANN model. Conventional adsorption kinetic equation (i.e., pseudosecond order) and feed-forward BP-ANN with 3-2-1 neurons and logistic sigmoid and hyperbolic tangent sigmoid functions were used for modeling the experimental data. A total of 219 experimental data were employed with 146 for training and 73 for prediction. The performance of these models was assessed, and ANN achieved the lowest mean relative error (5.81%). This study concluded that ANN was a predictive approach that could replace conventional kinetic models.

Yetilmezsoy and Demirel [114] proposed the use of a three-layer ANN for predicting the removal of lead with antep pistachio shells. The input variables were the adsorbent dosage (2–16 g/L), contact time (5–120 min), temperature (30–60 °C), pH (2–9), and lead initial concentration (5–100 mg/L), while the output variable was the lead removal (26.45-98.70%). 34, 16, and 16 data were used for training, validation, and testing, respectively. Tangent sigmoid function at the hidden layer and a linear function at the output layer were used, while LM algorithm was the best alternative for ANN modeling. This ANN model was able to fit the adsorption data showing a minimum value of the mean square error of 2.28×10^{-04} and $R^2 = 0.94$. Sensitivity analysis revealed that pH was the most influencing variable on the metal adsorption where a maximum lead removal of 99% was obtained.

Three-layer feed-forward ANN was used to model the adsorption kinetics of auramine O by activated carbon [115]. ANN were trained using the parameters obtained from the pseudosecond order kinetic equation. LM method was employed to train ANN with the next input variables: initial dye concentration (85–200 mg/L), contact time (1–120 min), agitation speed (400–800 rpm), temperature (305–333 K), initial solution pH (3–8), and activated carbon mass (0.3–1.8 g). The output variable was the dye adsorption capacity. The best ANN architecture was 6-7-1 with linear and hyperbolic tangent sigmoid activation functions. Overall, the difference of mean squared errors between the ANN and the pseudosecond order kinetic model varied only by <2%. This study was among the early attempts to combine ANN and a traditional kinetic adsorption equation to improve the adsorption modeling.

Garza-González et al. [116] proposed an approach to compare ANN and conventional isotherm models in the methylene blue adsorption by *Spirulina* sp. Simulated annealing and genetic algorithms were applied with ANN

Table 1: Summary of the ANN modeling of the adsorption of water pollutants at batch operating conditions.

Adsorbent	Adsorbate	ANN model	Experiment	Data used (Training-Testing-Validation)	Input variables	Output variable	Pollutant removal	Reference
Activated carbon	Methylene blue, Auramine-O, Crystal violet, Eosin yellow	Levenberg–Marquardt back propagation	Equilibrium and Kinetics	23-0-8	C_0, m, t	Removal percentage	99.42%	[4]
Polyaniline/carboxymethyl cellulose/TiO_2	Congo red	Multi-layered perceptron back propagation (5-1-8)	Kinetic, isotherm and RSM (CCD)	28-9-9	pH, t, C_0, T, m	Adsorption capacity	119.9 mg/g	[5]
Raw oak waste and NaOH-activated oak waste	Cd^{2+}	Three–layered feed forward back propagation	Kinetic and isotherm	153-33-33	pH, t, m, C_0, T	Removal percentage	99.50%	[6]
Zeolite	Diazinon	Multi-layered feed forward (4-7-1)	Equilibrium and Kinetics	21-5-5	t, pH	Removal percentage	98.2%	[8]
Magnetic walnut shell	Methyl violet, Rhodamine 6G	Multi-layered feed forward, Levenberg-Marquardt, Bayesian regularized and scaled conjugate gradient	Equilibrium and Kinetics	75-0-25	pH, C_0, m, t	Removal percentage	Methyl violet 140.7 mg/g, R6G 78.53 mg/g	[9]
Anammox bacteria	Nitrogen	Multi-layered feed forward, Levenberg-Marquardt	Isotherms	48-16-16	Treatment time, NLR, ammonia concentration and nitrite concentration	Adsorption capacity	17.79 mg/g	[11]
Nanobiosorbent derived from waste molasses	As^{3+}	Feed forward Levenberg Marquardt back propagation (4-20-1)	RSM (CCD)	21-5-4	C_0, m, pH, t	Removal percentage	878.03 mg/g	[12]
Magnetic rGO-chitosan composite	Cefixime	Random forest, Feed forward (3-60-50-1)	RSM and equilibrium	15-5-0	C_0, m, pH	Adsorption capacity	30.36 mg/g	[13]
Cu/F graphene aerogel	Perfluorooctanoic acid	Adaptive neuro-fuzzy inference system	RSM (CCD)	23-5-5	m, pH, ionic strength, T	Removal percentage	25 mg/g	[17]
Activated spent tea	Methylene blue	Three-layered feed forward back propagation (5-10-1)	Kinetics	61-10-10	C_0, m, pH, T, t	Removal percentage	1042 mg/g	[26]
SBA-15/CTAB composite	Reactive red 198	Adaptive neuro fuzzy inference system	Equilibrium and Kinetics	70-30-0	T, pH, t, m, C_0	Adsorption rate	99%	[44]
MOF-5-activated carbon	Fast green, eosin Y, quinine yellow	Multi-layered feed forward back propagation (6-11-3)	Equilibrium, Kinetics and RSM (CCD)	75-25-0	C_0, pH, m, t	Removal percentage	FG 98.1%, EY 98.1%, QY 91.9%	[45]
Orange peel	Paracetamol	Levenberg–Marquardt back propagation (3-18-1)	Kinetic	332-0-163	C_0, t, T	Pseudo second order kinetics	–	[47]
Activated carbon	Crystal violet	Three layered feed forward back propagation		23-8-0	C_0, pH, m, t	Removal percentage	99.82%	[185]

Table 1: Continued.

Adsorbent	Adsorbate	ANN model	Experiment	Data used (Training-Testing-Validation)	Input variables	Output variable	Pollutant removal	Reference
			Equilibrium, Kinetics and RSM (CCD)					
Sawdust	Basic red 46, Cu^{2+}	Levenberg–Marquardt back propagation (5-7-1)	Kinetics	38-6-6	C_0, pH, t, m	Removal percentage	–	[186]
Polyaniline/SiO_2 nanocomposite	Amido black 10B	Multi-layered feed forward (4-8-1)	Kinetic and isotherm	10-4-4	pH, t, C_0, m	Removal percentage	99.87%	[58]
Zeolite prepared from raw fly ash	Cr^{6+}	Multi-layered feed forward	Equilibrium and Kinetics	21-4-5	T, m, t, pH	Removal percentage	92.30%	[59]
Chemically modified sugarcane bagasse	Real textile effluent with mixture of dyes	Multilayer feed-forward	Kinetic and isotherm	60-20-20	pH, m, t, Ps,	Removal percentage	100%	[60]
Leucaena leucocephala seeds	As^{3+}, As^{5+}	Levenberg–Marquardt back propagation (4-14-1)	Kinetics	108-36-36	C_0, m, t, V	Removal percentage	>90 %	[61]
Acid-activated neutralized red mud	Phosphate	Three-layered feed forward and quasi-Newton back-propagation, scaled conjugate gradient and Levenberg–Marquardt (6-10-1)	Kinetic and equilibrium	25-8-8	C_0, m, pH, T, t	Adsorption capacity	31.34-192.62 mg/g	[74]
Polyaniline nano-adsorbent	Methyl orange	Multi-layered feed forward (5-8-1)	Kinetic and isotherm	60-20-20	pH, t, C_0, T, m	Removal percentage	32.04 mg/g	[75]
Clay mixture	Cu^{2+}	Three layered Levenberg–Marquardt back propagation	Kinetics, RSM	17-5-5	pH, m, T, C_0	Adsorption capacity	23.36 mg/g	[76]
Modified bentonite	Chlorobenzene	Radial basis function feed forward, Levenberg–Marquardt back propagation	Kinetic and isotherm	–	C_0, t, m, pH	Adsorption capacity	0.9223 mmol/g	[78]
Fe_3O_4/MIL-101(Fe))	Sarafloxacin	Multi-layered feed forward (4-8-1)	Kinetic, isotherm and RSM (CCD)	17-5-6	C_0, m, t, pH	Removal percentage	93.10%	[79]
UiO-66(Zr) and NH_2-UiO-66(Zr) metal organic frameworks	Pyrene	Multi-layered perceptron feed forward back propagation	RSM (CCD)	10-10-27	T, m, C_0, p H, T	Removal percentage	UiO-66(Zr) 99.2%, NH2-UiO-66(Zr) 95.67%	[80]
Penicillium YW 01	Acid black 172, Congo red	ANN and hybrid ANN-genetic algorithm (4-(3-10)-1)	Kinetics	77-26-26	pH, T, C_0, t	Adsorption capacity	AB172 225.38 mg/g, CR 411.53 mg/g	[96]
Activated carbon from opuntia *ficus indica*	As^{3+}	Hybridization of the traditional adsorption equations with a feed forward ANN	Kinetic and isotherm	Isotherm 21-3-3; Kinetics 44-5-5	C_0, T, pH, t (kinetics), Ce (for isotherms)	Adsorption capacity	8.32 mg/g	[106]

Table 1: Continued.

Adsorbent	Adsorbate	ANN model	Experiment	Data used (Training-Testing-Validation)	Input variables	Output variable	Pollutant removal	Reference
Activated carbon	Aliphatic and aromatic compounds	Three layered feed forward back propagation (4-3-1)	Isotherms	333-35-0	Molecular size, molecular volume, branching number, substituent length, heteroatoms and global substitution pattern	The parameter K log (qe/Ce)	–	[107]
Activated carbons	55 organic aromatic compounds	Three layered feed forward (5-3-1)	Isotherms	45-10-0	Molecular size and volume, branching number, substituent length, heteroatoms and global substitution pattern	The parameter K log (qe/Ce)	–	[108]
Hematite	Cd^{2+}	Adapted neural fuzzy and back propagation (5-20-1)	Kinetics	7-4-4	C_0, v, T, pH, Ps	Ce	11.5 mg/g	[112]
Powdered activated carbon	Acid orange 7	Three layered feed forward back propagation (3-2-1)	RSM, Equilibrium and Kinetics	146-73-0	pH, C_0, t	Ce	449.77 mg/g	[113]
Antep pistachio (*Pistacia Vera L.*) shells	Pb^{2+}	Three layered feed forward Levenberg–Marquardt back propagation (5-11-1)	Kinetics	34-16-16	pH, T, m, t, C_0	Removal percentage	98.70%	[114]
Activated carbon	Auramine O	Multi-layered feed forward back propagation (6-7-1)	Kinetics	272 data for training	C_0, pH, m, t, T, irradiation time	Adsorption capacity	700 mg/g	[115]
Spirulina sp. biomass	Methylene blue	Genetic algorithm (3-20-20-1)	Equilibrium	108-81-0	T, pH, m	Removal percentage or adsorption capacity	900 mg/g	[116]
Industrial sludge leachate with red mud	Pb^{2+}	Multi-layered perceptron feed forward Levenberg–Marquardt back propagation (3-12-1)	Kinetics and RSM (CCD and BBD)	15/05/2005	t, m, pH	Removal percentage	98.51%	[117]
Bacillus sp.	Total chromium	Feed forward back propagation (3-10-1)	Equilibrium	280-36-36	C_0, pH, t	Adsorption capacity	50 mg/g	[118]
Bentonite clay	Fe^{3+}	Multi-layered perceptron (3-9-1)	Equilibrium, Kinetics and RSM (CCD)	13-3-0	C_0, t, m	Removal percentage	90.12%	[119]
Fungal biomass	Reactive black 5	Feed forward Levenberg–Marquardt back propagation (9-10-1)	Equilibrium	135-45-45	C_0, pH, t, nitrogen content, carbon content, hydrogen content, BET area, pore volume and pore diameter	Adsorption capacity	179.26 mg/g	[187]

Table 1: Continued.

Adsorbent	Adsorbate	ANN model	Experiment	Data used (Training-Testing-Validation)	Input variables	Output variable	Pollutant removal	Reference
Date palm seeds	Cu^{2+}	Feed forward with neuro fuzzy logic (3-3-27-1)	Equilibrium	10-10-0	pH, m, T	Adsorption capacity	4.18 mg/g	[121]
Lentil straw	Lanaset red G	Three layered feed forward quick propagation (4-24-1)	Kinetics	784-184-184	Ps, m, pH, C_0, t	Adsorption capacity	271.12 mg/g	[122]
Activated almond shell	Zn^{2+}	Non-linear autoregressive model processes with exogenous input NARX (4-10-2)	Equilibrium	10-10-10	pH, m, particle size, C_0	Removal percentage, adsorption capacity	80%	[124]
Lignocellulosic Biomasses	Pb^{2+}, Cd^{2+}, Ni^{2+}, Zn^{2+}	Feed forward back propagation (6-10-1;10-10-1;5-10-1)	Equilibrium and Kinetics	169 data (kinetic) (70-15-15); 92 data (isotherm) (70-15-15)	Kinetics: C_0, t; Isotherms: Ce, BET area, content of cellulose, hemicellulose and lignin, concentration of acidic groups, MW, hydrated ionic radii, electronegativity, hydration energy	Adsorption capacity	1-7 mg/g	[125]
Gold nanoparticles loaded with activated carbon	Reactive orange 12	Hybrid three layered feed forward – Imperialist competitive (3-12-1)	Equilibrium and Kinetics	168-72-0	pH, m, T, t	Removal percentage	99%	[123]
Calcareous soil	Fe^{3+}	Quantum back propagation multi-layer perceptron (6-6-1)	Equilibrium and Kinetics	40-13-13	C_0, t, m, Ps, v, T	Removal percentage	99.20%	[127]
Magnetic/talc nanocomposite	Pb^{2+}, Ni^{2+}, Cu^{2+}	Wavelet neural network based on the incremental back propagation (3-(1-15)-3)	RSM (CCRD)	13-6-0	C_0, m, t	Removal percentage	Pb^{2+} 93.60%, Ni^{2+} 51.30%, Cu^{2+} 81%	[128]
Rice straw	Cd^{2+}	Feed-forward Levenberg–Marquardt back-propagation and neural-fuzzy inference system (3-6-1)	Equilibrium	26-9-8	C_0, m, pH	Removal percentage	80%	[129]
Typha domingensis	Ni^{2+}, Cd^{2+}	Adaptive neuro fuzzy inference system	Equilibrium	-	pH, m, C_0, t, Ps	Removal percentage	-	[131]
Multi-walled and single-walled carbon nanotubes	Triamterene	Levenberg–Marquardt back-propagation (3-(1-25)-1)	Equilibrium and Kinetics	45-0-19	C_0, m, t	Removal percentage	95%	[132]
Coffee grounds	Pb^{2+}	Three-layer feed forward and Levenberg–Marquardt back propagation (1-(4-13)-1)	Equilibrium	70-15-15	pH, C_0	Adsorption capacity	22.9 mg/g	[133]
ZnS nanoparticles-activated carbon	Brilliant green	Radial basis function	Equilibrium RSM (CCD)	36-0-18	C_0, t, m	Removal percentage	98.89%	[135]

Table 1: Continued.

Adsorbent	Adsorbate	ANN model	Experiment	Data used (Training-Testing-Validation)	Input variables	Output variable	Pollutant removal	Reference
Nanowires and activated carbon	Safranin-O, Indigo Carmine	Three layered feed forward backpropagation	Equilibrium, Kinetics and RSM (CCD)	70-15-15	C_0, m, t	Removal percentage	S-O 29.09 mg/g, IC 37.85 mg/g	[137]
Maize bran	Cr^{6+}	Multi-layered feed forward (4-10-1)	Kinetic	81-25-18	C_0, t, pH, T	Adsorption capacity	~13.5 mg/g	[138]
Clinoptilolite	Fluoride	Hybridization of ANN and Langmuir and Pseudo-second order equations (3-4-2)	Kinetic and isotherm	69-30-30	C_0, t, T, Ce, pH, T	Adsorption capacity and parameters of the models	12.4 mg/g	[139]
Calcined Ca-Al-(NO_3)	Fluoride	Three layered feed forward Levenberg-Marquardt (5-10-1)	Kinetic	650 data	C_0, m, T, pH	Adsorption capacity	45 mg/g	[140]
Palm kernel shell activated carbon	Zn^{2+}	Levenberg-Marquardt back propagation, gradient descent, resilient backpropagation and gradient descent with adaptive linear regression (5-7-1)	Kinetics, RSM (CCD)	190-40-40	pH, t, C_0, m, T	Removal percentage	90%	[141]
Centaurea stem	Crystal violet	Multi-layered feed forward network	Kinetic, isotherm, RSM (CCD)	26-0-6	pH, T, t, C_0, m	Removal percentage	476.19 mg/g	[142]
Poly-aluminium chloride	Disperse blue 79	Three layered Levenberg–Marquardt back propagation (4-4-1)	Kinetic, RSM (CCD)	27-9-9	pH, m, C_0, pH	Removal percentage	52.60%	[145]
Chitosan/nanodiopside	Crystal violet	Hybrid feed forward - genetic algorithm (4-9-1)	Kinetic and isotherm, RSM (CCD)	70-15-15	C_0, pH, m, t	Removal percentage	99.50%	[148]
Hydroxyapatite (Hap))/ chitosan nanocomposite	Pb^{2+}	Adaptive neuro-fuzzy inference system	Kinetic and isotherm	38-0-19	pH, t, v, T, m, C_0, Hap concentration	Removal percentage	99.20%	[150]
Activated carbon, carbon nanotubes, chitin, chitosan, corn straw, grape seeds, sugarcane bagasse, orange peel and rice husk	$Indium^{3+}$	Levenberg–Marquardt back propagation and adaptive neuro–fuzzy inference system	Kinetic	840-180-180	Surface area, point of zero charge, t, m	Adsorption capacity	1000 mg/g	[153]
Abelmoschus esculentus seeds	Nile blue	Three–layered feed–forward back propagation and Levenberg-Marquardt	Kinetic, isotherm and RSM (CCD)	21-5-5	C_0, m, pH, t	Adsorption capacity	42.34 mg/g	[154]

Table 1: Continued.

Adsorbent	Adsorbate	ANN model	Experiment	Data used (Training-Testing-Validation)	Input variables	Output variable	Pollutant removal	Reference
Mesoporous rGO/Fe/Co nanohybrids	Methylene blue	Hybrid ANN -particle swarm, hybrid ANN-genetic algorithm	Kinetic and isotherm, RSM (CCD)	24-0-6	pH, T, t, C_0	Removal percentage	88.40%	[156]
Biochar from rice husk	Fluoride	Multi-layered back propagation (4-10-10-10-1)	Kinetics	70-15-15	m, T, pH, C_0	Removal percentage	4.45 mg/g	[158]
Magnetic clay/Graphene Oxide/Fe_3O_4	pesticide diazinon	Multi-layered back propagation (5-13-1)	RSM(CCD)	23-7-7	pH, T, t, C_0, m	Removal percentage	7.2 mg/g	[159]
Magnetic Fe_3O_4 nanoparticles loaded with cocoa pod carbon composite	Methylene blue, crystal violet	Multi-layered feed forward Levenberg-Marquardt back propagation (4-9-1)	RSM(CCD)	18-6-6	C_0, m, pH, t	Removal percentage	MB 147.43 mg/g, CV 162.25 mg/g	[160]
Mesoporous $CoFe_2O_4$/ graphene oxide nanocomposites	Arsenide	Hybrid back propagation neural network - genetic algorithm (4-4-1)	RSM(CCD)	–	T, pH, C_0, t	Removal percentage	86.62%	[161]
Iron doped rice husk	Cr^{6+}	Feed forward Levenberg-Marquardt back propagation (5-1-1)	Kinetics	25 data	pH, m, T, t, v	Removal percentage	11.14 mg/g	[163]
Hydrochar derived from KOH activated *Crocus sativus* petals	Pb^{2+}	Support vector machine	Equilibrium	25-5-0	T, t, water/biomass ratio, $ZnCl_2$/biomass ratio	Adsorption capacity	89.52 mg/g	[165]
Water treatment plant residuals	Phosphate	Feed forward multilayer Levenberg–Marquardt back propagation (4-2-3)	Isotherms	7-1-1	pH and total phosphate in system	Adsorption capacity	400 mg/g	[188]
Activated carbon	Auramine O	Feed forward Levenberg–Marquardt back propagation (6-7-1)	Kinetic	272 data for training	C_0, t, v, T, pH, m, V	Adsorption capacity	850 mg/g	[189]
Sawdust of mangifera indica	Cu^{2+}	Multi-layered partial recurrent back-propagation (4-50-40-27-1)	Isotherms	4608-256-25	C_0, pH, T, Ps	Removal percentage	6 mg/g	[190]
Activated carbon	Chlorophenol	Three layered feed forward back propagation (4-8-1)	Isotherms and Kinetics	520-140-140	pH, C_0, T, t	Removal percentage	>60 %	[191]
Alga Chara sp.	Malachite green	Three layered feed forward back propagation (5-12-1)	Kinetics	180-60-60	C_0, m, pH, T, t	Removal percentage	92.75%	[192]
Chara contraria	Lanaset red (LR) G	Three layered feed forward back propagation (4-23-1)	Kinetics	1566-369-369	Ps, m, pH, C_0, t	Adsorption capacity	372.39 mg/g	[193]

Table 1: Continued.

Adsorbent	Adsorbate	ANN model	Experiment	Data used (Training-Testing-Validation)	Input variables	Output variable	Pollutant removal	Reference
Waste acorns of Quercus ithaburensis	Radioactive gallium-67	Multi-layered perceptron feed forward Levenberg–Marquardt back propagation (3-8-5-1)	Kinetics	172-44-44	T, m, t	Adsorption capacity	91.80%	[194]
Bacillus cereus biomass	As^{3+}	Feed forward back propagation	Isotherms and Kinetics	128-43-0	C_0, m, T, t	Removal percentage	85.24%	[195]
Alga Cladophora	Malachite green	Three layered feed forward back propagation (5-14-1)	Equilibrium and Kinetics	132-44-44	C_0, m, pH, t, T	Removal percentage	100%	[196]
Alga Xanthophyta sp	Malachite green	Three layered feed forward back propagation (5-12-1)	Kinetic, RSM	180-60-60	C_0, m, pH, T, t	Removal percentage	100%	[197]
Polyaniline (P)	Sodium dodecyl benzene sulfonate (SDBS)	Feed forward back propagation (5-5-5-1)	Equilibrium	69-0-69	pH, m, T, t, v	Adsorption capacity	P- $ZnCl_2$ 29.5 mg/g, P-$CuCl_2$ 32.3 mg/g	[198]
Leachate by hazelnut shell	Zn^{2+}	Three layered feed forward Levenberg–Marquardt back propagation (4-8-4)	Kinetics	100 data	pH, m, T, t	Removal percentage	98%	[199]
Leucaena Leucocephala seeds	Ni^{2+}	Levenberg–Marquardt back propagation	Kinetics	72-24-24	C_0, m, t, V	Removal percentage	76.23%	[200]
Black cumin	Pb^{2+}	Multi-Layer perceptrón	Equilibrium, RSM (CCD)	15-11-0	T, m, pH	Adsorption capacity	8.08 mg/g	[201]
Walnut husk	Lanaset red G	Multi-layered feed forward (3-20-1)	Kinetic	278-65-65	C_0, pH, t	Adsorption capacity	187.74 mg/g	[202]
Coconut shell	Indigo	Feed forward back propagation (6-5-5-1)	Equilibrium	152-21-0	Type of adsorbent, pH, m, Ps, C_0, type of activation	Removal percentage	94.83%	[203]
Activated carbon	Direct blue 86	Levenberg–Marquardt back propagation (5-(5-12)-1)	Kinetics	100-33-33	C_0, m, t, T, pH,	Adsorption capacity	2.26 mg/g	[204]
Organoclay	Reactive red 141	Three layered feed forward scaled conjugate gradient back propagation (4-5-1)	Kinetics	85-15-0	C_0, t, m, T	Removal percentage	100%	[205]
Nanocellulose fibers	Pb^{2+}	Multi-layered feed forward Levenberg–Marquardt back propagation	Equilibrium and Kinetics	108-36-36	C_0, pH, m, t, V	Removal percentage	94.21%	[206]
Alga Lemna minor L.	Acid blue 92	Three layered feed forward back propagation (5-14-1)	Kinetics	57-17-17	C_0, m, pH, T, t	Removal percentage	91%	[207]
Acinetobacter sp. bacteria	Cr^{6+}	Three-layered feed forward back propagation (3-7-1)	Equilibrium and Kinetics	48-22-0	C_0, m, t	Removal percentage	90.91%	[208]

Table 1: Continued.

Adsorbent	Adsorbate	ANN model	Experiment	Data used (Training-Testing-Validation)	Input variables	Output variable	Pollutant removal	Reference
Eggshells	Crystal violet	Three layered feed forward Levenberg–Marquardt back propagation (4-8-1)	Equilibrium	105-52-53	pH, m, C_0, T	Removal percentage	99%	[209]
Activated carbon	Pb^{2+}	Resilient back propagation (5-12-1)	Kinetics	10-5-5	pH, C_0, m, t, T	Removal percentage	–	[210]
Nanometer SiO2	Mn^{2+}, Co^{2+}	Hybrid ant colony optimization-ANN Levenberg–Marquardt (4-7-5-1 for Mn(II), 6-9-1 for Co(II))	Kinetics	37-10-10	pH, m, t, concentration of 1-(2-pyridylazo)-2-naphthol	Removal percentage	Mn^{2+} 99 %, Co^{2+} 98%	[211]
Zea mays Cob Powder	As^{3+}, As^{5+}	Levenberg–Marquardt back propagation (4-14-1)	Kinetics	108-36-36	C_0, m, t, V	Removal percentage	As^{3+} 81.88 %, As^{5+} 92.61 %	[212]
Moringa oleifera seeds	Methylene blue, Congo red	Levenberg–Marquardt back propagation (4-14-1)	Kinetics	108-36-36	C_0, m, t, V	Removal percentage	MB 90.27%, CR 98.52%	[213]
Carbon nanotubes	Methylene blue	Three layered feed forward Levenberg–Marquardt back propagation (5-10-1)	Equilibrium and Kinetics	43-21-21	C_0, m, T, pH, t	Final concentration	0.3-36.79 mg/L	[214]
Immobilized Bacillus subtilis	Cd^{2+}	Feed forward Levenberg–Marquardt back propagation (5-8-1)	Equilibrium and Kinetics	63-14-13	C_0, m, t, T, pH	Adsorption capacity	251.91 mg/g	[215]
Co (III) oxide nanoparticle loaded on activated carbon	Eosin Y	Multi-layered feed forward - genetic algorithm (3-23-1)	Kinetics	176-38-38	T, m, t	Removal percentage	>90%	[216]
Lemna major biomass	Carbaryl	Multi-layered perceptron (4-6-1)	Equilibrium and Kinetics, RSM	22-0-7	C_0, pH, m, t	Removal percentage	95%	[217]
Chromolaena odorata	Trichlorophenol	Two layered feed forward Levenberg–Marquardt back propagation (2-10-1)	Kinetics	-	C_0, t	Removal percentage	99%	[218]
Poly(vinyl alcohol) PVA/ chitosan nanofiber membrane	Ni^{2+}, Co^{2+}	Multi-layered perceptron (6-3-2-1)	Equilibrium and kinetics	70-30-0	C_0, t, pH, m, T	Removal percentage	Ni^{2+} 79.28%, Co^{2+} 77.12%	[219]
Copper sulfide nanoparticles loaded on activated carbon	Reactive orange 12	Principal component analysis-ANN Levenberg–Marquardt back propagation (3-12-1)	Equilibrium and Kinetics	182-39-39	C_0, m, t	Removal percentage	99.54%	[220]
Zn(OH)2 nanoparticles-activated carbon	Sunset yellow	Three-layered feed-forward–Imperialist competitive (3-9-1)	Equilibrium and Kinetics	224-96-0	C_0, m, t	Removal percentage	90%	[221]

Table 1: Continued.

Adsorbent	Adsorbate	ANN model	Experiment	Data used (Training-Testing-Validation)	Input variables	Output variable	Pollutant removal	Reference
Gold nanoparticles loaded on activated carbon and activated carbon Tamarisk	Methyl orange	Three layered feed forward Levenberg–Marquardt back-propagation and particle swarm (4-11-1)	Equilibrium and Kinetics	182-78-0	C_0, m, t	Removal percentage	>98%	[222]
Graphite oxide nanoparticle	Methylene blue, Brilliant green	Three layered feed forward Levenberg–Marquardt back propagation and genetic algorithm (3-23-1)	Equilibrium and Kinetics	235-101-0	C_0, m, t	Removal percentage	MB 97.4%, BG 97.3%	[223]
Gold nanoparticles-activated carbon	1,3,4-thiadiazole-2,5-dithiol	Adaptive neuro-fuzzy inference system (3-9-27-27-1)	Equilibrium and Kinetics	168-72-0	C_0, m, t	Removal percentage	>90 %	[224]
ZnO Nanoparticle	As^{3+}	Feed-Forward Levenberg–Marquardt back propagation (5-20-1)	Equilibrium and Kinetics	47-24-24	C_0, t, pH, m, v	Removal percentage	98%	[225]
Turkish lignite	Methylene blue	Three-layered feed forward back propagation (6-14-1)	Equilibrium and Kinetics	60-20-20	C_0, t, m, pH, v	Adsorption capacity	41.94 mg/g	[226]
Clinoptilolite	Cu^{2+}	Three layered back propagation (3-11-1)	Equilibrium and Kinetics	63-14-13	pH, T, C_0	Removal percentage	>60%	[227]
Activated carbon	Methylene blue	Hybrid multi-layered perceptron - genetic algorithm (5-7-1)	Equilibrium and Kinetics, RSM	70-27-11	pH, v, m, C_0, t	Removal percentage	99.75%	[228]
Silver nanoparticles	Molybdenum	Hybrid ANN–particle swarm (4-12-1)	Equilibrium and Kinetics	187-31-42	C_0, pH, m, t	Removal percentage	92.50%	[229]
Borasus Flabellifer Coir Powder	Cr^{6+}	Feed forward back propagation (3-18-1)	Equilibrium	38-16-0	pH, m, C_0	Removal percentage	>95 %	[230]
De-oiled algal biomass	Methylene blue	Feed forward Levenberg-Marquardt back propagation (6-10-1)	Equilibrium and Kinetics	369-79-79	pH, m, v, T, C_0	Removal percentage	>90 %	[231]
Hydrochar	Acridine orange, Rhodamine 6G	Levenberg–Marquardt back propagation (3-(1-25)-1)	Equilibrium and Kinetics	50-25-25	T, t, pH	Adsorption capacity	AO 70.36 mg/g, R6G 60.13 mg/g	[232]
Crab shell	Pb^{2+}, Zn^{2+}	Multi-layered perceptron back propagation	Equilibrium	-	-	Adsorption capacity	Pb^{2+} 564 mg/g, Zn^{2+} 71.46 mg/g	[233]
Sargassum filipendula	Ni^{2+}, Cr^{3+}	Multi-layered feed forward (2-2-2-2)	Equilibrium and Kinetics mono-Binary	26 data for training	Ce	Adsorption capacity	Ni^{2+} 1 mg/g, Cr^{3+} 2 mg/g	[234]

Table 1: Continued.

Adsorbent	Adsorbate	ANN model	Experiment	Data used (Training-Testing-Validation)	Input variables	Output variable	Pollutant removal	Reference
Microcrystalline cellulose	Cr^{3+}, Cr^{6+}	Multi-layered feed forward Levenberg–Marquardt back propagation	Equilibrium and Kinetics	160 data	C_0, t, m	Removal percentage	Cr^{3+} 42.36%; Cr^{6+} 5.88%	[235]
Light expended clay aggregate	Cu^{2+}	Three layered feed forward back propagation (4-4-1)	Equilibrium and Kinetics RSM (CCD)	27-8-0	pH, T, C_0, m	Adsorption capacity	113.64 mg/g	[236]
Bamboo biochar	Acid black 172	Three layered feed forward Levenberg–Marquardt back propagation	Equilibrium and Kinetics	108-36-36	pH, T, C_0, t, ionic strength	Adsorption capacity	81.88 mg/g	[237]
Intercalated tartrate-Mg–Al layered double hydroxides	Pb^{2+}	Hybrid multi-layered feed forward Levenberg–Marquardt back propagation – genetic algorithm	Equilibrium	19-3-3	C_0, t, m pH	Removal percentage	99.32%	[238]
Bauxsol	Phosphorus	Three layered feed forward back propagation (3-5-1)	Equilibrium	17-5-0	T, t, HCl concentration	Adsorption capacity	55.72 mg/g	[239]
Graphene oxide nanoplatelets	Safranin	Three layered feed forward back propagation (3-10-1)	Equilibrium and Kinetics	–	pH, m, T, t	Removal percentage	97.78%	[240]
Walnut husk	Basic red 46	Three layered feed forward back propagation (5-25-1)	Kinetics	1469-345-346	Ps, m, pH, C_0, t	Adsorption capacity	66.45 mg/g	[241]
Biomass	Ni^{2+}, Co^{2+}	Multi-layered feed forward	Equilibrium and Kinetics	70-30-0	pH, m, t	Removal percentage	Ni^{2+} 90.25%, Co^{2+} 86.13%	[242]
Activated carbon	Sunset yellow	Three layered back propagation (3-(1-20)-1)	Equilibrium and Kinetics	218-47-47	C_0, m, t	Removal percentage	>98 %	[243]
Copper nanowires loaded on activated carbon	Malachite green	Hybrid three layered feed forward -genetic algorithm (3-(1-30)-1)	Equilibrium and Kinetics	186-62-0	C_0, m, t	Removal percentage	99%	[244]
Zinc sulfide nanoparticle loaded on activated carbon	Brilliant green	Three-layered feed forward Levenberg–Marquardt back-propagation and hybrid ANN-particle swarm optimization (3-(1-35)-1)	Equilibrium and Kinetics	176-76-0	C_0, m, t	Removal percentage	>80 %	[245]
Gold and titanium dioxide nanoparticles loaded on activated carbon	Phenol red	Hybrid three layered feed forward -genetic algorithm	Equilibrium and Kinetics	70-15-15	pH, C_0, m, t	Removal percentage	Ti-NP-AC (97.3%), Au-NP-AC (97.4%)	[246]
Spent tea leaves	Cu^{2+}	Feed forward Levenberg–Marquardt back propagation (3-10-4-1)	Equilibrium and Kinetics, RSM (CCD)	12-4-4	pH, m, t	Removal percentage	96.12%	[247]

Table 1: Continued.

Adsorbent	Adsorbate	ANN model	Experiment	Data used (Training-Testing-Validation)	Input variables	Output variable	Pollutant removal	Reference
Zinc oxide nanorods loaded on activated carbon	Sunset yellow	Levenberg–Marquardt back propagation (3-6-1)	Equilibrium and Kinetics	189-81-0	C_0, m, t	Removal percentage	98.89%	[248]
Hybrid material (Ce-HAHCl)	As^{3+}	Feed forward back propagation (6-7-1)	Equilibrium and Kinetics	60-40-0	C_0, m, pH, t, v, T	Removal percentage	98.80%	[249]
Cerium oxide polyaniline composite	Cr^{6+}	Three layered feed forward back propagation (5-7-1)	Equilibrium and Kinetics	52-34-0	C_0, m, t, pH, T	Removal percentage	93.90%	[250]
Orange peel ash	Phenol	Multi-layer perceptron feed forward back propagation (6-6-1)	Equilibrium and Kinetics	–	C_0, pH, m, t, v, T	Removal percentage	97.34%	[251]
Apricot stones and corn cob	Cu^{2+}	Multi-layer perceptron and Levenberg–Marquardt back propagation (3-8-6)	Equilibrium	144-48-48	C_0, m, V	Removal percentage, adsorption capacity and Ce	AS 5.9 mg/g, CC 5.3 mg/g	[252]
Sepiolite-stabilized zero-valent iron nanocomposite	Cr^{6+}	Three-layered feed forward, train scaled conjugate gradient (4-8-1)	Kinetics	71-23-23	pH, C_0, m, chloride ion concentration.	Removal percentage	99.78%	[253]
Olive stone	Pb^{2+}	Neural fuzzy inference system and multi-layered feed forward back propagation	Equilibrium	27-3-0	Chemical solution concentration for treatment, pH, C_0	Adsorption capacity	25.45mg/g	[254]
Azadirachta indica (neem) bark powder	As^{4+}	Three-layered feed forward (7-4-2)	Kinetics	14-7-7	pH, t, C_0, m, v, T	Removal percentage and adsorption capacity	95%	[255]
Biomass of Rhizopus arrhizus	Reactive orange 13	Three-layered feed forward (4-3-1)	Equilibrium and Kinetics	25-0-5	pH, m, C_0, t, v	Adsorption capacity	132.63 mg/g	[256]
Hyacinth roots, neem leaves and coconut shells	Pb^{2+}	Levenberg–Marquardt back propagation and scaled conjugate gradient	Kinetics	114 data	pH, C_0, m, t, type of adsorbent	Removal percentage	98.67%	[257]
Sargassum bevanom (S. bevanom) algae	Hg^{2+}	Multi-layered feed forward, Levenberg–Marquardt back propagation (4-(4-7)-1)	Equilibrium and Kinetics	26-6-6	m, C_0, t, pH.	Removal percentage	90.24%	[258]
Valonia tannin resin	Cd^{2+}	Four-layered fast artificial neural network (6-25-5-1)	Equilibrium and Kinetics	365-91-0	T, pH, C_0, v, Ps, t	Removal percentage	63.29 mg/g	[259]
ZnS nanoparticles loaded activated carbon	Brilliant green, eosin B	Multi-layered feed forward and Levenberg–Marquardt back propagation	Equilibrium, Kinetics and RSM (CCD)	41-0-13	C_0, t, m	Removal percentage	100%	[260]

Table 1: Continued.

Adsorbent	Adsorbate	ANN model	Experiment	Data used (Training-Testing-Validation)	Input variables	Output variable	Pollutant removal	Reference
Rice straw and Fe3O4 nanoparticles	Pb^{2+}, Cu^{2+}	Quick propagation, batch back propagation, genetic algorithm and Levenberg-Marquardt (3-9-2)	Kinetics	15-0-5	C_0, m, t	Removal percentage	Pb(II) 91.18%, Cu(II) 75.98%	[261]
CaO_2 nanoparticle	Benzeneacetic acid	Multi-layered perceptron feed forward (2-0-5-5-3)	Equilibrium	16 data	C_0, m	Ce, amount of CaO_2 and removal percentage	97.47%	[262]
Activated carbon (Bean husk)	Ibuprofen	Three-layered feed forward back propagation (3-x-1)	Equilibrium, Kinetics and RSM (CCD)	20 data	C_0, m, t, pH, v, T	Removal percentage	99%	[263]
Flax meal biomaterial	Cu^{2+}	Multi-layer feed forward perceptron	Equilibrium, RSM (CCD)	528 data	C_0, m, pH	Removal percentage	40.11 mg/g	[264]
$Zn(OH)_2$ nanoparticles on activated carbon	Methylene blue	Multi-layered feed forward Levenberg Marquardt back propagation	Equilibrium, RSM (CCD)	21-5-5	C_0, pH, m, t	Removal percentage	98.70%	[265]
Carbon nanotube	Microcystins-LR	Three-layered Levenberg–Marquardt back propagation (4-13-1)	Kinetic	46-10-10	pH, C_0, t, m	Removal percentage	175.43 μg/g	[266]
Copper oxide nanoparticle loaded on activated carbon	Pb^{2+}, malachite green	Three-layered feed forward (5-20)-2)	Isotherm, RSM (CCD)	20-6-6	C_0, pH, t, m	Removal percentage	Pb^{2+} 98.33 mg/g, MG 87.72 mg/g	[267]
Parthenium hysterophorus derived activated char	Ranitidine hydrochloride	Feed forward back-propagation	Kinetics, RSM (CCD)	–	C_0, m, t, pH, T, v	Removal percentage	99.65%	[268]
Graphene oxide	Fluoride	Three-layered feed forward, Levenberg–Marquardt back propagation	Kinetic and isotherm, RSM (CCD)	14-2-4	m, t, T	Removal percentage	28.72 mg/g	[269]
Tamarindus indica	As^{3+}	Hybrid ANN-genetic algorithm (4-6-1)	Kinetic, isotherm and RSM (CCD)	24-0-7	C_0, t, pH, m, T	Adsorption capacity	91.10%	[270]
Zn-loaded pinecone biochar	As^{3+}	Hybrid back propagation ANN-genetic algorithm	Kinetic and isotherm, RSM	13-4-0	C_0, pH, ratio Ethanol - adsorbate	Adsorption capacity	10.47 μg/g	[271]
Iron composite	Amido black	Three-layered feed forward (5-8-1)	Kinetics	60-20-20	pH, t, C_0, T, m	Removal percentage	88%	[272]
Iron/olivine composite	As^{3+}	Multi-layered perceptron (5-(12-14)-1)	Kinetics, RSM	22-8-8	C_0, m, t, v, pH	Removal percentage	99%	[273]

Table 1: Continued.

Adsorbent	Adsorbate	ANN model	Experiment	Data used (Training-Testing-Validation)	Input variables	Output variable	Pollutant removal	Reference
Graphene-like carbon	Methylene blue	Multi-layered perceptron (4-13-1)	Kinetics	73-16-16	C_0, m, t, pH	Removal percentage	20 mg/g	[274]
Activated carbon	Ni^{2+}	ANN and adaptive neuro–fuzzy inference system	Kinetic and isotherm	420-90-90	C_0, t, pH, BET area	Adsorption capacity	63.50 mg/g	[275]
Activated carbon (Medlar seed)	Cr^{2+}	Multi-layered perceptron back propagation (5-1-8)	Kinetic and isotherm	41-0-18	pH, C_0, m, t	Removal percentage	200 mg/g	[276]
Sunflower seed husk	Cu^{2+}	Levenberg–Marquardt back propagation (6-20-1)	Kinetic and equilibrium	119-39-39	C_0, flow rate, dosage and surfactant concentration, t, pH, T	Removal percentage	–	[277]
Chitosan	Acid orange 7	Multi-layer perceptron (4-5-1)	Kinetic and isotherm, RSM	26-4-4	pH, C_0, m, t	Removal percentage	98%	[278]
ZnO nanoparticles and copper-metal organic frameworks	Cyanide	Multi-layer perceptron and Levenberg–Marquardt back propagation (1-35-5)	Kinetic, isotherm, RSM	70-15-15	pH, t, T, m, C_0	Removal percentage	6.34 mg/g	[279]
Ho-CaWO4	Methylene blue	Multi-layer perceptron and Levenberg–Marquardt back propagation (4-8-1)	Kinetics, RSM (CCD)	15-3-3	pH, t, m, C_0	Removal percentage	71.17%	[280]
Catecholamine/starch	Methylene blue	Hybrid multi-layer feed forward - particle swarm (3-7-1)	Kinetics, RSM (CCD)	–	pH, C_0, t	Adsorption capacity	2276.5 mg/g	[281]
Neodymium modified ordered mesoporous carbon	Sunset yellow	Three-layered back propagation	Kinetic and isotherm	47-10-10	C_0, t, m	Removal percentage	–	[282]
Biochar	Methylene blue	Feed forward back propagation	Isotherm	504-108-108	Adsorbent type, Ps, C_0, pyrolysis temperature	Adsorption capacity	0.047 mmol/g	[283]
Olive pips	Pb^{2+}	Three-layered feed forward back propagation	Kinetic and equilibrium	60-20-20	T, t, pH, m, C_0, v	Removal percentage	99%	[284]
Microwave-synthesized akaganeite nanoparticles	Congo red	Back-propagation	Kinetic and isotherm	27-5-5	C_0, t, m	Removal percentage	>150 mg/g	[285]

Nomenclature: adsorbent dosage (m), Box-Behnken Design (BBD), central composite design (CCD), final adsorbate concentration (Ce), initial adsorbate concentration (C_0), particle size (Ps), response surface methodology (RSM), temperature (T), time (t), stirring rate (v), and volume (V).

Table 2: Summary of the ANN modeling of the multicomponent adsorption of water pollutants at batch operating conditions.

Adsorbent	Adsorbate	ANN model	Experiment	Data used (Training-Testing-Validation)	Input variables	Output variable	Pollutants removal	Reference
Chitosan-based hybrid hydrogels	Acid blue, allura red	Levenberg-Marquardt back propagation (5-10-10-10-2)	Binary kinetics	221-47-47	$C_0$1, $C_0$2, carbon content, porosity, t	Adsorption capacity	AB 242.5 mg/g, AR 219.35 mg/g	[7]
Ultrasound-modified chitin	Co^{2+}, Ni^{2+}, methylene blue	Levenberg-Marquardt, Bayesian regulation and back propagation with gradient derivatives	Isotherms	140-30-30	C_0, T	Adsorption capacity	Co^{2+} 62.34 mg/g, Ni^{2+} 52.53 mg/g, methylene blue 11.30 mg/g	[27]
Bone char	Cd^{2+}, Ni^{2+}, Zn^{2+}, Cu^{2+}	Multi-layer feed forward (4-(10-20)-(5-10)-4)	Multi-component isotherms	99-28-14	C_0	Adsorption capacity	Cd^{2+} 1.62 mmol/g, Ni^{2+} 1.35 mmol/g, Zn^{2+} 0.90 mmol/g, Cu^{2+} 1 mmol/g	[28]
Activated carbons	Acid orange, acid blue, caffeine, acetaminophen, benzotriazole	Hybrid ANN - homogeneous surface diffusion model	Binary and ternary kinetics	90-5-5	Type of adsorbent, pH, T, C_0, ratio m/V	Removal percentage	AO 65%, AB74 85%, ACT 64%, CAF 82%, BTA 78%	[29]
Activated carbon	Nimesulide, paracetamol	Bayesian regularization back propagation algorithm	Isotherms	85-0-15	Ps, m, t, C_0	Adsorption capacity	Nimesulide 0.22 mmol/g, paracetamol 0.16 mmol/g	[30]
Activated carbon from kiwi peel, cucumber peel and potato peel	Methylene blue, malachite green, rhodamine B	Three-layered feed forward (3-7-1)	Single, binary and ternary equilibrium	184-40-40	pH, t, T, m, C_0	Adsorption capacity	MB 400 mg/g	[46]
Activated carbon	Herbicides 2,4-D and 4-chloro-2-methylphenoxyacetic acid	Multi-layer perceptron	Binary isotherms	21-0-9	Ce	Adsorption capacity	D 0.48 mmol/g, M 0.54 mmol/g	[48]
Graphite oxide nano particle	Methylene blue, brilliant green	Principal component analysis - three layered feed forward Levenberg–Marquardt back-propagation (4-4-1)	Binary equilibrium	100-40-0	Ce in mixture	Ce	MB 410 mg/g, BG 129.41 mg/g	[43]
Granulated activated carbon	Nitrobenzene, phenol, aniline	Three-layered feed forward Levenberg-Marquardt back propagation (3-1-1)	Ternary equilibrium	40-41-0	Ce1, Ce2, Ce3	Adsorption capacity	NI 0.39 mmol/g, AN 0.4 mmol/g, PH 0.32 mmol/g	[147]
Mixture of bentonite, zeolite, biochar, cockleshell, cement	Atenolol, ciprofloxacin, diazepan	Three-layered feed forward Levenberg-Marquardt back propagation (2-5-1)	Multicomponent equilibrium, RSM	45-15-15	t, C_0	Removal percentage	ATN 90.2%, CIP 94%, DIA 95.5%	[286]
Microbioal biosorbent	Cu^{2+}-Cd^{2+}	Feed forward back propagation (3-10-2)	Binary isotherms	16-17-17	C_0, pH	Adsorption capacity	Cu^{2+} 9.75 mg/g, Cd^{2+} 4.48 mg/g	[110]

Table 2: Continued.

Adsorbent	Adsorbate	ANN model	Experiment	Data used (Training-Testing-Validation)	Input variables	Output variable	Pollutants removal	Reference
MnO_2-loaded activated	Brilliant green, crystal violet, methylene blue	Three-layered feed forward Levenberg Marquardt back-propagation (6-12-3)	Ternary equilibrium, RSM (CCD)	62-14-14	m, t, C_0, Ce	Removal percentage of each dye	BG 206 mg/g, CV 234 mg/g, MB 263 mg/g	[126]
Magnetic ϒ-Fe_2O_3-loaded activated carbon	Methylene blue, malachite green	Feed forward Levenberg-Marquardt back propagation (5-11-2)	Binary equilibrium, RSM (CCD)	36-7-7	pH, m, t, $C_0$1, $C_0$2	Removal percentage of each dye	MB 195.55 mg/g, MG 207.04 mg/g	[130]
Mn@CuS/ZnS nanocomposite-loaded activated carbon	Methylene blue, malachite green	Radial basis function neural network with Kernel stone algorithm	Binary, RSM (CCD)	22-10-0	pH, m, t, $C_0$1, $C_0$2	Removal percentage of each dye	MB 126.42 mg/g, MG 115.08 mg/g	[136]
SnO_2 nanoparticles loaded on activated carbon	Sunset yellow, disulfine blue	Three-layered feed forward back propagation (5-11-2)	Binary equilibrium, RSM (CCD)	26 data	pH, m, t, $C_0$1, $C_0$2	Removal percentage	SY 83.34 mg/g, DB 94.94 mg/g	[143]
CuO nanoparticles supported on activated carbon	Rose bengal, safranin O, malachite green	Three-layered feed forward Levenberg-Marquardt back propagation (6-10-3)	Ternary equilibrium, RSM (CCD)	65-16-0	pH, m, t, $C_0$1, $C_0$2, $C_0$3	Removal percentage	MG 94.26%, SO 71%, MG 76%	[146]
Zeolite	Ag^{1+}, Co^{2+}, Cu^{2+}	ANN Bayesian regularization backpropagation (4-10-1) and Adaptive Neuro-fuzzy Inference Systems (4-8-X-X-1)	Isotherms	275-49-0	T, Si/Al ratio, C0, molecular weight of adsorbate	Adsorption capacity	Ag^{1+} 5 mmol/g, Co^{2+} 2.51 mmol/g, Cu^{2+} 3.88 mmol/g	[157]
Sargassum filipendula biomass	Cd^{2+}-Zn^{2+}	Feed forward back propagation (7-5-2)	Binary isotherms	16	Ce	Adsorption capacity	Cd^{2+} 291.2, Zn^{2+} 169 mg/g	[287]
Activated carbon, wood charcoal and rice husk ash	Phenol, Resorcinol	Three-layer feed forward Levenberg-Marquardt back propagation	Binary kinetics	15-7-7	pH, t, C_0, m	Removal percentage	Phenol 75%, Resorcinol 90%	[288]
Chitosan foams	Cu^{2+}, Zn^{2+}, Cr^{6+}	Multi-layer perceptron Levenberg Marquardt (3-1-1)	Multicomponent Isotherms	–	Ce	Adsorption capacity	Cu^{2+} 61mg/g, Zn^{2+} 68 mg/g, Cr^{6+} 58 mg/g	[289]
Aegel marmelos fruit shell	Ni^{2+} Cr^{6+}	Elite-ANN with ACM model (4-10-10-6)	Equilibrium	17-0-4	C_0, m, type of adsorbent	Removal percentage, adsorption capacity and Ce	Ni^{2+} 59.26 mg/g, Cr^{6+} 12.67 mg/g	[290]
SnO_2 nanoparticle-loaded activated carbon	Acid yellow 41, sunset yellow	Principal component analysis-artificial neural network	Binary equilibrium, RSM (CCD)	10-5-5	pH, m, t	Removal percentage	AY41 95.6%, SY 97.9%	[291]

Nomenclature: adsorbent dosage (m), central composite design (CCD), final adsorbate concentration (Ce), initial adsorbate concentration (C_0), particle size (Ps), response surface methodology (RSM), temperature (T), time (t), and volume (V).

with two hidden layers and hyperbolic tangent sigmoid function. Temperature (25–50 °C), pH (2–8), and adsorbent dosage (1.2–10 g/L) were used as input neurons, while the adsorption capacities (3.09–66.98 mg/g) or the removal efficiency (23.56–86.89%) were considered as the output neurons. Results showed that genetic algorithm outperformed simulated annealing. Sensitivity analysis indicated that the removal efficiency was impacted by the operating variables as follows: pH > adsorbent dosage > temperature, while the adsorption capacity was depended on adsorbent dosage > pH > temperature. Finally, the experimental isotherms indicated a maximum adsorption capacity of 900 mg/g. The optimized ANN model outperformed significantly the Fritz-Schlunder equation.

Yang et al. [96] proposed the application of ANN and genetic algorithm to determine the importance of adsorption variables (e.g., initial dye concentration, time, temperature, and pH) on the adsorption of dyes congo red and acid black 172 by *Penicillium* YW01 biomass. Experimental results showed that the maximum adsorption capacities of this biomass were 411.53 mg/g for congo red and 225.38 mg/g for acid black 172. This dye separation process was endothermic and pH dependent. Adsorption kinetics were modeled with the pseudosecond order and Weber-Morris models, and the isotherms were fitted with Langmuir equation. ANN modeling was performed with 129 experimental data divided in 77, 26, and 26 for training, validation, and testing. The input variables were the contact time (5–360 min), initial dye concentration (50–800 mg/L), pH (1–10), and temperature (20–40 °C), while the output variable was the dye adsorption capacity (21.45–411.53 mg/g). R^2 values > 0.99 were obtained for the prediction of congo red and acid black 172 adsorption using ANN and genetic algorithm. This combined approach was more effective than ANN. The authors concluded that the initial adsorbate concentration and temperature showed the highest impact on the adsorption of both dyes.

Response surface methodology (RSM) and ANN were used to model the lead removal from industrial sludge leachate using red mud [117]. pH (3–7), contact time (5–60 min), and adsorbent mass (1.25–10 g/L) were the input variables, and the lead removal was the output variable. Box–Behnken design (BBD) was utilized for RSM and to obtain the data involved in ANN training. From this experimental design, the lead removal ranged from 38.84 to 96.82% where adsorbent dosage was the main operating variable followed by the contact time and pH. Feed-forward multilayer ANN with hyperbolic tangent sigmoid and logistic sigmoid functions and 3-12-1 architecture was used to predict the lead removal. R^2 and root mean squared error were used as the statistical metrics to assess the model performance. Both ANN and RSM models were satisfactory to correlate the experimental data of this adsorption system but with an evident advantage of ANN for predictive purposes.

Masood et al. [118] applied an ANN to predict the removal of total chromium using *Bacillus sp*. Experimental results showed that this removal process was pH dependent achieving a maximum adsorption capacity of 50 mg/g according to the equilibrium data, which were fitted to Freundlich equation. Feed-forward BP-ANN with three layers and logistic sigmoid activation function was employed in data analysis. Solution pH (4–9), contact time (2–6 h), and initial adsorbate concentration (100–400 mg/L) were the input layer variables, while the adsorption capacity (16.5–50 mg/g) was the output variable. 360 data from adsorption experiments were utilized for training (80%), testing (10%), and validation (10%). Modeling errors and R^2 were utilized to test the ANN accuracy. A minimum root mean squared error of 0.0001 and $R^2 = 0.971$ were obtained for ANN with 10 neurons. It was identified that pH was the most influencing factor to model the chromium removal followed by the adsorbate concentration and contact time.

Savic et al. [119] proposed a comparative study of a central composite design (CCD) and multilayer ANN to model and optimize the adsorption of iron on bentonite clay. This experimental design consisted of 16 tests, and results showed that the adsorption efficiency ranged from 71.24 to 89.85% at pH 7 and room temperature. For the ANN modeling, the training sample was 80%, and the test sample was 20%. The initial metal concentration (17.09–51.91 mg/L), contact time (10–120 min), and adsorbent concentration (1000–7000 mg/L) corresponded to the input layer, and the metal removal was the output layer where the ANN architecture was 3-9-1 with radial basis activation function. 3D and contour plots for CCD and ANN were obtained. Multilayer ANN showed higher R^2 and lower errors than CCD thus confirming its better prediction performance.

The performance of 9 adsorbents obtained from dead fungal biomass was analyzed in the adsorption of reactive black 5 from aqueous solution [120]. Adsorption isotherms and kinetics were quantified to study the adsorption mechanisms. ANN were utilized to predict the impact of adsorbent textural parameters and physicochemical properties on the dye adsorption capacities. Experimental adsorption capacities of these adsorbents were 34.18-179.26 mg/g. The pseudosecond order and Langmuir equations were suitable to fit the experimental kinetics and isotherms, respectively. BP-ANN was used with the next input variables: pH (1–9), contact time (5–360 min), initial dye concentration (50–250 mg/L), BET area (0.0698–0.7656 m^2/g), pore volume (1.62×10^{-04} – 2.40×10^{-03} m^3/g), pore diameter (4.21–4.70 nm), nitrogen content (2.29–4.70%), carbon content (45.78–60.21%), and hydrogen content (9.18–7.20%), while the output variable was the adsorption capacities (0.65–172.67 mg/g). 135, 45, and 45 experimental data were utilized for training, validation, and testing. LM algorithm was the training method with a feed-forward BP-ANN with 3 layers. A sensitivity analysis was performed via the Garson method obtaining the next tendency for tested input variables: pH (22%) > nitrogen content of adsorbent (16%) > adsorbate concentration (15%) > carbon content of adsorbent (10%). The authors concluded that the adsorption capacities were affected by the chemical composition and not by the surface area of these adsorbents.

Bingöl et al. [121] carried out a comparison between the multiple linear regression and the adaptive neuro-fuzzy inference system (ANFIS) for the cadmium adsorption with date palm seeds. This analysis considered 20 experiments to

assess the effect of adsorbent mass (0.05–0.5 g), initial adsorbate concentration (5–100 mg/L), and pH (2–6) on the adsorption capacity (0.01-4.18 mg/g). ANFIS was trained with 50% of the experimental data, and the remaining 50% was utilized in testing. Results showed $R^2 = 0.9843$ for ANFIS and $R^2 = 0.7594$ for the multiple linear regression. These authors concluded that the multiple linear regression could not represent the nonlinearity of this adsorption process, and ANFIS was a better modeling alternative.

The application of ANN and gene expression programming (GEP) was studied by Çelekli et al. [122] in the prediction of the adsorption of lanaset red G dye using low-cost lentil straw. They applied a three-layer BP-ANN with 1 input layer consisting of 4 input neurons, namely, adsorbent particle size (125–500 μm), pH (1–4), contact time (0–360 min), and adsorbate concentration (50–800 mg/L), and an output layer corresponding to the adsorption capacity (30.57–271.12 mg/g). The training algorithm was the quick propagation method with the logistic sigmoid function where the data were divided in training (784), validation (184), and testing (184). The maximum adsorption capacity of this adsorbent was 271.12 mg/g. R^2 values were 0.999, 0.989, and 0.989 for ANN, pseudosecond order, and GEP models, respectively. Therefore, ANN was the best to adjust the experimental data. Solution pH and initial dye concentration were the operating variables with a significant impact on the adsorption of this organic pollutant.

Khajeh and Hezaryan [120] employed a hybrid ant colony optimization and ANN for the simulation and optimization of manganese and cobalt adsorption on SiO_2 nanoparticles. Feed-forward multilayer ANN was utilized where pH (7.5–10.5), adsorbent dosage (0.05–0.015 g), contact time (10–30 min), and the concentration of 1-(2-pyridylazo)-2-naphthol (0.5–1.5 mol/L) were the input neurons, while the removal of manganese and cobalt (29–99%) was the output neuron. Tangent sigmoid and linear activation functions were used. LM algorithm was employed in ANN training where 57 experimental data were split into 64, 18, and 18% for training, validation, and testing, respectively. The experimental conditions optimized with the ant colony optimization were well predicted with ANN thus obtaining $R^2 = 0.94$ and 0.98 and a root mean square error of 0.0979 and 0.04 for manganese and cobalt, respectively.

Multilayer feed-forward ANN and genetic algorithm were applied to analyze the effect of several operating parameters on the adsorption of eosin Y dye by Co_2O_3-activated carbon [123]. The experimental maximum adsorption capacity was 555.56 mg/g at 25°C and pH 3. A three-layer ANN with linear and tangent sigmoid functions were tested. LM method was the training algorithm. Input neurons included the adsorbent dosage (0.005 – 0.02 g), initial adsorbate concentration (30 – 80 mg/L), and contact time (0.5–30 min), while the removal percentage (%) was the output neuron. 70% of experimental data was used for training, 15% for validation, and 15% for testing. The lowest values of mean squared error (0.00015) and highest R^2 (0.9991) of ANN and genetic algorithm confirmed their suitability to model this adsorption system.

Çoruh et al. [124] proposed the use of nonlinear autoregressive model with exogenous input (NARX) neural network for predicting the zinc adsorption on activated almond shell. This model was developed considering as input variables the adsorbent dosage (0.125–4.0 g), pH (2–10), particle size (0.23–2.0 mm), and initial metal concentration (15–100 mg/L), where the output layer consisted of 2 neurons, i.e., adsorption capacity (mg/g) and removal percentage. These authors indicated that NARX was a dynamic recurrent model that converged faster and generalized better than other ANN. NARX architecture was 4-10-2 with a tangent sigmoid function and BP algorithm with a gradient descent momentum optimization. The performance of this model was tested thus obtaining a mean squared error < 0.001, and numerical results showed that NARX was successfully to model this batch adsorption system.

Mendoza-Castillo et al. [125] implemented a classical BP-ANN for modeling the adsorption isotherms and kinetics of four heavy metals (i.e., lead, cadmium zinc, and nickel) on several lignocellulosic wastes (i.e., jacaranda fruit, plum kernels, and nut shells). These authors discussed that the heavy metal adsorption on lignocellulosic biomasses was a complex process with highly nonlinear interactions among the adsorbent characteristics, the physicochemical properties of adsorbates, and the removal operating conditions. The input data were the biomass specific surface area (23–33 m^2/g), the biomass contents of cellulose (29.54–50.16%), hemicellulose (21.46–25.87%), and lignin (26.58–20.50%), the concentration of acidic groups (0.87–1.14 mmol/g), the molecular weight (58.69–207.20 g/mol), hydrated ionic radii (4.01–3.30 Å), electronegativity (1.60–1.90), and hydration energy (-1485–-2106 kJ/mol) of tested heavy metals, the initial metal concentration (40 and 100 mg/L), or equilibrium metal concentration (20–250 mg/L) depending on kinetics or isotherms were analyzed. The experimental adsorption capacities (1-7 mg/g) of all heavy metals were considered as the ANN outputs. Different structures of ANN were assessed in terms of input variables where 70% of experimental data were used for training, 15% for testing, and 15% for validation. Linear and tangent sigmoid activation functions were used with one hidden layer and 10 neurons to avoid model overfitting. Results of the mean relative errors and R^2 showed that this ANN fitted properly the experimental data. The lignin content, acidic group amount, molecular weight, and hydration energy of heavy metals were the main factors affecting the adsorption process.

Nia et al. [123] reported the reactive orange 12 adsorption on gold nanoparticle-activated carbon and its modeling with ANN using an imperialist competitive algorithm. Neural Network Toolbox of MATLAB R2011a was utilized in this study. LM and BP algorithm were utilized. The input variables for ANN modeling were the adsorbent amount, contact time, and dye initial concentration, while the output variable was the dye removal (%). 168 experimental data were used for training and 72 for testing. ANN model with 9 hidden neurons showed $R^2 = 0.972$ and a mean squared error of 0.0007 for this adsorption system.

A hybrid approach using principal component analysis and ANN was proposed by Zeinali et al. [43] for modeling the competitive adsorption of brilliant green and methylene blue by graphite oxide nanoparticles. The experimental results indicated that the dye adsorption was pH dependent where the maximum adsorption capacities were 410 and 129.41 mg/g for methylene blue and brilliant green, respectively. Dye adsorption was inhibited by the presence of the second dye molecule in the aqueous solution. Adsorption data were divided in 100 for training and 40 for testing of ANN model. Input variable was the equilibrium concentration (mg/L) of dye mixture, and the output variable was concentrations (mg/L). Tangent sigmoid and linear activation functions with BP algorithm were used for ANN. The optimal ANN architecture included 10 neurons with $R^2 > 0.9944$ and mean squared error < 0.0674. The competitive isotherms were fitted with the conventional equations and the extended Freundlich model adjusted properly the data. Finally, the principal component analysis and ANN were effective for the simultaneous modeling of the adsorption capacity of brilliant green and methylene blue in binary solutions.

The ternary adsorption of three dyes (i.e., methylene blue, crystal violet, and brilliant green) on MnO_2-loaded activated carbon was optimized and predicted with RSM and ANN [126]. Specifically, CCD and a three-layer feed-forward structure for RSM and ANN were used, respectively. Different ANN training algorithms were tested where the LM method was the most suitable. Hyperbolic tangent sigmoid and linear functions were used for hidden and output layers, respectively. 90 experimental data were divided into 70% for training, 15% for testing, and 15% for validating. R^2 and modeling errors were used to test the performance of the ANN model. Results indicated that ANN outperformed RSM with $R^2 > 0.99$.

A novel quantum BP multilayer ANN was implemented by Bhattacharyya et al. [127] to predict the adsorption of iron by calcareous soil. Specifically, the quantum computing is based on the principles of quantum mechanics with operations like superposition and entanglement. Superposition is the characteristic of dynamical equations, while the entanglement is the property that produces a nonlocal interaction among bipartite correlated states. 6-6-1 topology was used for the multilayer ANN and the quantum-based ANN. The input variables were the initial adsorbate concentration (1.5–15 mg/L), adsorbent amount (0.01–0.11 g/mL), pH (2-10), contact time (20–180 min), stirring rate (100–300 rpm), and temperature (303-330 K), while the output variable was the iron removal (39.56–97.34%). Tangent and sigmoid activation functions were evaluated. Calculations demonstrated that the architecture of quantum ANN was superior to multilayer ANN for describing this adsorption process. The adsorbent achieved a maximum adsorption capacity of 2.475 mg/g, and the removal process depended on solution pH and temperature.

Darajeh et al. [128] carried out a comparative study between wavelet ANN and RSM to optimize the adsorption of copper, nickel, and lead onto a magnetic/talc nanocomposite. This ANN used wavelet functions as an alternative to the conventional sigmoid activation function. The initial adsorbate concentration (32–368 mg/L), adsorbent dosage (0.07–0.13 g), and adsorption time (13–147 s) were the input variables, and the removal percentages (21.6–98.5%) of these adsorbates were the output variables. This ANN was trained with 13 data, and the incremental BP, batch BP, quick-propagation, genetic algorithm, and LM were applied and assessed to obtain the best network. The best architecture was the incremental BP with 3-14-3 with $R^2 = 0.982 - 0.993$. It was concluded that the initial adsorbate concentration was the most influential factor (35.16%) on the heavy metal adsorption followed by the adsorbate dosage. This alternative ANN was more suitable than RSM to predict the adsorption process.

The adsorption of cadmium on rice straw was modeled with ANFIS [129]. As the authors stated, this model combined the advantages of both fuzzy systems and ANN. The influence of initial cadmium concentration (10 and 100 mg/L), solution pH (2 and 7), and adsorbent mass (0.1 and 0.5 g/L) was analyzed. These operating conditions were the ANFIS input variables, and the output variable was the removal efficiency (%). LM method was utilized for ANN training where the data were distributed in 70% for training and 30% for validation. Hyperbolic tangent activation function was used with an architecture of 3-6-1. ANFIS showed that the initial cadmium concentration had the highest impact on the adsorption followed by pH and adsorbent dose. This model achieved $R^2 = 0.99$ for training, 0.82 for validation, and 0.97 for testing, respectively.

The individual and simultaneous ultrasonic-assisted removal of malachite green and methylene blue dyes by a magnetic γ-Fe_2O_3-loaded activated carbon were studied by Asfaram et al. [130] including its modeling with RSM and ANN. A feed-forward BP ANN was used with the next input variables: pH (4.5-7.5), initial dye concentration (10-20 mg/L), sonication time (3-5), and adsorbent mass (0.01-0.02 g). Dye removal (%) was the output variable. Hyperbolic tangent sigmoid function was used in hidden layer, and linear activation function was applied in output layer. 50 data were divided for training, testing, and validation (70/15/15 %) where LM was the training method. R^2 and different error functions were applied to test the ANN performance. Both RSM and ANN were capable of predicting the dye adsorption with high values of R^2 but ANN outperformed RSM.

Esfandian et al. [8] tested ANN using the experimental data of the removal of pesticide diazinon using acid-treated zeolite and modified zeolite by Cu_2O nanoparticles. Experimental results indicated that these zeolites showed adsorption capacities of 15.10 and 61.73 mg/g, respectively. Adsorption depended on pH and temperature where an exothermic process was identified. Data modeling was performed considering pH (3-8), initial adsorbate concentration (50–120 mg/L), adsorbent dosage (0.05–0.35 g), and contact time (10–105 min) as input variables, and the target variable was the removal efficiency (%). Experimental data was divided in training (70%), validation (15%), and testing (15%). In this study, the multilayer feed-forward ANN with 7 hidden layer neurons and sigmoid function was utilized.

This ANN showed the lowest modeling errors and was suitable to fit the experimental data of this adsorption system.

Fawzy et al. [131] also proposed the use of ANFIS to establish the impact of operational parameters on the nickel and cadmium adsorption by *Typha domingensis* biomass. Five variables were analyzed: pH (2–8), adsorbent dosage (2.5–40 g/L), particle size (0.25–1.0 mm), contact time (5–150 min), and metal concentration (25–300 mg/L). The output variable was the metal removal efficiency (%). Experimental data showed that this biomass achieved a maximum adsorption capacity of 4.51 and 28.49 mg/g for nickel and cadmium at pH 6 and 25 ± 3°C, respectively. ANFIS training was carried out with a hybrid methodology consisting of a combination of the least-squares method and the BP gradient descent method where the Sugeno-type fuzzy inference system was applied. Results indicated that the initial concentration and pH had a significant influence on the metal adsorption. ANFIS was useful to identify the role of these operational parameters.

Ghaedi et al. [132] studied the application of ANN-particle swarm optimization approach for the modeling of methyl orange removal on lead oxide nanoparticles-loaded activated carbon. The input ANN variables were the contact time, adsorbent dosage, and dye concentration, while the output variable was the removal of methyl orange (%). ANN training was performed with LM algorithm using 270 data and 90 data for testing. ANN-PSO modeling with 6 neurons in the hidden layer offered the best results ($R^2 = 0.9685$).

Gomez-Gonzalez et al. [133] utilized ANN to model the lead adsorption by coffee ground. Its performance was compared with traditional equations as Langmuir and Freundlich. Specifically, pattern search, simulated annealing, and genetic algorithm were used to adjust the parameters of Langmuir and Freundlich and then to compare with ANN. Tangent sigmoid function was used with ANN (3 layers) and LM training. Input neuron was the equilibrium concentration, and the adsorption capacity (mg/g) was the output neuron. The architecture used was 1-13-1 for pH 3 and 1-4-1 for pH 4 and 5. Experimental data were distributed in 70% for training, 15% for validation, and 15% for testing with a tangent sigmoid activation function. A maximum adsorption capacity of 22.9 mg/g was obtained with coffee ground at pH 5 and 30 °C. These authors concluded that pattern search was the best optimization method, and ANN outperformed the conventional isotherm equations used in adsorption.

Podstawczyk and Witek-Krowiak [134] studied the malachite green adsorption using a novel composite. Specifically, the rapeseed meal was modified with magnetic nanoparticles. Adsorption kinetic data were modeled with the surface diffusion, pseudosecond order, and pseudofirst order models as well as ANN. These authors proposed a feed-forward ANN with 2-3-1 topology that was trained with LM method. The input variables were the adsorption time (0–270 min) and pH (4–6), while the adsorption capacity (0–40 mg/g) was the output variable. ANN outperformed the conventional kinetic equations showing $R^2 = 0.995$. Dye adsorption isotherm indicated a maximum adsorption capacity of 836.2 mg/g.

Ahmadi et al. [135] tested random forest, radial basis function ANN and CCD polynomial model to simulate and optimize the ultrasonic-assisted removal of brilliant green with ZnS nanoparticles loaded on activated carbon. In particular, the random forest is based on decision trees and uses voting for classification and averaging for regression and predictions. The effect of several operational conditions such as adsorbent dosage (10–30 mg), initial adsorbate concentration (4–20 mg/L), and sonication time (2–6 min) on the removal efficiency (15.4–100%) was evaluated. Experimental data were divided in 70% for training and 30% for validation. Results showed that these approaches were suitable for data fitting. However, the random forest outperformed the other models. The optimized adsorption conditions allowed to achieve 98% of brilliant green removal.

Asfaram et al. [136] applied RSM, ANN, and radial basis function neural network (RBFNN) to model and predict the efficiency of Mn@CuS/ZnS nanocomposite-loaded activated carbon to remove malachite green and methylene blue dyes in binary adsorption systems assisted by ultrasound. The effect of pH (4-8), initial dye concentration (5-25 mg/L), sonication time (1-5 min), and adsorbent mass (0.01-0.03 g) on the dye removal percentage was tested. For ANN modeling, 32 experiments were used and randomly divided in 70% (training), 15% (testing), and 15% (validating) where LM algorithm was the best training method. Hyperbolic tangent sigmoid and linear functions with a BP algorithm were applied. For RBFNN, the Kernel stone algorithm was used as training method with 70% of data for training and 30% for testing. The results demonstrated the effectiveness of these models to predict the binary adsorption with the next tendency RBFNN > ANN > RSM with R^2 values of 0.9984-0.9997, 0.9787-0.9997, and 0.917-0.9850, respectively.

The removal of indigo carmine and safranin-O using nanowires loaded on activated carbon was analyzed by Dastkhoon et al. [137]. Models based on RSM, multilayer ANN, and Doolittle factorization algorithm were tested for this adsorption system. CCD experimental design of 4 factors and 5 levels with a total of 30 experiments was employed. ANN model consisted of 3 layer feed-forward with tangent sigmoid and linear functions. Input neurons were the indigo carmine concentration (4–16 mg/L), safranin-O concentration (4–16 mg/L), adsorbent mass (20–40 mg), and sonication time (1–5 min), while the neuron output was the removal of these dyes (71.91–96.32%). Hyperbolic tangent sigmoid was the activation function. Doolittle factorization algorithm consisted of a factorized matrix that contained all the experimental data. Modeling results indicated that ANN offered a better precision in comparison to the other models, although Doolittle factorization algorithm was faster. The sensitivity analysis showed that the sonication time was the most important parameter. The maximum adsorption capacities were 29.09 and 37.85 mg/g for indigo carmine and safranin-O, respectively.

Parveen et al. [138] evaluated the support vector regression, multiple linear regression and ANN model to predict the chromium adsorption on maize brain waste. The effect of adsorption time (10-180 min), initial adsorbate concentration (200-300 mg/L), pH (1.4–8.5), and temperature (20-

40 °C) on the adsorption capacity (mg/g) was analyzed. For support vector regression model, the Gaussian radial basis function was selected as the kernel function. 124 data were utilized: 80% for training and 20% for testing. ANN with a topology 4-10-1 was used where the experimental data were divided in 65% for training, 15% for validations, and 20% for testing where the kernel function was used as activation function. Results indicated that the support vector regression model was the best to predict the chromium adsorption capacity with the highest R^2 (i.e., 0.9986), followed by ANN ($R^2 = 0.9331$) and multiple linear regression ($R^2 = 0.8955$), respectively.

Natural and modified clinoptilolite were tested in the fluoride adsorption from aqueous solutions, and the modeling was performed via the hybridization of ANN with Langmuir and pseudosecond order equations [105]. Specifically, ANN was employed to calculate the parameters of pseudosecond order and Langmuir equations, and the adsorption capacities were determined with these parameters and the corresponding adsorption equation. A feed-forward ANN was used where the input layer contained the temperature, time, and initial fluoride concentration for the adsorption kinetics and initial fluoride concentration, pH, and temperature for the adsorption isotherms. The output layer corresponded to the adjustable parameters of tested adsorption kinetic and isotherm equations. Experimental data were divided in 70% for training and 30% for validation and testing where a logistic sigmoid activation function was also utilized. This hybrid ANN model outperformed the classical adsorption equations showing R^2 from 0.95 to 0.99. These authors also indicated that the classical equations failed to predict the experimental data in some particular operating conditions. The maximum experimental adsorption capacities of these zeolites were 5.3 and 12.4 mg/g at 40 °C and pH 6, respectively.

Yildiz [139] reported the use of ANN for the modeling of zinc adsorption on peanut shells. Input variables were the initial solution pH, initial zinc concentration, and adsorbent dosage, and the output variable was the adsorbed amount of zinc. ANN with an architecture 3-16-1 and BP were utilized where Matlab® was the software employed in these calculations. 12, 4, and 4 data were used for training, testing, and validation of ANN. Overall, this ANN showed satisfactory results in adsorption data modeling.

Ghosal and Gupta [140] studied the application of ANN and Pareto front analysis for fluoride removal using Al/olivine. The impact of solution pH, agitation rate, temperature, contact time, initial fluoride concentration, and adsorbent dosage was studied. ANN modeling was performed with these input variables, and the output variables were the adsorption capacity and removal efficiency. LM was selected as the training algorithm. Finally, the results of ANN showed $R^2 > 0.99$ and mean square errors of 2.035 and 0.018 for the removal efficiency and adsorption capacity, respectively.

Karri and Sahu [141] tested the use of palm kernel shell derived-activated carbon for the zinc removal. RSM and particle swarm optimization-ANN were compared to obtain the optimal removal. First, RSM and CCD were utilized to correlate the zinc removal with the independent variables: pH (2-8), adsorbent mass (2-20 g/L), initial adsorbate concentration (10-100 mg/L), contact time (15-75 min), and temperature (30-70 °C). Different training algorithms as LM-BP, gradient descent, resilient BP, and gradient descent with adaptive linear regression were assessed. A feed-forward ANN and PSO were employed to obtain better estimations of this adsorption system. Several learning methods and topologies were analyzed, and the optimal ANN model was obtained with LM-BP training and 5-6-1 topology. Particle swarm optimization and ANN outperformed the RSM approach.

Mendoza-Castillo et al. [28] studied and discussed the advantages and limitations of ANN for the modeling of multicomponent adsorption of heavy metals on bone char. Experimental isotherms of single, binary, ternary, and quaternary solutions of copper, nickel, cadmium, and zinc were quantified experimentally and employed in ANN modeling. A multilayer feed-forward ANN was utilized with 141 data divided in 70% for training, 20% for testing, and 10% for validation. Input layer included the initial concentration of the metals in the solution, while the equilibrium concentration and adsorption capacity were analyzed as the output layer. Experimental results showed that the heavy metal adsorption in single solutions followed the tendency: copper > nickel > cadmium > zinc. The adsorption in multimetallic systems showed an antagonistic effect caused by the presence of other coions. ANN showed a proper fit of multicomponent systems with $R^2 \geq 0.96$. However, these results depended on the activation function and selected output variable. Specifically, the use of equilibrium concentration was not recommended because this extensive variable can generate wrong predictions (i.e., desorption behavior not observed in the experimental data) for this adsorption system. These authors concluded that intensive variables such as the adsorption capacity must be utilized in ANN modeling with the aim of generating reliable predictions. Results of this study also revealed that a proper ANN training and architecture are fundamental for a reliable prediction of the complex adsorption behavior in multicomponent systems.

Naderi et al. [142] applied a hybrid model consisting of simulated annealing and ANN to optimize and predict the crystal violet dye removal on centaurea stem. RSM was used to find the best experimental conditions. The maximum adsorption capacity was 476.19 mg/g. ANN with 6-10-1 topology and tangent sigmoid and linear activation functions was employed to model the adsorption data. This network was trained with the feed-forward BP algorithm where 32 data were divided in 80% for training and 20% for validation and testing. Input neurons were pH (5–13), temperature (20-40 °C), contact time (5–25 min), initial dye concentration (20-300 mg/L), and adsorbent dosage (3–15 mg), while the dye removal (%) was the output variable. R^2 of RSM (0.9942) and simulated annealing-ANN (0.9968) was very similar but the lowest prediction errors were obtained with the approach based on ANN.

The ultrasonic-assisted binary adsorption of sunset yellow and sidulfine blue dyes on oxide nanoparticles loaded on activated carbon was optimized and modeled with RSM and ANN [143]. A total of 26 experiments were performed

where the effects of sonication time (6-12 min), adsorbent dosage (0.016-0.030 g), pH (7), and initial dye concentration (8-16 mg/L) on the dye removal percentage were tested. 17 BP algorithms were evaluated with ANN where LM and resilient methods were the best. The performance of these models was statistically compared by considering R^2, root mean squared error, mean absolute error, and absolute average deviation. Results showed that ANN ($R^2 > 0.999$) outperformed RSM ($R^2 \sim 0.986$).

The modeling of adsorption of salicylic acid on SiO_2/Al_2O_3 nanoparticles was performed by Arshadi et al. [144] with ANN. In this study, the input variables were the initial salicylic acid concentration (5–1000 mg/L), initial solution pH (1–12), contact time (0.25–30 min), temperature (15–80 °C), and adsorbent dosage (0.25–10). The output variable was the adsorption capacity of salicylic acid (mg/g). ANN architecture of 5-12-1 was utilized. Results indicated that the ANN-based simulation of the adsorption of this compound was satisfactory obtaining $R^2 = 0.9841$.

Gadekar and Ahammed [145] tested a hybrid RSM and ANN model in the prediction of blue 79 dye removal using aluminum-based water treatment residuals. RSM was used to identify the optimum experimental conditions to achieve a high dye removal, and these data were employed to train ANN. ANN with 4-4-1 topology, tangent sigmoid, and linear activation functions was used. For ANN training, LM, gradient descent, and scaled conjugate BP algorithms were utilized. 45 data were employed in training (60%), validation (20%), and testing (20%). ANN input layer contained the adsorbent dose (10–30 g/L), initial pH (3–5), initial dye concentration (25–75 mg/L), and final pH (3.01–5.80). Dye removal (31.2-52%) was the ANN output neuron. Results indicated that ANN and RSM were a reliable alternative to predict the removal of this dye.

Ghaedi et al. [146] modeled the simultaneous ultrasonic-assisted ternary adsorption of rose bengal, safranin O, and malachite green dyes on copper oxide nanoparticles supported on activated carbon. ANN with 3 layers was applied where the initial dye concentrations (8-12 mg/L), pH (6-8), adsorbent dosage (0.05-0.025 g), and sonication time (2-4 min) were the input variables, while the output variable was the dye removal percentage (18.2-92.67%). LM and BP were employed as learning method. Hyperbolic tangent sigmoid and linear functions were utilized at hidden and output layers. High R^2 of ANN (>0.99) revealed a satisfactory fitting of tested experimental data.

The multicomponent adsorption of nitrobenzene, phenol, and aniline from a ternary aqueous system using granulated activated carbon was studied by Jadhav and Srivastava [147]. ANN was tested with BP and different activation functions. The equilibrium concentrations of nitrobenzene (0.003–0.8 mmol/L), aniline (0.01–1.6 mmol/L), and phenol (0.01–1.8 mmol/L) were the input variables, and the adsorption capacities were the output variable. Adsorption data were divided in 50% for training and 50% for testing. R^2 and mean squared errors were used to verify the model performance. ANN model accurately predicted ($R^2 > 0.99$) the ternary adsorption in comparison to other models.

Similarly, Nasab et al. [148] proposed a hybrid model consisting of genetic algorithm and ANN to predict the adsorption of crystal violet on chitosan/nanodiopside. CCD with 5 levels and 4 factors (30 experiments) was chosen to obtain the optimal dye removal. The input variables for the ANN model were pH (4.5–8.5), contact time (15–55 min), initial dye concentration (15-35 mg/L), and adsorbent amount (0.001–0.01 g), while the output variable was the dye removal (%). Feed-forward ANN with hyperbolic tangent sigmoid and linear activation functions and LM algorithm were employed. 70, 15, and 15% of experimental data were used in training, validation, and testing, respectively. The maximum dye removal was 99.5%. Genetic algorithm was applied to identify the optimal factors for obtaining the maximum adsorption. Results of ANN-genetic algorithm showed a higher R^2 (0.9708) than that of RSM (0.9652). Overall, both approaches provided accurate dye removal percentages.

Sharafi et al. [149] reported the phenol adsorption from aqueous solution using scoria stone modified with different acids (e.g., nitric, acetic, and phosphoric). Modeling of adsorption data was performed with RSM and ANN. Clonal selection algorithm was used with ANN modeling where the input variables were the phenol concentration, adsorbent dosage, and contact time. The output variable was the phenol removal. Overall, both RSM and ANN showed satisfactory results in data correlation.

Sadeghizadeh et al. [150] used ANFIS to predict the lead adsorption with a hydroxyapatite/chitosan nanocomposite. This adsorbent showed a maximum adsorption capacity of 225 mg/g, and this removal process was also endothermic. Concerning the data modeling, the input variables were temperature (25–55 °C), adsorption time (15–360 min), shaker velocity (80–400 rpm), adsorbent amount (0.05–1.5 g), initial lead concentration (0–5000 mg/L), pH (2–6), and hydroxyapatite concentration (15–75%). Output variable was the lead adsorption capacity (mg/g) where 57 experimental data were modeled (38 for training and 19 for testing). ANFIS was able to predict the lead adsorption with $R^2 = 0.999$.

Takdastan et al. [6] used ANN to model the cadmium adsorption on modified oak waste. Kinetic and isotherms were quantified to characterize the effect of adsorption operating conditions. Experimental results revealed that the adsorption increased with temperature, initial concentration, adsorbent dosage, and pH. Isotherms were modeled with Liu, Temkin, Redlich-Peterson, Freundlich, and Langmuir equations, while the kinetics were fitted to intraparticle diffusion, pseudosecond and pseudo-first order, Elovich, and Avrami fractional order equations. Raw adsorbent and the NaOH-modified adsorbent had a maximum adsorption capacity of 155.9 and 771.4 mg/g, respectively. A feed-forward BP-ANN was applied using pH (2–8), contact time (5–240 min), adsorbent dosage (0.1–10 g/L), cadmium initial concentration (25–100 mg/L), and temperature (10–40 °C) in the input layer with a hidden layer of 8 neurons, and the cadmium removal (16–92.4% for ROW and 26–99.5% for AOW) was in the output ANN layer. 219 experimental data were employed in training (153), validation (33), and testing (33). $R^2 > 0.999$ for ANN modeling where pH had

the highest impact on cadmium removal, while the adsorption temperature showed a slight effect.

ANN were used to model the lead adsorption on rice husks treated with HNO_3 [151]. Specifically, a feed-forward BP-ANN and LM training were used. The input variables of ANN were the adsorbent dosage, initial lead concentration, and contact time, and the output variable was the lead adsorption capacity. These authors concluded that the adsorption modeling with ANN was effective.

The adsorption of 6 heavy metals (arsenic, nickel, cadmium, lead, zinc, and copper) on 44 biochars obtained from lignocellulosic feedstocks was modeled using a multilayer ANN and random forest [152]. 353 adsorption data were collected from literature, and 14 input variables were studied and divided in 4 sets (adsorbent properties, initial heavy metal concentration, operational conditions, and heavy metal properties), while the removal efficiency was the output variable. ANN architecture included 14 input neurons, 8-28 hidden neurons, and 1 output neuron with sigmoid activation function. Results showed that random forest outperformed in 28% the ANN performance with $R^2 = 0.973$. It was concluded that biochar characteristics were the most important variables in heavy metal adsorption. Surface area did not show a significant impact on the metal removal.

Afolabi et al. [47] reported the use of ANN to model the pseudosecond order kinetics of the paracetamol adsorption using orange peel-activated carbon. The experimental conditions used as input variables were the initial paracetamol concentration (10–50 mg/L), contact time (0–330 min), and temperature (30–50 °C), and the output variable was the pseudosecond order kinetics. ANN with different hidden neurons, training algorithms, and activation functions were used for the data modeling. A total of 495 data were used (i.e., 330 for training and 165 for testing). Results showed the impact of training algorithms and activation functions on the ANN performance. The best ANN showed $R^2 \cong 1$.

The removal of lead, cadmium, nickel, and zinc using a natural zeolite was modeled with ANN, multivariate nonlinear regression, particle swarm optimization-adaptive neuro-fuzzy inference system, genetic programming (GP), and the least squares support-vector machine [10]. The input modeling variables were the initial and equilibrium solution pH, silica concentration, molecular weight, first ionization energy, hydrated ionic radii, and electronegativity of tested metals. The adsorption capacity of heavy metals of the zeolite was the output variable. Results showed that ANN outperformed traditional adsorption equations with $R^2 = 0.9948$. Other tested models also offered a satisfactory data correlation.

Gopinath et al. [29] proposed the use of ANN with a homogeneous surface diffusion model to analyze the single, binary, and ternary adsorption kinetics of acid orange, acid blue, caffeine, acetaminophen, and benzotriazole on activated carbon. The mass transfer model considered bulk diffusion in the fluid phase and surface diffusion via the internal adsorbent structure. Note that these phenomena are not considered by the conventional pseudosecond and pseudofirst order models. Feed-forward ANN with 5 layers was utilized. Input variables were the type of adsorbent (carbon labelled and active char products), pH (3–8), temperature (25–45 °C), initial concentration (100–300 mg/L), and ratio of mass/volume (0.8–2 g/L), while the output variable was the removal efficiency (%). Tangent sigmoid and linear activation functions were used. Datasets were distributed in 90, 5, and 5 for training, testing, and validation, respectively, where ANN was trained with LM algorithm. R^2 of 0.999, 0.986, and 0.993 were obtained using the mass transfer model and ANN for single, binary, and ternary systems, respectively. Results of this study proved the advantages of ANN in the simulation of multicomponent adsorption kinetics considering more complex models based on mass transfer phenomena.

The treatment of water polluted with atenolol, ciprofloxacin, and diazepam in presence of COD and ammonia was performed in a sequencing batch reactor with a composite adsorbent consisted of bentonite, zeolite, biochar, and cockleshell mixed with Portland cement [11]. Contact time (2-24 h) and initial pharmaceutical concentration (1-5 mg/L) were the input variables for ANN modeling, while the output variable was the pharmaceutical removal (90.3% for atenolol, 95.5% for ciprofloxacin, and 95.6% for diazepam). ANN with three layers (2-5-1) was utilized where the model performance using the mean squared sum errors and R^2. Data were divided in training (60%), validation (20%), and testing (20%), and LM was used for ANN training. Overall, ANN showed $R^2 > 0.99$ for the modeling of this system.

The single and competitive adsorption of acid blue 9 and allura red AC on chitosan-based hybrid hydrogels were modeled with ANN [7]. Experimental data indicated that acid blue 9 was better adsorbed than allura red on five adsorbents. In binary dye solutions, an antagonistic adsorption was observed. Input layer of ANN with the initial concentration of both dyes (0-0.126 mmol/L and 0–0.201 mmol/L for acid blue 9 and allura red AC, respectively), carbonaceous mass percentage of adsorbent (0-10% g/g), adsorbent porosity (0.724–0.880), and contact time (0–200 min). All experimental data were used for training (70%), validation (15%), and testing (15%). Several topologies were investigated, and the best ANN architecture was 5-10-10-10-2 with tangent sigmoid activation function. $R^2 > 0.99$ and root mean square error of 0.119 thus indicating that ANN could be an effective model to predict the adsorption of dyes by these hybrid hydrogels.

Franco et al. [153] applied the ANN and ANFIS to analyze the indium adsorption on 10 adsorbents: commercial activated carbon, multiwalled carbon nanotubes, chitin, chitosan, and other lignocellulosic agroindustrial wastes. The indium adsorption capacities of these materials ranged from 8.20 to 1000 mg/g. Modeling was performed considering the next input variables: specific surface area (0.85–200.40 m^2/g), pH of point of zero charge (4.5–7), adsorbent dosage (0.05–2.0 g/L), and contact time (5–120 min). Output variable was the indium adsorption capacity. 1200 data were employed in the modeling where 70% for training and 30% for testing and/or validation. ANFIS utilized the Sugeno type with 4 hidden layers, while ANN was used with a 4-4-1 topology. ANN obtained $R^2 = 0.9913$ and a mean squared error of 1×10^{-03}. On the other hand, ANFIS achieved $R^2 = 0.9998$ and a mean

squared error of 8.42×10^{-05}. Both models were capable of predicting the adsorption data.

Nayak and Pal [154] employed ANN for the prediction of nile blue A dye adsorption with overripe *Abelmoschus esculentus* seeds. CCD with 31 experiments was utilized to optimize the dye adsorption where the effect of adsorbent dosage (1–9 g/L), initial adsorbate concentration (140–750 mg/L), pH (2-9), and contact time (5–125 min) was tested. The maximum dye adsorption capacity was 71.78 mg/g. ANN with 3 layers and BP algorithm was used. ANN architecture included 4 input neurons (contact time, pH, initial dye concentration, and adsorbent dosage), one output neuron (adsorption capacity), and 12 hidden neurons. 31 experiments (including 16 factorial points, 8 axial points, and 7 replicates) were divided in training (70%), validation (15%), and testing (15%), and tangent sigmoid activation function was used. R^2 and modeling errors were the metrics to analyze the ANN performance. Sensitivity analysis demonstrated that pH and contact time were the most important parameters in this adsorption system. This adsorbent showed a maximum adsorption capacity of 105 mg/g according to the experimental isotherms.

Thirunavukkarasu and Nithya [155] reported the removal of acid orange 7 using CaO/CeO_2 and its modeling via RSM and ANN. The input variables for ANN were the adsorption temperature (301–338 K), contact time (0–300 min), initial concentration of acid orange 7 (10–50 mg/L), adsorbent dose (0.02–0.2 g), and initial solution pH (2–12). The output variable was the dye removal (%). LM and BP were used in ANN training where the best architecture was 5-10-1. ANN results indicated a satisfactory modeling with a root mean square error of 0.3020.

Qi et al. [156] employed RSM, ANN-genetic algorithm, and ANN-particle swarm optimization to analyze the methylene blue adsorption on mesoporous rGO/Fe/Co nanohybrids. The effect of pH (2–6), temperature (20–40°C), contact time (3–15 min), and initial dye concentration (200–600 mg/L) on the dye adsorption was analyzed using a CCD consisting of 30 experiments. The experimental results showed that the nanohybrids achieved a maximum dye removal of 89.41%, while a maximum adsorption capacity of 909.1 mg/g was obtained from the Langmuir isotherm. ANN with 3 layers, BP algorithm, and linear and tangent sigmoid activation functions was utilized. For the case of ANN-genetic algorithm, its parameters were population size = 20, crossover rate = 0.8, number of generations = 100, and mutation probability = 0.01. On the other hand, the parameters of particle swarm optimization were maximum inertia weight = 0.9, minimum inertia weight = 0.3, global learning coefficient = 2, individual learning coefficient = 2, maximum iteration = 50, and swarm size = 20. The absolute errors between the experimental and predicted values were 2.88, 0.52, and 1.35 for CCD, ANN-particle swarm optimization, and ANN-genetic algorithm, respectively. Therefore, ANN–particle swarm optimization was the best option for this adsorption system.

In the study of Samadi-Maybodi and Nikou [79], ANN was used to predict the sarafloxacin adsorption on magnetized metal-organic framework Fe_3O_4/MIL-101(Fe). RSM with CCD of 30 experiments was used to optimize the removal efficiency obtaining a maximum value of 88.26%. A multilayer ANN with three layers was employed where the input variables were the solution pH (3-11), initial concentration (10–50 mg/L), adsorbent dosage (5–25 mg), and contact time (15–45 min), while the removal percentage (35.73–88.26%) was the output variable. LM was the training method with sigmoid tangent hyperbolic function for input to hidden layers and linear transfer function for hidden to output layers, while ANN was assessed using R^2 and mean squared error. Overall, ANN was reliable for predicting the sarafloxacin removal with $R^2 = 0.9861$.

Netto et al. [157] applied ANFIS and ANN to model the adsorption equilibrium of silver, cobalt, and copper on three zeolites ZSM-5, ZHY, and Z4A. Adsorption experiments were conducted at different temperatures. The input variables for the models were the Si/Al ratios of zeolites (50:50, 71:29, 90:3), molecular weights of metal ions (58.93–107.87 g/mol), temperature (298-328 K), and initial adsorbate concentration (0–300 mg/L), while the equilibrium adsorption capacities of these metals were the output variables. ANN was tested with two training functions (LM-BP and Bayesian regularization BP). The linear and hyperbolic tangent sigmoid functions were utilized. For the case of ANFIS, the Gaussian curve was the input function, and the tune sugeno-type was used for training. 324 experimental data were divided in 85% for training and 15% for testing. The performance of ANN and ANFIS was analyzed with different statistical metrics. Overall, both models predicted accurately the adsorption data where ANFIS was slightly better. Z4A zeolite showed the best adsorption capacities where silver was more adsorbed in comparison to cobalt and copper.

Other recent studies on the ANN modeling of adsorption isotherms and kinetics include the fluoride adsorption on rice husk-derived biochar modified with Fe or Zn [158], the removal of brilliant green dye using mesoporous Pd–Fe magnetic nanoparticles immobilized on reduced graphene oxide [15], the adsorption of diazinon pesticide on a magnetic composite clay/graphene oxide/Fe_3O_4 [159], the removal of crystal violet and methylene blue on magnetic iron oxide nanoparticles loaded with cocoa pod carbon composite [160], the arsenide removal employing mesoporous $CoFe_2O_4$/graphene oxide nanocomposites [161], the adsorption of perfluorooctanoic acid on copper nanoparticles and fluorine-modified graphene aerogel [17], the uptake of dicamba (3,6-dichloro-2-methoxy benzoic acid) by MIL-101(Cr) metal-organic framework [16], the phosphorous adsorption on polyaluminum chloride water treatment residuals [162], the use of iron doped-rice husk for the chromium adsorption/reduction [163], the removal of methyl orange dye by an activated carbon derived from *Acalypha indica* leaves [164], the lead adsorption by a hydrochar obtained from the KOH activated *Crocus sativus* petals [165], the adsorption of the cefixime antibiotic using magnetic composite beads of reduced graphene oxide-chitosan [13], the use of graphene oxide-cyanuric acid nanocomposite for the lead adsorption [14], the arsenic removal by an adsorbent consisting of iron oxide incorporated

carbonaceous nanomaterial derived from waste molasses [12], the fluoride adsorption by chemically activated carbon prepared from industrial paper waste [18], the methylene blue adsorption with polyvinyl alcohol/carboxymethyl cellulose-based hydrogels [166], the modeling of adsorption properties of biochar and resin for the removal of organic compounds [167], and the removal of lead from waster with a magnetic nanocomposite [168].

3.2. Breakthrough Curves. The dynamic adsorption experiments provide important engineering information about the adsorption process especially for real-scale applications. Breakthrough curves are commonly represented via the ratio of effluent adsorbate(s) concentration(s) and feed adsorbate(s) concentration(s) (i.e., $C_i/C_{0,i}$) versus the operating time or treated volume. These curves characterize the adsorbent performance at dynamic operating conditions. Overall, the breakthrough curves of water pollutants can correspond to symmetric and asymmetric profiles depending on the process operating conditions (e.g., feed flow, residence time, and column length) and the impact of mass transfer phenomena. The modeling of asymmetrical breakthrough is more challenging because the conventional models like Thomas and Yang equations are limited because they were developed to handle the ideal "S" profile expected and desired for adsorption columns. Therefore, ANN have been utilized to improve the correlation and prediction of breakthrough curves of the adsorption of water pollutants. ANN modeling of breakthrough curves has covered the adsorption of fluoride, dyes, heavy metals, pesticides, organic compounds, and phosphates with bone char, activated carbon, graphene, biochar, zeolites, biomasses, composites, nanomaterials, and other adsorbents like agroindustrial wastes. Different operating conditions such as temperature (15–50 °C), feed flow (0.5–30 mL/min), and pH (2–9) have been tested in the modeling of breakthrough curves in aqueous solutions with one or more adsorbates. Details of several studies on the ANN modeling of dynamic adsorption process for different pollutants and adsorbents are shown in Tables 3 and 4. A brief description of the main findings and representative studies of the ANN-based breakthrough adsorption modeling are provided in this subsection.

Texier et al. [169] proposed the application of a multilayer ANN to model the breakthrough curves of the adsorption of lanthanide ions (La, Eu, and Yb) using an immobilized *Pseudomonas aeruginosa* in polyacrylamide gel and a fixed-bed adsorber. The effect of superficial liquid velocity (0.76–2.29 m/h), particle size (125–500 μm), influent concentration (2–6 mM), and bed depth (250–400 mm) on the adsorption capacities was analyzed. Experimental breakthrough curves showed that the maximum bed adsorption capacities were 208 μmol/g for La, 219 μmol/g for Eu, and 192 μmol/g for Yb in single aqueous solutions. ANN modeling was performed considering the next input variables: initial concentration (2–6 mM), bed depth (250 and 330 mm), operating time (min), and the modified Reynolds number. Ratio C/C_0 was the output variable. BP algorithm was used in ANN training where the activation function of the hidden layer was the hyperbolic tangent. Training and validation were carried out with 392 adsorption data, and 40 additional data were used for testing the ANN performance. Root mean square error was used as the statistical metric to analyze the calculations with ANN. Results showed that the prediction ability of ANN was satisfactory for the first zone of the breakthrough curve, which corresponded to the zone before the breakthrough point. These authors also concluded that it should be necessary to extend the experimental column database to improve the ANN performance with the objective of predicting reliably all the zones of breakthrough curves.

Park et al. [170] modeled the breakthrough curves of chromium adsorption using a column packed with brown seaweed *Ecklonia* biomass. These authors discussed the effect of the operating parameters (feed concentration, initial concentration, pH, flow rate, and temperature) on the adsorption of this priority water pollutant. The experimental results showed that this biomass achieved an adsorption capacity of 50.2 mg/g by the 274th bed. Chromium adsorption reduced with pH decrements, and this removal process was endothermic. ANN modeling was done with the next input variables: influent chromium concentration (100–200 mg/L), biomass concentration (70–140 g/L), pH (2), flow rate (10–20 mL/min), temperature (25–45 °C), and the bed number (i.e., flow rate operating time/total column volume). Chromium concentration of treated fluid (0–200 mg/L) was utilized in the output ANN layer. 127 data were utilized for obtaining the ANN model with hyperbolic tangent function in the hidden layers and a linear function in the output layer. The performance of the feed-forward BP-ANN was assessed. Root mean square errors ranged from 2.52 to 3.20, thus, indicating that ANN was successful to model the breakthrough curves of chromium adsorption.

The adsorption breakthrough curves of 3 pesticides (namely, atrazine, atrazine-desethyl, and triflusulfuron-methyl) using 5 commercial activated carbon filters were modeled by Faur et al. [171]. Experimental isotherms of pesticides in aqueous solutions and natural waters were carried out in single and competitive adsorption between pesticide and natural organic matter. In a second stage, the breakthrough curves of pesticide were quantified for solutions with only one adsorbate. 15 variables were identified and ranked, in order of decreasing relevance and impact on the pesticide adsorption, by Gram-Schmidt orthogonalization. A static feed-forward ANN was used with the next input variables: micropore volume (%), mesopore volume (cm^3/g), solubility (g/L), molecular weight (g/mol), initial concentration (mg/L), initial total organic carbon, flow velocity (m/h), time (min), Freundlich constants K ($(mg/g)(L/mg)^{1/n}$), and $1/n$ and elimination of natural organic matter (%). Also, a recurrent ANN was used with the next inputs: solubility (g/L), molecular weight (g/mol), initial concentration (mg/L), initial total organic carbon, secondary micropore volume (%), $(C/C_0)_{(k-1)T}$, isotherm constants like K ($(mg/g)(L/mg)^{1/n}$) and $1/n$. In both models, the output variable was C/C_0. 9749 data were employed and distributed in 67% for training and model selection and 33% for the final testing. ANN provided reliable predictions with $R^2 > 0.981$ and a root mean square error < 0.035. However, the recurrent ANN outperformed

Table 3: Summary of the ANN modeling of the adsorption of water pollutants at dynamic operating conditions.

Adsorbent	Adsorbate	ANN model	Experiment	Data used (Training-Testing-Validation)	Input variables	Output variables	Pollutant removal	Reference
Bone char	Naproxen	Feed forward back propagation algorithm (2-10-1)	Fixed-bed	98-21-21	C_0, m, t	Ct/C_0	3.2 mg/g	[36]
Bone char	Acid blue 25, acid blue 74, reactive blue 4	Feed forward network back propagation (5-10-3)	Kinetic, equilibrium and fixed-bed	70-15-15	C_0, pH, t, ratio M/W, T	Adsorption capacity and Ct/C_0	AB25 34.91 mg/g, AB74 32.17 mg/g, RB4 27.98 mg/g	[38]
Montmorillonite–iron oxide composite	Cs^{1+} and Sr^{2+}	Hybrid Freundlich isotherm-ANN Levenberg-Marquardt back propagation (4-25-1)	Fixed-bed	80-0-20	C_0, t, Db, F	Ct	~ 20 mg/L	[42]
Date palm biochar	Ortho-cresol and phenol	Feed forward and nonlinear regression generalized decay-function	Fixed-bed	–	C_0, F, Db, m, t	Residual concentration	–	[49]
Activated carbon, Amberlite XAD-2	Rhamnolipid	Back propagation (4-6-1)	Fixed-bed	66.7-0-33.3	F, Db, C_0, t	Ct/C_0	–	[50]
Macroporous resins	Solanesol	Feed forward back propagation with gradient descent	Fixed-bed	331-148-0	C_0, F, t, Ratio of Height/Diameter, bed void volume fraction, particle void volume fraction, Ps, BET area	Ct	110 mg/mL	[55]
Bone char	Fluoride	Hybrid model based on Thomas equation and feed forward ANN (3-18-18-1)	Fixed-bed	192-96-96	C_0, m, t	Ct/C_0	2.52 mg/g	[57]
Pseudomonas aeruginosa immobilized in polyacrylamide gel	La, Eu and Yb	Multi-Layer perceptron (6-3-1)	Fixed-bed	392 data	C_0, Db, superficial liquid velocity based on empty column, Reynolds number	Ct/C_0	190 μmol/g	[169]
Brown seaweed Ecklonia biomass	Cr^{6+}	Feed-forward back-propagation (6-5-3-1)	Fixed-bed	127 data	C_0, m, pH, Db, F, T	Ct	50.2 mg/g	[170]
Eucalyptus camaldulensis barks	Basic blue 41, reactive black 5	Multi-Layer Perceptron (3-5-1)	Fixed-bed	–	Volume of water, Db, C_0	Ct/C_0	BB 41 162.2 mg/g, RB5 4.8 mg/g	[172]
Posidonia oceanica (L.) Biomass	Methylene blue	Multi-Layer feed forward (3-15-1)	Fixed-bed	608-304-304	F, Db, t	Ct/C_0	482.6 mg/g	[173]
Hydrated ferric oxide-based nanocomposite	Phosphate	Three-layer feed-forward back-propagation (4-(6-20)-1)	Equilibrium and fixed-bed	75-25-0	Batch: pH, C_0, T, m, Dynamic: pH, C_0, T, F, Db	Removal efficiency, Ct	99.50%	[174]
Activated carbon			Fixed-bed	106-20-20	Db, F, C_0, T	Ct/C_0	–	[175]

Table 3: Continued.

Adsorbent	Adsorbate	ANN model	Experiment	Data used (Training-Testing-Validation)	Input variables	Output variables	Pollutant removal	Reference
	Phenol, 2-chlorophenol, 4-nitrophenol	Multi-layered feed forward back propagation						
Aluminum-doped bone char	Fluoride	Feed forward back propagation (3-2-1)	Fixed-bed	474-237-237	F, C_0, t	Ct/C_0	18.5 mg/g	[176]
Nanofibers, rice polish, living bacillus, walnut husk, black cumin, oleifera seed, hyacinth root, flax meal and rice straw	As^{3+}, Pb^{2+}, Cu^{2+}, Red G	Feed-forward back propagation perceptron (5-(6-16)-1)	Fixed-bed	215-0-47	Ratio of the contact time to the maximum time, BET area, rotation of packing, ratio of inertia to viscosity, mass ratio of pollutants to packing per unit volume	Normalized adsorption capacity	–	[179]
Pongamia	Zn^{2+}	Multilayer perceptron Levenberg Marquardt back propagation (3-7-1)	RSM (CCD)	60-20-20	pH, C_0, T, m, F, Db	Removal percentage	66.29 mg/g	[180]
Jackfruit, mango and rubber leaves	Cd^{2+}	Hybrid artificial neural network–genetic algorithm	Fixed-bed	70-20-10	C_0, F, Db, t	Removal percentage	98.26%	[181]
Activated carbon from leaves of Calotropis Gigantea	Methylene blue	ANFIS	Fixed-bed	40-20-0	C_0, Db, pH, F, T	Removal percentage	–	[182]
Sodium dodecyl sulfate modified graphene	Cu^{2+}, Mn^{2+}	Artificial neural network (3-5-1)	Fixed-bed	–	T, pH, m, C_0	Removal efficiency	Cu^{2+} 48.83 mg/g, Mn^{2+} 45.62 mg/g	[183]
Activated carbon	Phenol, toluene, benzene, caffeine, ciprofloxacin, flumequine, diclofenac	Feed forward back propagation (8-45-1)	Fixed-bed	4761-595-595	Molar weight, C_0, F, Db, Ps, surface area, pore diameter, t	Ct/C_0	–	[184]
NaOH-modified rice husk	Methylene blue	Feed forward back propagation (3-13-1)	Fixed-bed	50-25-25	F, Db, t	Ct	101.32 mg/g	[209]
Silver nanoparticles	Methylene blue	Hybrid artificial neural network–particle swarm optimization (6-14-1)	Fixed-bed	75-13-12	pH, m, sample flow, sample volume, eluent volume and eluent flow	Removal percentage	99.40%	[211]
Light expanded clay aggregate (LECA)	Aniline	Feed forward back propagation (3-(2-7)-(2-5)-2)	Fixed-bed	298-0-122	t, F, influent chemical oxygen demand	Reactor efficiency, Ct	90%	[292]
Shells of sunflower	Cu^{2+}	Multi-layered neural network back propagation (7:7-5-1:1)	Fixed-bed	162-81-81	t, C_0, m, pH, F, Db, Ps	Ct/C_0	25.95 mg/g	[293]
	Crystal violet		Fixed-bed	50-25-25	F, Db, t	Ct	77.18 mg/g	[294]

Table 3: Continued.

Adsorbent	Adsorbate	ANN model	Experiment	Data used (Training-Testing-Validation)	Input variables	Output variables	Pollutant removal	Reference
Citric-acid-modified rice straw		Feed forward back propagation (3-17-1)						
Zinc oxide nanoparticles–chitosan	Methyl orange	Cuckoo Search–ANN Levenberg–Marquardt (5-11-1)	Fixed-bed	29-0-12	pH, volume of elution solvent, m, F, elution solvent	Removal percentage	481 mg/g	[295]
Alginate-based composite	Ni^{2+}	Three-layered feed-forward (4-10-2)	Dynamic	22-5-5	C_0, m, t, pH	Adsorption capacity and Removal percentage	248.7 mg/g	[296]
Hyacinth root	Pb^{2+}	Multi-layer perceptron with Levenberg–Marquardt back-propagation (4-(2-20)-1)	Fixed-bed	534 data	F, Db, t	Ct	10.94 mg/g	[297]
Hydrous ferric oxide	Fluoride	Hybrid model based on Thomas equation - ANN	Fixed-bed	–	C_0, m, t	Ct/C_0	6.71 mg/g	[298]
Shells of sunflower	Co^{2+}	Multi-layered feed forward back propagation (7-5-1)	Fixed-bed	147-74-74	C_0, t, m, pH, F, Db, Ps	Ct/C_0	11.68 mg/g	[299]
Silica-molecular imprinting	Cholesterol	Feed forward back-propagation Levenberg-Marquardt	Fixed-bed	50-25-25	Db, t, F	Removal efficiency	67.80%	[300]
Bacillus subtilis beads	Cd^{2+}	Two layer feed forward back propagation combined with the Thomas and Yan models (6-(2-22)-1)	Fixed-bed	273-59-59	C_0, t, Db, m, column internal diameter of column	Ct/C_0	104.2 mg/g	[301]
Activated carbon	Dyes	Feed forward back propagation (4-(9-12-8)-1)	Fixed-bed	156-0-52	High gravity factor, liquid Reynolds number, adsorption time to the maximum adsorption time and packing density to liquid concentration	Normalized adsorption capacity	–	[302]
Ignimbrite	Fe^{3+}	Multi-layered back propagation (6-4-1)	Fixed-bed	293-147-147	C_0, t, m, pH, F, Db, Ps	Ct/C_0	3.65 mg/g	[303]
Spherical nanoscale zerovalent iron on cellulose	Phosphate	Multilayer perceptron back propagation	Fixed-bed	–	C_0, pH, t, T	Removal percentage	561.mg/g	[304]
Olive stone, pinion shell	Cu^{2+}	ANN -Fuzzy Inference System	Fixed-bed	–	F, C0, Db, t	Ct/C_0	Olive stone 5.06 mg/g, pinion shell 7.14 mg/g	[305]

Nomenclature: central composite design (CCD), depth of bed (Db), flow rate (F), inlet concentration (C_0), mass of bed (m), outlet concentration (Ct), and response surface methodology (RSM).

Table 4: Summary of the ANN modeling of the multicomponent adsorption of water pollutants at dynamic operating conditions.

Adsorbent	Adsorbate	ANN model	Experiment	Data used (Training-Testing-Validation)	Input variables	Output variables	Pollutants removal	Reference
Biochar	Cd^{2+}, Ni^{2+}, Zn^{2+}, Cu^{2+}	Feed forward back propagation, feed forward back propagation with distributed time delay, Cascade forward, Elman	Fixed-bed	994-213-213	C_0, t	Ct/C_0	Cd^{2+} 5.17 mmol/g, Ni^{2+} 2.01 mmol/g, Zn^{2+} 4.38 mmol/g, Cu^{2+} 5.40 mmol/g	[41]
Date palm biochar	Ortho-cresol and phenol	Feed-forward and nonlinear regression generalized decay-function	Fixed-bed column	–	C_0, F, Db, m, t	Residual concentration	–	[49]
Chitosan/zeolite	Bisphenol A, carbamazepine, ketoprofen, tonalide	Three-layer feed-forward Levenberg Marquardt (2-4-1)	Fixed-bed, RSM (CCD)	60-20-20	C_0, pH	Adsorption capacity	Bisphenol A 37.11 mg/g, carbamazepine 41.24 mg/g, ketoprofen 5.92 mg/g, tonalide 3.61 mg/g	[77]
Activated carbon	Pesticides	Static and recurrent neural network (13-6-1), (8-3-1)	Fixed-bed	6044-0-3705	Solubility, molecular weight, C_0, initial total organic carbon, Freundlich parameters, secondary micropore volume, C/Co at time $(k\text{-}1)_T$	Normalized concentration C/C_0 at time k_T.	160 mg/g	[171]
Bone char	Cu^{2+}, Zn^{2+}	Feed-forward network and backpropagation algorithm	Fixed-bed	504-108-108 single, 1008-216-216 binary	Metal properties (molecular weight, electronegativity and ionic radius), C_0, F, Db, t	Ct/C_0	Cu^{2+} 51.8 mg/g, Zn^{2+} 41.1 mg/g	[177]
Bone char	Cd^{2+}, Ni^{2+}, Zn^{2+}	Fuzzy ANN	Fixed-bed	70-15-15	C_0, hydration energy, electronegativity, hydrated ionic radii, molecular weight	Ct/C_0	–	[178]
Rice bran	As^{3+}, As^{5+}	Multi-layer feed-forward back-propagation, Levenberg-Marquardt back-propagation (4-7-5-1), (3-5-7-1)	Equilibrium and fixed-bed, RSM /CCD)	41-0-10	Batch: pH, C_0, T, m; Dynamic: Db, F, C_0	Adsorption capacity	As^{3+} 41.55 μg/g, A^{5+} 45.60 μg/g	[306]
Anion base resin	Residual color in palm oil mill effluent	Wavelet ANN (3-6-1)	Fixed-bed	70 data	pH, F, Db	Residual color was the experimental response	4.63 mg/g	[307]

Nomenclature: central composite design (CCD), depth of bed (Db), flow rate (F), inlet concentration (C_0), mass of bed (m), outlet concentration (Ct), and response surface methodology (RSM).

the static ANN particularly for the breakthrough and saturation zones. Note that this behavior was expected since the dynamic character of the adsorption process was considered in the recurrent ANN. Operating conditions and pesticide properties exhibited a significant impact on this adsorption process according to both ANN models, while the adsorbent properties showed a low impact on the pesticide removal.

Balci et al. [172] used the bed depth service time model and multilayer ANN for the correlation of breakthrough curves of the adsorption of reactive black 5 and basic blue 41 on *Eucalyptus camaldulensis* barks. The input variables were the volume of water treated (0.04–32.4 L), bed depth (5–20 cm), and dye concentration (100-400 mg/L), while the output variable was the final concentration of treated water (mg/L). These authors proposed a multilayer perceptron ANN with 3-5-1 architecture to model this adsorption process. This ANN was able to fit the adsorption data showing low modeling errors. They concluded that ANN was effective in the modeling, prediction, and estimation of adsorption processes.

Cavas et al. [173] applied the Thomas equation and ANN for modeling the breakthrough curves of methylene blue adsorption via *Posidonia oceanica* dead leaves. These authors used a multilayer feed-forward ANN with LM algorithm. Data modeling was performed considering the next input variables: bed height (3–9 cm), flow rate (3.64–7.28 mL/min), and time (min), while the effluent methylene blue concentration was the output. 1215 experimental data were used to train and test the performance of ANN with a hyperbolic tangent sigmoid activation function. Results showed that this ANN outperformed Thomas equation with $R^2 = 0.998$ and a mean square error lower than 0.001453.

Tovar-Gómez et al. [57] applied a hybrid neural network model and conventional adsorption models to predict the breakthrough curves of fluoride adsorption on two commercial bone chars. This study introduced the development of a hybrid approach based on ANN to improve the prediction of breakthrough curves with traditional adsorption equations. In particular, ANN was used to estimate the parameters of Thomas equation, and these estimated parameters were used to calculate the corresponding concentration profiles of asymmetric breakthrough curves. Input data for the hybrid ANN were the feed fluoride concentration (9–40 mg/L), column operating time (12.7-178.0 h), and feed flow rate (0.198–0.396 L/h). The output variable was the ratio C/C_0 for fluoride adsorption. All experimental data of two bone chars (186 and 198 for these bone chars) were used for training (75%) and 25% remaining data for verification and testing. A feed-forward ANN with two hidden layers with 18 neurons was chosen. This study utilized the classical BP algorithm for ANN training and the sigmoid activation function. This hybrid Thomas-ANN model outperformed the traditional Thomas equation showing the lowest mean square error thus reflecting its better accuracy for correlating and predicting the fluoride adsorption breakthrough curves. This study opened the possibilities of improving the performance of traditional breakthrough equations via their hybridization with ANN.

A comparison between hybrid Freundlich and wave propagation model with ANN was carried out to simulate the breakthrough curves of cesium and strontium on montmorillonite-iron oxide composite [42]. For ANN modeling, the input variables were the column operating time (min), feed concentration (2–50 mg/L), bed height (5–15 cm), and feed flow rate (0.5–8 mL/min), while the output variable was the outlet concentration. LM algorithm was applied in ANN training. ANN showed root mean square error values of 0.321–0.561 with $R = 0.99$ for the modeling of breakthrough curves of cesium and strontium adsorption.

A three-layer feed-forward BP-ANN was applied to model the adsorption of phosphate by hydrated ferric oxide-based nanocomposite in a fixed bed column [174]. ANN with tangent sigmoid and linear activation functions was able to predict the performance of this adsorption system. Input variables were pH (3–9), sulfate concentration (0.42–1.68 mM), phosphate (0.042–0.084 mM), and temperature (15–35 °C). Removal efficiency (%) was the output variable. A feed-forward BP-ANN with 3 layers, 20 neurons, quasi-Newton training algorithm, and logistic sigmoid activation function was utilized. Overall, this surrogate model was suitable to predict the breakthrough curves, but it failed to follow the trend of some experimental data. The authors concluded that high-quality experimental data were required to obtain reliable predictions of dynamic adsorption systems. However, the characteristics of the studied breakthrough curves were well described by this ANN ($R^2 = 0.9931$).

Masomi et al. [175] studied the dynamic adsorption of 4-nitrophenol, 2-chlorophenol, and phenol using activated carbon obtained from pulp and paper mill sludge where ANN was also applied to model this removal process. The experimental variables were bed height (2, 4, and 6 cm equivalent to 0.1, 0.2, and 0.3 g of activated carbon), feed flow rate (2, 3.5, and 5 mL/min), feed concentration (50–400 mg/L), and temperature (20, 3,5 and 50 °C). C/C_0 from the breakthrough curves was the output variable for ANN. An architecture with several hidden layers and neurons was employed. 106 data were utilized for training, 20 for testing, and 20 for validation. The authors concluded that the use of ANN satisfactorily predicted the dynamic adsorption of phenol compounds.

Rojas-Mayorga et al. [176] performed a comparative study of the prediction of asymmetric breakthrough curves of fluoride adsorption on a modified bone char. The traditional models of Yan and Thomas, mass transfer model, and ANN were assessed. ANN input variables were the operating time (8–24 h), fluoride feed concentration (10–100 mg/L), and flow rate (0.18–0.36 L/h), while the output variable was the ratio of C/C_0 for fluoride removal. 948 experimental data were divided in 50, 25, and 25% for training, validation, and testing. Modeling results showed that ANN outperformed other models to predict these breakthrough curves. In fact, the model performance was ANN > mass transfer model > Thomas and Yan equations.
Due to the asymmetry of fluoride breakthrough curves, the Thomas and Yan equations showed the worst fitting. In fact, the main advantage of ANN relied on its capabilities

to model asymmetric breakthrough curves that commonly occur during water treatment.

Reynel-Avila et al. [38] applied an ANN model to analyze and characterize the adsorption of anionic dyes (i.e., reactive blue 4, acid blue 74, and acid blue 25) using fixed-bed columns packed with bone char. ANN modeling was performed considered dye feed concentration (50–300 mg/L), column operating time (2-448 min), molecular weight of the dye (g/mol), adsorption temperature (30–40 °C), and dye molecular dimensions (X = length, Y = width, Z = depth, Å) as the input neurons. Output neuron was associated to the profile C/C_0 of the breakthrough curves. Adsorption experimental data and BP algorithm were used for training (70%), validation (15%), and testing (15%). Experimental results indicated that the maximum adsorption capacities of bone char were 34.91, 32.2, and 27.9 mg/g for acid blue 25, acid blue 74, and reactive blue 4 molecules, respectively. ANN was reliable to correlate the adsorption profile of packed bed columns with $R^2 > 0.99$. In particular, the molecular dimensions of dyes were relevant in the dynamic adsorption with this adsorbent.

A stratified adsorption column packed with bone char was used for the binary adsorption of cadmium and zinc where the data modeling was performed with ANN [177]. Results showed that the use of this adsorber configuration reduced the antagonistic effects present in binary metallic systems and outperformed the conventional fixed-bed columns. A feed-forward BP-ANN was applied to model the binary breakthrough adsorption curves. Input variables were the molecular weight (g/mol), electronegativity and hydrated ionic radius (Å) of heavy metals, feed concentration of both adsorbates (100-200 mg/L), feed flow rate (4-6 mL/min), stratified bed length (5–15 g), and the column operating time (0-750 min), while the profiles C/C_0 for both metals were the output variables. ANN was able to fit the highly asymmetric behavior of cadmium and zinc breakthrough curves. These authors indicated that the breakthrough zone was challenging due to ANN showed the highest modeling errors. This study highlighted a limitation of ANN to model asymmetric breakthrough curves in multicomponent adsorption systems.

Gordillo et al. [178] reported the study of dynamic fuzzy ANN for the simulation of a fixed bed adsorption of zinc, nickel, and cadmium on bone char in single and bimetallic systems. Experimental dynamic adsorption studies were performed at pH 5 and 30 °C with feed concentrations of 2–60 mg/L in single and binary systems. Breakthrough curves were employed to calculate several parameters of fixed-bed columns. The modeling of concentration profiles via ANN considered the next input variables: initial feed concentration, hydration energy, electronegativity, hydrated ionic radii, and molecular weight of tested metals besides the column operating time. The output variables were the ratios C/C_0 for both metals. 3 hidden layers were employed in the ANN architecture where 70% of experimental data were utilized for training, 15% for validation, and 15% for testing. Results of this study indicated that this ANN was effective to represent the main characteristics and behavior of the breakthrough curves in the heavy metal adsorption in single and binary systems with antagonistic adsorption.

Liu et al. [179] performed the ANN modeling of a collection of experimental data reported in the literature for the adsorption of copper, chromium, and methylene blue on different waste residues (i.e., rice husk, tamarind fruit shell, and catla fish scales) using a rotating packed bed. Cascade-forward BP-ANN, Elman BP-ANN, and feed-forward BP-ANN were employed in this study. Experimental data were divided in 82 and 18% for training and testing, respectively. The input variables were the Reynolds number, ratio of contact time to maximum contact time, average high gravity factor, ratio of particle size to bed height, and ratio of feed concentration to packing density. The ratio of adsorption capacity at given time to the maximum adsorption capacity was the output variable. Tangent hyperbolic sigmoid function and a topology with 5 neurons in the hidden layer were utilized. Feed-forward BP-ANN showed the highest R^2 values and better accuracy followed by Cascade-forward BP-ANN and Elman BP-ANN.

Moreno-Pérez et al. [41] analyzed and discussed the capabilities and limitations of feed-forward BP-ANN, feed-forward BP-ANN with distributed time delay, cascade forward ANN, and Elman ANN for the modeling of multicomponent adsorption of heavy metals on bone char. The dynamic adsorption of these heavy metals generated asymmetric breakthrough curves, which were difficult to model with traditional adsorption equations. Twenty breakthrough curves were obtained for the adsorption of zinc, nickel, copper, and cadmium and their combinations in multimetallic solutions. Initial concentration of column feed (0.52–0.85 mmol/L) and column operating time (0–8 h) was the input variables, while the concentration profiles C/C_0 were the output variable. 1420 experimental data were divided into 70, 15, and 15% for training, validation, and testing of these ANN models. LM, Bayesian regularization, and scaled conjugate gradient were used and assessed as training algorithms. Experimental results showed that the highest adsorption capacities were obtained for copper in single and multicomponent solutions, which were 2.15-5.14 mmol/g. An antagonistic adsorption was identified in the solutions containing two or more heavy metals, which competed for the binding sites of the adsorbent surface. ANN performance depended on the hidden layers and their neurons, activation function, and training algorithm. Cascade forward ANN outperformed the other tested ANN models. Note that feed-forward BP-ANN is the most used ANN in adsorption literature but it could fail in the modeling of high asymmetric breakthrough curves of both single and multicomponent systems.

Shanmugaprakash et al. [180] developed an ANN model and optimized the zinc adsorption using Pongamia oil cake in both batch and dynamic systems. CCD was employed to improve both batch (31 experiments) and dynamic adsorption (20 experiments). A multilayer ANN with a topology of 3-7-1 and tangent sigmoid and linear activation functions was used. LM algorithm was the training method. For the column modeling, the input variables were the feed flow rate (5–15 mL/min), feed concentration (50–500 mg/L), and bed height (4–12 cm), while the output variable was the adsorption capacity (13.58–66.29 mg/g). This adsorbent had an

adsorption capacity of 66.29 mg/g, and ANN outperformed RSM modeling with R values of 0.99 and 0.84, respectively.

Cadmium adsorption on green adsorbents (i.e., jackfruit, mango and rubber leaves) in a down-flow fixed-bed columns was studied by Nag et al. [181]. They used a hybrid model ANN-genetic algorithm for the simulation and optimization of this adsorption process where the influence of bed height, flow rate, and initial concentration was determined. ANN model used the type of adsorbent, bed height (3–9 cm), feed flow rate (10–25 mL/min), column operating time (5–600 min), and feed concentration (20–80 mg/L) as input variables. Cadmium percentage removal (6–99.95%) was the output variable. 556 experimental data were divided in 70, 20, and 10% for training, validation, and testing, respectively. ANN modeling was done with the hyperbolic tangent activation function. Cadmium adsorption capacities followed the next trend: jackfruit > mango > rubber. The adsorption of this metal depended on the operating parameters thus achieving a maximum removal of 98.26% at optimized conditions. This ANN model showed $R^2 \geq 0.997$.

Vakili et al. [77] applied ANN to model the removal of organic micro-pollutants (tonalide, ketoprofen, carbamazepine, and bisphenol) with fixed-bed columns packed with chitosan/zeolite. 30 experiments from CCD were employed to optimize the removal of these pollutants. A three-layer feed-forward ANN with 2-4-1 topology was used where the input variables were pH (4–8) and adsorbate concentration (0.5–2 mg/L), and the removal percentage (47.3–96.1%) was the output variable. LM algorithm was used for ANN training with several activation function as linear, hyperbolic tangent, and logistic sigmoid. This ANN showed a high accuracy with $R^2 = 0.993 - 0.999$ indicating that it can be used to optimize the adsorption process of organic micropollutants.

Anbazhagan et al. [182] analyzed the application of ANFIS and ANN for the methylene blue adsorption using activated carbon from leaves of Calotropis Gigantea (CGLAC) in a fixed–bed column. Different experimental conditions were tested including the initial concentration of methylene blue (100–500 mg/L), bed height (1-2 cm), solution pH (2-10), flow rate (3.5-6.5 mL), and temperature (303-333 K). These operating conditions were also used as inputs in the ANN analysis, while the methylene blue removal was the output variable. 60 experimental data were used for ANN where 40 were employed for training and 20 for prediction. Bed Depth Service Time, Yoon-Nelson, Wolbroska, Adams-Bohar,t and Thomas models were also employed to model this adsorption column. Results showed that ANN was effective to predict the adsorption of methylene blue in dynamic operating conditions.

Yusuf et al. [183] predicted the copper and manganese adsorption on surfactant decorated graphene packed in a down-flow bed column using ANN. Breakthrough curves were determined to identify the saturation time and bed adsorption capacity. The optimum adsorption capacities were 48.83 and 45.62 mg/g for copper and manganese, respectively, at bed height of 3 cm. A multilayer feed-forward ANN with hyperbolic tangent sigmoid function and a quick propagation algorithm were used. ANN model with 4-5-1 topology obtained $R^2 > 0.996$ for both heavy metals where the input variables were the adsorbent dosage (0.01–0.1 g), initial concentration (25–250 mg/L), temperature (25–50 °C), and pH (2–5), and the output variable was the heavy metal removal percentage.

ANN modeling of the adsorption of phenolic compounds on activated date palm biochar in a down-flow fixed-bed column was studied by Dalhat et al. [49]. Breakthrough curves at several operating conditions were determined and modeled with ANN and nonlinear regression generalized decay function model. A two-layer feed-forward ANN was used with next input data: bed height (10–40 cm), adsorbent mass (21.8–87.0 g), feed initial concentration (10–100 mg/L), feed flow rate (5–30 mL/min), and column operating time (0–720 min). Output data were the final effluent concentration or the ratio C/C_0. Adsorption data was divided in 70% for training, 15% for validation, and 15% for testing. LM algorithm was used for ANN training with hyperbolic tangent sigmoid activation function. Adsorption capacities were 560.55 and 647.28 mg/g for orto-cresol and phenol, respectively. ANN outperformed the nonlinear regression model to fit the dynamic adsorption data. The use of final effluent concentration as output variable offered better adjustments that those with C/C_0. Sensitivity analysis revealed that column operating time and feed initial concentration were the most relevant parameters for the adsorption of these pollutants.

Finally, the modeling of simultaneous dynamic adsorption of organic pollutants (e.g., phenol, toluene, benzene, caffeine, ciprofloxacin, flumequine, and diclofenac) on activated carbon was carried out with ANN [184]. A set of 15 systems with 5951 data collected from published papers were used to build the ANN model where the input variables were the molar mass (78.11-361.37 g/mol), initial concentration (0.00019-500 mg/L), feed flow rate (0.05-456.62 mL/min), bed height (2-200 cm), adsorbent particle diameter (0.1-2.4 mm), specific surface area (678-2869 m^2/g), average pore diameter (1.29-3015 nm), and operating time (0-57170 min), while the ratio C/C_0 was the output variable. ANN was implemented using BP algorithm for learning with logistic sigmoid and hyperbolic tangent sigmoid as activation functions for hidden and output layers, respectively. The data were divided into 80% for learning, 10% for testing, and 10% for validation. ANN architecture was 8-45-1. Modeling results demonstrated the applicability of ANN to predict these dynamic adsorption systems with $R = 0.997$, root mean square error of 0.029, and absolute deviation of 1.81%. The sensitive analysis showed that all variables impacted the system performance where the flow rate and specific surface area were the most relevant.

4. Remarks on the Application of ANN for a Reliable Adsorption Modeling

This literature review indicates that the application of ANN for the modeling and correlation of adsorption data has been successfully adopted as an alternative approach to overcome the limitations of traditional models. Unfortunately, it has been identified that several published papers contain common mistakes related to the ANN implementation thus

affecting the quality and reliability of developed models and the corresponding conclusions obtained from them in the adsorption modeling.

First, the output variables used in ANN modeling must be intensive variables especially for multicomponent adsorption systems. Several studies have reported the ANN training with removal percentages or final adsorbate concentrations as the output variables especially in batch adsorption systems. They are extensive variables whose values are directly related to the adsorbent amount and, consequently, the ANN-based models can learn incorrectly the system performance thus providing wrong estimations. In particular, Mendoza-Castillo et al. [28] have demonstrated that the use of extensive variables in the ANN modeling of binary, ternary, and quaternary antagonistic adsorption of heavy metal ions generated inaccurate estimations of the adsorption isotherms where a desorption process was erroneously predicted. It is convenient to indicate that the selection of proper output variables for ANN training will be more relevant for systems with multiple adsorbates that could display simultaneously different multicomponent adsorption behaviors. One example is the simultaneous adsorption of heavy metals and acid dyes where this system has the presence of both synergistic and antagonistic adsorption. Overall, the adsorption capacities should be the output variable used in the ANN modeling especially for real fluids (e.g., industrial effluents and groundwater) where several adsorbates could interact with the adsorbent utilized as separation medium.

After defining the ANN architecture (i.e., the number of neurons and layers), ANN training should be performed to determine the corresponding model parameters. This training relies on the resolution of a parameter estimation problem that is characterized by the presence of multiple solutions (i.e., a global optimization problem should be resolved). Training methods used in ANN-based adsorption modeling are commonly based on the application of local optimization methods, which are effective to find a set of the ANN parameters but their numerical performance is strongly related to the initial estimates, and there is no guarantee to find the global optimal solution that corresponds to the best data modeling. Under this scenario, the ANN parameters obtained with conventional training methods generally correspond to a local optimum of the objective function used. The identification of the ANN parameters via the traditional training algorithms (e.g., LM method) should imply several calculations with different initial estimates to identify the best solution based on results from proper statistical metrics. Therefore, ANN training should be recognized as a global optimization problem that requires reliable optimizers for its resolution. Stochastic global optimization methods like differential evolution, particle swarm optimization, genetic algorithm, and other recent metaheuristics are an alternative to solve the parameter identification of ANN training. Some studies on adsorption research have applied these optimizers as already discussed in Section 3 of this review. However, it is important to remark that the ANN training based on these optimizers will imply a significant increment on the computer time of the adsorption data modeling.

Another common failure identified in several adsorption studies is the ANN training with a limited number of experimental data. Overall, the increment of hidden layers and their neurons will improve the ANN performance thus reducing the modeling errors and increasing the determination coefficient (R^2). But the number of ANN parameters to be determined on the model training should be significantly lower than the number of available experimental data with the aim of obtaining a reliable ANN model from a statistical point of view. With this in mind, the verification of ANN overtraining is a relevant issue that should be also analyzed in adsorption modeling. This step is usually not considered in the papers reported on the ANN-based adsorption modeling. As a general rule, the authors should select the ANN architecture with the least number of parameters that offered the best data fitting and modeling errors. These remarks also apply for hybrid models obtained from the combination of adsorption equations and ANN.

5. Conclusions

Artificial neural networks have proved to be a useful numerical approach to develop new models for the adsorption analysis. Several studies have demonstrated that ANN-based models can outperform the traditional equations for the correlation and prediction of isotherms, kinetics, and, in less extent, breakthrough curves. ANN-based models have been widely applied in the analysis and modeling of adsorption systems with one water pollutant. There are few studies on the multicomponent adsorption modeling with ANN, which are mainly related to the removal of heavy metals, dyes, and other few organic pollutants. Therefore, the application of ANN-based models in the analysis and simulation of multicomponent adsorption systems is an interesting topic to be studied and analyzed in forthcoming papers. Also, the studies related to the modeling of dynamic adsorption systems involving several adsorbates should be increased to complement the characterization of the capabilities and limitations of ANN in this configuration mode, which is fundamental for industrial and real-life applications. Literature review also indicated that several authors have reported the utilization of ANN with extensive variables (e.g., removal percentages or final adsorbate concentrations) as the output variables thus generating models that could predict wrongly the performance of adsorption system under analysis. ANN training with intensive adsorption variables is fundamental and mandatory to obtain reliable model for the process design of fluids with multiple adsorbates. The overtraining and the application of global optimization methods in the training stage are key issues to be analyzed and resolved during the adsorption data modeling via ANN. Data sets with a suitable amount of experimental information of adsorption systems are also required to obtain reliable ANN models from a statistical perspective. In this context, it is convenient to remark that the main drawback of ANN-based models relies on their limitation to provide a theoretical understanding of the physical and chemical phenomena present to the systems to be modeled. These models are considered as black-box and empirical

approaches that are effective for both data correlation and prediction and, consequently, they can be employed as surrogate model when the theoretical models are not proper to simulate the adsorption system at hand. The hybridization of ANN with theoretical-based adsorption equations is an option to face this drawback and to develop advanced models. Overall, this artificial intelligence tool has a significant potential to overcome the limitations of traditional adsorption models for real fluids where several adsorbates are present thus causing different removal behaviors.

Data Availability

Data of this paper are available on request to the corresponding author.

Conflicts of Interest

The authors declared no potential conflicts of interest with respect to the research, authorship, and/or publication of this article.

References

[1] A. H. Khan, H. A. Aziz, N. A. Khan et al., "Impact, disease outbreak and the eco-hazards associated with pharmaceutical residues: a critical review," *International Journal of Environmental Science and Technology*, vol. 19, no. 1, pp. 677–688, 2022.

[2] M. A. Mazhar, N. A. Khan, A. H. Khan et al., "Upgrading combined anaerobic-aerobic UASB-FPU to UASB-DHS system: cost comparison and performance perspective for developing countries," *Journal of Cleaner Production*, vol. 284, article 124723, 2021.

[3] G. Crini, "Kinetic and equilibrium studies on the removal of cationic dyes from aqueous solution by adsorption onto a cyclodextrin polymer," *Dyes and Pigments*, vol. 77, no. 2, pp. 415–426, 2008.

[4] E. A. Dil, M. Ghaedi, A. M. Ghaedi et al., "Modeling of quaternary dyes adsorption onto ZnO-NR-AC artificial neural network: Analysis by derivative spectrophotometry," *Journal of Industrial and Engineering Chemistry*, vol. 34, pp. 186–197, 2016.

[5] M. Tanzifi, M. T. Yaraki, M. Karami et al., "Modelling of dye adsorption from aqueous solution on polyaniline/carboxymethyl cellulose/TiO_2 nanocomposites," *Journal of Colloid and Interface Science*, vol. 519, pp. 154–173, 2018.

[6] A. Takdastan, S. Samarbaf, Y. Tahmasebi, N. Alavi, and A. A. Babaei, "Alkali modified oak waste residues as a cost-effective adsorbent for enhanced removal of cadmium from water: Isotherm, kinetic, thermodynamic and artificial neural network modeling," *Journal of Industrial and Engineering Chemistry*, vol. 78, pp. 352–363, 2019.

[7] P. S. Pauletto, J. O. Gonçalves, L. A. A. Pinto, G. L. Dotto, and N. P. G. Salau, "Single and competitive dye adsorption onto chitosan-based hybrid hydrogels using artificial neural network modeling," *Journal of Colloid and Interface Science*, vol. 560, pp. 722–729, 2020.

[8] H. Esfandian, A. Samadi-Maybodi, M. Parvini, and B. Khoshandam, "Development of a novel method for the removal of diazinon pesticide from aqueous solution and modeling by artificial neural networks (ANN)," *Journal of Industrial and Engineering Chemistry*, vol. 35, pp. 295–308, 2016.

[9] M. Ashrafi, M. A. Chamjangali, G. Bagherian, and N. Goudarzi, "Application of linear and non-linear methods for modeling removal efficiency of textile dyes from aqueous solutions using magnetic Fe_3O_4 impregnated onto walnut shell," *Spectrochimica Acta Part A: Molecular and Biomolecular Spectroscopy*, vol. 171, pp. 268–279, 2017.

[10] A. Dashti, F. Amirkhani, M. Jokar, A. H. Mohammadi, and K. W. Chau, "Insights into the estimation of heavy metals ions sorption from aqueous environment onto natural zeolite," *International Journal of Environmental Science and Technology*, vol. 18, pp. 1773–1784, 2020.

[11] A. Mojiri, A. Ohashi, N. Ozaki, Y. Aoi, and T. Kindaichi, "Integrated anammox-biochar in synthetic wastewater treatment: performance and optimization by artificial neural network," *Journal of Cleaner Production*, vol. 243, article 118638, 2020.

[12] J. Baruah, C. Chaliha, B. K. Nath, and E. Kalita, "Enhancing arsenic sequestration on ameliorated waste molasses nanoadsorbents using response surface methodology and machine-learning frameworks," *Environmental Science and Pollution Research*, vol. 28, no. 9, pp. 11369–11383, 2021.

[13] Z. Cigeroglu, G. Kucukyildiz, B. Erim, and E. Alp, "Easy preparation of magnetic nanoparticles-rGO-chitosan composite beads: Optimization study on cefixime removal based on RSM and ANN by using Genetic Algorithm Approach," *Journal of Molecular Structure*, vol. 1224, article 129182, 2021.

[14] D. Ghadirimoghaddam, M. Gheibi, and M. Eftekhari, "Graphene oxide-cyanuric acid nanocomposite as a novel adsorbent for highly efficient solid phase extraction of Pb^{2+} followed by electrothermal atomic absorption spectrometry; statistical, soft computing and mechanistic efforts," *International Journal of Environmental Analytical Chemistry*, vol. 1, pp. 1–22, 2021.

[15] Y. Hou, J. M. Qi, J. W. Hu, W. Q. Ruan, Y. Q. Xiang, and X. H. Wei, "Decolorizing brilliant green by mesoporous Pd-Fe magnetic nanoparticles immobilized on reduced graphene oxide: artificial neural network modeling," *International Journal of Environmental Science and Technology*, vol. 1, 2021.

[16] H. A. Isiyaka, K. Jumbri, N. S. Sambudi et al., "Experimental and modeling of dicamba adsorption in aqueous medium using MIL-101(Cr) metal-organic framework," *Processes*, vol. 9, no. 3, p. 419, 2021.

[17] L. Liu, N. Che, S. Wang, Y. Liu, and C. Li, "Copper nanoparticle loading and F doping of graphene aerogel enhance its adsorption of aqueous perfluorooctanoic acid," *ACS Omega*, vol. 6, no. 10, pp. 7073–7085, 2021.

[18] S. Mukherjee, B. Kamila, S. Paul, B. Hazra, S. Chowdhury, and G. Halder, "Optimizing fluoride uptake influencing parameters of paper industry waste derived activated carbon," *Microchemical Journal*, vol. 160, article 105643, 2021.

[19] P. Ziarati, P. Kozub, S. Vambol et al., "Kinetics of Cd, Co and Ni adsorption from wastewater using red and black tea leaf blend as a bio-adsorbent," *Ecological Questions*, vol. 32, pp. 59–70, 2020.

[20] A. H. Khan, H. A. Aziz, N. A. Khan et al., "Pharmacueticals of emerging concern in hospital wastewater: removal of ibuprofen and ofloxacin drugs using MBBR method," *International Journal of Environmental Analytical Chemistry*, 2021.

[21] S. Afshin, Y. Rashtbari, M. Vosough et al., "Application of Box-Behnken design for optimizing parameters of hexavalent chromium removal from aqueous solutions using Fe_3O_4 loaded on activated carbon prepared from alga: Kinetics and equilibrium study," *Journal of Water Process Engineering*, vol. 42, article 102113, 2021.

[22] F. A. Tapouk, R. Nabizadeh, S. Nasseri et al., "Embedding of L-arginine into graphene oxide (GO) for endotoxin removal from water: modeling and optimization approach," *Colloids and Surfaces A: Phyisicochemical and Engineering Aspects*, vol. 607, article 125491, 2020.

[23] L. Lv, Y. Zhang, K. Wang, A. K. Ray, and X. S. Zhao, "Modeling of the adsorption breakthrough behaviors of Pb^{2+} in a fixed bed of ETS-10 adsorbent," *Journal of Colloid and Interface Science*, vol. 325, no. 1, pp. 57–63, 2008.

[24] V. C. Taty-Costodes, H. Fauduet, C. Porte, and Y. S. Ho, "Removal of lead (II) ions from synthetic and real effluents using immobilized _Pinus sylvestris_ sawdust: Adsorption on a fixed-bed column," *Journal of Hazardous Materials*, vol. 123, no. 1-3, pp. 135–144, 2005.

[25] M. C. Ramirez, M. Pereira da Silva, S. G. L. Ferreira, and O. E. Vasco, "Mathematical models applied to the Cr(III) and Cr(VI) breakthrough curves," *Journal of Hazardous Materials*, vol. 146, no. 1-2, pp. 86–90, 2007.

[26] A. A. Babaei, A. Khataee, E. Ahmadpour, M. Sheydaei, B. Kakavandi, and Z. Alaee, "Optimization of cationic dye adsorption on activated spent tea: equilibrium, kinetics, thermodynamic and artificial neural network modeling," *Korean Journal of Chemical Engineering*, vol. 33, no. 4, pp. 1352–1361, 2016.

[27] P. S. Pauletto, G. L. Dotto, and N. P. Salau, "Optimal artificial neural network design for simultaneous modeling of multicomponent adsorption," *Journal of Molecular Liquids*, vol. 320, 2020.

[28] D. I. Mendoza-Castillo, H. E. Reynel-Ávila, F. J. SÁnchez-Ruiz, R. Trejo-Valencia, J. E. Jaime-Leal, and A. Bonilla-Petriciolet, "Insights and pitfalls of artificial neural network modeling of competitive multi-metallic adsorption data," *Journal of Molecular Liquids*, vol. 251, pp. 15–27, 2018.

[29] A. Gopinath, B. G. Retnam, A. Muthukkumaran, and K. Aravamudan, "Swift, versatile and a rigorous kinetic model based artificial neural network surrogate for single and multicomponent batch adsorption processes," *Journal of Molecular Liquids*, vol. 297, article 111888, 2020.

[30] P. S. Pauletto, S. F. Lütke, G. L. Dotto, and N. P. Salau, "Forecasting the multicomponent adsorption of nimesulide and paracetamol through artificial neural network," *Chemical Engineering Journal*, vol. 412, article 127527, 2021.

[31] K. Koopal, W. Tan, and M. Avena, "Equilibrium mono- and multicomponent adsorption models: from homogeneous ideal to heterogeneous non-ideal binding," *Advances in Colloid and Interface Science*, vol. 280, article 102138, 2020.

[32] E. D. Revellame, D. L. Fortela, W. Sharp, R. Hernandez, and M. E. Zappi, "Adsorption kinetic modeling using pseudo-first order and pseudo-second order rate laws: a review," *Cleaner Engineering and Technology*, vol. 1, article 100032, 2020.

[33] T. Liu, Y. Lawluvy, Y. Shi et al., "Adsorption of Cadmium and Lead from Aqueous Solution Using Modified Biochar: A Review," *Journal of Environmental Chemical Engineering*, vol. 10, no. 1, article 106502, 2022.

[34] M. Majd, V. Kordzadeh-Kermani, V. Ghalandari, A. Askari, and M. Sillanpaa, "Adsorption Isotherm Models: A Comprehensive and Systematic Review (2010-2020)," *Science of Total Environment*, vol. 10, no. 1, article 106502, 2021.

[35] X. Luo, Z. Zhang, P. Zhou, Y. Liu, G. Ma, and Z. Lei, "Synergic adsorption of acid blue 80 and heavy metal ions (Cu^{2+}/Ni^{2+}) onto activated carbon and its mechanisms," *Journal of Industrial and Engineering Chemistry*, vol. 27, pp. 164–174, 2015.

[36] H. E. Reynel-Avila, D. I. Mendoza-Castillo, A. Bonilla-Petriciolet, and J. Silvestre-Albero, "Assessment of naproxen adsorption on bone char in aqueous solutions using batch and fixed-bed processes," *Journal of Molecular Liquids*, vol. 209, pp. 187–195, 2015.

[37] M. A. Martín-Lara, G. Blázquez, M. Calero, A. I. Almendros, and A. Ronda, "Binary biosorption of copper and lead onto pine cone shell in batch reactors and in fixed bed columns," *International Journal of Mineral Processing*, vol. 148, pp. 72–82, 2016.

[38] H. E. Reynel-Avila, D. I. Mendoza-Castillo, and A. Bonilla-Petriciolet, "Relevance of anionic dye properties on water decolorization performance using bone char: Adsorption kinetics, isotherms and breakthrough curves," *Journal of Molecular Liquids*, vol. 219, pp. 425–434, 2016.

[39] N. P. Jovic-Jovicic, A. D. Milutinovic-Nikolic, M. J. Zunic et al., "Synergic adsorption of Pb^{2+} and reactive dye – RB5 on two series of organomodified bentonites," *Journal of Contaminant Hydrology*, vol. 150, pp. 1–11, 2013.

[40] H. E. Reynel-Avila, D. I. Mendoza-Castillo, A. A. Olumide, and A. Bonilla-Petriciolet, "A survey of multi-component sorption models for the competitive removal of heavy metal ions using bush mango and flamboyant biomasses," *Journal of Molecular Liquids*, vol. 224, pp. 1041–1054, 2016.

[41] J. Moreno-Pérez, A. Bonilla-Petriciolet, D. I. Mendoza-Castillo, H. E. Reynel-Ávila, Y. Verde-Gómez, and R. Trejo-Valencia, "Artificial neural network-based surrogate modeling of multi-component dynamic adsorption of heavy metals with a biochar," *Journal of Environmental Chemical Engineering*, vol. 6, no. 4, pp. 5389–5400, 2018.

[42] A. Ararem, A. Bouzidi, B. Mohamedi, and O. Bouras, "Modeling of fixed-bed adsorption of Cs^{+} and Sr^{2+} onto clay-iron oxide composite using artificial neural network and constant-pattern wave approach," *Journal of Radioanalytical and Nuclear Chemistry*, vol. 301, no. 3, pp. 881–887, 2014.

[43] N. Zeinali, M. Ghaedi, and G. Shafie, "Competitive adsorption of methylene blue and brilliant green onto graphite oxide nano particle following: derivative spectrophotometric and principal component-artificial neural network model methods for their simultaneous determination," *Journal of Industrial and Engineering Chemistry*, vol. 20, no. 5, pp. 3550–3558, 2014.

[44] K. Aghajani and H. A. Tayebi, "Adaptive neuro-fuzzy inference system analysis on adsorption studies of reactive red 198 from aqueous solution by SBA-15/CTAB composite," *Spectrochimica Acta Part A: Molecular and Biomolecular Spectroscopy*, vol. 171, pp. 439–448, 2017.

[45] H. Askari, M. Ghaedi, K. Dashtian, and M. H. Azghandi, "Rapid and high-capacity ultrasonic assisted adsorption of ternary toxic anionic dyes onto MOF-5-activated carbon: artificial neural networks, partial least squares, desirability function and isotherm and kinetic study," *Ultrasonics Sonochemistry*, vol. 37, pp. 71–82, 2017.

[46] N. M. Mahmoodi, M. Mohsen Taghizadeh, and A. Taghizadeh, "Mesoporous activated carbons of low-cost agricultural bio-wastes with high adsorption capacity: preparation and artificial neural network modeling of dye removal from single and multicomponent (binary and ternary) systems," *Journal of Molecular Liquids*, vol. 269, pp. 217–228, 2018.

[47] I. C. Afolabi, S. I. Popoola, and O. S. Bello, "Modeling pseudo-second-order kinetics of orange peel-paracetamol adsorption process using artificial neural network," *Chemometrics and Intelligent Laboratory Systems*, vol. 203, article 104053, 2020.

[48] W. Kaminski, K. Kusmierek, and A. Swiatkowski, "Sorption equilibrium prediction of competitive adsorption of herbicides 2, 4-D and MCPA from aqueous solution on activated carbon using ANN," *Adsorption*, vol. 20, no. 7, pp. 899–904, 2014.

[49] M. A. Dalhat, N. D. Mu'azu, and M. H. Essa, "Generalized decay and artificial neural network models for fixed-bed phenolic compounds adsorption onto activated date palm biochar," *Journal of Environmental Chemical Engineering*, vol. 9, no. 1, article 104711, 2021.

[50] C. E. A. Padilha, C. A. A. Padilha, D. F. S. Souza, J. A. Oliveira, G. R. Macedo, and E. S. Santos, "Prediction of rhamnolipid breakthrough curves on activated carbon and amberlite XAD-2 using artificial neural network and group method data handling models," *Journal of Molecular Liquids*, vol. 206, pp. 293–299, 2015.

[51] D. M. Himmelblau, "Accounts of experiences in the application of artificial neural networks in chemical engineering," *Industrial & Engineering Chemistry Research*, vol. 47, no. 16, pp. 5782–5796, 2008.

[52] T. Zarra, M. G. Galang Jr., F. Ballesteros, V. Belgiornoa, and N. V. Vincenzo, "Environmental odour management by artificial neural network - A review," *Environment International*, vol. 133, article 105189, Part B, 2019.

[53] P. Sihag, M. R. Sadikhani, V. Vambol, S. Vambol, A. K. Prabhakar, and N. Sharma, "Comparative study for deriving stage-discharge-sediment concentration relationships using soft computing techniques," *Journal of Achievements in Materials and Manufacturing Engineering*, vol. 2, no. 104, pp. 57–76, 2021.

[54] S. Golbaz, R. Nabizadeh, M. Rafiee, and M. Yousefi, "Comparative study of RSM and ANN for multiple target optimization in coagulation/precipitation process of contaminated waters: mechanism and theory," *International Journal of Environmental Analytical Chemistry*, vol. 1, 2020.

[55] X. Du, Q. Yuan, J. Zhao, and Y. Li, "Comparison of general rate model with a new model–artificial neural network model in describing chromatographic kinetics of solanesol adsorption in packed column by macroporous resins," *Journal of Chromatography*, vol. 1145, no. 1-2, pp. 165–174, 2007.

[56] H. Karimi and F. Yousefi, "Correlation of vapour liquid equilibria of binary mixtures using artificial neural networks," *Chinese Journal of Chemical Engineering*, vol. 15, no. 5, pp. 765–771, 2007.

[57] R. Tovar-Gómez, M. R. Moreno-Virgen, J. A. Dena-Aguilar, V. Hernández-Montoya, A. Bonilla-Petriciolet, and M. A. Montes-Morán, "Modeling of fixed-bed adsorption of fluoride on bone char using a hybrid neural network approach," *Chemical Engineering Journal*, vol. 228, pp. 1098–1109, 2013.

[58] M. Tanzifi, M. T. Yaraki, A. D. Kiadehi et al., "Adsorption of amido black 10B from aqueous solution using polyaniline/SiO_2 nanocomposite: experimental investigation and artificial neural network modeling," *Journal of Colloid and Interface Science*, vol. 510, pp. 246–261, 2018.

[59] S. M. Asl, M. Ahmadi, M. Ghiasvand, A. Tardast, and R. Kata, "Artificial neural network (ANN) approach for modeling of Cr(VI) adsorption from aqueous solution by zeolite prepared from raw fly ash (ZFA)," *Journal of Industrial and Engineering Chemistry*, vol. 19, no. 3, pp. 1044–1055, 2013.

[60] V. Brocardo de León, B. A. Ferraz, C. Z. Brusamarello, G. Petroli, M. Domenico, and F. Batista, "Artificial neural network for prediction of color adsorption from an industrial textile effluent using modified sugarcane bagasse: characterization, kinetics and isotherm studies," *Environmental Nanotechnology, Monitoring & Management*, vol. 14, article 100387, 2020.

[61] K. R. Raj, A. Kardam, J. K. Arora, and S. Srivastava, "An application of ANN modeling on the biosorption of arsenic," *Waste and Biomass Valorization*, vol. 4, no. 2, pp. 401–407, 2013.

[62] H. E. Reynel-Avila, A. Bonilla-Petriciolet, and G. de la Rosa, "Analysis and modeling of multicomponent sorption of heavy metals on chicken feathers using Taguchi's experimental designs and artificial neural networks," *Desalination and Water Treatment*, vol. 55, no. 7, pp. 1885–1899, 2015.

[63] J. J. Hopfield, "Artificial neural networks," *Circuits and Devices Magazine, IEEE*, vol. 4, no. 5, pp. 3–10, 1988.

[64] B. Yegnanarayana, *Artificial neural networks*, vol. 476, PHI Learning Pvt. Ltd, 2009.

[65] P. J. Drew and J. R. Monson, "Artificial neural networks," *Surgery*, vol. 127, no. 1, pp. 3–11, 2000.

[66] A. Abraham, "Artificial Neural Networks," in *Handbook of measuring system design*, John Wiley and Sons, 2005.

[67] K. S. Narendra and K. Parthasarathy, "Identification and control of dynamical systems using neural networks," *IEEE Transactions on Neural Networks*, vol. 1, no. 1, pp. 4–27, 1990.

[68] K. Mäkisara, O. Simulates, J. Kangas, and T. Kohonen, *Artificial Neural Networks*, vol. 2, Elsevier, 2014.

[69] M. Gupta, L. Jin, and N. Homma, *Static and Dynamic Neural Networks: From Fundamentals to Advanced Theory*, vol. 752, John Wiley & Sons, 2004.

[70] Y. M. Chiang, L. C. Chang, and F. J. Chang, "Comparison of static-feedforward and dynamic-feedback neural networks for rainfall-runoff modeling," *Journal of Hydrology*, vol. 290, no. 3-4, pp. 297–311, 2004.

[71] B. A. Pearlmutter, "Learning state space trajectories in recurrent neural networks," *Neural Computation*, vol. 1, no. 2, pp. 263–269, 1989.

[72] W. T. Miller, P. J. Werbos, and R. S. Sutton, *Neural Networks for Control*, vol. 525, MIT Press, 1995.

[73] I. A. Basheer and M. Hajmeer, "Artificial neural networks: fundamentals, computing, design, and application," *Journal of Microbiological Methods*, vol. 43, no. 1, pp. 3–31, 2000.

[74] J. Ye, X. Cong, P. Zhang et al., "Operational parameter impact and back propagation artificial neural network modeling for phosphate adsorption onto acid-activated neutralized red mud," *Journal of Molecular Liquids*, vol. 216, pp. 35–41, 2016.

[75] M. Tanzifi, S. H. Hosseini, A. D. Kiadehi et al., "Artificial neural network optimization for methyl orange adsorption onto

polyaniline nano-adsorbent: Kinetic, isotherm and thermodynamic studies," *Journal of Molecular Liquids*, vol. 244, pp. 189–200, 2017.

[76] M. K. Uddin, R. A. K. Rao, and K. V. Mouli, "The artificial neural network and box-behnken design for Cu^{2+} removal by the pottery sludge from water samples: equilibrium, kinetic and thermodynamic studies," *Journal of Molecular Liquids*, vol. 266, pp. 617–627, 2018.

[77] M. Vakili, A. Mojiri, T. Kindaichi et al., "Cross-linked chitosan/zeolite as a fixed-bed column for organic micropollutants removal from aqueous solution, optimization with RSM and artificial neural network," *Journal of Environmental Management*, vol. 250, article 109434, 2019.

[78] N. Messikh, N. Bougdah, S. Bousba, and F. Djazi, "Modeling the adsorption of chlorobenzene on modified bentonite using an artificial neural network," *Current Research in Green and Sustainable Chemistry*, vol. 3, article 100026, 2020.

[79] A. Samadi-Maybodi and M. Nikou, "Removal of sarafloxacin from aqueous solution by a magnetized metal-organic framework; artificial neural network modeling," *Polyhedron*, vol. 179, article 114342, 2020.

[80] Z. U. Zango, A. Ramli, K. Jumbri et al., "Optimization studies and artificial neural network modeling for pyrene adsorption onto UiO-66(Zr) and NH_2-UiO-66(Zr) metal organic frameworks," *Polyhedron*, vol. 192, article 114857, 2020.

[81] A. N. Kolmogorov, "The representation of continuous functions of many variables by superposition of continuous functions of one variable and addition," in *Akademii Doklady Akademii Nauk SSSR*, vol. 114, pp. 953–956, Russian Academy of Sciences, 1957.

[82] R. Hecht-Nielsen, "Theory of the backpropagation neural network," in *Neural Networks, 1989. IJCNN*, pp. 593–605, International Joint Conference on IEEE, 1989.

[83] K. Hornik, M. Stinchcombe, and H. White, "Multilayer feedforward networks are universal approximators," *Neural networks*, vol. 2, no. 5, pp. 359–366, 1989.

[84] R. Hecht-Nielsen, *Neurocomputing*, vol. 433, Addison-Wesley, 1990.

[85] A. M. Chen and R. Hecht-Nielsen, "On the geometry of as a feedforward/feedback controller neural network weight spaces," in *Artificial Neural Networks*, pp. 1–4, Second International Conference, 1991.

[86] T. Kohonen, "Self-organized formation of topologically correct feature maps," *Biological Cybernetics*, vol. 43, no. 1, pp. 59–69, 1982.

[87] K. Mehrotra, C. K. Mohan, and S. Ranka, *Elements of Artificial Neural Networks*, MIT Press, Cambridge, MA, 1997.

[88] G. Cybenko, "Approximation by superpositions of a sigmoidal function," *Mathematics of Control Signals and Systems*, vol. 2, no. 4, pp. 303–314, 1989.

[89] S. Hashem, "Sensitivity analysis for feedforward artificial neural networks with differentiable activation functions," *International Joint Conference on Neural Networks*, vol. 1, pp. 419–424, 1992.

[90] W. Shen, X. Guo, C. Wu, and D. Wu, "Forecasting stock indices using radial basis function neural networks optimized by artificial fish swarm algorithm," *Knowledge-Based Systems*, vol. 24, no. 3, pp. 378–385, 2011.

[91] R. Rojas, *Neural networks: a systematic introduction*, vol. 502, Springer Science & Business Media, 2013.

[92] J. Leonard and M. A. Kramer, "Improvement of the backpropagation algorithm for training neural networks," *Computers & Chemical Engineering*, vol. 14, pp. 337–341, 1990.

[93] H. White, *Artificial neural networks: approximation and learning theory*, vol. 320, Blackwell Publishers, Inc, 1992.

[94] A. T. C. Goh, "Back-propagation neural networks for modeling complex systems," *Artificial Intelligence in Engineering*, vol. 9, no. 3, pp. 143–151, 1995.

[95] S. S. Haykin, *Neural networks and learning machines*, vol. 3, Pearson Education, Upper Saddle River, 2009.

[96] Y. Yang, G. Wang, B. Wang et al., "Biosorption of Acid Black 172 and Congo Red from aqueous solution by nonviable _Penicillium_ YW 01: Kinetic study, equilibrium isotherm and artificial neural network modeling," *Bioresource Technology*, vol. 102, no. 2, pp. 828–834, 2011.

[97] H. Y. Chong, H. J. Yap, S. C. Tan, K. S. Yap, and S. Y. Wong, "Advances of metaheuristic algorithms in training neural networks for industrial applications," *Soft Computing*, vol. 25, no. 16, pp. 11209–11233, 2021.

[98] A. Poznyak, I. Chairez, and T. Poznyak, "A survey on artificial neural networks application for identification and control in environmental engineering: biological and chemical systems with uncertain models," *Annual Reviews in Control*, vol. 48, pp. 250–272, 2019.

[99] G. Alam, I. Ihsanullah, M. Naushad, and M. Sillampaa, "Applications of artificial intelligence in water treatment for optimization and automation of adsorption processes: recent advances and prospects," *Chemical Engineering Journal*, vol. 427, article 130011, 2022.

[100] S. A. Aani, T. Bonny, S. W. Hasan, and N. Hilal, "Can machine language and artificial intelligence revolutionize process automation for water treatment and desalination?," *Desalination*, vol. 458, pp. 84–96, 2019.

[101] Z. Ye, J. Yang, N. Zhong, X. Tu, J. Jia, and J. Wang, "Tackling environmental challenges in pollution controls using artificial intelligence: a review," *Science of the Total Environment*, vol. 699, article 134279, 2020.

[102] B. Pomeroy, M. Grile, and B. Likozar, "Artificial neural networks for bio-based chemical production or biorefining: a review," *Renewable and Sustainable Energy Reviews*, vol. 153, article 111748, 2022.

[103] B. Noroozi and G. A. Sorial, "Applicable models for multicomponent adsorption of dyes: a review," *Journal of Environmental Sciences*, vol. 25, no. 3, pp. 419–429, 2013.

[104] S. V. Manjunath, R. Baghel, and M. Kumar, "Antagonistic and synergistic analysis of antibiotic adsorption on Prosopis juliflora activated carbon in multicomponent systems," *Chemical Engineering Journal*, vol. 381, article 122713, 2020.

[105] B. G. Saucedo-Delgado, D. A. De Haro-Del Rio, L. M. GonzÁlez-Rodríguez et al., "Fluoride adsorption from aqueous solution using a protonated clinoptilolite and its modeling with artificial neural network-based equations," *Journal of Fluorine Chemistry*, vol. 204, pp. 98–106, 2017.

[106] J. A. Rodríguez-Romero, D. I. Mendoza-Castillo, H. E. Reynel-Avila et al., "Preparation of a new adsorbent for the removal of arsenic and its simulation with artificial neural network-based adsorption models," *Journal of Environmental Chemical Engineering*, vol. 8, no. 4, article 103928, 2020.

[107] C. Brasquet and P. Le Cloirec, "QSAR for organics adsorption onto activated carbon in water: what about the use of neural

networks?," *Water Research*, vol. 33, no. 17, pp. 3603–3608, 1999.

[108] C. Brasquet and P. Le Cloirec, "Effects of activated carbon cloth surface on organic adsorption in aqueous solutions: use of statistical methods to describe mechanisms," *Langmuir*, vol. 15, no. 18, pp. 5906–5912, 1999.

[109] D. J. Blum, I. H. Suffet, and J. P. Duguet, "Quantitative structure-activity relationship using molecular connectivity for the activated carbon adsorption of organic chemicals in water," *Water Research*, vol. 28, no. 3, pp. 687–699, 1994.

[110] K. H. Chu and E. Y. Kim, "Predictive modeling of competitive biosorption equilibrium data," *Biotechnology and Bioprocess Engineering*, vol. 11, no. 1, pp. 67–71, 2006.

[111] F. Pagnanelli, M. Trifoni, F. Beolchini, A. Exposito, L. Toro, and F. Veglio, "Equilibrium biosorption studies in single and multi-metal systems," *Process Biochemistry*, vol. 37, no. 2, pp. 115–124, 2001.

[112] T. N. Singh, V. K. Singh, and S. Sinha, "Prediction of cadmium removal using an artificial neural network and a neuro-fuzzy technique," *Mine Water and the Environment*, vol. 25, no. 4, pp. 214–219, 2006.

[113] S. Aber, N. Daneshvar, S. M. Soroureddin, A. Chabok, and K. Asadpour-Zeynali, "Study of acid orange 7 removal from aqueous solutions by powdered activated carbon and modeling of experimental results by artificial neural network," *Desalination*, vol. 211, no. 1-3, pp. 87–95, 2007.

[114] K. Yetilmezsoy and S. Demirel, "Artificial neural network (ANN) approach for modeling of Pb(II) adsorption from aqueous solution by Antep pistachio (_Pistacia Vera_ L.) shells," *Journal of Hazardous Materials*, vol. 153, no. 3, pp. 1288–1300, 2008.

[115] K. V. Kumar and K. Porkodi, "Modelling the solid-liquid adsorption processes using artificial neural networks trained by pseudo second order kinetics," *Chemical Engineering Journal*, vol. 148, no. 1, pp. 20–25, 2009.

[116] M. T. Garza-González, M. M. Alcalá-Rodríguez, R. Pérez-Elizondo et al., "Artificial neural network for predicting biosorption of methylene blue by Spirulina sp," *Water Science & Technology*, vol. 63, no. 5, pp. 977–983, 2011.

[117] F. Geyikçim, E. Kılıç, S. Çoruh, and S. Elevli, "Modelling of lead adsorption from industrial sludge leachate on red mud by using RSM and ANN," *Chemical Engineering Journal*, vol. 183, pp. 53–59, 2012.

[118] F. Masood, M. Ahmad, M. A. Ansari, and A. Malik, "Prediction of biosorption of total chromium by Bacillus sp. using artificial neural network," *Bulletin of Environmental Contamination and Toxicology*, vol. 88, no. 4, pp. 563–570, 2012.

[119] I. M. Savic, S. T. Stojiljkovic, I. M. Savic, S. B. Stojanovic, and K. Moder, "Modeling and optimization of Fe(III) adsorption from water using bentonite clay: comparison of central composite design and artificial neural network," *Chemical Engineering & Technology*, vol. 35, no. 11, pp. 2007–2014, 2012.

[120] M. Khajeh and S. Hezaryan, "Combination of ACO-artificial neural network method for modeling of manganese and cobalt extraction onto nanometer SiO_2 from water samples," *Journal of Industrial and Engineering Chemistry*, vol. 19, no. 6, pp. 2100–2107, 2013.

[121] D. Bingöl, M. Inal, and S. Çetintaş, "Evaluation of copper biosorption onto date palm (*Phoenix* dactyliferaL.) seeds with MLR and ANFIS models," *Industrial & Engineering Chemistry Research*, vol. 52, no. 12, pp. 4429–4435, 2013.

[122] A. Çelekli, H. Bozkurt, and F. Geyik, "Use of artificial neural networks and genetic algorithms for prediction of sorption of an azo-metal complex dye onto lentil Straw," *Bioresource Technology*, vol. 129, pp. 396–401, 2013.

[123] R. Nia, M. Ghaedi, and A. M. Ghaedi, "Modeling of reactive orange 12 (RO 12) adsorption onto gold nanoparticle- activated carbon using artificial neural network optimization based on an imperialist competitive algorithm," *Journal of Molecular Liquids*, vol. 195, pp. 219–229, 2014.

[124] S. Çoruh, F. Geyikçi, E. Kılıç, and U. Çoruh, "The use of NARX neural network for modeling of adsorption of zinc ions using activated almond shell as a potential biosorbent," *Bioresource Technology*, vol. 151, pp. 406–410, 2014.

[125] D. I. Mendoza-Castillo, N. Villalobos-Ortega, A. Bonilla-Petriciolet, and J. C. Tapia-Picazo, "Neural network modeling of heavy metal sorption on lignocellulosic biomasses: effect of metallic ion properties and sorbent characteristics," *Industrial & Engineering Chemistry Research*, vol. 54, pp. 443–453, 2015.

[126] A. Asfaram, M. Ghaedi, S. Hajati, and A. Goudarzi, "Ternary adsorption onto MnO_2 nanoparticle-loaded activated carbon: derivative spectrophotometry and modeling," *RSC Advances*, vol. 88, pp. 72300–72320, 2015.

[127] S. Bhattacharyya, S. Bhattacharjee, and N. K. Mondal, "A quantum backpropagation multilayer perceptron (QBMLP) for predicting iron adsorption capacity of calcareous soil from aqueous solution," *Applied Soft Computing*, vol. 27, pp. 299–312, 2015.

[128] N. Darajeh, H. R. Masoumi, K. Kalantari et al., "Optimization of process parameters for rapid adsorption of Pb(II), Ni(II), and Cu(II) by magnetic/talc nanocomposite using wavelet neural network," *Research on Chemical Intermediates*, vol. 42, no. 3, pp. 1977–1987, 2016.

[129] M. Nasr, A. D. Mahmoud, M. Fawzy, and A. Radwan, "Artificial intelligence modeling of cadmium(II) biosorption using rice straw," *Applied Water Science*, vol. 7, no. 2, pp. 823–831, 2017.

[130] A. Asfaram, M. Ghaedi, S. Hajati, and A. Goudarzi, "Synthesis of magnetic γ-Fe_2O_3-based nanomaterial for ultrasonic assisted dyes adsorption: Modeling and optimization," *Ultrasonics Sonochemistry*, vol. 32, pp. 418–431, 2016.

[131] M. Fawzy, M. Nasr, S. Adel, H. Nagy, and S. Helmi, "Environmental approach and artificial intelligence for Ni(II) and Cd(II) biosorption from aqueous solution using *Typha domingensis* biomass," *Ecological Engineering*, vol. 95, pp. 743–752, 2016.

[132] A. M. Ghaedi, M. Ghaedi, A. R. Pouranfard et al., "Adsorption of triamterene on multi-walled and single-walled carbon nanotubes: artificial neural network modeling and genetic algorithm optimization," *Journal of Molecular Liquids*, vol. 216, pp. 654–665, 2016.

[133] R. Gomez-Gonzalez, F. J. Cerino-Córdova, A. M. Garcia-León, E. Soto-Regalado, N. E. Davila-Guzman, and J. J. Salazar-Rabago, "Lead biosorption onto coffee grounds: comparative analysis of several optimization techniques using equilibrium adsorption models and ANN," *Journal of the Taiwan Institute of Chemical Engineers*, vol. 68, pp. 201–210, 2016.

[134] D. Podstawczyk and A. Witek-Krowiak, "Novel nanoparticles modified composite eco-adsorbents–A deep insight into kinetics modelling using numerical surface diffusion and artificial neural network models," *Chemical engineering research and design*, vol. 109, pp. 1–17, 2016.

[135] M. H. Ahmadi, M. Ghaedi, F. Yousefi, and M. Jamshidi, "Application of random forest, radial basis function neural networks and central composite design for modeling and/or optimization of the ultrasonic assisted adsorption of brilliant green on ZnS-NP-AC," *Journal of Colloid and Interface Science*, vol. 505, pp. 278–292, 2017.

[136] A. Asfaram, M. Ghaedi, M. H. Azqhandi, A. Goudarzi, and S. Hajati, "Ultrasound-assisted binary adsorption of dyes onto CuS/ZnS- NC-AC as a novel adsorbent: Application of chemometrics for optimization and modeling," *Journal of Industrial and Engineering Chemistry*, vol. 54, pp. 377–388, 2017.

[137] M. Dastkhoon, M. Ghaedi, A. Asfaram, M. H. Azqhandi, and M. K. Purkait, "Simultaneous removal of dyes onto nanowires adsorbent use of ultrasound assisted adsorption to clean waste water: chemometrics for modeling and optimization, multicomponent adsorption and kinetic study," *Chemical Engineering Research and Design*, vol. 124, pp. 222–237, 2017.

[138] N. Parveen, S. Zaidi, and M. Danish, "Development of SVR-based model and comparative analysis with MLR and ANN models for predicting the sorption capacity of Cr(VI)," *Process Safety and Environmental Protection*, vol. 107, pp. 428–437, 2017.

[139] S. Yildiz, "Artificial neural network (ANN) approach for modeling Zn(II) adsorption in batch process," *Korean Journal of Chemical Engineering*, vol. 34, no. 9, pp. 2423–2434, 2017.

[140] S. Ghosal and A. Gupta, "Sorptive equilibrium profile of fluoride onto aluminum olivine $[(Fe_xMg_{1-x})_2SiO_4]$ composite (AOC): physicochemical insights and isotherm modeling by non-linear least squares regression and a novel neural-network-based method," *Journal of Environmental Science and Health, Part A*, vol. 53, no. 12, pp. 1102–1114, 2018.

[141] R. R. Karri and J. N. Sahu, "Modeling and optimization by particle swarm embedded neural network for adsorption of zinc (II) by palm kernel shell based activated carbon from aqueous environment," *Journal of Environmental Management*, vol. 206, pp. 178–191, 2018.

[142] P. Naderi, M. Shirani, A. Semnani, and A. Goli, "Efficient removal of crystal violet from aqueous solutions with Centaurea stem as a novel biodegradable bioadsorbent using response surface methodology and simulated annealing: Kinetic, isotherm and thermodynamic studies," *Ecotoxicology and Environmental Safety*, vol. 163, pp. 372–381, 2018.

[143] J. Pooralhossini, M. A. Zanjanchi, M. Ghaedi, A. Asfaram, and B. Azqhandi, "Statistical optimization and modeling approach for azo dye decolorization: combined effects of ultrasound waves and nanomaterial-based adsorbent," *Applied Organometallic Chemistry*, vol. 32, no. 3, p. e4205, 2018.

[144] M. Arshadi, M. K. Abdolmaleki, H. Eskandarloo, and A. Abbaspourrad, "A supported dendrimer with terminal symmetric primary amine sites for adsorption of salicylic acid," *Journal of Colloid and Interface Science*, vol. 540, pp. 501–514, 2019.

[145] M. R. Gadekar and M. M. Ahammed, "Modelling dye removal by adsorption onto water treatment residuals using combined response surface methodology-artificial neural network approach," *Journal of Environmental Management*, vol. 231, pp. 241–248, 2019.

[146] A. M. Ghaedi, S. Karamipour, A. Vafaei, M. Baneshi, and V. Kiarostami, "Optimization and modeling of simultaneous ultrasound-assisted adsorption of ternary dyes using copper oxide nanoparticles immobilized on activated carbon using response surface methodology and artificial neural network," *Ultrasonics – Sonochemistry*, vol. 51, pp. 264–280, 2019.

[147] A. Jadhav and V. C. Srivastava, "Multicomponent adsorption isotherm modeling using thermodynamically inconsistent and consistent models," *AIChE Journal*, vol. 65, no. 11, pp. 1–12, 2019.

[148] S. G. Nasab, A. Semnani, A. Teimouri, M. J. Yazd, T. M. Isfahani, and S. Habibollahi, "Decolorization of crystal violet from aqueous solutions by a novel adsorbent chitosan/nano-diopside using response surface methodology and artificial neural network-genetic algorithm," *International Journal of Biological Macromolecules*, vol. 124, pp. 429–443, 2019.

[149] K. Sharafi, M. Pirsaheb, V. Gupta et al., "Phenol adsorption on scoria stone as adsorbent - Application of response surface method and artificial neural networks," *Journal of Molecular Liquids*, vol. 274, pp. 699–714, 2019.

[150] A. Sadeghizadeh, F. Ebrahimi, M. Heydari, M. Tahmasebikohyani, F. Ebrahimi, and A. Sadeghizadeh, "Adsorptive removal of Pb (II) by means of hydroxyapatite/chitosan nanocomposite hybrid nanoadsorbent: ANFIS modeling and experimental study," *Journal of Environmental Management*, vol. 232, pp. 342–353, 2019.

[151] S. Ullah, M. Assiri, A. Al-Sehemi et al., "Characteristically insights, artificial neural network, (ANN), equilibrium, and kinetic studies of PB(II) ion adsorption on rice husks treated with nitric acid," *International Journal of Environmental Research*, vol. 14, pp. 43–60, 2020.

[152] X. Zhu, X. Wang, and Y. S. Ok, "The application of machine learning methods for prediction of metal sorption onto biochars," *Journal of Hazardous Materials*, vol. 378, article 120727, 2019.

[153] D. S. Franco, F. A. Duarte, N. P. Salau, and G. L. Dotto, "Analysis of indium (III) adsorption from leachates of LCD screens using artificial neural networks (ANN) and adaptive neuro-fuzzy inference systems (ANIFS)," *Journal of Hazardous Materials*, vol. 384, article 121137, 2020.

[154] A. K. Nayak and A. Pal, "Statistical modeling and performance evaluation of biosorptive removal of Nile blue A by lignocellulosic agricultural waste under the application of high- strength dye concentrations," *Journal of Environmental Chemical Engineering*, vol. 8, no. 2, article 103677, 2020.

[155] A. Thirunavukkarasu and R. Nithya, "Adsorption of acid orange 7 using green synthesized CaO/CeO2 composite: an insight into kinetics, equilibrium, thermodynamics, mass transfer and statistical models," *Journal of the Taiwan Institute of Chemical Engineers*, vol. 111, pp. 44–62, 2020.

[156] J. Qi, Y. Hou, J. Hu, W. Ruan, Y. Xiang, and X. Wei, "Decontamination of methylene Blue from simulated wastewater by the mesoporous rGO/Fe/Co nanohybrids: artificial intelligence modeling and optimization," *Materials Today Communications*, vol. 24, article 100709, 2020.

[157] M. S. Netto, J. S. Oliveira, N. P. G. Salau, and G. L. Dotto, "Analysis of adsorption isotherms of Ag^{+}, Co^{+2}, and Cu^{+2} onto zeolites using computational intelligence models," *Journal of Environmental Chemical Engineering*, vol. 9, no. 1, article 104960, 2021.

[158] K. Yadav and S. Jagadevan, "Influence of torrefaction and pyrolysis on engineered biochar and its applicability in defluoridation: Insight into adsorption mechanism, batch adsorber design and artificial neural network modelling,"

Journal of Analytical and Applied Pyrolysis, vol. 154, article 105015, 2021.

[159] N. Sohrabi, R. Mohammadi, H. R. Ghassemzadeh, and S. S. Seyedloo, "Equilibrium, kinetic and thermodynamic study of diazinon adsorption from water by clay/GO/Fe_3O_4: Modeling and optimization based on response surface methodology and artificial neural network," *Journal of Molecular Liquids*, vol. 328, article 115384, 2021.

[160] P. Thomas, N. P. Rumjit, C. W. Lai, and M. R. Johan, "EDTA functionalised cocoa pod carbon encapsulated SPIONs via green synthesis route to ameliorate textile dyes - Kinetics, isotherms, central composite design and artificial neural network," *Sustainable Chemistry and Pharmachy*, vol. 19, article 100349, 2021.

[161] X. Wu, J. Hu, X. Wang, L. Xin, C. Li, and X. Wei, "Effective Removal of Arsenide from Aqueous Solutions Using Mesoporous CoFe2O4/Graphene Oxide Nanocomposites Assisted by Artificial Intelligence," *Carbon Letters*, vol. 31, no. 6, pp. 1163–1178, 2021.

[162] R. Duan and C. Fedler, "Modeling phosphorus adsorption onto polyaluminium chloride water treatment residuals," *Water Supply*, vol. 21, no. 1, pp. 458–469, 2021.

[163] V. Singh, J. Singh, and V. Mishra, "Development of a cost-effective, recyclable and viable metal ion doped adsorbent for simultaneous adsorption and reduction of toxic Cr (VI) ions," *Journal of Environmental Chemical Engineering*, vol. 9, no. 2, article 105124, 2021.

[164] A. J. Veeraragavan, R. Shanmugavel, N. Abraham, D. Subramanian, and S. Pandian, "Kinetic studies validated by Artificial Neural Network simulation for the removal of dye from simulated waste water by the activated carbon produced from *Acalypha indica* leaves," *Environmental Technology & Innovation*, vol. 21, article 101244, 2021.

[165] S. Rasam, M. K. Moraveji, A. Soria-Verdugo, and A. Salimi, "Synthesis, characterization and absorbability of *Crocus sativus* petals hydrothermal carbonized hydrochar and activated hydrochar," *Chemical Engineering and Processing – Process Intensification*, vol. 159, article 108236, 2021.

[166] A. H. Alibak, M. Khodarahmi, P. Fayyazsanavi, S. M. Alizadeh, A. J. Hadi, and E. Aminzadehsarikhanbeglou, "Simulation the adsorption capacity of polyvinyl alcohol/carboxymethyl cellulose based hydrogels towards methylene blue in aqueous solutions using cascade correlation neural network (CCNN) technique," *Journal of Cleaner Production*, vol. 337, article 130509, 2022.

[167] Y. Zhao, D. Fan, Y. Li, and F. Yang, "Application of machine learning in predicting the adsorption capacity of organic compounds onto biochar and resin," *Environmental Research*, vol. 208, article 112694, 2022.

[168] K. Zeng, K. Hachem, M. Kuznetsova et al., "Molecular dynamic simulation and artificial intelligence of lead ions removal from aqueous solution using magnetic-ash-graphene oxide nanocomposite," *Journal of Molecular Liquids*, vol. 347, article 118290, 2022.

[169] A. C. Texier, Y. Andrès, C. Faur-Brasquet, and P. Le Cloirec, "Fixed-bed study for lanthanide (La, Eu, Yb) ions removal from aqueous solutions by immobilized *Pseudomonas aeruginosa*: experimental data and modelization," *Chemosphere*, vol. 47, no. 3, pp. 333–342, 2002.

[170] D. Park, Y. S. Yun, D. S. Lee, S. R. Lim, and J. M. Park, "Column study on Cr(VI)-reduction using the brown seaweed Ecklonia biomass," *Journal of Hazardous Materials*, vol. B137, pp. 1377–1384, 2006.

[171] C. Faur, A. Cougnaud, G. Dreyfus, and P. Le Cloirec, "Modelling the breakthrough of activated carbon filters by pesticides in surface waters with static and recurrent neural networks," *Chemical Engineering Journal*, vol. 145, no. 1, pp. 7–15, 2008.

[172] B. Balci, O. Keskinkan, and M. Avci, "Use of BDST and an ANN model for prediction of dye adsorption efficiency of *Eucalyptus camaldulensis* barks in fixed-bed system," *Expert Systems with Applications*, vol. 38, no. 1, pp. 949–956, 2011.

[173] L. Cavas, Z. Karabay, H. Alyuruk, H. Doğan, and G. K. Demir, "Thomas and artificial neural network models for the fixed-bed adsorption of methylene blue by a beach waste *Posidonia oceanica* (L.) dead leaves," *Chemical Engineering Journal*, vol. 171, no. 2, pp. 557–562, 2011.

[174] Y. Zhang and B. Pan, "Modeling batch and column phosphate removal by hydrated ferric oxide-based nanocomposite using response surface methodology and artificial neural network," *Chemical Engineering Journal*, vol. 249, pp. 111–120, 2014.

[175] M. Masomi, A. A. Ghoreyshi, G. D. Najafpour, and A. R. B. Mohamed, "Dynamic adsorption of phenolic compounds on activated carbon produced from pulp and paper mill sludge: experimental study and modeling by artificial neural network (ANN)," *Desalination and Water Treatment*, vol. 55, no. 6, pp. 1453–1466, 2015.

[176] C. K. Rojas-Mayorga, A. Bonilla-Petriciolet, F. J. Sánchez-Ruiz et al., "Breakthrough curve modeling of liquid-phase adsorption of fluoride ions on aluminum-doped bone char using micro-columns: effectiveness of data fitting approaches," *Journal of Molecular Liquids*, vol. 208, pp. 114–121, 2015.

[177] L. E. Hernández-Hernández, A. Bonilla-Petriciolet, D. I. Mendoza-Castillo, and H. E. Reynel-Ávila, "Antagonistic binary adsorption of heavy metals using stratified bone char columns," *Journal of Molecular Liquids*, vol. 241, pp. 334–346, 2017.

[178] F. A. Gordillo-Ruiz, F. J. Sánchez-Ruiz, D. Mendoza-Castillo, H. E. Reynel-Avila, and A. Bonilla-Petriciolet, "Dynamic fuzzy neural network for simulating the fixed-bed adsorption of cadmium, nickel and zinc on bone char," *International Journal of Environmental Science and Technology*, vol. 15, no. 5, pp. 915–926, 2018.

[179] Z. W. Liu, F. N. Liang, and Y. Z. Liu, "Artificial neural network modeling of biosorption process using agricultural wastes in a rotating packed bed," *Applied Thermal Engineering*, vol. 140, pp. 95–101, 2018.

[180] M. Shanmugaprakash, S. SVenkatachalam, K. Rajendran, and A. Pugazhendhi, "Biosorptive removal of Zn(II) ions by *Pongamia* oil cake (*Pongamia pinnata*) in batch and fixed-bed column studies using response surface methodology and artificial neural network," *Journal of Environmental Management*, vol. 227, pp. 216–228, 2018.

[181] S. Nag, N. Bar, and S. K. Das, "Sustainable bioremadiation of Cd(II) in fixed bed column using green adsorbents: application of Kinetic models and GA-ANN technique," *Environmental technology & innovation*, vol. 13, pp. 130–145, 2019.

[182] S. Anbazhagan, V. Thiruvengatam, and K. Kulanthai, "Adaptive neuro-fuzzy inference system and artificial neural network modeling for the adsorption of methylene blue by novel adsorbent in a fixed-bed column method," *Iranian*

Journal of Chemistry and Chemical Engineering, vol. 39, pp. 75–93, 2020.

[183] M. Yusuf, K. Song, and L. Li, "Fixed bed column and artificial neural network model to predict heavy metals adsorption dynamic on surfactant decorated graphene," *Colloids and Surfaces A*, vol. 585, article 124076, 2020.

[184] Y. Mesellem, A. E. H. Abdallah, M. Laidi, S. Hanini, and M. Hentabli, "Artificial neural network modelling of multi-system dynamic adsorption of organic pollutants on activated carbon," *Journal of Chemists and Chemical Engineers of Croatia*, vol. 70, no. 1-2, pp. 1–12, 2021.

[185] A. E. Dil, M. Ghaedi, A. Ghaedi, A. Asfaram, M. Jamshidi, and M. K. Purkait, "Application of artificial neural network and response surface methodology for the removal of crystal violet by zinc oxide nanorods loaded on activate carbon: kinetics and equilibrium study," *Journal of the Taiwan Institute of Chemical Engineers*, vol. 59, pp. 210–220, 2016.

[186] M. Dolatabadi, M. Mehrabpour, M. Esfandyari, H. Alidadi, and M. Davoudi, "Modeling of simultaneous adsorption of dye and metal ion by sawdust from aqueous solution using of ANN and ANFIS," *Chemometrics and Intelligent Laboratory Systems*, vol. 181, pp. 72–78, 2018.

[187] Y. Y. Yang, Z. L. Li, G. Wang, X. P. Zhao, D. E. Crowley, and Y. H. Zhao, "Computational identification and analysis of the key biosorbent characteristics for the biosorption process of reactive black 5 onto fungal biomass," *PLoS One*, vol. 7, no. 3, article e33551, 2012.

[188] L. Achenie, M. A. Butkus, D. Grasso, C. P. Schulthess, T. Morris, and J. Hyde, "A comparative study of neural network and mechanistic models for surface complexation," *Advances in Environmental Research*, vol. 5, no. 2, pp. 137–143, 2001.

[189] K. V. Kumar, K. Porkodi, R. L. A. Rondon, and F. Rocha, "Neural network modeling and simulation of the solid/liquid activated carbon adsorption process," *Industrial & Engineering Chemistry Research*, vol. 47, no. 2, pp. 486–490, 2008.

[190] N. Prakash, S. A. Manikandan, L. Govindarajan, and V. Vijayagopal, "Prediction of biosorption efficiency for the removal of copper(II) using artificial neural networks," *Journal of Hazardous Materials*, vol. 152, no. 3, pp. 1268–1275, 2008.

[191] K. P. Singh, P. Ojha, A. Malik, and G. Jain, "Partial least squares and artificial neural networks modeling for predicting chlorophenol removal from aqueous solution," *Chemometrics and Intelligent Laboratory Systems*, vol. 99, no. 2, pp. 150–160, 2009.

[192] A. R. Khataee, G. Dehghan, A. Ebadi, M. Zarei, and M. Pourhassan, "Biological treatment of a dye solution by Macroalgae *Chara* sp.: Effect of operational parameters, intermediates identification and artificial neural network modeling," *Bioresource Technology*, vol. 101, no. 7, pp. 2252–2258, 2010.

[193] A. Çelekli and F. Geyik, "Artificial neural networks (ANN) approach for modeling of removal of Lanaset Red G on *Chara contraria*," *Bioresource Technology*, vol. 102, no. 10, pp. 5634–5638, 2011.

[194] H. Eroglu, M. Aktan, and G. Akkaya, "Artifical neural network (ANN) modeling and analysis of radioactive gallium-67 adsorption from aqueous solution with waste acorns *ofQuercus ithaburensis*," *Journal of Chemical & Engineering Data*, vol. 56, no. 5, pp. 1910–1917, 2011.

[195] A. K. Giri, R. K. Patel, and S. S. Mahapatra, "Artificial neural network (ANN) approach for modelling of arsenic (III) biosorption from aqueous solution by living cells of *Bacillus cereus* biomass," *Chemical Engineering Journal*, vol. 178, pp. 15–25, 2011.

[196] A. R. Khataee, G. Dehghan, M. Zarei, E. Ebadi, and M. Pourhassan, "Neural network modeling of biotreatment of triphenylmethane dye solution by a green macroalgae," *Chemical Engineering Research and Design*, vol. 89, no. 2, pp. 172–178, 2011.

[197] A. R. Khataee, M. Zarei, G. Dehghan, E. Ebadi, and M. Pourhassan, "Biotreatment of a triphenylmethane dye solution using a Xanthophyta alga: modeling of key factors by neural network," *Journal of the Taiwan Institute of Chemical Engineers*, vol. 42, no. 3, pp. 380–386, 2011.

[198] U. Özdemir, B. Özbay, S. Veli, and S. Zor, "Modeling adsorption of sodium dodecyl benzene sulfonate (SDBS) onto polyaniline (PANI) by using multi linear regression and artificial neural networks," *Chemical Engineering Journal*, vol. 178, pp. 183–190, 2011.

[199] N. G. Turan, B. Mesci, and O. Ozgonenel, "Artificial neural network (ANN) approach for modeling Zn(II) adsorption from leachate using a new biosorbent," *Chemical Engineering Journal*, vol. 173, no. 1, pp. 98–105, 2011.

[200] J. K. Arora and S. Srivastava, "Simulation and optimization of biosorption studies for prediction of sorption efficiency of *Leucaena Leucocephala* seeds for the removal of Ni (II) from Waste Water," *Chemistry of Phytopotentials: Health, Energy and Environmental Perspectives*, vol. 53, pp. 253–257, 2012.

[201] D. Bingöl, M. Hercan, S. Elevli, and E. Kiliç, "Comparison of the results of response surface methodology and artificial neural network for the biosorption of lead using black cumin," *Bioresource Technology*, vol. 112, pp. 111–115, 2012.

[202] A. Çelekli, S. S. Birecikligil, F. Geyik, and H. Bozkurt, "Prediction of removal efficiency of Lanaset Red G on walnut husk using artificial neural network model," *Bioresource Technology*, vol. 103, no. 1, pp. 64–70, 2012.

[203] S. K. Deshmukh, "Indigo dye removal by using coconut shell adsorbent and performance evaluation by artificial neural network," *Engineering and Technology*, pp. 255–263, 2012.

[204] M. Dutta, P. Ghosh, and J. K. Basu, "Application of artificial neural network for the decolorization of direct blue 86 by using microwave assisted activated carbon," *Journal of the Taiwan Institute of Chemical Engineers*, vol. 43, no. 6, pp. 879–888, 2012.

[205] S. Elemen, E. P. Kumbasar, and S. Yapar, "Modeling the adsorption of textile dye on organoclay using an artificial neural network," *Dyes and Pigments*, vol. 95, no. 1, pp. 102–111, 2012.

[206] A. Kardam, K. R. Raj, J. K. Arora, and S. Srivastava, "Artificial neural network modeling for biosorption of Pb (II) ions on nanocellulose fibers," *BioNanoScience*, vol. 2, no. 3, pp. 153–160, 2012.

[207] A. R. Khataee, A. Movafeghi, S. Torbati, S. Y. SalehiLisar, and M. Zarei, "Phytoremediation potential of duckweed (*Lemna minor* L.) in degradation of C.I. Acid Blue 92: Artificial neural network modeling," *Ecotoxicology and Environmental Safety*, vol. 80, pp. 291–298, 2012.

[208] K. V. Shetty, L. Namitha, S. N. Rao, and M. Narayani, "Experimental investigation and artificial neural network-based modeling of batch reduction of hexavalent chromium by immobilized cells of newly isolated strain of chromium-

resistant bacteria," *Water Air & Soil Pollution*, vol. 223, no. 4, pp. 1877–1893, 2012.

[209] S. Chowdhury and P. D. Saha, "Artificial neural network (ANN) modeling of adsorption of methylene blue by NaOH-modified rice husk in a fixed-bed column system," *Environmental Science and Pollution Research*, vol. 20, no. 2, pp. 1050–1058, 2013.

[210] M. Dutta and J. K. Basu, "Application of artificial neural network for prediction of Pb(II) adsorption characteristics," *Environmental Science and Pollution Research*, vol. 20, no. 5, pp. 3322–3330, 2013.

[211] M. Khajeh, M. Kaykhaii, and A. Sharafi, "Application of PSO-artificial neural network and response surface methodology for removal of methylene blue using silver nanoparticles from water samples," *Journal of Industrial and Engineering Chemistry*, vol. 19, no. 5, pp. 1624–1630, 2013.

[212] K. R. Raj, A. Kardam, J. K. Arora, S. Srivastava, and M. M. Srivastava, "Prediction of the As(III) and As(V) abatement capacity of zea mays cob powder: ANN modelling," *National Academy Science Letters*, vol. 36, no. 1, pp. 41–47, 2013.

[213] K. R. Raj, A. Kardam, J. K. Arora, S. Srivastava, and M. M. Srivastava, "Adsorption behavior of dyes from aqueous solution using agricultural waste: modeling approach," *Clean Technologies and Environmental Policy*, vol. 15, no. 1, pp. 73–80, 2013.

[214] Z. Shahryari, A. Mohebbi, A. S. Goharrizi, and A. A. Forghani, "Application of artificial neural networks for formulation and modeling of dye adsorption onto multiwalled carbon nanotubes," *Research on Chemical Intermediates*, vol. 39, no. 8, pp. 3595–3609, 2013.

[215] M. F. Ahmad, S. Haydar, A. A. Bhatti, and A. J. Bari, "Application of artificial neural network for the prediction of biosorption capacity of immobilized *Bacillus subtilis* for the removal of cadmium ions from aqueous solution," *Biochemical Engineering Journal*, vol. 84, pp. 83–90, 2014.

[216] P. Assefi, M. Ghaedi, A. Ansari, M. H. Habibi, and M. S. Momeni, "Artificial neural network optimization for removal of hazardous dye Eosin Y from aqueous solution using Co_2O_3-NP-AC: isotherm and kinetics study," *Journal of Industrial and Engineering Chemistry*, vol. 20, no. 5, pp. 2905–2913, 2014.

[217] S. Chattoraj, N. K. Mondal, B. Das, P. Roy, and B. Sadhukhan, "Carbaryl removal from aqueous solution by *Lemna major* biomass using response surface methodology and artificial neural network," *Journal of Environmental Chemical Engineering*, vol. 2, no. 4, pp. 1920–1928, 2014.

[218] D. S. Dlamini, A. K. Mishra, and B. B. Mamba, "Artificial neural network simulations and experimental results: removal of trichlorophenol from water using *Chromolaena odorata* stem," *Water SA*, vol. 40, no. 2, pp. 369–378, 2014.

[219] A. Esmaeili and A. A. Beni, "A novel fixed-bed reactor design incorporating an electrospun PVA/chitosan nanofiber membrane," *Journal of Hazardous Materials*, vol. 280, pp. 788–796, 2014.

[220] M. Ghaedi, A. M. Ghaedi, F. Abdi, M. Roosta, R. Sahraei, and A. Daneshfa, "Principal component analysis-artificial neural network and genetic algorithm optimization for removal of reactive orange 12 by copper sulfide nanoparticles-activated carbon," *Journal of Industrial and Engineering Chemistry*, vol. 20, no. 3, pp. 787–795, 2014.

[221] M. Ghaedi, A. M. Ghaedi, E. Negintaji, A. Ansari, and F. Mohammadi, "Artificial neural network - Imperialist competitive algorithm based optimization for removal of sunset yellow using $Zn(OH)_2$ nanoparticles-activated carbon," *Journal of Industrial and Engineering Chemistry*, vol. 20, no. 6, pp. 4332–4343, 2014.

[222] M. Ghaedi, A. M. Ghaedi, A. Ansari, F. Mohammadi, and A. Vafaei, "Artificial neural network and particle swarm optimization for removal of methyl orange by gold nanoparticles loaded on activated carbon and Tamarisk," *Spectrochimica Acta Part A: Molecular and Biomolecular Spectroscopy*, vol. 132, pp. 639–654, 2014.

[223] M. Ghaedi, N. Zeinali, A. M. Ghaedi, M. Teimuori, and J. Tashkhourian, "Artificial neural network-genetic algorithm based optimization for the adsorption of methylene blue and brilliant green from aqueous solution by graphite oxide nanoparticle," *Spectrochimica Acta Part A: Molecular and Biomolecular Spectroscopy*, vol. 125, pp. 264–277, 2014.

[224] M. Ghaedi, R. Hosaininia, A. M. Ghaedi, A. Vafaei, and F. Taghizadeh, "Adaptive neuro-fuzzy inference system model for adsorption of 1,3,4-thiadiazole-2,5-dithiol onto gold nanoparticales-activated carbon," *Spectrochimica Acta Part A: Molecular and Biomolecular Spectroscopy*, vol. 131, pp. 606–614, 2014.

[225] D. Gnanasangeetha and S. D. Thambavani, "Neural network modeling of placid ZNO nanoparticle as a sensible adsorbent for removal of as(III) ions ingrained on activated silica using acalypha indica (ZNO-NPS-AS-AI)," *International Journal of ChemTech Research*, vol. 6, pp. 3546-3547, 2014.

[226] A. Hassani, F. Vafaei, S. Karaca, and A. R. Khataee, "Adsorption of a cationic dye from aqueous solution using Turkish lignite: kinetic, isotherm, thermodynamic studies and neural network modeling," *Journal of Industrial and Engineering Chemistry*, vol. 20, no. 4, pp. 2615–2624, 2014.

[227] J. Kabuba, A. Mulaba-Bafubiandi, and K. Battle, "Neural network technique for modeling of Cu (II) removal from aqueous solution by clinoptilolite," *Arabian Journal for Science and Engineering*, vol. 39, no. 10, pp. 6793–6803, 2014.

[228] H. Karimi and M. Ghaedi, "Application of artificial neural network and genetic algorithm to modeling and optimization of removal of methylene blue using activated carbon," *Journal of Industrial and Engineering Chemistry*, vol. 20, no. 4, pp. 2471–2476, 2014.

[229] M. Khajeh and K. Dastafkan, "Removal of molybdenum using silver nanoparticles from water samples: particle swarm optimization–artificial neural network," *Journal of Industrial and Engineering Chemistry*, vol. 2, pp. 3014–3018, 2014.

[230] D. Krishna and R. P. Sree, "Artificial neural network (ANN) approach for modeling chromium (VI) adsorption from aqueous solution using a borasus flabellifer coir powder," *International Journal of Applied Science and Engineering*, vol. 3, pp. 177–192, 2014.

[231] R. Maurya, T. Ghosh, C. Paliwal et al., "Biosorption of methylene blue by de-oiled algal biomass: equilibrium, kinetics and artificial neural network modelling," *PLoS One*, vol. 9, no. 10, article e109545, 2014.

[232] G. K. Parshetti, S. Chowdhury, and R. Balasubramanian, "Hydrothermal conversion of urban food waste to chars for removal of textile dyes from contaminated waters," *Bioresource Technology*, vol. 161, pp. 310–319, 2014.

[233] S. Ramalingam, L. Parthiban, and P. Rangasamy, "Biosorption modeling with multilayer perceptron for removal of lead and zinc ions using crab shell particles," *Arabian Journal for Science and Engineering*, vol. 39, no. 12, pp. 8465–8475, 2014.

[234] A. A. Seolatto, T. D. Martins, R. Bergamasco, C. R. G. Tavares, E. S. Cossich, and E. A. da Silva, "Biosorption study of Ni^{2+} and Cr^{3+} by sargassum filipendula: kinetics and equilibrium," *Brazilian Journal of Chemical Engineering*, vol. 31, no. 1, pp. 211–227, 2014.

[235] K. Singh, J. K. Arora, T. J. M. Sinha, and S. Srivastava, "Functionalization of nanocrystalline cellulose for decontamination of Cr(III) and Cr(VI) from aqueous system: computational modeling approach," *Clean Technologies and Environmental Policy*, vol. 16, no. 6, pp. 1179–1191, 2014.

[236] T. Shojaeimehr, F. Rahimpour, M. A. Khadivi, and M. Sadeghi, "A modeling study by response surface methodology (RSM) and artificial neural network (ANN) on Cu^{2+} adsorption optimization using light expended clay aggregate (*LECA*)," *Journal of Industrial and Engineering Chemistry*, vol. 20, no. 3, pp. 870–880, 2014.

[237] Y. Yang, X. Lin, B. Wei, Y. Zhao, and J. Wang, "Evaluation of adsorption potential of bamboo biochar for metal-complex dye: equilibrium, kinetics and artificial neural network modeling," *Environmental Science and Technology International Journal*, vol. 11, no. 4, pp. 1093–1100, 2014.

[238] Y. Yasin, F. Ahmad, M. Ghaffari-Moghaddam, and M. Khajeh, "Application of a hybrid artificial neural network-genetic algorithm approach to optimize the lead ions removal from aqueous solutions using intercalated tartrate-Mg-Al layered double hydroxides," *Environmental Nanotechnology, Monitoring & Management*, vol. 1-2, pp. 2–7, 2014.

[239] J. Ye, P. Zhang, E. Hoffmann et al., "Comparison of response surface methodology and artificial neural network in optimization and prediction of acid activation of bauxsol for phosphorus adsorption," *Water Air & Soil Pollution*, vol. 225, no. 12, p. 2225, 2014.

[240] P. Banerjee, S. Sau, P. Das, and A. Mukhopadhayay, "Optimization and modelling of synthetic azo dye wastewater treatment using Graphene oxide nanoplatelets: characterization toxicity evaluation and optimization using artificial neural network," *Ecotoxicology and Environmental Safety*, vol. 119, pp. 47–57, 2015.

[241] A. Çelekli, H. Bozkurt, and F. Geyik, "Artificial neural network and genetic algorithms for modeling of removal of an azo dye on walnut husk," *Desalination and Water Treatment*, vol. 57, no. 33, pp. 15580–15591, 2016.

[242] A. Esmaeili and A. A. Beni, "Novel membrane reactor design for heavy-metal removal by alginate nanoparticles," *Journal of Industrial and Engineering Chemistry*, vol. 26, pp. 122–128, 2015.

[243] A. M. Ghaedi, M. Ghaedi, and P. Karami, "Comparison of ultrasonic with stirrer performance for removal of sunset yellow (SY) by activated carbon prepared from wood of orange tree: artificial neural network modeling," *Spectrochimica Acta Part A: Molecular and Biomolecular Spectroscopy*, vol. 138, pp. 789–799, 2015.

[244] M. Ghaedi, E. Shojaeipour, A. Ghaedi, and R. Sahraei, "Isotherm and kinetics study of malachite green adsorption onto copper nanowires loaded on activated carbon: artificial neural network modeling and genetic algorithm optimization," *Spectrochimica Acta Part A: Molecular and Biomolecular Spectroscopy*, vol. 142, pp. 135–149, 2015.

[245] M. Ghaedi, A. Ansari, F. Bahari, A. Ghaedi, and A. Vafaei, "A hybrid artificial neural network and particle swarm optimization for prediction of removal of hazardous dye brilliant green from aqueous solution using zinc sulfide nanoparticle loaded on activated carbon," *Spectrochimica Acta Part A: Molecular and Biomolecular Spectroscopy*, vol. 137, pp. 1004–1015, 2015.

[246] M. Ghaedi, A. Daneshfar, M. Ahmadi, and M. Momeni, "Artificial neural network-genetic algorithm based optimization for the adsorption of phenol red (PR) onto gold and titanium dioxide nanoparticles loaded on activated carbon," *Journal of Industrial and Engineering Chemistry*, vol. 21, pp. 587–598, 2015.

[247] A. Ghosh, P. Das, and K. Sinha, "Modeling of biosorption of Cu(II) by alkali-modified spent tea leaves using response surface methodology (RSM) and artificial neural network (ANN)," *Applied Water Science*, vol. 5, no. 2, pp. 191–199, 2015.

[248] M. Maghsoudi, M. Ghaedi, A. Zinali, A. M. Ghaedi, and M. H. Habibi, "Artificial neural network (ANN) method for modeling of sunset yellow dye adsorption using zinc oxide nanorods loaded on activated carbon: Kinetic and isotherm study," *Spectrochimica Acta Part A: Molecular and Biomolecular Spectroscopy*, vol. 134, pp. 1–9, 2015.

[249] S. Mandal, S. S. Mahapatra, M. K. Sahu, and R. Patel, "Artificial neural network modelling of As(III) removal from water by novel hybrid material," *Process Safety and Environmental Protection*, vol. 93, pp. 249–264, 2015.

[250] S. Mandal, S. S. Mahapatra, and R. K. Patel, "Enhanced removal of Cr(VI) by cerium oxide polyaniline composite: Optimization and modeling approach using response surface methodology and artificial neural networks," *Journal of Environmental Chemical Engineering*, vol. 3, no. 2, pp. 870–885, 2015.

[251] N. K. Mondal, R. Bhaumik, B. Das et al., "Neural network model and isotherm study for removal of phenol from aqueous solution by orange peel ash," *Applied Water Science*, vol. 5, no. 3, pp. 271–282, 2015.

[252] M. S. Petrović, T. D. Šoštarić, L. L. Pezo et al., "Usefulness of Ann-based model for copper removal from aqueous solutions using agro industrial waste materials," *Chemical Industry & Chemical Engineering Quarterly*, vol. 21, no. 2, pp. 249–259, 2015.

[253] A. Ramazanpour, S. Hojati, A. Azimi, M. Farzadiana, and A. Khataee, "Enhanced hexavalent chromium removal from aqueous solution using a sepiolite- stabilized zero-valent iron nanocomposite: Impact of operational parameters and artificial neural network modeling," *Journal of the Taiwan Institute of Chemical Engineers*, vol. 49, pp. 172–182, 2015.

[254] A. Ronda, M. A. Martín-Lara, A. I. Almendros, A. Pérez, and G. Blázquez, "Comparison of two models for the biosorption of Pb(II) using untreated and chemically treated olive stone: experimental design methodology and adaptive neural fuzzy inference system (ANFIS)," *Journal of the Taiwan Institute of Chemical Engineers*, vol. 54, pp. 45–56, 2015.

[255] P. Roy, U. Dey, S. Chattoraj, D. Mukhopadhyay, and N. K. Mondal, "Modeling of the adsorptive removal of arsenic(III) using plant biomass: a bioremedial approach," *Applied Water Science*, vol. 1, pp. 1–15, 2015.

[256] S. Saraf and V. K. Vaidya, "Statistical optimization of biosorption of reactive orange 13 by dead biomass of Rhizopus arrhizus NCIM 997 using response surface methodology," *International Journal of Industrial Chemistry*, vol. 6, no. 2, pp. 93–104, 2015.

[257] B. Singh, N. Bar, and S. K. Das, "The use of artificial neural network (ANN) for modeling of Pb(II) adsorption in batch process," *Journal of Molecular Liquids*, vol. 211, pp. 228–232, 2015.

[258] M. Sharifzadeh and R. H. Alizadeh, "Artificial neural network approach for modeling of mercury adsorption from aqueous solution by *Sargassum Bevanom* algae," *International Journal of Engineering Transactions B: Applications*, vol. 28, pp. 1124–1133, 2015.

[259] U. Yurtsever, M. Yurtsever, I. A. Şengil, and N. K. Yılmazçoban, "Fast artificial neural network (FANN) modeling of Cd(II) ions removal by valonia resin," *Desalination and Water Treatment*, vol. 56, pp. 83–96, 2015.

[260] M. Jamshidi, M. Ghaedi, K. Dashtian et al., "Highly efficient simultaneous ultrasonic assisted adsorption of brilliant green and eosin B onto ZnS nanoparticles loaded activated carbon: artificial neural network modeling and central composite design optimization," *Spectrochimica Acta Part A: Molecular and Biomolecular Spectroscopy*, vol. 153, pp. 257–267, 2016.

[261] R. Khandanlou, H. R. Masoumi, M. B. Ahmad, K. Shameli, M. Basri, and K. Kalantari, "Enhancement of heavy metals sorption via nanocomposites of rice straw and Fe_3O_4 nanoparticles using artificial neural network (ANN)," *Ecological Engineering*, vol. 91, pp. 249–256, 2016.

[262] S. S. Madan, K. L. Wasewar, and S. L. Pandharipande, "Modeling the adsorption of benzeneacetic acid on CaO_2 nanoparticles using artificial neural network," *Resource-Efficient Technologies*, vol. 2, pp. S53–S62, 2016.

[263] S. Mondal, K. Bobde, K. Aikat, and G. Halder, "Biosorptive uptake of ibuprofen by steam activated biochar derived from mung bean husk: Equilibrium, kinetics, thermodynamics, modeling and eco- toxicological studies," *Journal of Environmental Management*, vol. 182, pp. 581–594, 2016.

[264] D. Podstawczyk, A. Witek-Krowiak, A. Dawiec, and A. Bhatnagar, "Biosorption of copper(II) ions by flax meal: empirical modeling and process optimization by response surface methodology (RSM) and artificial neural network (ANN) simulation," *Ecological Engineering*, vol. 83, pp. 364–379, 2015.

[265] P. S. Ardekani, H. Karimi, M. Ghaedi, A. Asfaram, and M. K. Purkait, "Ultrasonic assisted removal of methylene blue on ultrasonically synthesized zinc hydroxide nanoparticles on activated carbon prepared from wood of cherry tree: experimental design methodology and artificial neural network," *Journal of Molecular Liquids*, vol. 229, pp. 114–124, 2017.

[266] M. Baziar, A. Azari, M. Karimaei et al., "MWCNT-Fe_3O_4 as a superior adsorbent for microcystins LR removal: investigation on the magnetic adsorption separation, artificial neural network modeling, and genetic algorithm optimization," *Journal of Molecular Liquids*, vol. 241, pp. 102–113, 2017.

[267] E. A. Dil, M. Ghaedi, A. Asfaram, S. Hajati, F. Mehrabi, and A. Goudarzi, "Preparation of nanomaterials for the ultrasound-enhanced removal of Pb^{2+} ions and malachite green dye: chemometric optimization and modeling," *Ultrasonics Sonochemistry*, vol. 34, pp. 677–691, 2017.

[268] S. Mondal, K. Aikat, K. Siddharth et al., "Optimizing ranitidine hydrochloride uptake of *Parthenium hysterophorus* derived N-biochar through response surface methodology and artificial neural network," *Process Safety and Environmental Protection*, vol. 107, pp. 388–401, 2017.

[269] S. Roy, S. Manna, S. Sengupta, A. Ganguli, S. Goswami, and P. Das, "Comparative assessment on defluoridation of waste water using chemical and bio-reduced graphene oxide: batch, thermodynamic, kinetics and optimization using response surface methodology and artificial neural network," *Process Safety and Environmental Protection*, vol. 111, pp. 221–231, 2017.

[270] D. K. Singh, D. K. Verma, Y. Singh, and S. H. Hasan, "Preparation of CuO nanoparticles using *Tamarindus indica* pulp extract for removal of As(III): Optimization of adsorption process by ANN-GA," *Journal of Environmental Chemical Engineering*, vol. 5, no. 1, pp. 1302–1318, 2017.

[271] M. Zafar, N. V. Vinh, S. K. Behera, and H. S. Park, "Ethanol mediated As(III) adsorption onto Zn-loaded pinecone biochar: experimental investigation, modeling, and optimization using hybrid artificial neural network-genetic algorithm approach," *Journal of environmental sciences*, vol. 54, pp. 114–125, 2017.

[272] I. Ali, O. M. L. Alharbi, Z. A. Alothman, A. Y. Badjah, A. Alwarthan, and A. A. Basheer, "Artificial neural network modelling of amido black dye sorption on iron composite nano material: kinetics and thermodynamics studies," *Journal of Molecular Liquids*, vol. 250, pp. 1–8, 2018.

[273] P. S. Ghosal, K. V. Kattil, M. K. Yadav, and A. K. Gupta, "Adsorptive removal of arsenic by novel iron/olivine composite: insights into preparation and adsorption process by response surface methodology and artificial neural network," *Journal of Environmental Management*, vol. 209, pp. 176–187, 2018.

[274] L. P. Lingamdinne, J. Singh, J. S. Choi et al., "Multivariate modeling via artificial neural network applied to enhance methylene blue sorption using graphene-like carbon material prepared from edible sugar," *Journal of Molecular Liquids*, vol. 265, pp. 416–427, 2018.

[275] P. R. Souza, G. L. Dotto, and N. P. Salau, "Artificial neural network (ANN) and adaptive neuro-fuzzy interference system (ANFIS) modelling for nickel adsorption onto agro-wastes and commercial activated carbon," *Journal of Environmental Chemical Engineering*, vol. 6, no. 6, pp. 7152–7160, 2018.

[276] M. Solgi, T. Najib, S. Ahmadnejad, and B. Nasernejad, "Synthesis and characterization of novel activated carbon from Medlar seed for chromium removal: experimental analysis and modeling with artificial neural network and support vector regression," *Resource-Efficient Technologies*, vol. 3, pp. 236–248, 2017.

[277] S. A. Abdulhussein and A. I. Alwared, "The use of artificial neural network (ANN) for modeling of Cu (II) ion removal from aqueous solution by flotation and sorptive flotation process," *Environmental Technology & Innovation*, vol. 13, pp. 353–363, 2019.

[278] C. Cojocaru, P. Samoila, and P. Pascariu, "Chitosan-based magnetic adsorbent for removal of water-soluble anionic dye: artificial neural network modeling and molecular docking insights," *International Journal of Biological Macromolecules*, vol. 123, pp. 587–599, 2019.

[279] N. Ghasemi and S. Rohani, "Optimization of cyanide removal from wastewaters using a new nano-adsorbent containing ZnO nanoparticles and MOF/Cu and evaluating its efficacy and prediction of experimental results with artificial neural networks," *Journal of Molecular Liquids*, vol. 285, pp. 252–269, 2019.

[280] C. A. Igwegbe, L. Mohmmadi, S. Ahmadi et al., "Modeling of adsorption of methylene blue dye on Ho-$CaWO_4$

nanoparticles using response surface methodology (RSM) and artificial neural network (ANN) techniques," *Methods X*, vol. 6, pp. 1779–1797, 2019.

[281] N. Mahmoodi-Babolan, A. Heydari, and A. Nematollahzadeh, "Removal of methylene blue via bioinspired catecholamine/starch superadsorbent and the efficiency prediction by response surface methodology and artificial neural network-particle swarm optimization," *Bioresource Technology*, vol. 294, p. 122084, 2019.

[282] Z. U. Ahmad, L. Yao, Q. Lian, F. Islam, M. E. Zappi, and D. D. Gang, "The use of artificial neural network (ANN) for modeling adsorption of sunset yellow onto neodymium modified ordered mesoporous carbon," *Chemosphere*, vol. 256, p. 127081, 2020.

[283] A. Albalasmeh, M. A. Gharaibeh, O. Mohawesh et al., "Characterization and artificial neural networks modelling of methylene blue adsorption of biochar derived from agricultural residues: effect of biomass type, pyrolysis temperature, particle size," *Journal of Saudi Chemical Society*, vol. 24, no. 11, pp. 811–823, 2020.

[284] A. A. Faisal, Z. S. Nassir, L. A. Naji, M. Naushad, and T. Ahamad, "A sustainable approach to utilize olive pips for the sorption of lead ions: numerical modeling with aid of artificial neural network," *Sustainable Chemistry and Pharmacy*, vol. 15, p. 100220, 2020.

[285] L. T. N. Nguyen, Q. Bui, and T. T. Khieu, "Artificial neural network modeling for congo red adsorption on microwave-synthesized akaganeite nanoparticles: optimization, kinetics, mechanism, and thermodynamics," *Environmental Science and Pollution Research*, vol. 28, no. 8, pp. 9133–9145, 2020.

[286] A. Mojiri, J. Zhou, M. Vakili, and H. Le, "Removal performance and optimisation of pharmaceutical micropollutants from synthetic domestic wastewater by hybrid treatment," *Journal of Contaminant Hydrology*, vol. 235, article 103736, 2020.

[287] M. R. Fagundes-Klen, P. Ferri, T. D. Martins, C. R. G. Tavares, and E. A. Silva, "Equilibrium study of the binary mixture of cadmium-zinc ions biosorption by the *Sargassum filipendula* species using adsorption isotherms models and neural network," *Biochemical Engineering Journal*, vol. 34, no. 2, pp. 136–146, 2007.

[288] R. M. Aghav, S. Kumar, and S. N. Mukherjee, "Artificial neural network modeling in competitive adsorption of phenol and resorcinol from water environment using some carbonaceous adsorbents," *Journal of Hazardous Materials*, vol. 188, no. 1-3, pp. 67–77, 2011.

[289] E. Tomczak, "Application of ANN and EA for description of metal ions sorption on chitosan foamed structure–Equilibrium and dynamics of packed column," *Computers and Chemical Engineering*, vol. 35, no. 2, pp. 226–235, 2011.

[290] S. L. Pandharipande and A. R. Deshmukh, "Artificial neural network approach for modeling of Ni(II) adsorption from aqueous solution using aegel marmelos fruit shell adsorbent," *International Journal of Engineering Sciences & Emerging Technologies*, vol. 4, pp. 27–36, 2013.

[291] S. Hajati, M. Ghaedi, Z. Mahmoudi, and R. Sahraei, "SnO_2 nanoparticle-loaded activated carbon for simultaneous removal of acid yellow 41 and sunset yellow; derivative spectrophotometric, artificial neural network and optimization approach," *Spectrochimica Acta Part A: Molecular and Biomolecular Spectroscopy*, vol. 150, pp. 1002–1012, 2015.

[292] M. Delnavaz, B. Ayati, and H. Ganjidoust, "Prediction of moving bed biofilm reactor (MBBR) performance for the treatment of aniline using artificial neural networks (ANN)," *Journal of Hazardous Materials*, vol. 179, no. 1-3, pp. 769–775, 2010.

[293] E. Oguz and M. Ersoy, "Removal of Cu^{2+} from aqueous solution by adsorption in a fixed bed column and neural network modelling," *Chemical Engineering Journal*, vol. 164, no. 1, pp. 56–62, 2010.

[294] S. Chakraborty, S. Chowdhury, and P. D. Saha, "Artificial neural network (ANN) modeling of dynamic adsorption of crystal violet from aqueous solution using citric-acid-modified rice (*Oryza sativa*) straw as adsorbent," *Clean Technologies Environmental Policy*, vol. 15, no. 2, pp. 255–264, 2013.

[295] M. Khajeh and A. R. Golzary, "Synthesis of zinc oxide nanoparticles-chitosan for extraction of methyl orange from water samples: Cuckoo optimization algorithm-artificial neural network," *Spectrochimica Acta Part A: Molecular and Biomolecular Spectroscopy*, vol. 131, pp. 189–194, 2014.

[296] A. A. Oladipo and M. Gazi, "Nickel removal from aqueous solutions by alginate-based composite beads: central composite design and artificial neural network modeling," *Journal of Water Process Engineering*, vol. 8, pp. e81–e91, 2015.

[297] T. Mitra, B. Singha, N. Bar, and S. K. Das, "Removal of Pb(II) ions from aqueous solution using water hyacinth root by fixed-bed column and ANN modeling," *Journal of Hazardous Materials*, vol. 273, pp. 94–103, 2014.

[298] T. Nur, P. Loganathan, T. C. Nguyen, S. Vigneswaran, G. Singh, and J. Kandasamy, "Batch and column adsorption and desorption of fluoride using hydrous ferric oxide: solution chemistry and modeling," *Chemical Engineering Journal*, vol. 247, pp. 93–102, 2014.

[299] E. Oguz and M. Ersoy, "Biosorption of cobalt(II) with sunflower biomass from aqueous solutions in a fixed bed column and neural networks modelling," *Ecotoxicology and Environmental Safety*, vol. 99, pp. 54–60, 2014.

[300] G. R. Oliveira, A. V. Santos, A. S. Lima, C. M. Soares, and M. S. Leite, "Neural modelling in adsorption column of cholesterol-removal efficiency from milk," *LWT-Food Science and Technology*, vol. 64, no. 2, pp. 632–638, 2015.

[301] M. F. Ahmad and S. Haydar, "Evaluation of a newly developed biosorbent using packed bed column for possible application in the treatment of industrial effluents for removal of cadmium ions," *Journal of the Taiwan Institute of Chemical Engineers*, vol. 62, pp. 122–131, 2016.

[302] W. Li, S. Wei, W. Jiao, G. Qi, and Y. Liu, "Modelling of adsorption in rotating packed bed using artificial neural networks (ANN)," *Chemical engineering research and design*, vol. 114, pp. 89–95, 2016.

[303] E. Oguz, "Fixed-bed column studies on the removal of Fe^{3+} and neural network modelling," *Arabian Journal of Chemistry*, vol. 10, no. 3, pp. 313–320, 2017.

[304] M. Arshadi, M. K. Abdolmaleki, H. Eskandarloo, M. Azizi, and A. Abbaspourrad, "Synthesis of highly monodispersed, stable, and spherical NZVI of 20-30 nm on filter paper for the removal of phosphate from wastewater: batch and column study," *Sustainable Chemistry & Engineering*, vol. 6, no. 9, pp. 11662–11676, 2018.

[305] M. Calero, I. Iáñez-Rodríguez, A. Pérez, M. A. Martín-Lara, and G. Blázquez, "Neural fuzzy modelization of copper removal from water by biosorption in fixed-bed columns

using olive stone and pinion shell," *Bioresource Technology*, vol. 252, pp. 100–109, 2018.

[306] D. Ranjan, D. Mishra, and S. H. Hasan, "Bioadsorption of arsenic: an artificial neural networks and response surface methodological approach," *Industrial & Engineering Chemistry Research*, vol. 50, no. 17, pp. 9852–9863, 2011.

[307] M. M. Bello, M. M. Nourouzi, L. C. Abdullah, T. S. Choong, Y. S. Koay, and S. Keshani, "POME is treated for removal of color from biologically treated POME in fixed bed column: applying wavelet neural network (WNN)," *Journal of Hazardous Materials*, vol. 262, pp. 106–113, 2013.

Hindawi
Adsorption Science & Technology
Volume 2022, Article ID 2323836, 13 pages
https://doi.org/10.1155/2022/2323836

Research Article

Petrochemical Wastewater Treatment by Eggshell Modified Biochar as Adsorbent: Atechno-Economic and Sustainable Approach

Andy G. Kumi,[1] **Mona G. Ibrahim**,[1,2] **Manabu Fujii**,[1,3] **and Mahmoud Nasr**[1,4]

[1]*Environmental Engineering Department, Egypt-Japan University of Science and Technology (E-JUST), New Borg El-Arab City, Alexandria 21934, Egypt*
[2]*Environmental Health Department, High Institute of Public Health, Alexandria University, Alexandria 21544, Egypt*
[3]*Civil and Environmental Engineering Department, Tokyo Institute of Technology, Meguro-Ku, Tokyo 152-8552, Japan*
[4]*Sanitary Engineering Department, Faculty of Engineering, Alexandria University, P.O. Box 21544, Alexandria 21526, Egypt*

Correspondence should be addressed to Mahmoud Nasr; mahmmoudsaid@gmail.com

Received 26 November 2021; Revised 15 January 2022; Accepted 27 January 2022; Published 14 February 2022

Academic Editor: Chinenye Adaobi Igwegbe

Petrochemical industrial wastewater (PIW)contains toluene and xylene (TX), and various organic and inorganic pollutants, causing severe risks to human health if improperly released into the environmental matrices. For the long-term reliability of environmental conservation, this study illustrates the interlinkage between PIW treatment and the three pillars of sustainable development. Sewage sludge biochar was modified with eggshell, showing a relatively high fixed C content (increase in carbonization degree), and small O/C and N/C ratios. The prepared biochar was employed for TX adsorption in mono-component solutions, giving removal efficiencies of 79.1% (T) and 86.6% (X), at pH = 10, adsorbent dosage = 2 g/L, and C_o = 40 mg/L within 60 min. The main adsorption mechanism was physisorption, including precipitation/pore-filling, π-π dispersive interaction, and van der Waals force. The modified biochar also treated real PIW under five adsorption/regeneration cycles, providing essential steps toward large-scale applications. According to an economic feasibility estimation, the biochar application for treating 1 m^3 of PIW would offer a payback period of 6.9 yr. The study outputs could be linked to the restoration of water-related ecosystems, biochar modification for industrial applications, and climate change mitigation, adopting the 2030 agenda and its sustainable development goals (SDGs).

1. Introduction

Petrochemical manufacturing industries generate large amounts of wastewater composed of aromatic hydrocarbons and organic solvents, e.g., toluene and xylene (TX) [35]. The TX compounds of petrochemical industrial wastewater (PIW) are considered slowly biodegradable and highly toxic, imposing harmful and emerging threats on human health [31]. The unsafe disposal of these hydrocarbons would damage the human organs and central nervous system, or could even cause death at high doses [24]. Because PIW should be managed properly using sustainable and feasible pathways, its treatment should be investigated regarding the environmental and economic points of view.

Various physicochemical methods have been adopted to treat PIW, providing a rapid process accompanied by convenient operation and control. Unlike in biological systems, the physicochemical-based processes could withstand fluctuating temperature patterns and complex discharges within a shorter treatment time [9]. Among thephysicochemical treatment techniques, adsorption is becoming a cost-effective, simple, andenvironmentally friendly option to mitigate PIW-related pollution [1]. Adsorption is not considered an energy-intensive technique because it does not usually require aeration, heating, and/or mixing [16]. Adsorption does not also suffer from sludge handling and management due to the utilization of low quantities of chemical reagents, providing an economically feasible approach [28]. Previous

researchers have investigated the treatment of PIW by adsorption onto crumb rubber [3], graphene [16], Na-P1 zeolite [5], silica [24], biocomposite [1], carbon nanotubes [4], and solid waste biochar [15]. Based on these studies, the adsorbent should be abundantly available, eco-friendly, and prepared with a cheap materialfor providing a standalone wastewater treatment system.

In most developing countries, wastewater treatment processes generate large amounts of sewage sludge that could pose serious burdens tothe environment (soil and groundwater) [25]. A proper and smart waste (e.g., sludge) management system should be outlined according to the sustainable development goals (SDGs), tackling multiple environmental, economic, and social aspects [8]. Waste sludge could be utilized as a renewable biomass to produce biochar (a carbon-rich material) via pyrolysis [27]. Biochar has been employed as an innovative and effective adsorbent for removing aqueous contaminants such as complex organic compounds fromindustrial effluents [11]. However, under improper sludge pyrolysis, biochar might be unable to capture large amounts of pollutants due to the associated insufficient surface area and poor porosity [14]. Adding food residues and optimizing the pyrolysis temperature are efficient options to modifythe texture, surface functional groups, molecular structure, and pore-size distribution of biochars [22, 32]. For example, eggshell wastescould be utilized for providing multiple functional groups and mineral components (calcite) to biochars [6]. This pattern would enhance the intrinsic features and pore structure of biochars to improve the adsorption performance.

A significant gap exists in the literature regarding the relationship between biochar manufacturing, SDGs, and economic feasibility, which should be comprehensively addressed. Hence, this study is the first toillustrate the interlinkage between PIW treatmentand the three pillars of sustainability via the techno-economic feasibility of a modified biochar adsorbent. In particular, the study objectives are fourfold (i) characterize biocharproduced from sludge and eggshell wastes, (ii) determine optimum pyrolysis temperature, effects of adsorption conditions on TX removal, and suggested adsorption mechanisms, (iii) test the synthesized biochar for treating real PIW under successive adsorption/regeneration cycles, and (iv) highlight the achievable SDGs, environmental considerations, and economic feasibility associated with the study outputs.

2. Materials and Methods

2.1. Wastewater Preparation/Collection. The synthetic medium was prepared by initially dissolving calculated volumes of each of T and X compounds in a small amount of methanol, not exceeding 1% in the stock solutions. The standard stock solutions (1000 mg/L of each of T and X) were dilutedwith appropriate amounts of distilled water to prepare mono-component systems (T and X: 40 – 200 mg/L). The suspension pH was regulatedby adding either 0.1 M NaOH or 0.1 M HCl solutions. For treatingreal PIW, a petrochemical industry situated in Alexandria, Egypt, was selected to collect the wastewater samples. The received PIW samples were directly used in the adsorption treatment assays without further adjustments. All solutions were stored in glass-stoppered bottles under the dark condition at 4°C. All reagents and solvents were of analytical grade (Sigma–Aldrich; >99% purity) and used without further purification.

2.2. Biochar Adsorbentpreparation. Sewage sludge was collected from the Alexandria East wastewater treatment plant (WWTP) located in Alexandria, Egypt. All the sludge samples were oven-dried (100°C for 24 hrs), and then screened using a 60-mesh sieve. Sludge pyrolysis was performed in an oxygen-deprived condition using a muffle furnace (Asahi Rika tabletop, AMF-25 N, Japan) to prepare the raw biochar (BC) material. The pyrolysis temperatures were investigated at300, 350, 400, 450, 500, and 550°C with a 5°C/min heating rate for 60 min, based on the methods of earlier reports [2, 39]. These biochars were labelled as BC300, BC350, BC400, BC450, BC500, and BC550, respectively. The raw biochars (300–550°C) were examined for TX adsorption, and the best pyrolysis temperature was selected to prepare eggshell-modified biochar (EMBC), following our previous study [18].

2.3. Adsorption Experiment. In the first experiment, single-component sorption assayswere performed in 250 mL flasks under 100 rpm stirring rate at room temperature (25 ± 2°C). The influences of adsorption factorson TX removal were statistically investigated using a one-factor-at-a-time method. Briefly, the first run was conducted by varying the pH values from 2 to 12 at adsorbent dosage = 1 g/L and C_o =100 mg/L within 60 min. The optimized pH was used in the second assay at C_o =100 mg/L for 60 min with increasing the adsorbent dosagefrom 2 to 10 g/L. Theseoptimum pH and dosage values were further used to operate the adsorption system for 60 min with varying C_o from 40 to 200 mg/L.The optimum pH, adsorbent dosage, and C_o were used in the fourth experimental assay to investigate the influence of adsorption time (5–240 min) on TX removal. The measured TX concentrations were used to estimate the adsorption performance in Eqs. (1) and (2).

$$R = \frac{C_o - C_e}{C_o} \times 100 \quad (1)$$

$$q = (C_o - C_e) \times \frac{V}{m} \quad (2)$$

where R is the adsorbate removal percentage (%), q is uptake capacity (mg adsorbate/g biochar), C_o and C_e are the initial and equilibrium adsorbate concentrations (mg/L), respectively, m is biochar mass (g), and V is the flask working volume (L).

The second experiment was conducted to determine the adsorption performance and stability of biochar for real PIW treatment. For this purpose, five adsorption/regeneration cycles were conducted to assess biochar reusability. Before each re-adsorption trial, the utilized biochar was washed with methanol and then dried overnight at 105°C. All experiments were conducted in triplicate, and the average results were recorded.

Table 1: Physiochemical, BET surface area and pore properties of biochars produced at various pyrolysis temperatures (300–550°C).

Properties	BC 300	BC 350	BC 400	BC 450	BC 500	BC 550
Yield (wt. %)	66.10	54.20	45.82	38.60	38.55	38.09
pH	7.87	8.13	8.49	8.68	8.76	8.88
C (w/w %)	84.79	77.55	73.4	69.28	65.56	67.43
N (w/w %)	5.90	5.56	5.23	4.71	4.18	4.16
O (w/w %)	18.09	17.82	15.68	12.62	9.86	6.73
C/N ratio	14.37	13.95	14.03	14.71	15.68	16.21
O/C ratio	0.21	0.23	0.21	0.18	0.15	0.10
S (w/w %)	0.92	0.48	2.13	3.82	2.94	1.79
Ca (w/w %)	3.40	3.79	7.69	7.81	7.62	9.00
BET (m^2/g)	0.227	0.282	1.266	22.680	27.240	52.210
Total pore volume (cm^3/g)	0.00562	0.00745	0.00919	0.02962	0.01087	0.03238
Average pore size (nm)	14.00	12.60	12.20	1.29	1.27	1.23

2.4. Analytical Analysis. Biochars were characterized for their specific surface area and pore-size distribution using the methods of Brunauer–Emmett–Teller (BET) and the Barrett–Joyner–Halenda (BJH) [23].BELSORP-mini II instrument (BEL Japan, Inc.) was assigned for measuring the N_2 adsorption–desorption isotherms at 77 K, following Shaheen et al. [27]. Proximate analysis and pH of biochars were determined as adapted from Fidel et al. [10]. X-ray diffractometer (XRD) (Shimadzu Xlab 6100, Kyoto, Japan) was used to analyze the biochar crystallinity over a 2θ range of 5–80° (0.02° step size @ 12°C/min). The XRD instrument was operated with Cu-Kα radiation ($\lambda = 1.5406$ Å) at 40 kV and 30 mA.A Fourier Transform Infrared (FTIR) spectroscopy (Vertex 70, Bruker Optics Inc., Ettlingen, Germany) was used to detect the shift in peak wavenumbers associated with the adsorption process. The change in FTIR bands was recorded over the 4000–400 1/cm region. The surface morphology of biochars was characterized by scanning electron microscopy (SEM, JSM-6010LV JEOL, Tokyo, Japan). Energy Dispersive X-ray analysis in conjunction with the SEM instrument was employed to provide information ofthe biochars' elemental composition (e.g., C, N, and O), following the procedures reported elsewhere [2, 15]. For identifying the benzene, T, ethylene, and X components, the liquid samples were treated through a 0.22 μm filter (Whatman syringe filters). The resulting filtrates were analyzed byGas Chromatography-Mass Spectrometry (GC-MS), with a QP2010 PLUS system (Shimadzu, Japan) and helium as a carrier gas.

3. Results and Discussion

3.1. Biochar Characterization

3.1.1. Biochar Yield Andnutrient Content. Table 1 represents the variation in the properties and nutrient availability of biochars under different pyrolysis temperature conditions. The pyrolysis temperature substantially affected the yield of biochars. For instance, at 300°C the biochar yield was 66.1%, representing about 2-folds the yield at 450°C. The negative correlation between the biochar yield and the pyrolysis temperature could be ascribed to the thermal decomposition and gasification of the sludge components, such as volatile compounds and other non-carbon elements [32]. The volatilization of organic acids under high-temperature conditions also contributed to the rise in pH values (Table 1). Shaaban et al. [26] reported that elevated pyrolysis temperatures would increase the amounts of basic OH groups on the biochar surface, accompanied byeliminating various acidic functional groups. Increasing the total surface basicity of biochars, owing to organic acid decomposition, at elevated pyrolysis temperatures has also been verified [25]. However, increasing the pyrolysis temperature to550°C provided an insignificant ($p > 0.05$) impact on the biochar yield, assigning that the carbonization process was almost completed.

Table 1 also revealed that biochars contained nutrient species (e.g., N, S, and Ca) that have probably been embedded in the components of the collected sewage sludge. The reduction of the C, N, and O fractions for biochars pyrolyzed at 300–550°C could be ascribed to the pyrogenic decompositions and emission of volatile matters at elevated temperatures [26]. Hence, a high proportion of nutrientswould be maintained in biochars synthesizedat low pyrolysis temperatures. The variation of the nitrogen properties with temperature (Table 1) could be assigned to the loss of volatile nitrogen species, such as ammonia or volatile amines, obtaining stable pyridine compounds at elevated temperatures [14]. Moreover, the C/N ratio of the biochar products varied as a result of carbonization along with the conversion and transformation of the organic nitrogen fractions [30]. The change in the O/C ratio between 0.10 and 0.23 could be linked to the degree of polarity [2], attaining a minimum O/C ratio of 0.10 at 550°C. A low O/C ratio at elevated pyrolysis temperatures is an indication of the high aromatic nature (i.e., the aromatic linkages were more stable) of the investigated biochars [30]. This O/C range is comparable to O/C 0.07 – 0.27 for biochar-based crop residues [2], but lower than O/C 0.59 – 0.71 for biochars obtained from digested sludge [32].

3.1.2. BET Surface Area. Increasing the pyrolysis temperature from 300 to 550°C provided a positive impact on

theBET surface area, which improved from 0.23 to 52.21 m^2/g, respectively (Table 1). This BET surface area is higher than that (2.0–3.2 m^2/g) of biochar prepared from poultry litter [30]. For the preparation of rice husk biochars [28], the BET surface area was increasedfrom 45.2 to 193.1 m^2/g with raising the pyrolysis temperature from 500 to 700°C, respectively. Comparable patterns were noticed for the total pore volume (Table 1), which could be linked to a high degree of carbonization and the release of most volatiles with elevating the temperature from 300 to 550°C.These observations were also confirmed by the BET N_2 adsorption/desorption assays and BJH pore-size distribution of different biochars (Figure 1(a)), implying the presence of mesopores and micropores. The pore-size distribution of BC 300–400°Cwas within the 2–50 nm range, denoting a mesoporous material classification. The pore-size of biochars BC 450–550°C obeyed the micropores region (< 2 nm). Based on the aforementioned results, a high pyrolysis temperature would develop the biochar surface area, i.e., an essential property for entrapping high amounts of molecules via the pore-filling mechanism [26]. Additionally, an increase in pyrolysis temperature would provide an appropriate condition for attaining a high ash content and a stable physicochemical quality, which complied with the study by Song and Guo [30].

3.1.3. XRD Pattern. The crystallinity of biochars synthesized at different pyrolysis temperatures was estimated using the XRD analysis (Figure 1(b)). The XRD patterns of biochars BC 300–550°C exhibited the predominance of two main crystalline minerals, i.e., quartz (SiO_2) and calcite ($CaCO_3$). Similarly, Kraiem et al. [17] indicated the occupancy of quartz and calcite in biochar prepared from the pyrolysis of waste fish fats at a temperature of 500°C. The XRD peaks observed at 2θ approximately of 20.9°, 36.6°, 50.2°, and 60.0° could be associated with (100), (110), (112) and (121) planes of SiO_2, respectively [13]. This result suggests that SiO_2 was the main crystalline phase for all biochars pyrolyzed throughout the temperature 300–550°C range. Some peaks of quartz for BC450–550 were higher than those for BC300–400, indicating the increment of quartz crystallization in biochars when the heating temperature increased. However, the peak intensities of calcite decreased with an increase in temperature, which could be due to decomposing carbonaceous materials (calcite) after thermal treatment with elevated temperatures [26]. The presence of calcite in all biochar samples would elucidate the pH distribution within the alkaline range (Table 1), as previously recognized by Yuan et al. [34]. Similarly, Fidel et al. [10] demonstrated that the intensities of XRD peaks ascribed to the mineral content (e.g., sylvite, calcite, and dolomite) of biochar were diminished under a high thermal treatment condition.

3.1.4. FTIR and Functional Groups. Figure 1(c) shows the functional groups on the biochar surface treated at various-pyrolysistemperatures (300–550°C). The intensity of peaks between 3270 and 3380 1/cmdecreased largely withincreasing the pyrolysis temperature. This finding suggested that the organic O – H group was unstable at elevated temperatures, probably due to the biochar structure dehydration [14]. Similarly, the reduction in peak intensities at 3250–3400 1/cm under higher temperature conditions could be associated with decomposing the organic nitrogen (N – H) groups in amines and amides. This finding could also explain the variation in the C/N ratio along with the pyrolysis temperature, as previously listed in Table 1. Thedominance of alkyl and oxygenated functional groups (e.g., C–O–C, COOH, –OH, and C=O)for BC300°C indicated that the biochar surface was more aliphatic at lower pyrolysis temperature. However, the structures of BC400–550°C were more aromaticat higher pyrolysis temperature (>400°C) because of the dehydroxylation and volatilization process, supporting crystallization [20]. Again, this finding complied with the XRD pattern (Figure 1(b)), suggesting that biochars were more crystalline at higher pyrolysis temperatures. Hence, the arrangement of carbon structures was adjusted from aliphatic to aromatic, with raising the pyrolysis temperature from 300 to 550°C. Moreover, some adsorption bands between 2850 and 2950 1/cm for BC300–400°C were gradually disappeared at pyrolysis temperatures over 400°C dueto the instability of the aliphatic hydrocarbon ($–CH_x$) groups. The change in C=O stretching (around 1700 1/cm) with temperature could be ascribed to the formation of some conjugated aromatic carbonyl/carboxyl groups at exceeding the pyrolysis temperature over 300°C[39]. A slight change in the peak intensity at 1604 1/cm with elevating the pyrolysis temperature could be associated with the stability of conjugated aromatic ring stretching of C=C groups [22], *viz*., this observation also supports the decrease of O/C ratio (see Table 1). Moreover, the biochar surface would be more hydrophobic at elevated temperatures because of the evolvement of oxygen functional groups via gasification [20, 26]. Accordingly, the –OH, –NH, and – CH_3 groups were unstable, with a concomitant increase in aromaticity at elevated temperatures. The decrease in the polar functional groups for BC400–550°C revealed the establishment of a condensed and carbonized structure owing to higher mass loss (Figure 1(c)). The presence of more functional groups (Figure 1(d)) for EMBC, *viz*., alkane (CH_2 and CH_3bands), aromatic (C=C stretching), esters (S-OR) group, and alcohol (OH stretch andH-bonded), would be usefulto form interactions and complexations with the adsorbate compounds.

3.1.5. SEM. Figure 2 shows the surface morphologies of the biochar samples (BC300–550°C). The SEM micrographs clearly indicated the development of irregular and uneven biochar surfaces with channels and well-defined and vacant pores. A smooth textureand incomplete decomposition were noticed for BC300 – 400°C. However, the surfaceroughness and intensity increased for BC450 – 550°C, suggesting an improved porosity. This finding could be ascribed to the release of volatiles during carbonization with elevating the pyrolysis temperature [37].

3.2. Toluene and Xylene (TX)Removals in Single-Solute System

3.2.1. Effect of pH on TX Adsorption. Figure 3(a) shows the influence of solution pH on TX adsorption by biochars

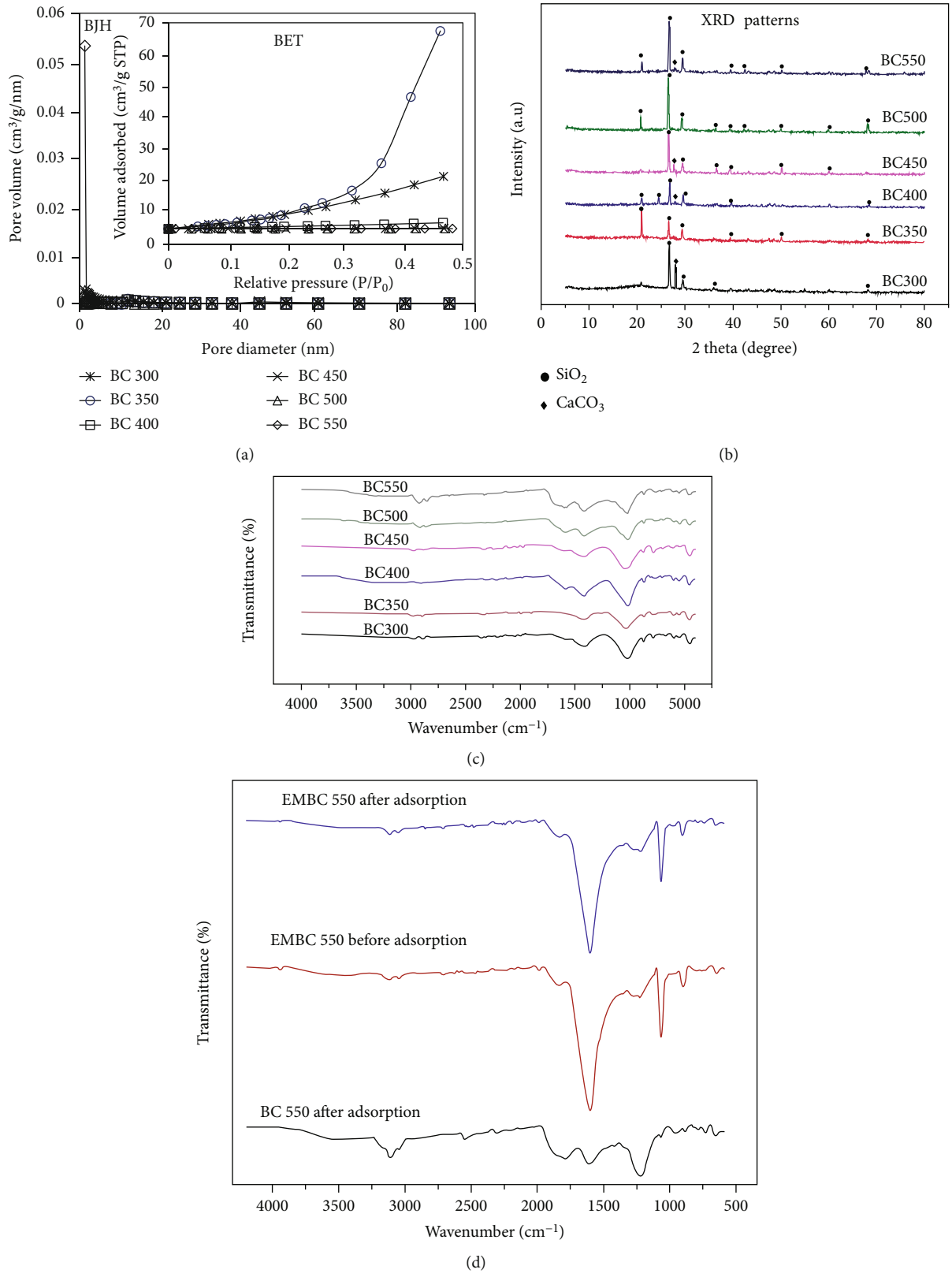

Figure 1: Biochar adsorbent characterization: (a) BET nitrogen adsorption/desorption isotherms and BJH pore-size distribution, (b) XRD patterns of BC 300–550°C, (c) FTIR spectra of BC 300–550°C before adsorption, and (d) FTIR spectra of BC 550°C and EMBC 550°C after adsorption.

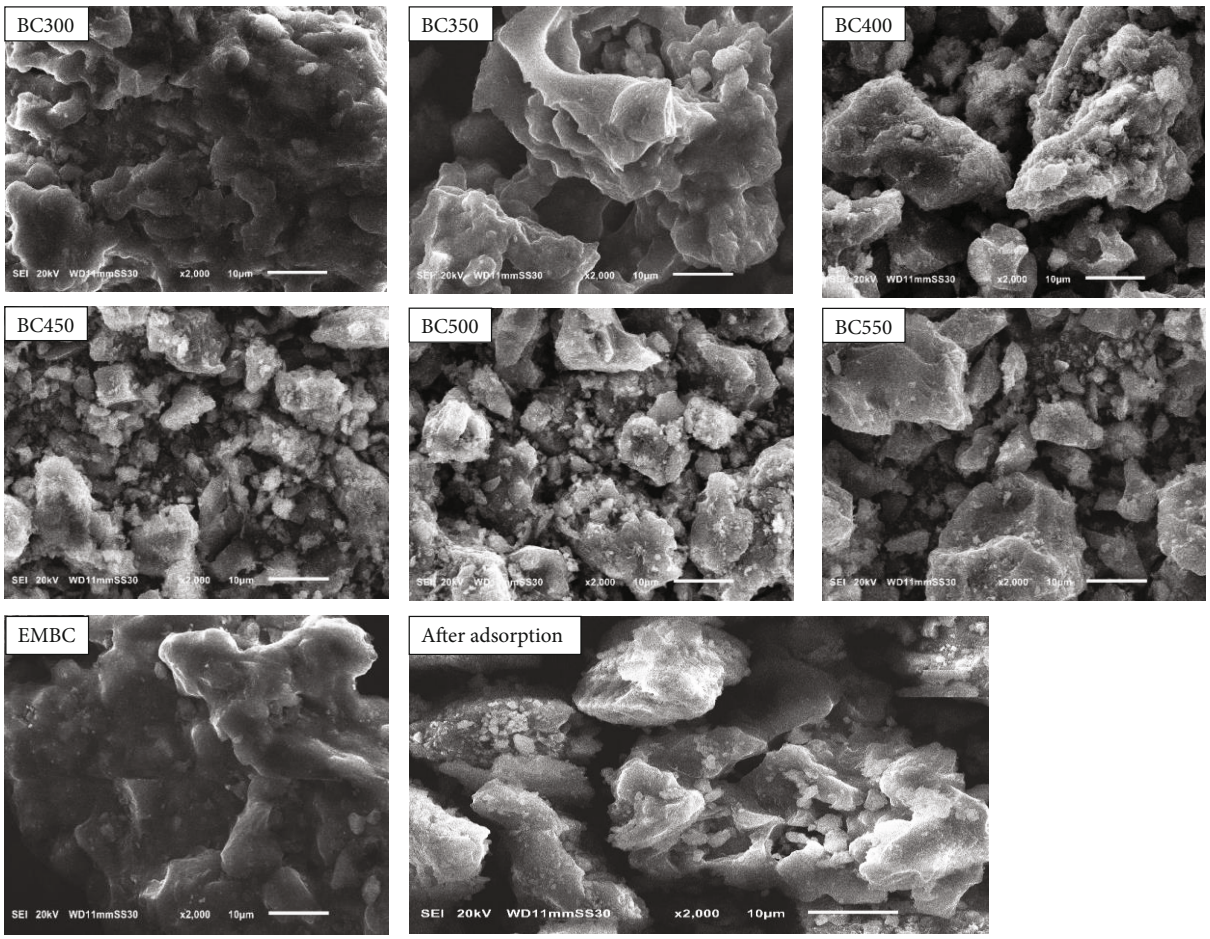

Figure 2: SEM of biochar and modified biochar adsorbents prepared under different pyrolysis conditions (300–550°C).

(BC and EMBC). For BC, the T removal efficiency improved from 46.8 to 75.1%, with an increase in the solution pH from 2 to 10, respectively, suggesting that pH around 10 was favourable for the adsorption process. At the pH 10 condition, the X removal efficiency was comparable toT and reached 73.4%. The EMBC adsorbent attained better adsorption capabilities compared with BC, exhibiting the highest removal efficiencies of82.1% for T and 86.1% for X. At lower pH, the high concentration and mobility of H^+ ions tended to generate extremely protonated sorption sites [9], causing electrostatic repulsion to hinder the TX uptake ability. The data in Figure 3(a) also revealed that a further increase in solution pH over 10 caused an insignificant ($p > 0.01$) enhancement in the removal efficiencies of the TX adsorbate. This result could be ascribed to the competition between the adsorbate molecules and hydroxide (OH^-) ions for the active sites occupying the biochar surface [21]. The point of zero charge (pH_{PZC}) also showed a zero electrical charge density on the biochar surface at a solution pH of about 10 (Supplementary Figure S1). In another study, Jayawardhana et al. [15] found that pH conditions of 8.3 and 9.0 were favorable for the adsorption of toluene and *m*-xylene onto biochar prepared from municipal solid waste.

The affinity of EMBC towards TX adsorption over a wide pH scalecould be ascribed to the increase in the degree of ionization of surface functional groups (see Figure 1(d)) essential for binding the hydrophobic TX compounds with the biochar adsorbent. Moreover, the TX removalsundervarious pH conditions implied the occurrence of additionaladsorption mechanisms such as π-π bonding interaction and hydrophobic interaction [37].

3.2.2. Effect of Biochar Dosage on TX Adsorption. Figure 3(b) represents the influence of biochar dosage on TX removal by BC and EMBC. The removal efficiencies were improved from 77.8 to 84.1% for T and from 80.2 to 87.8% for X with increasing the EMBC dosage from 2 to10 g/L, respectively. These efficiencies were higher than the adsorption patterns attainedusing the unmodified BC biochar. The increase in the number of active adsorption sites on biochars, following the increment in biochar dosage, tended to uptake additional amounts of TX molecules [31]. Due to the insignificant ($p > 0.05$) variation in the TX removal efficiencies within the range of biochar dosage investigated, 2 g/L was selected for further investigations. This selection would minimize the requirement of chemical regeneration, disposal of exhausted adsorbents, and operational and maintenance issues.

3.2.3. Effect of Initial Concentration (C_o) on TX Adsorption. Figure 3(c) shows the effect of C_o on TX adsorption at the optimum factors (pH = 10, biochar dosage = 2 g/L, and time = 60 min). For the EMBC adsorbent, an increase in

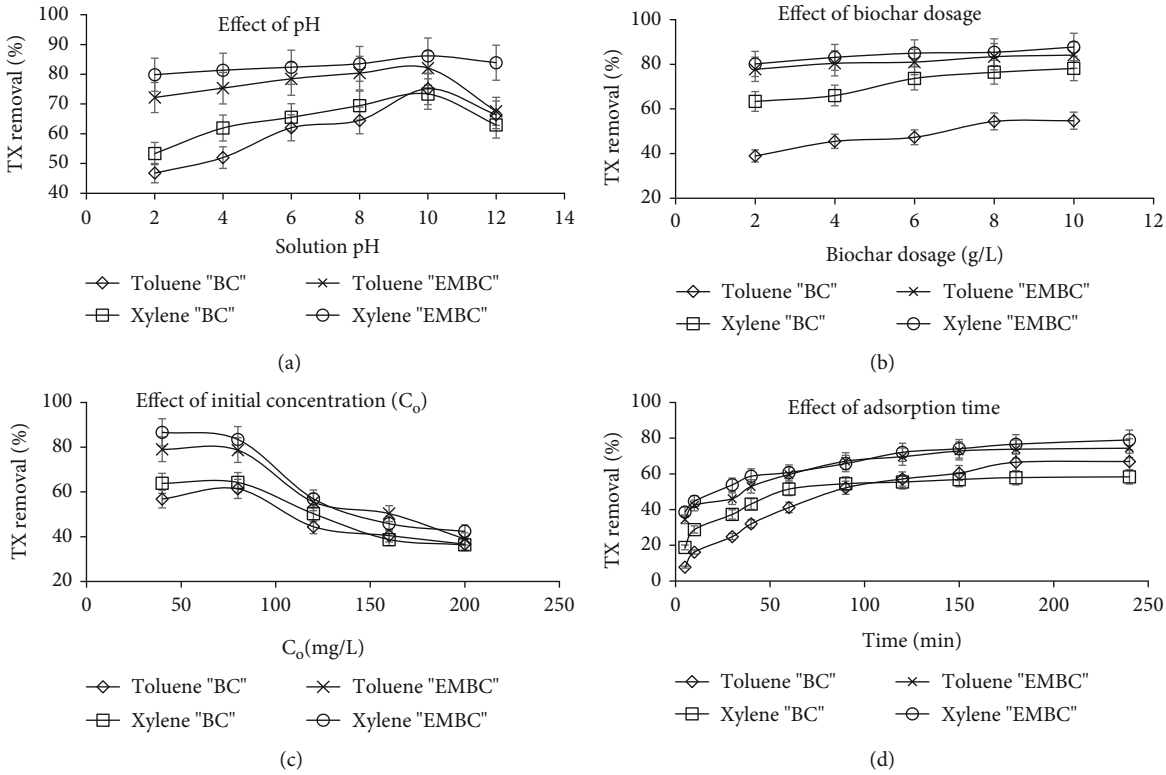

Figure 3: Effect of operational conditions on toluene and xylene (TX) removal efficiencies: (a) solution pH, (b) biochar dosage, (c) initial TX concentration, and (d) adsorption time.

C_o from 40 to 200 mg/L, respectively, caused a significant ($p < 0.05$) drop in the removal efficiencies of T from 79.1 to 39.0% and Xfrom 86.6 to 42.4%. These data were better than the removal efficiencies observed when using raw BC biochars as an adsorbent material (Figure 3(c)). The negative correlation between the TX removal efficiency and C_o could be ascribed to the low ratio of adsorption sites-to-TX molecules (or the full occupancy of the available adsorption sites) at elevated C_o [3]. Moreover, the active binding sites of biochars would be saturated with an increase inthe TX concentrations [33], suggesting that the removal efficiencies of the TX molecules by biochars were dependent on theC_o 40–200 mg/L range.

3.2.4. Effect of Adsorption Time on TX Adsorption. Figure 3(d) shows the effect of adsorption time on the removal percentage of TX by biochars (BC and EMBC) at pH = 10 and dosage = 2 g/L.For the EMBC material, the removal efficiencies of T and X were 69.6 and 72.1% at adsorption time = 120 min, respectively. These removal efficiencies were insignificantly ($p > 0.05$) improved to 74.4 and 79.0%, respectively, with anadditional increase in adsorption time to 240 min. The rapid enhancement in TX adsorption within the initial 120 min could be ascribed to the accessibility of large amounts of vacant active sites [35]. The slight increase in the removal efficiencies after 120 min could be attributed to (i) a reduction in the number of vacant active sites of biochars [5], and (ii) a formation of repulsion between the adsorbate molecules [15]. A fast removal rate, followed by a reduced pattern indicated a two-step adsorption process [33].

These results depicted that the equilibrium condition for adsorbing TX onto biochars would occur after a contact time of 120 min. A longer equilibrium time of 24 h was reported for the adsorption of T and X onto zeolite Na-P1, with removal efficiencies of 55% and 77–99%, respectively [5]. Jayawardhana et al. [15] found that about 5 h was suitable to attain an equilibrium time for adsorbing toluene and *m*-xylene by municipal solid waste biochar.

3.2.5. Adsorption Mechanisms. The results of adsorption isotherms revealed that the TX adsorbates were strongly attached to the EMBC surface via higher binding energy, as compared with BC (supplementary Figure S2; Table S1). Moreover, X had a better adsorption intensity or degree of favorability for adsorption than T. The TX molecules would form a uniform monolayer on the biochar surface within specific sites having equivalent sorption energy. In addition, all binding sites on biochars have equal affinity for the TX sorbate.

The adsorption favourability followed the order of X > T, and X needed a shorter time than T to attain a specific fractional uptake (supplementary Figure S3; Table S2). This pattern could be linked to an increase in both molecular weight (X 106.17 g/mol > T 92.14 g/mol) and hydrophobicity (X 2.77 – 3.15 > T 2.69), and a decrease in water solubility (X 175 – 198 mg/L < T 515 mg/L) [5]. A similar arrangement of adsorption favourability was established for the adsorption of

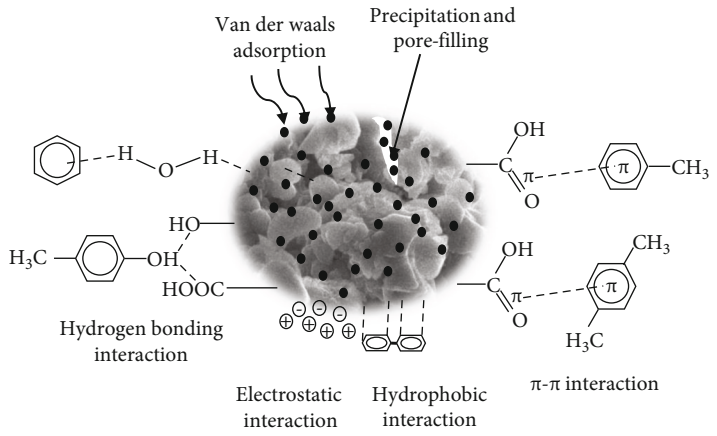

Figure 4: Possible mechanisms for adsorption of TX onto biochars.

TX ontosilica-based adsorbents [24] and multiwall carbon nanotubes [4]. Moreover, a higher affinity for X removal could be associated with the presence of two methyl groups connected to the benzene ring, augmenting the interaction with the biochar surface [16]. The reusability and recyclability of TX-loaded biochars were attained for five consecutive adsorption-desorption cycles (supplementary Figure S4).

According to the overall observation above, the adsorption of TX onto biochars could be graphically represented by Figure 4.

These adsorption mechanisms, occurring either in series or in parallel, could be summarized as follows:

(a) Monolayer adsorptiononto nearly homogenous binding sites, and no interaction would occur among adsorbate species, as revealed by the high fitting accuracy of the Langmuir isotherm model (see supplementary Figure S2 and Table S1).

(b) Precipitation and pore-filling, as depictedby the physical properties of adsorbents having many pores of different sizes (micropores and mesopores) (Table 1 and Figures 1 and 2).

(c) Electrostatic interactions due to the significant influence of solution pHon TX removal (Figure 3(a)), and the corresponding variation in electric charges (solution pH vs. biochar pH_{PZC}).

(d) Hydrogen bonding interaction with carboxyl and ester carbonyl groups of biochars

(e) π-π dispersive interaction between carboxylic oxygen-atom of biochar (electron-donor) and the aromatic ring of TX (electron-acceptor).

(f) Van der Waals sorption interaction between TX aromatic ring and electron-donating functional groups, as depicted by the surface functional group changes after adsorption (Figure 1(d)).

(g) Multiple diffusion mechanisms (surface/porediffusions), as revealed by thekinetic model parameters (see supplementary Figure S3; Table S2).

(h) A minor contribution of chemisorption

3.3. Real Petrochemical Wastewaterapplication. The treatment of real PIW by biochars is an essential step towards the practical use of sludge-based adsorbents for industrial-scale applications. Wastewater samples collected from a petrochemical industry were composed of TOC = 127.4 ± 6.1 mg/L, benzene = 94.1 ± 4.6 mg/L, T = 340.2 ± 13.0 mg/L, ethylene = 457.0 ± 32.0 mg/L, and X = 55.2 ± 3.4 mg/L, representing a multi (competitive) aqueous solution. After the first adsorption cycle, the reductions of TOC, benzene, T, ethylene, and X denoted C/C_o = 0.61, 0.66, 0.61, 0.78, and 0.61, respectively, within 60 min (Figure 5(a) - 5(e)). Further, the EMBC material was regenerated and subjected to PIW (i.e., second cycle within60 min). TheC/C_o values were changed to 0.67, 0.73, 0.64, 0.80, and 0.66, respectively, suggesting a slight decline in the adsorption performance. After five regeneration cycles, the removal efficiencies of TOC, benzene, T, ethylene, and X decreased by 51.6%, 58.3%, 43.9%, 66.6%, and 48.8%, respectively. The decline in the biochar adsorption performance along with the successive adsorption/regeneration cycles could be ascribed to (i) the loss of the adsorbent active binding sites, and/or (ii) the presence of multiple anions and cations in the real-world industrial discharges [3, 24]. With a goodregeneration ability, this high adsorption capacity validates the application of biochar-based adsorption as a tertiary treatment phase for real PIW.

3.4. Application Prospects and Cost Estimation. The environmental and economic aspects relating to the adsorption system were described for both BC and EMBC to determine the feasibility and cost-effectiveness of the adsorbent material. The cost estimation was derived as reported byHamdy et al. (2019) and Mahmoud et al. [21]. The calculations in Table 2 were represented with a precision of ±10% due to variations in local currency among countries used for assumptions.

3.4.1. Total Capital Investment (TCI). The total capital investment (TCI) refers tothe sum of money spent on buildings and equipment to establish the project objectives [36]. TCI can be calculated in terms of fixed capital cost (FCC)

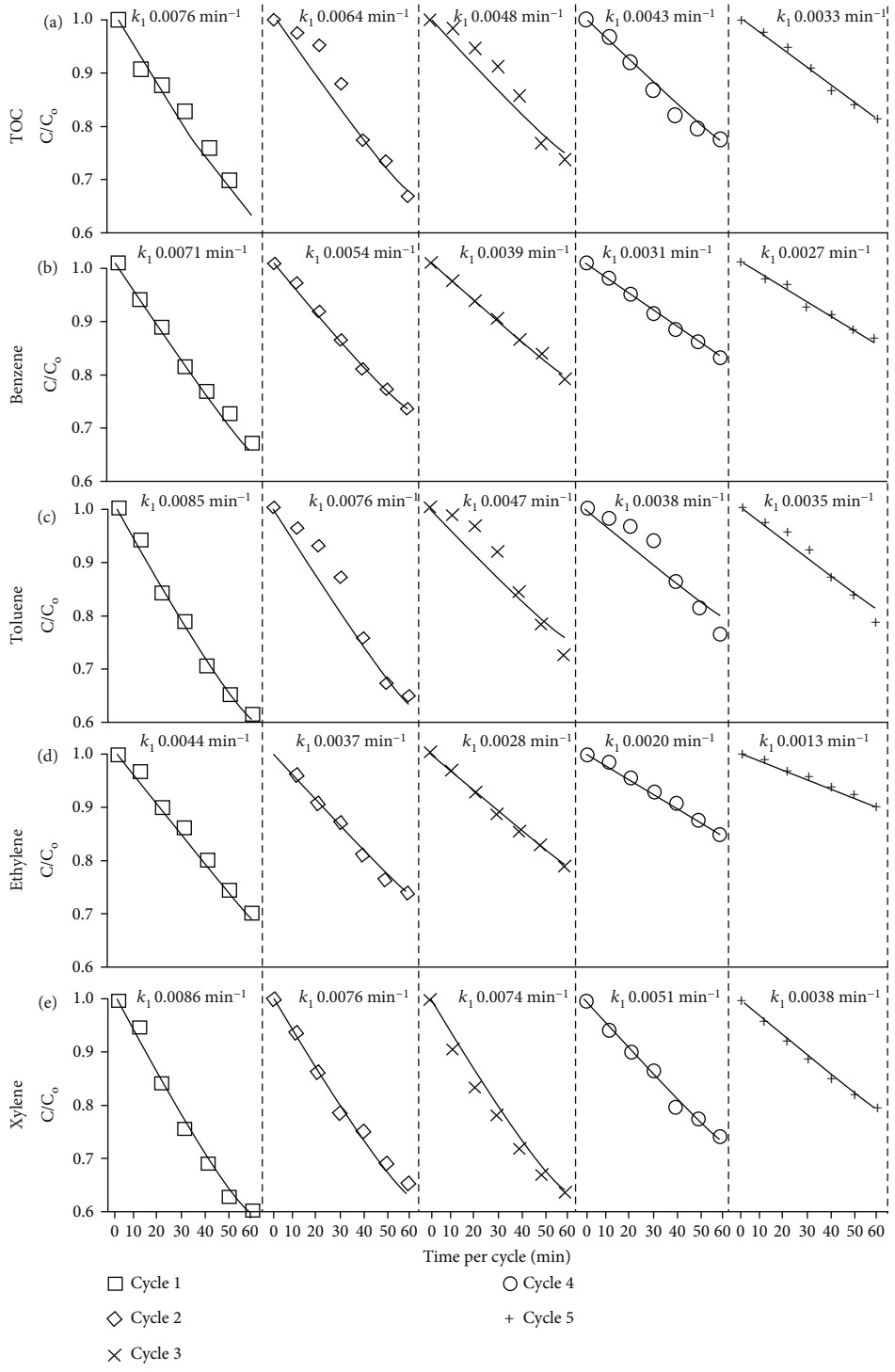

Figure 5: Performance of EMBC for treating real petrochemical effluents under five successive adsorption/regeneration cycles.

and working capital cost (WCC). As listed in Table 2, FCC was presumed regarding the land footprint, building of the offices and laboratories, electro-mechanical equipment, and piping and fitting, as reported by Elhafez et al. [7]. The low land and building costs were assigned to the financial support of the local government, attaining a "Waste Recycling" program. The equipment cost of EMBC was higher than that of BC due to the use of additional machines for handling, washing, drying, and crushing the eggshell waste [29]. The installation and construction processes were estimated as 50% of the equipment cost. Accordingly, the FCC values were 4.20 USD/m^3 for BC and5.60 USD/m^3 for EMBC. The WCC of the project was assigned to 6.5% of the FCC and regeneration costs, denoting the financing expenses used to run the adsorption process on a daily basis. Hence, the WCC values used to maintain the daily operations were

Table 2: Primary techno-economic estimation for producing biochars to treat wastewater-containing aromatic hydrocarbons, with ±10% precision.

Item	BC	EMBC	Unit
Calculation of total capital investment (TCI) in USD/m^3			
Building and construction	0.97	1.23	USD/m^3
Equipment purchase and installation	1.51	2.02	USD/m^3
Instrumentation and control	0.71	0.90	USD/m^3
Electrical system	0.67	1.01	USD/m^3
Piping system	0.34	0.45	USD/m^3
Fixed capital cost (FCC)	4.20	5.60	USD/m^3
Regeneration and recycling system	2.10	2.80	USD/m^3
Working capital cost (WCC)	0.41	0.55	USD/m^3
Total capital investment (TCI)	6.71	8.95	USD/m^3
Calculation of annual operation cost (AOC) in USD/m^3/yr			
Raw material and chemicals	0.17	0.23	USD/m^3/yr
Waste generation and disposal	0.23	0.29	USD/m^3/yr
Utilities (water and electricity)	0.25	0.31	USD/m^3/yr
Extra cost	0.22	0.30	USD/m^3/yr
Maintenance	0.08	0.11	USD/m^3/yr
Insurance	0.04	0.06	USD/m^3/yr
Annual operation cost (AOC)	0.98	1.30	USD/m^3/yr
Calculation of net profit (NP in USD/m^3/yr) and payback period (years)			
Annual profitability and revenue	1.49	2.48	USD/m^3/yr
Benefits of tertiary treated wastewater	0.23	0.36	USD/m^3/yr
Net profit (NP)	0.74	1.54	USD/m^3/yr
Tax	0.11	0.23	USD/m^3/yr
Net profit (after tax)	0.62	1.30	USD/m^3/yr
Payback period = TCI/net profit (after tax)	10.74	6.86	Years

0.41 USD/m^3 for BC and 0.55 USD/m^3 for EMBC. In this regard, the synthesis of BC and EMBC adsorbents entailed TCI values of 6.71 and 8.95 USD/m^3, respectively. A higherTCI of EMBC could be linked to the additional preparation procedures, including washing, drying/heating, and milling/sieving steps.

3.4.2. Annual Operation Cost (AOC). The annual operation cost (AOC) was estimated on a yearly basis, concerning raw material, utilities, operating labor, laboratory cost, maintenance and repair, and necessary extra costs [36]. The components of AOC were derived based on an operating time of 336 days per year, *viz.*, 8-h shifts per day, 7 days per week, and 48 weeks per year, including 5 weeks for maintenance. The cost of raw material depended on sewage sludge and eggshells required for the pyrolysis process, as well as reagents (e.g., about 9 USD for each liter of H_2SO_4 95% and 10 USD for each kg of pure NaOH) [29]. The sewage sludge is not always available for free, and the chemicals were purchased from local chemical suppliers. Table 2 also lists the cost of utilities, including tariff levels of 0.12 USD/m^3 for water supply and 0.03 USD/kWh for electricityrequirement [9]. The operators and workers earned low hourly wages as the adsorption process is relatively simple and requires little experiencefor operation [12]. Extra costs include adsorbent regeneration and recycling, and waste released during the preparation process. The maintenance and insurance expenses required for the regular repairing of damages were equivalent to 2% and 1% of FCC, respectively. According to the above calculations and data obtained from previous studies, the AOC of 0.98 USD/m^3/y for BC and 1.30 USD/m^3/y for EMBC could be determined.

3.4.3. Net Profit and Payback Period. The annual revenue could be obtained from selling the adsorbent material for removing toxic species with high concentrations [36]. The annual profitability should also includethe prices paid by the municipality to treat industrial wastewater, avoiding negative environmental consequences from releasing the contaminants via uncontrolled pathways [9]. Referring to the real market and contacts with potential customers, the EMBC price could reach up to 0.32 USD/kg compared with 0.15 USD per kg of BC for industrial applications. These prices could be compared with 0.09–0.33, 0.60, and 1.50 USD/kg forwood biochar, zeolite, and activated carbon, respectively [27]. The estimated values corresponded to a cost of about 8 USD to eliminate 1 kg of TX pollutantsfrom the environment (i.e., calculated from dividing the adsorbent price in USD/kg by adsorption capacity in mg/g). Hence, the net profit (NP) values were 0.74 and 1.54 USD/m^3/y for BC

Table 3: Possible achievement of SDGs relevant to the study outputs.

SDG	Description
Goal 2: Zero hunger	Biochar can improve agricultural soil fertility and facilitate soil carbon sequestration, increasing crop productivity. This advantage is essential to ensure sustainable food production systems and raise the incomes of small-scale food suppliers.
Goal 6: Clean water and sanitation	Biochar can be applied in wastewater treatment by eliminating (or immobilizing) heavy metals, dyes, oils, and organic and inorganic pollutants from aqueous solutions. This benefit would protect and restore water-related ecosystems, improve decentralized wastewater treatment systems, minimize nutrient leaching during irrigation, and enhance the sanitation in rural communities.
Goal 7: Affordable and clean energy	The elevated carbon content in biochar increases the energy value compared with traditional cooking fuels (e.g., firewood). Moreover, energy and synthetic gas are typically generated during biochar production. Hence, biochar could be an ideal alternative source of energy, especially for remote areas with limited electricity access [11].
Goal 9: Industry, innovation and infrastructure	Biochar synthesized from pyrolysis can act as direct catalysts in various industrial applications, which have been covered by Lee et al. [19]. These applications have also been outlined by the Biochar Industry Technology Innovation Strategic Alliance of China-BITISAC.
Goal 13: Climate action	Generally, N-based fertilizers are associated with N_2O emissions. Hence, the biochar application in agricultural fields to reduce excessive fertilizers would mitigate the GHG emission.
Goal 14: Life below water	According to the biochar-goal 6 description, biochar has additional benefits in protecting marine and coastal ecosystems from pollution (i.e., enriching life in water).

and EMBC, respectively. Further, the adsorption process was economically evaluated using the payback period; i.e., a general criterion obtained from TCI divided by NP. The payback periods (after 15% local tax) were 10.7 years for BC and 6.9 years for EMBC. These periodsare shorter than theproject lifetime (i.e., 15 years), signifying a profitability scheme. In addition, the payback period of EMBC wasshorter than that of BC because the modified biochar-related project would recover its initial investment rapidly.

3.5. Sludge-Based Biochar Technology for Meeting Sustainable Development Goals (SDGs). The increasingly stringent environmental regulations have strongly imposed the researchers to find viable and economically feasible scenarios for industrial effluent treatment. Table 3 summarizes the number of SDGs that could be relevant to the study objectives. In this work, the EMBC adsorbent showed appropriate PIW treatment under repeated adsorption-regeneration (five) cycles, expressing a good reusable and recycling ability for industrial applications. This property would reduce the environmental risks caused by industrial effluents; hence, goal 6 (Clean Water and Sanitation) and goal 14 (Life below Water) could be partially achieved. The study also represented the utilization of material of natural origin (eggshells) for synthesizing biochar with unique properties, such as a low O/C ratio (see Table 1). Hence, no toxic chemicals or reagents were used during preparation, implying that biochar would act as a competitive and sustainable resource. The prepared biochar would have other applications such as soil quality improvement, catalysts, additives for anaerobic digestion/composting, and reducing GHG emissions. These applications have been comprehensively reviewed by Zhang et al. [38]. The public should have adequate education, skills, and awareness about the potential human health, socio-economic, and environmental advantagesassociated with biochar production. Proper mass media, advertisements, and programs should transfer the understanding of biochar-based projects to the public sector, especially in developing countries. The social benefit relevant to achievable SDGs should ensure jobs creation, awareness, education, and the standard of living.

3.6. Progress and Future Perspectives. Because the reusability of exhausted biochars is essential under real PIW wastewater applications, further studies are required to develop a convenient and economical regeneration method. Various thermal, biological, micro-wave, and ultrasound methods could be used to enhance the biochar regeneration process by liberating the complex organic contaminations. Several parameters, such as breakthrough time, desorption cycles and capacity, and bed exhaustion time, should be optimized to improve the regeneration efficiency. Moreover, the solvent used as an eluting agent for biochar regeneration should be appropriately selected based on its concentration, volume, and preferable pH condition, improving the economic viability of the adsorption/desorption cycles. The ability of biochars to eliminate other compounds in PIW such as ethylene glycol, formaldehyde, tetrachloroethylene, and 1,3-butadiene by adsorption should be further investigated.

4. Conclusions

The current worksuccessfully synthesized and characterized sludge-based biochars having high aromaticity, carbonization degree, and quartz crystallization. Biochar adsorbent showed high performance for removing toluene and xylene pollutants with efficiencies of 79.1% and 86.6% at solution pH = 10, biochar dosage of 2 g/L, and C_o = 40 mg/L within 60 min. The proposed adsorption mechanism also revealed a high ability to remove petroleum hydrocarbons from both synthetic and real PIW. Moreover, the synthesized biochar exhibited an economic benefit for industrialization with a payback period = 6.9 yr. The interlinkagesbetween PIW treatment and SDGs (e.g., SDG 3, SDG 6, SDG 9, and SDG 14) were identified via (i) reducing the environmental risks

caused by industrial effluents, (ii) utilizing eggshell residues and sewage sludge for biochar preparation, avoiding waste disposal issues, (iii) synthesizing a cost-effective EMBC adsorbent showing a twofold increase in the specific surface area than conventional biochars, improving biochar production technology, and (iv) raising public awareness about waste management.

Data Availability

All data generated or analyzed during this study are included in this published article, and its supplementary information files.

Conflicts of Interest

The authors declare that they have no known competing financial interests or personal relationships that could have appeared to influence the work reported in this paper.

Authors' Contributions

AGK: Methodology, Formal analysis, Writing - original draft; MGI: Conceptualization, Visualization, Writing - review & editing; MF: Supervision, Visualization, Writing - review & editing; MN: Conceptualization, Supervision, Writing - review & editing.

Acknowledgments

We acknowledge Japan International Cooperation Agency (JICA)and Egypt-Japan University of Science and Technology (E-JUST) for financial support.

Supplementary Materials

Supplementary figures and tables illustrate(i) points of zero charge (pH_{pzc}) of the biochar adsorbents, (ii) studies of Langmuir and Freundlich adsorption isotherms, (iii) studies ofPseudo-first-order, Pseudo-second-order, and intraparticle diffusion (IPD) model kinetics, and (iv)regeneration of biochars. *(Supplementary Materials)*

References

[1] M. Abdel-Aziz, S. Younis, Y. Moustafa, and M. Khalil, "Synthesis of recyclable carbon/lignin biocomposite sorbent for _in-situ_ uptake of BTX contaminants from wastewater," *Journal of Environmental Management*, vol. 233, pp. 459–470, 2019.

[2] M. Ahmad, S. S. Lee, X. Dou et al., "Effects of pyrolysis temperature on soybean Stover- and peanut shell-derived biochar properties and TCE adsorption in water," *Bioresource Technology*, vol. 118, pp. 536–544, 2012.

[3] L. Alamo-Nole, O. Perales-Perez, and F. Roman-Velazquez, "Sorption study of toluene and xylene in aqueous solutions by recycled tires crumb rubber," *Journal of Hazardous Materials*, vol. 185, no. 1, pp. 107–111, 2011.

[4] H. Anjum, K. Johari, N. Gnanasundaram, A. Appusamy, and M. Thanabalan, "Investigation of green functionalization of multiwall carbon nanotubes and its application in adsorption of benzene, toluene & p-xylene from aqueous solution," *Journal of Cleaner Production*, vol. 221, pp. 323–338, 2019.

[5] L. Bandura, D. Kołodyńska, and W. Franus, "Adsorption of BTX from aqueous solutions by Na-P1 zeolite obtained from fly ash," *Process Safety and Environmental Protection*, vol. 109, pp. 214–223, 2017.

[6] J. Carvalho, J. Araujo, and F. Castro, "Alternative low-cost adsorbent for water and wastewater decontamination derived from eggshell waste: an overview," *Waste and Biomass Valorization*, vol. 2, no. 2, pp. 157–167, 2011.

[7] S. Elhafez, H. Hamad, A. Zaatout, and G. Malash, "Management of agricultural waste for removal of heavy metals from aqueous solution: adsorption behaviors, adsorption mechanisms, environmental protection, and techno-economic analysis," *Environmental Science and Pollution Research*, vol. 24, no. 2, pp. 1397–1415, 2017.

[8] Y. Fatimah, K. Govindan, R. Murniningsih, and A. Setiawan, "Industry 4.0 based sustainable circular economy approach for smart waste management system to achieve sustainable development goals: A case study of Indonesia," *Journal of Cleaner Production*, vol. 269, article 122263, 2020.

[9] M. Fawzy, M. Nasr, A. M. Abdel-Rahman, G. Hosny, and B. R. Odhafa, "Techno-economic and environmental approaches of Cd2+adsorption by olive leaves (Olea europaeaL.) waste," *International Journal of Phytoremediation*, vol. 21, no. 12, pp. 1205–1214, 2019.

[10] R. Fidel, D. Laird, M. Thompson, and M. Lawrinenko, "Characterization and quantification of biochar alkalinity," *Chemosphere*, vol. 167, pp. 367–373, 2017.

[11] W. Gwenzi, N. Chaukura, F. N. D. Mukome, S. Machado, and B. Nyamasoka, "Biochar production and applications in sub-Saharan Africa: opportunities, constraints, risks and uncertainties," *Journal of Environmental Management*, vol. 150, pp. 250–261, 2015.

[12] A. Hamdy, M. Mostafa, and M. Nasr, "Techno-economic estimation of electroplating wastewater treatment using zero-valent iron nanoparticles: batch optimization, continuous feed, and scaling up studies," *Environmental Science and Pollution Research*, vol. 26, no. 24, pp. 25372–25385, 2019.

[13] Z. Han, B. Sani, W. Mrozik et al., "Magnetite impregnation effects on the sorbent properties of activated carbons and biochars," *Water Research*, vol. 70, pp. 394–403, 2015.

[14] M. Hossain, V. Strezov, K. Y. Chan, A. Ziolkowski, and P. F. Nelson, "Influence of pyrolysis temperature on production and nutrient properties of wastewater sludge biochar," *Journal of Environmental Management*, vol. 92, no. 1, pp. 223–228, 2011.

[15] Y. Jayawardhana, S. R. Gunatilake, K. Mahatantila, M. P. Ginige, and M. Vithanage, "Sorptive removal of toluene and m-xylene by municipal solid waste biochar: simultaneous municipal solid waste management and remediation of volatile organic compounds," *Journal of Environmental Management*, vol. 238, pp. 323–330, 2019.

[16] N. Klomkliang, D. Do, and D. Nicholson, "Affinity and packing of benzene, toluene, andp-Xylene adsorption on a graphitic surface and in pores," *Industrial and Engineering Chemistry Research*, vol. 51, no. 14, pp. 5320–5329, 2012.

[17] T. Kraiem, A. Ben Hassen-Trabelsi, S. Naoui, and H. Belayouni, "Characterization of syngas and bio-char: co-products from pyrolysis of waste fish fats," in *IREC 2014 - 5th International Renewable Energy Congress*, Hammamet, Tunisia, 2014.

[18] A. Kumi, M. Ibrahim, M. Fujii, and M. Nasr, "Synthesis of sludge-derived biochar modified with eggshell waste for monoethylene glycol removal from aqueous solutions," *SN Applied Sciences*, vol. 2, no. 10, 2020.

[19] J. Lee, K.-H. Kim, and E. Kwon, "Biochar as a catalyst," *Renewable and Sustainable Energy Reviews*, vol. 77, pp. 70–79, 2017.

[20] D.-C. Li and H. Jiang, "The thermochemical conversion of non-lignocellulosic biomass to form biochar: A review on characterizations and mechanism elucidation," *Bioresource Technology*, vol. 246, pp. 57–68, 2017.

[21] A. Mahmoud, M. Mostafa, and M. Nasr, "Regression model, artificial intelligence, and cost estimation for phosphate adsorption using encapsulated nanoscale zero-valent iron," *Separation Science and Technology (Philadelphia)*, vol. 54, no. 1, pp. 13–26, 2019.

[22] T. Mimmo, P. Panzacchi, M. Baratieri, C. A. Davies, and G. Tonon, "Effect of pyrolysis temperature on miscanthus (Miscanthus × giganteus) biochar physical, chemical and functional properties," *Biomass and Bioenergy*, vol. 62, pp. 149–157, 2014.

[23] M. Naderi, "Surface area: Brunauer–Emmett–Teller (BET)," in *Progress Infiltration and Separation*, E. S. Tarleton, Ed., pp. 585–608, Academic Press, 2014.

[24] T. Ncube, K. S. K. Reddy, A. Al Shoaibi, and C. Srinivasakannan, "Benzene, toluene, m-xylene adsorption on silica-based adsorbents," *Energy and Fuels*, vol. 31, no. 2, pp. 1882–1888, 2017.

[25] N. Ren, Y. Tang, and M. Li, "Mineral additive enhanced carbon retention and stabilization in sewage sludge-derived biochar," *Process Safety and Environmental Protection*, vol. 115, pp. 70–78, 2018.

[26] A. Shaaban, S.-M. Se, M. F. Dimin, J. M. Juoi, M. H. M. Husin, and N. M. M. Mitan, "Influence of heating temperature and holding time on biochars derived from rubber wood sawdust via slow pyrolysis," *Journal of Analytical and Applied Pyrolysis*, vol. 107, pp. 31–39, 2014.

[27] S. Shaheen, N. K. Niazi, N. E. E. Hassan et al., "Wood-based biochar for the removal of potentially toxic elements in water and wastewater: a critical review," *International Materials Reviews*, vol. 64, no. 4, pp. 216–247, 2019.

[28] J. Shi, X. Fan, D. C. W. Tsang et al., "Removal of lead by rice husk biochars produced at different temperatures and implications for their environmental utilizations," *Chemosphere*, vol. 235, pp. 825–831, 2019.

[29] B. Silva, M. Martins, M. Rosca et al., "Waste-based biosorbents as cost-effective alternatives to commercial adsorbents for the retention of fluoxetine from water," *Separation and Purification Technology*, vol. 235, article 116139, 2020.

[30] W. Song and M. Guo, "Quality variations of poultry litter biochar generated at different pyrolysis temperatures," *Journal of Analytical and Applied Pyrolysis*, vol. 94, pp. 138–145, 2012.

[31] P. Stähelin, A. Valério, S. M. . A. Guelli Ulson de Souza, A. da Silva, J. A. Borges Valle, and A. A. Ulson de Souza, "Benzene and toluene removal from synthetic automotive gasoline by mono and bicomponent adsorption process," *Fuel*, vol. 231, pp. 45–52, 2018.

[32] Y. Tang, M. S. Alam, K. O. Konhauser et al., "Influence of pyrolysis temperature on production of digested sludge biochar and its application for ammonium removal from municipal wastewater," *Journal of Cleaner Production*, vol. 209, pp. 927–936, 2019.

[33] H. Tran, S.-J. You, A. Hosseini-Bandegharaei, and H.-P. Chao, "Mistakes and inconsistencies regarding adsorption of contaminants from aqueous solutions: A critical review," *Water Research*, vol. 120, pp. 88–116, 2017.

[34] J.-H. Yuan, R.-K. Xu, and H. Zhang, "The forms of alkalis in the biochar produced from crop residues at different temperatures," *Bioresource Technology*, vol. 102, no. 3, pp. 3488–3497, 2011.

[35] F. Yu, J. Ma, and Y. Wu, "Adsorption of toluene, ethylbenzene and xylene isomers on multi-walled carbon nanotubes oxidized by different concentration of NaOCl," *Frontiers of Environmental Science and Engineering in China*, vol. 6, no. 3, pp. 320–329, 2012.

[36] Z. Yunus, A. al-Gheethi, N. Othman, R. Hamdan, and N. N. Ruslan, "Removal of heavy metals from mining effluents in tile and electroplating industries using honeydew peel activated carbon: A microstructure and techno- economic analysis," *Journal of Cleaner Production*, vol. 251, article 119738, 2020.

[37] L. Zhang, T. Xu, X. Liu, Y. Zhang, and H. Jin, "Adsorption behavior of multi-walled carbon nanotubes for the removal of olaquindox from aqueous solutions," *Journal of Hazardous Materials*, vol. 197, pp. 389–396, 2011.

[38] Z. Zhang, Z. Zhu, B. Shen, and L. Liu, "Insights into biochar and hydrochar production and applications: A review," *Energy*, vol. 171, pp. 581–598, 2019.

[39] Y. Zhao, D. Feng, Y. Zhang, Y. Huang, and S. Sun, "Effect of pyrolysis temperature on char structure and chemical speciation of alkali and alkaline earth metallic species in biochar," *Fuel Processing Technology*, vol. 141, pp. 54–60, 2016.

Hindawi
Adsorption Science & Technology
Volume 2021, Article ID 6066906, 12 pages
https://doi.org/10.1155/2021/6066906

Research Article

Experimental and Computational Approaches for the Structural Study of Novel Ca-Rich Zeolites from Incense Stick Ash and Their Application for Wastewater Treatment

Virendra Kumar Yadav,[1] **Nisha Choudhary**,[2] **Daoud Ali**,[3] **G. Gnanamoorthy**,[4] **Gajendra Kumar Inwati**,[5] **Mohammed HA. Almarzoug**,[3] **Gokhlesh Kumar**,[6] **Samreen Heena Khan**,[2] **and Mitesh B. Solanki**[7]

[1]*Department of Microbiology, School of Sciences, P P Savani University, Surat, 394125 Gujarat, India*
[2]*Research and Development Centre, YNC Envis Pvt. Ltd., New Delhi, 110059 Delhi, India*
[3]*Department of Zoology, College of Science, King Saud University, P.O. Box 2455 Riyadh 11451, Saudi Arabia*
[4]*Department of Inorganic Chemistry, University of Madras, Guindy Campus, Chennai 600025, India*
[5]*Department of Chemistry, H.V.H.P. Institute of Post Graduate Studies and Research, S. V. Campus, Sarva Vishwavidyalaya University, Kadi, Gujarat 382715, India*
[6]*Clinical Division of Fish Medicine, University of Veterinary Medicine Vienna, 1210 Vienna, Austria*
[7]*Step-Up Jewels PVT. LTD. Khatodara Gate, Surat, 395002 Gujarat, India*

Correspondence should be addressed to Virendra Kumar Yadav; yadava94@gmail.com

Received 16 August 2021; Accepted 19 October 2021; Published 20 November 2021

Academic Editor: Ming Hua

At present, chemical Si/Al sources are mainly used as precursor materials for the manufacturing of zeolites. Such precursor materials are quite expensive for commercial synthesis. Here, we have reported the synthesis of Ca-based zeolite from incense stick ash waste by the alkali-treatment method for the first time. Incense stick ash (ISA) was used as a precursor material for the synthesis of low Si zeolites by the alkali-treatment method. The as-synthesized zeolites were characterized by various instruments like particle size analyzer (PSA), Fourier transform infrared (FTIR), X-ray diffraction (XRD), field emission scanning electron microscope (FESEM), electron diffraction spectroscopy (EDS), transmission electron microscopy (TEM), and X-ray fluorescence (XRF). FTIR and XRD helped in the identification of the microstructure and crystalline nature of the zeolites and also confirmed the synthesis of Ca-based zeolite with two thetas at 25.7°. The microscopic analysis by FESEM and TEM exhibited that the size of synthesized Ca-rich zeolites varies from 200 to 700 nm and they are aggregated and cuboidal in shape. Additionally, structural, electronic, and density of states' characteristics of gismondine ($Ca_2Al_4Si_4O_{16}{\cdot}_9H_2O$) structures were evaluated by computational simulations (first principle, density functional theorem). The structural optimization of structures was carried out in the first stage under the lowest condition of total energy and forces acting on atoms for the lattice constant, as well as the available experimental and theoretical findings. The present research approach predicted the transformation of ISA waste into a value-added mineral, i.e., zeolite, which was further used for the removal of both heavy metals and alkali metals from fly ash-based wastewater using inductively coupled plasma-optical emission spectroscopy (ICP-OES).

1. Introduction

Zeolites are crystalline aluminosilicates having elements either from group I or II as counter ions [1]. Zeolites mainly consist of Al, Si, and O, which forms their basic framework [2]. The structure of zeolites comprises the framework of $[SiO_4]^{4-}$ and $[AlO_4]^5$ tetrahedra linked to each other at the corners by sharing their oxygen [3, 4]. The tetrahedral 3D network of zeolites has a lot of voids and spaces in them [5], and these voids supplement the characteristics to the zeolites, for instance, the adsorption of molecules in the huge internal channels [6, 7]. Zeolites can be readily dehydrated and

rehydrated [8] and are used as cation exchangers [9], soil decontamination [9, 10], and molecular sieves [11]. The unique and remarkable properties of zeolites viz. porous nature, negative charge, water-insoluble, higher melting point, and water trapping property [12–14] make them a potential material as an adsorbent [15] for wastewater treatment [16], as fertilizers in agriculture [17], and as an ion exchanger [18–26]. Based on their origin, zeolites can be of two types, i.e., natural or synthetic [27, 28]. Synthetic zeolites are synthesized in laboratory conditions by optimizing the conditions.

Presently, for commercial production, synthetic zeolites are preferred over natural zeolites, as they can be modified as per the need of the industry. Moreover, synthetic zeolites are more precise, ordered, crystalline, and uniform in size of the particles. However, the synthesis of zeolites from Al- and Si-rich chemical sources is not economical [29]. On the other hand, natural zeolites are present in nature in the form of volcanic ashes [30, 31], sedimentary rocks [32], clay and kaolins [33, 34], fly ash [28, 35], bauxite minerals [36], and other earthy materials which may reduce the cost of the zeolites but purity remains a major concern. Incense stick ash (ISA) being a waste material of household and religious places can act as a source of zeolites owing to its similar composition to the natural zeolites [37, 38]. Yet to date, no attempt has been made by the scientific community for the synthesis of zeolites from overlooked waste like ISA [39]. Every day, tons of incense sticks are consumed at religious places and homes in countries like China, Thailand, Japan, Burma, and India for deity purposes which in turn produces ISA. The burning of incense stick leaves behind ashes as a residue that has to be disposed of in the river or other water sources especially in India where it holds religious values and is considered holy [40, 41]. Indian incense stick ash has high Ca, Mg, Fe, Si, and Al content where Ca and Mg alone constitute 50-60% total weight of the ash [42–44], while silica is 20% and alumina is 5-10% forming 25-30% of the total weight. All these elements are essential for the synthesis of zeolites [35]. So, instead of disposing the ashes into the river, it can be utilized for the synthesis of zeolites which may have potential to treat wastewater and protect the environment.

ISA was employed in the synthesis of zeolites, by the alkali-treatment method under laboratory conditions. As per our knowledge, ISA-based synthesis of zeolites has been reported for the first time over here. The synthesized zeolites were characterized by particle size analyzer (PSA), Fourier transform infrared (FTIR), field emission scanning electron microscope (FESEM), electron diffraction spectroscopy (EDS), transmission electron microscopy (TEM), X-ray diffraction (XRD), and X-ray fluorescence (XRF). The synthesized zeolites belong to the sodalite class and are crystalline, aggregated, and cuboidal in shape with size ranging from 200 nm to 700 nm. Further, the potential of synthesized zeolites was explored for the removal of heavy metals and alkali metals from fly ash aqueous solutions with respect to time using inductively coupled plasma-optical emission spectroscopy (ICP-OES) analysis. In conclusion, the utilization of ISA for zeolites will reduce the disposal problem of ISA and water pollution.

2. Materials and Methods

2.1. Materials. Incense stick ash, Conc. HCl (RENKEM), Conc. H_2SO_4 (RENKEM), NaOH (SRL), ethanol (SRL, India), round bottom flasks, 100 ml beakers, Whatman filter paper no. 42 (Axiva, India), and reflux condenser were used.

2.2. Method. The incense stick ash was transferred in a 100 ml beaker and washed 2-3 times with distilled water to eliminate the carbon and other unburnt particles. Further, from the ISA slurry, ferrous fractions were extracted using an external neodymium magnet [44]. Removal of ferrous from ash enhances the zeolitic property as it interferes with the transformation of zeolites [45]. The nonferrous fractions were dried either at room temperature or in an oven at 60°C till complete dryness. Thereafter, the nonferrous part was treated with 2 N H_2SO_4 in a round-bottomed (RB) flask in solid to liquid ratio of 1 : 10 at room temperature (RT). The mixture was continuously stirred using a magnetic stirrer under reflux. It removes the excess of Ca in the form of chlorides from the ash. The residue was collected by centrifuging the mixture at 7000 rpm for 5 minutes and discarding the supernatant.

The dried residue was further treated with 2 N-6 N H_2SO_4 at 95°C under stirring in a reflux condenser which removes Al from the ash by dissolving it at higher temperature. Further, the residue was collected by centrifuging the mixture at 7000 rpm for 5 minutes. The supernatant was removed, and the residue was washed 2-3 times with distilled water to eliminate any acidic moieties.

Further, in a RB flask, the dried residue was treated with 4-8 M NaOH in a ratio of 1 : 5 at 95°C along with continuous stirring for 90 minutes under reflux. The residue was collected by centrifuging the mixture at 7000 rpm for 10 minutes. The residue was collected, and the supernatant was discarded. The final residue was washed 2-3 times using distilled water to eliminate any NaOH or NaCl particles from the surface and dried in a hot air oven at 60°C. The complete schematic process for synthesis of zeolites from ISA is shown in Figure 1.

2.2.1. Preparation of 20% Fly Ash Aqueous Solutions. 50-gram fly ash was weighed and mixed with the 250 ml distilled water in a plastic bottle, and the mixture was placed inside a horizontal shaker at 200 rpm for 24-48 hours. After the time interval, the mixture was allowed to settle down at RT and filtered using Whatman filter paper no. 42 where the aqueous solution was retained while the residue was discarded. The aqueous solution was stored in a glass bottle which was used as a source of heavy and alkali metals.

2.2.2. Batch Adsorption Study of Heavy and Alkali Metals from CFA Aqueous Solutions. Batch adsorption study was conducted for the remediation of heavy and alkali metals from aqueous solutions of fly ash using ISA synthesized zeolites. For this, 150 ml of CFA aqueous solution was transferred in a 250 ml Erlenmeyer flask. To this aqueous solution, 9 mg synthesized zeolites were added. The mixture was kept in an incubator shaker at 150 rpm and 25°C. An aliquot of the sample was collected initially at time 0 minute

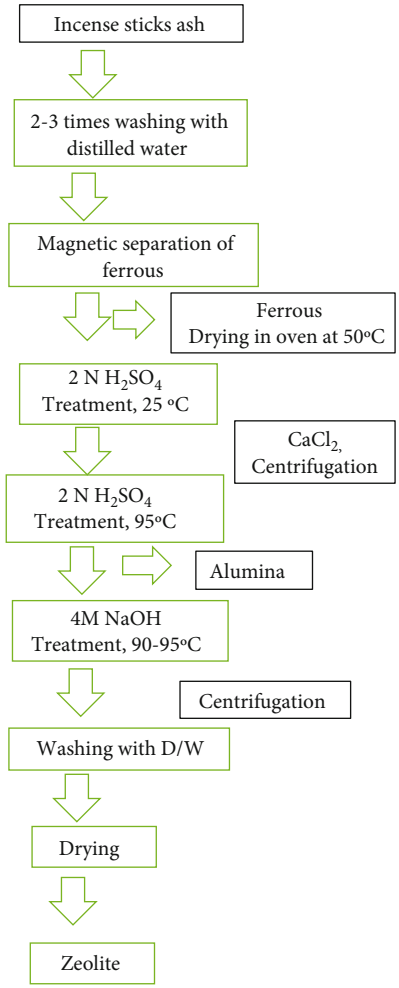

Figure 1: Schematic flowchart for zeolite synthesis from ISA.

while the final sample was collected after 120 minutes. Both the samples were analyzed by the ICP-OES for the detection of the concentration of various heavy and alkali metals after the specified time.

2.3. Characterization of Ca-Rich Zeolites. X-ray fluorescence spectroscopy (XRF) was used for the analysis of major elemental oxides of Ca-rich zeolites. The analysis was done to detect the chemical content of the zeolite sample, and for that, 5 grams of Ca-rich zeolite powder sample was taken and measured with PANalytical Epsilon 5, The Netherlands, fitted with a 4 KW with 60 kV, 125 mA, Rh anode X-ray tube. FTIR analysis was carried out using PerkinElmer, "Spectrum 6500" (USA) by solidifying the samples with KBr pellets at a resolution of 2 cm^{-1}. The mid-IR region, i.e., from 400-4000 cm^{-1}, provided the transmission measurement. The particle size measurement and distribution of the ISA sample were analyzed by Malvern Zetasizer, Z-90 (UK), particle size analyzer with a detection range of 0.1 nm to 300 microns, and it was analyzed by three average runs. The FESEM-EDS helps in revealing the size and eternal features, porosity, and shape of the synthesized calcium-rich zeolites. The surface structural analysis of zeolites was analyzed by the FESEM, Nova, NANOSEM 450 (*FEI*, USA), besides trace and minor elements by the EDS analysis using Oxford elemental analyzer attached with it. The XRD patterns of the calcium-rich zeolites were obtained using a D-8 Advance, Bruker (Germany), instrument that analyzed the sample in powdered form to confirm the nature and class of the synthesized zeolites. The XRD patterns were recorded in the 2-theta range of 5-70, with a step size of 0.02 and a time of 2 seconds/step at 30 kV and a current of 30 mA. The HRTEM was used for the identification of morphological details of zeolites, d-spacing, and diffraction pattern. The zeolite was dispersed into the double-distilled water and sonicated for 10 minutes, and using the drop cast method, a thin layer was deposited on carbon-coated copper grids which were analyzed by FEI Model Tecnai G2 20 Twin (200 kV) (USA).

3. Results and Discussion

The basic chemical composition of ISA comprises oxides such as CaO (49.6%), SiO_2 (20.3%), Al_2O_3 (4.7%), Fe_2O_3 (4.28%), MgO (3.9%), and K_2O (8.2%), making it a suitable material for the synthesis of the zeolite [44]. The Si/Al ratio of ISA was four which indicates a higher amount of silica in the ISA. Through alkali activation and simultaneous heating, the silica phase (15-20%) existing in ISA participates in the zeolitization process by dissolving into the solution whereas quartz or mullite remains in the nonreactive mineral phase [46]. Materials with higher Ca content form calcium hydroxide in aqueous media, and owing to its lower water solubility, Ca forms calcium carbonate during zeolitization [46]. During this step, there is a rise in the pH of the solution, due to calcium hydroxide along with NaOH; moreover, Ca substitutes the native Na^+ ions in the sodium zeolites with Ca^{2+} ions; hence, it may generate some calcium-exchanged zeolites [46, 47]. The ISA treatment with the NaOH hydrothermal method synthesizes zeolites by the following mechanism or chemical reactions:

$$\text{ISA} + x\text{mol}dm^{-3}\text{NaOH} \underset{\text{Time},\Delta}{\longrightarrow} \text{Zeolite} + \text{Residum} \quad (1)$$

3.1. FTIR for Identification of Functional Groups of Zeolites. FTIR spectroscopy is an important analytical technique that is used for the identification of the functional groups present in the synthesized zeolites. On the basis of functional group, a zeolite can be classified into its specific class along with XRD and EDS data. Figure 2 shows a typical FTIR spectrum of ISA-based Ca-rich zeolite products like calcium carbonate which shows polymorphism [48]. The bands around 460 cm^{-1} are attributed to the interstitial pore formation in the synthesized zeolites [49–52]. The bands around 1135 cm^{-1} are ascribed to the silicate bond Si-O-Si [53, 54], while sharper and deeper nature of the bands indicates enhanced crystallinity of the synthesized zeolites [55]. The bands near 1600 cm^{-1} are due to the -OH molecule, and another band near 3435 cm^{-1} is because of the bending vibration of the water molecule in the samples [56]. Incidentally, broader transmittance bands are detected between 3450 and

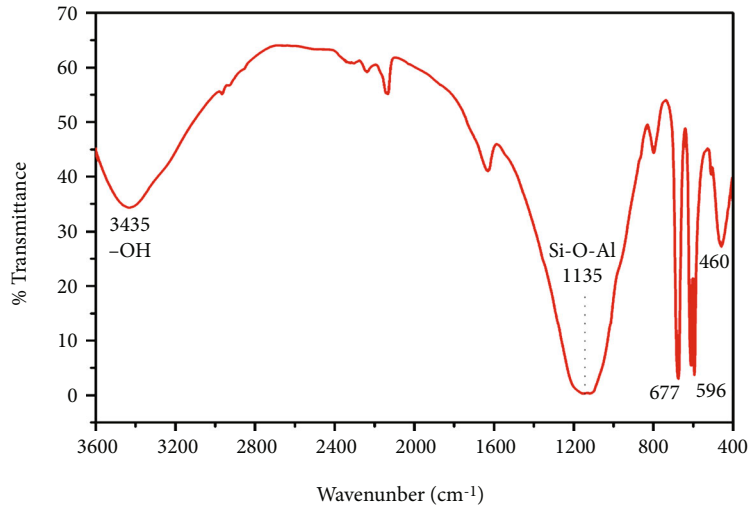

Figure 2: FTIR spectra of calcium-rich zeolite particles.

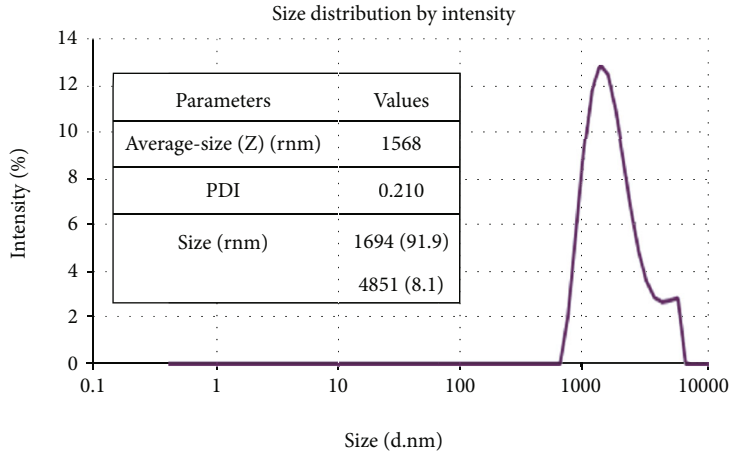

Figure 3: Particle size distribution of calcium zeolite particles.

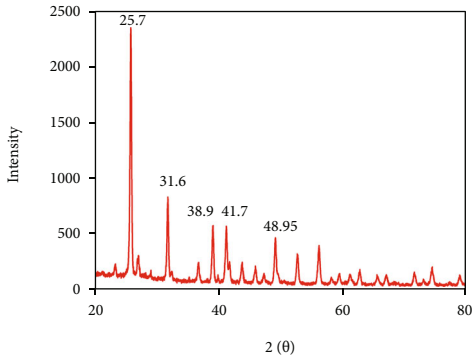

Figure 4: XRD diffractogram of calcium-rich zeolite particles.

3440 cm^{-1} and centered at 3435 cm^{-1} which can be assigned to an asymmetrical O-H- stretching linked to Na^{+}, Ca^{2+}, Si^{4+}, and/or Al^{3+} [57].

This indicates that there is bridging between Si and Al tetrahedra by the –OH ion. However, hydrated aluminum silicates comprised of such OH- bonding in the end products also exist. The stretching vibrations near 3450 cm^{-1} and bending vibrations at 1640-1620 cm^{-1} in the end products suggest zeolite crystallization and higher cation exchange capacity (CEC) [58].

3.2. PSA for the Particle Size Distribution of Zeolites. Figure 3 shows the particle size distribution of calcium zeolite particles. The average particle size is 1568 nm while the graph displays two peaks, a major peak at 1694 nm and a minor peak near 4851 nm. The PSA shows a larger particle size as compared to the TEM (200-700 nm) due to the fact that in PSA there is a formation of hydrodynamic layer (includes core and molecules adsorbed over the surface) around the nanoparticle which gives overall larger particle size [59]. Moreover, TEM analysis requires a dry sample; however, PSA uses a sample in a solvated state where solvent molecules associate with the nanoparticle surface to form a hydration layer [60], while calculating the particle size using TEM, this hydration layer is absent over the nanoparticle surface; hence, the obtained particle size was comparatively

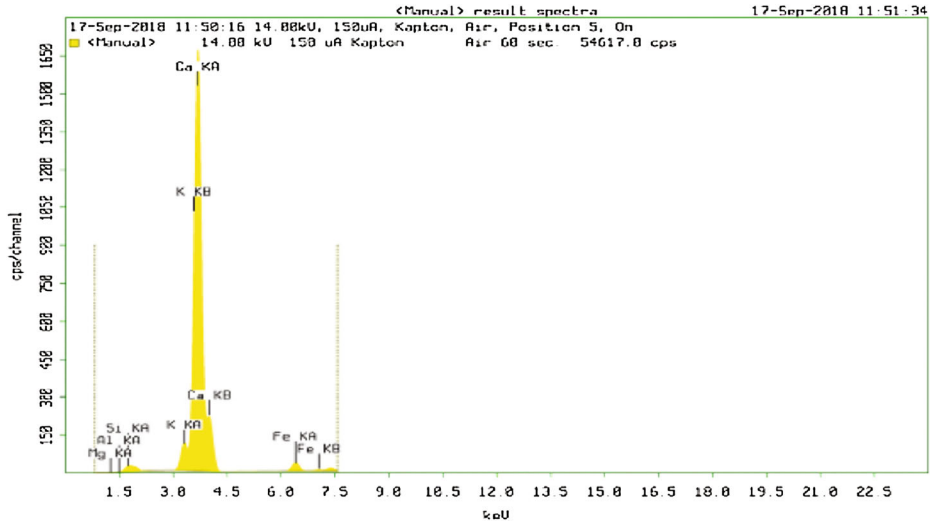

Figure 5: XRF spectra of Ca-rich zeolites.

Table 1: Major chemical components of calcium-rich zeolites by XRF.

Al	Si	Fe	Ca	Mg	K
9.684	586.197	888.618	44060.21	10.112	2826.267

lower [61]. The PDI of the particle is 0.210 which proves that the particles are monodispersed in the solvent.

3.3. XRD for Phase Identification and Confirmation of Zeolite Synthesis. The XRD diffractogram in Figure 4 revealed the minerals and crystalline nature of the Ca-zeolite which shows a major intensity peak at 25° and several minor intensity peaks at 31.6, 38.9, 41.7, and 48.95°. The formation of zeolites was determined based on the peak at 25° and d-spacing values. The most common Ca-based zeolites are gismondine ($Ca_2Al_4Si_4O_{16}{\cdot}9H_2O$) which have the characteristic peaks at 21.7°, 26.6°, and 27.9° and the peak at 32.6° could be due to calcite [62].

3.4. XRF Analysis of Zeolites for Chemical Composition of Zeolites. XRF technique is the most reliable technique for the detection of major elemental oxides present in a sample. Figure 5 shows a typical XRF spectrum of an ISA-based zeolite material, whose elemental composition is provided in Table 1. The spectra clearly show that the zeolite has the highest amount of Ca, followed by potassium, Fe, Silica, Mg, and Al. Higher Ca content confirms the presence of Ca-based zeolites. But the lower value of Al indicates that the zeolite needs to be supplemented with Al from outsource to maintain the Si/Al ratio. Lower Al content, i.e., 5-8%, in ISA can be maintained during the zeolitization step [62]. The resultant zeolite is low Si/Al-based zeolites [63]. The Ca-based zeolite nature is also supported by the FTIR and FESEM-EDS.

3.5. Morphological Analysis of ISA and Ca-Rich Zeolites by FESEM-EDS. Figures 6(a) and 6(b) show the FESEM micrographs of incense stick ash which shows irregularly shaped particles displaying higher aggregation. The size of the particles is mainly in microns, i.e., 1-12 microns. The aggregated particles are carbon- and calcium-rich particles which are also evident from XRF. The ISA particles are mainly dominated by the Ca and carbon particles. The brighter regions are metal-rich regions like Al, Si, Fe, and Ca while the darker rich regions are carbon-rich regions. Figure 6(g) is the EDS spot of the zeolites while Figure 6(h) is the EDS spectra and elemental composition table of the synthesized calcium-rich zeolites from ISA. The EDS spectra are showing mainly Ca, O, C, and S while Al and Si are present in a much lesser amount. Ca, O, Si, and Al indicate the formation of Ca-based zeolites mainly gismondine [64]. C and S are present as impurities which can be attributed due to the improper washing of the zeolite sample. As ISA has high Ca and C, so the synthesized Ca-based zeolite has both the elements in higher amount.

The absence of ferrous from EDS elemental composition analysis indicates the removal of most of the ferrous particles, which have a positive effect on the property of zeolites [65] since ferrous may interfere with the purity of the zeolites.

3.6. TEM Analysis for Morphology of Synthesized Calcium-Rich Zeolites. At the time of exposure of zeolites with the electron beams, there is a possibility of damage and charging of zeolites, so there is a requirement of sophisticated techniques such as high-resolution TEM for visualization [66]. The TEM micrographs shown in Figures 7(a)–7(d) reveal the morphology similar to the FESEM, where the cuboidal-shaped particles have lengths varying between 200 nm and 700 nm and a width ranging from 100 nm to 300 nm. Besides, there are several aggregations of smaller particles which are visible as brighter particles under the TEM field. The first three images depict Ca-rich zeolite particles in groups, while Figures 7(d) and 7(e) show two and single particle, respectively. In both, the image particles are cuboidal in shape, while in Figure 7(e), the dimension of a single

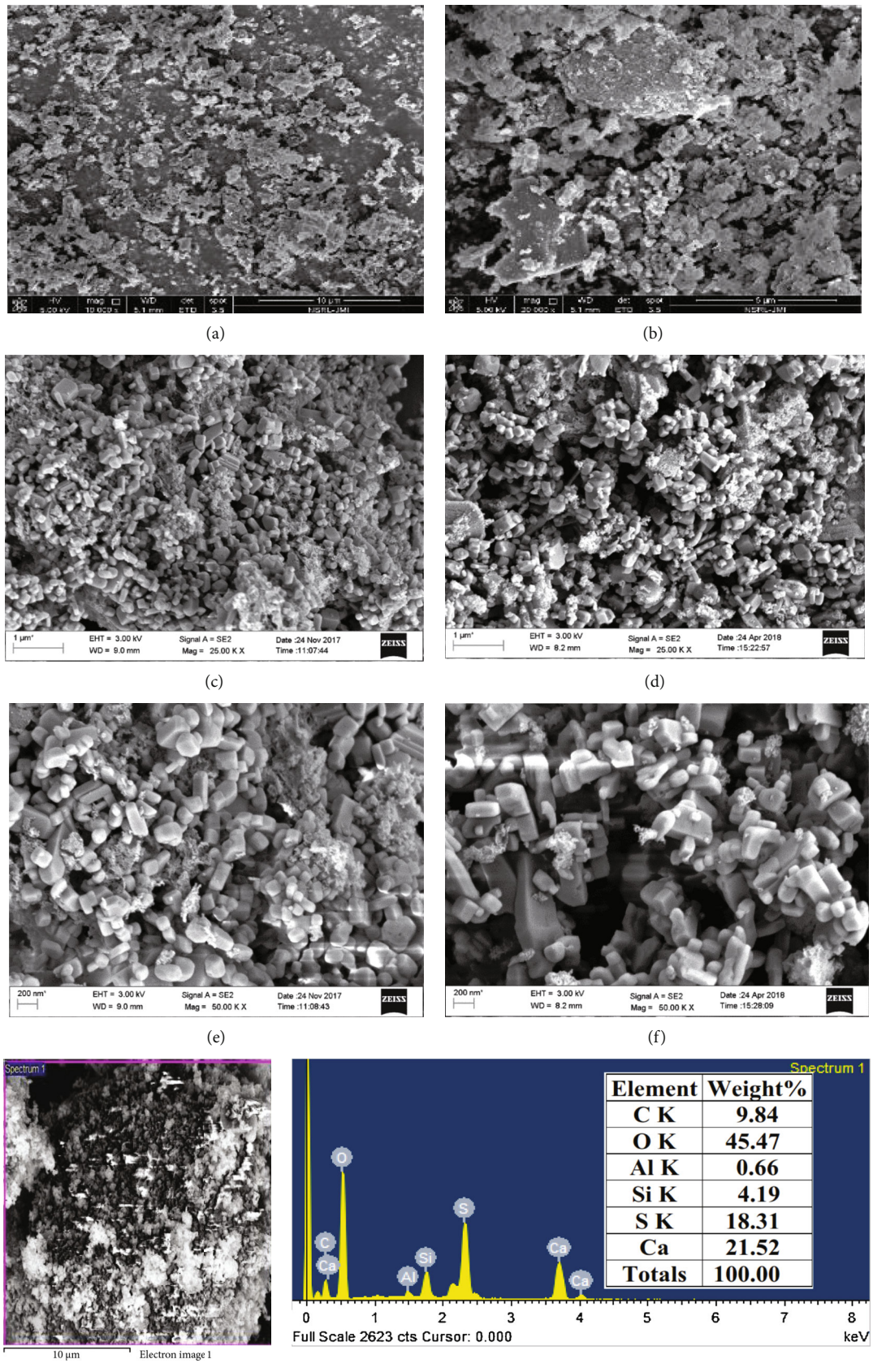

Figure 6: FESEM images of (a, b) incense stick ash, (c–f) calcium-rich zeolites, (g) EDS spot, and (h) EDS spectra.

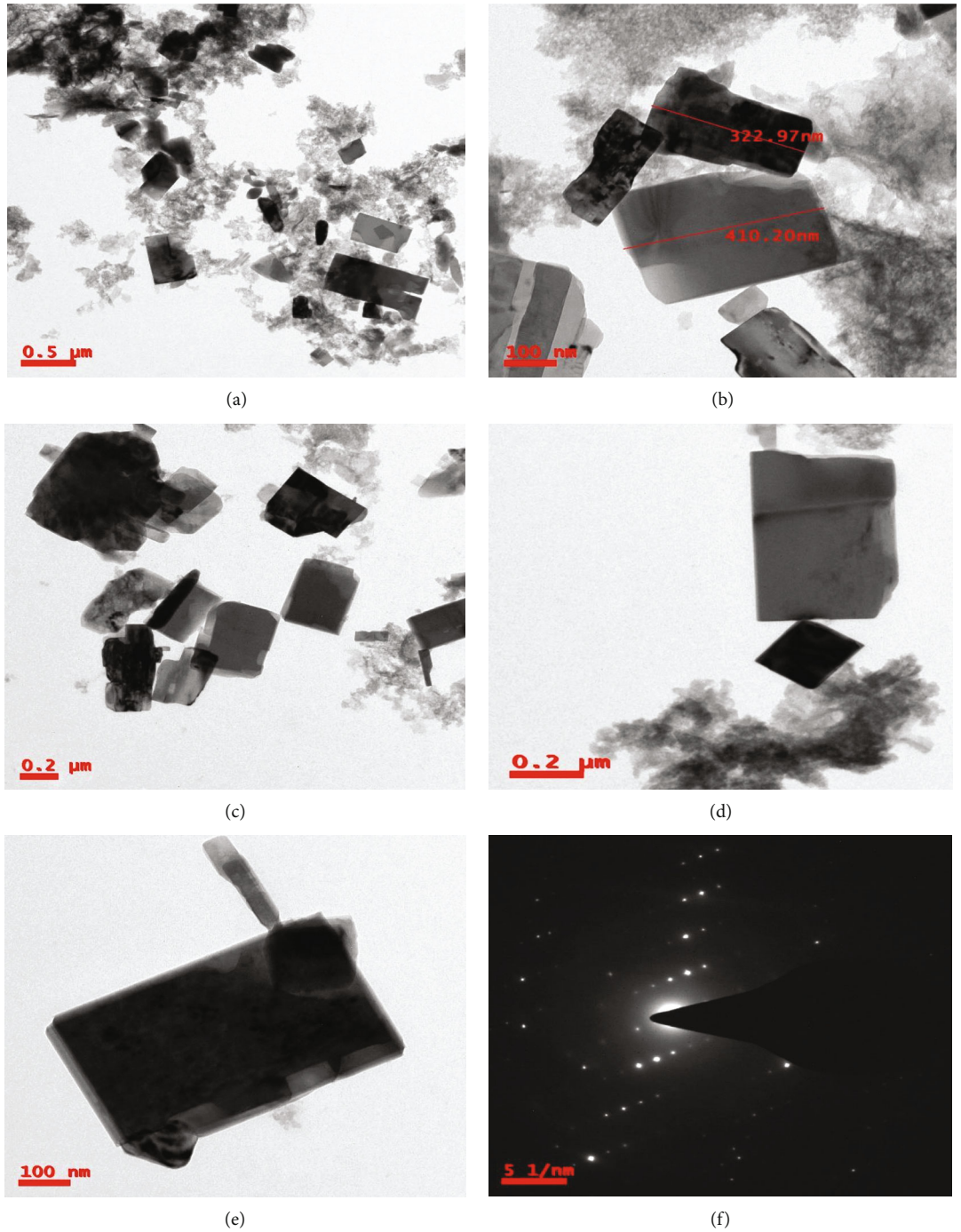

Figure 7: TEM micrographs of (a–e) calcium-rich zeolites and (f) SAED pattern.

Table 2: Heavy metal concentration after different time intervals.

Time	Concentration (mg/l)						
Minutes	Cu	Cd	Cr	Co	Ni	Pb	Zn
0	1.340	0.092	0.15	0.293	0.833	0.014	4.49
120	0.97	0.033	0.03	0.233	0.638	-0.034	2.30

particle is 250 nm wide and 700 nm long. The crystal images of zeolite are overlapping to some extent; the edges of the crystal are obvious. Moreover, the scattering area electron diffraction (SAED) pattern in Figure 7(f) shows that the particles have polycrystalline nature.

The Ca-based or Ca-rich zeolites have several advantages over Na-based zeolites. The application of Na-based zeolite is restricted in soil and water and is not an appropriate material to be used in agricultural- and aqua-based products as

Table 3: Concentration of nonheavy metals after different time intervals.

Time	Concentration (mg/l)				
Minutes	Ba	Ca	Mg	Mn	Al
0	1.02	1.340	0.092	5.540	152.0
120	0.27	0.97	0.033	3.74	56.9

higher sodium content enhances the salinity and sodicity of the soil/water [67]. The challenging problems in such situations are (a) to reduce the harsh conditions of Na-based ISA zeolites during its application in soil and water and (ii) to increase the Ca-exchanged zeolites. So the synthesized zeolites from the ISA will solve the problem associated with these issues.

3.7. Remediation of Heavy Metals and Alkali Metals by Ca-Rich Zeolites. Here, the dosage of the zeolite particles was fixed, i.e., 10 mg in 200 ml solution of the wastewater. The remediation of heavy (Cd, Mn, Zn, Pb, Al, Cu, Co, Cr, and Ni) and alkali metals (Ca, Mg, Ba, and Al) by adsorption process in a multicomponent system was performed by shake flask method in an incubator shaker. The percent removal of heavy metals was calculated by the following formula:

$$\text{Removal\%} = [(C_o - C_f)C_o] \times 100, \quad (2)$$

where C_o and C_f are the initial and equilibrium concentration (ppm) of metal ions in solution, respectively.

The removal efficiency of all the seven heavy metals (Cu, Co, Ni, Pb, Cr, Zn, and Cd) decreased, in the solution after 2 hours as shown in Table 2, while the value of Pb reached below the detection level of ICP-OES as the Pb concentration was already less in the wastewater solution in comparison to the other heavy metals. Moreover, higher electronegativity of Pb can also be a contributing factor [68]. In the process of metal ion adsorption, the elemental property of electronegativity becomes highly significant as higher electronegativity is responsible for the stronger covalent formation of metals with O atoms situated on the surface of zeolites [69].

As far as the remediation of the nonheavy metals (Ba, Ca, Mg, Mn, and Al) is concerned, a reduction in the value of Ba, Ca, Mg, Mn, and Al was noticed after 2 hours as shown in Table 3. All these are alkali metals that are present significantly in fly ash, and their disposal into the river or other water bodies will increase the alkalinity or hardness of water [70]. So zeolites can be an efficient and economical adsorbent for the removal of alkali metals from wastewater [70]. Here, the adsorption of both heavy metals and alkali metals takes place on the surface of zeolite particles due to the electrostatic attraction and coordination. Several investigators have also reported the remediation of numerous heavy metals from wastewater by nanoadsorbents due to electrostatic attraction and coordination [71]. The zeolite surface is positively charged at neutral or slightly acidic pH, which gives rise to PZC repulsion to cations. The coordination between CH on the zeolite surface and the bivalent metal ions is responsible for the adsorption of cations on the zeolites. Such phenomenon of adsorption and deposition was observed because the fly ash aqueous solutions are a multicomponent system where several heavy metals and nonheavy metals compete for the limited adsorption sites. Once these binding sites are occupied, there is a healthy competition among ions and nonmetallic ions, which results in desorption of the heavy metals.

4. Computation Approach

A theoretical simulation to investigate the structural, electronic, and density of states' characteristics of gismondine ($Ca_2Al_4Si_4O_{16}{\cdot}9H_2O$) structures was carried out. Figure 8 shows the estimated theoretical models using first principles, density functional theory calculations [72] as implemented in the Quantum Espresso program [73]. Interaction of atomic cores and valence electrons utilizing the extremely soft pseudopotential technique is proposed by Vanderbil [73]. Perdew-Burke-Ernzerhof (PBE) [74] exchange correlational functional was used to solve the Kohn–Sham equation [75], using the generalized gradient approximation [76]. It has shown its ability to replicate ground state energy characteristics across a broad range of a variety of crystals that are similar to the experimental findings. An electronic wave function was added. 70 Ry energy cutoff values at particular k-points were produced by the $18 \times 18 \times 18$ Monkhorst-Pack mesh in the Brillouin zone for gismondine ($Ca_2Al_4Si_4O_{16}{\cdot}9H_2O$) structures. The energy convergence threshold between two successive steps was maintained at 10-6 eV, and the maximal Hellmann-Feynman force acting on each atom was kept to a minimum [77] less than 0.001 eV. Finally, the optimized structures were utilized to compute the electronic and density of states' properties calculated in the present study.

4.1. Electronic and PDOS Structure Calculation. In Figure 9, the structural optimization of gismondine ($Ca_2Al_4Si_4O_{16}{\cdot}$ 9H2O) structures was carried out in the first stage under the lowest condition of total energy and forces acting on atoms for the lattice constant, as well as the available experimental [78] and theoretical findings. The computed value of the lattice constant agrees well with observed values [78] and differs by less than 1% from other theoretical work [79]. The differences can be attributed to the differences in calculating methods.

To better comprehend the electronic characteristics, the density of states (DOS) and projected DOS (PDOS) are computed, since they may explain the cause for bandgap modulation and the gap of gismondine ($Ca_2Al_4Si_4O_{16}{\cdot}$ $9H_2O$) structures was in 4.734 eV. The DOS and PDOS of Ca, Al, Si, and O atoms are shown in Figure 9. The picture clearly shows that s, p, and d are the most contributed energy in the formation of gismondine type zeolite; the Ca and Al d orbital is the strong peak at Fermi level just above the conduction band maxima (CBM) in the range 0 to -8 eV, as well as some density contribution near the valence band minima (VBM) in the region 4 eV to 18 eV. This additional

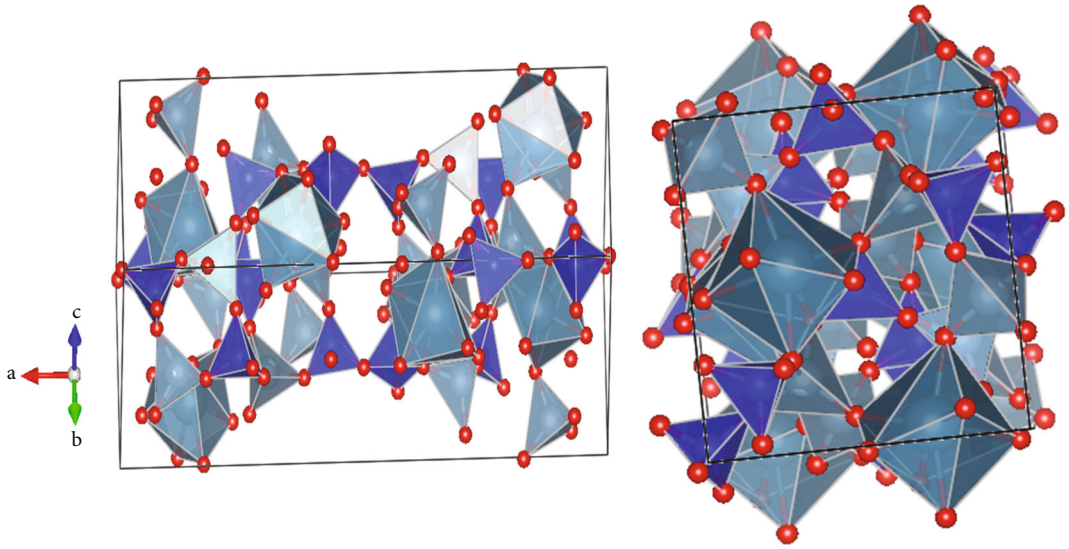

Figure 8: The crystal structure of gismondine ($Ca_2Al_4Si_4O_{16}{\cdot}9H_2O$).

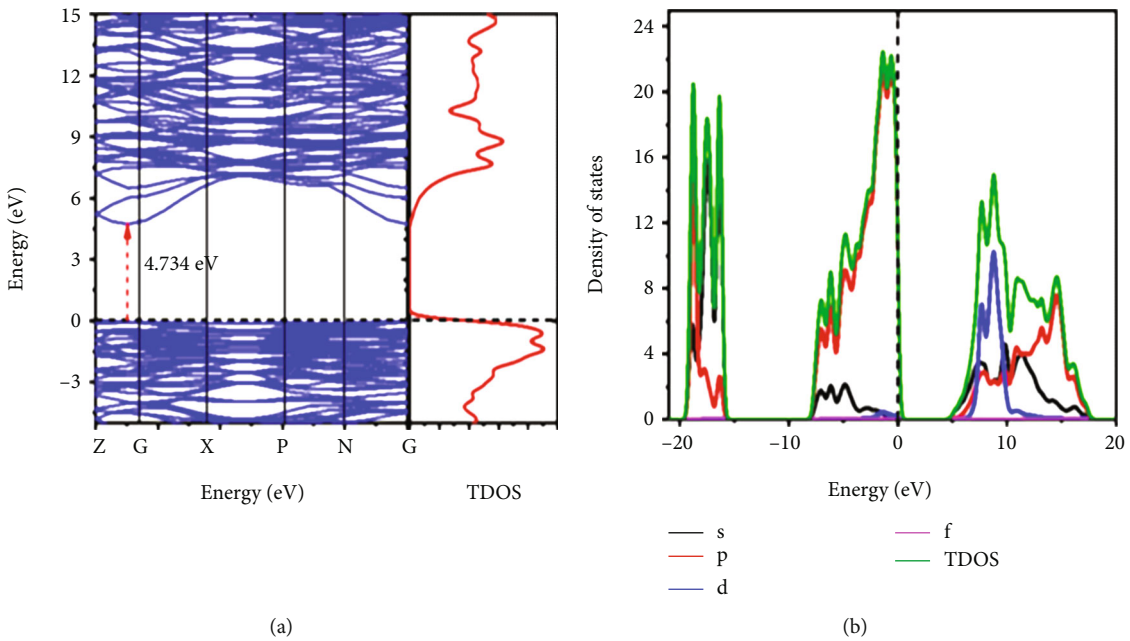

Figure 9: Band structures. (a) Electronic band structure and TDOS. (b) Projection density of states (PDOS) plot of gismondine ($Ca_2Al_4Si_4O_{16}{\cdot}9H_2O$).

peak results from the contribution of 2s and 2p orbital electrons in Ca and Al at both CBM and VBM. The 3d orbit electron of Si and O has a little effect on the VBM between -11 and -20 eV.

5. Conclusion

Increasing global awareness towards environmental issues acts as a driving force towards the recovery of value-added minerals from waste materials. The present paper focuses on the green synthesis of zeolites using incense stick ash waste. The synthesis of zeolites from the household waste incense stick ash is justified as the waste, whose disposal causes environmental problem especially in water, is utilized. The obtained Ca-rich zeolites were cuboidal in shape with size between 200 and 700 nm as revealed by TEM analysis. The zeolites were microporous and crystalline in nature suitable as an adsorbent material for the remediation of contaminants present in water. The other analysis results such as FTIR, PSA, XRD, and XRF also confirmed the successful synthesis of zeolites from ISA. The present work effectively draws possibility to utilize the ISA for the synthesis of Ca-rich zeolites. Besides, theoretical calculations were also established for the band structure and density of states'

characteristics of gismondine ($Ca_2A_{l4}Si_4O_{16}{\cdot}9H_2O$) structures. The structural optimization was carried out in the first stage under the lowest condition of total energy and forces acting on atoms for the lattice constant. The bandgap of gismondine structures was in 4.734 eV. The quality of the fabricated zeolite product strongly relies on environmental treatments and the strength of the raw materials [80]. The ISA-based zeolites have the potential to remediate both heavy and alkali metals from wastewater. Hence, the ISA-based synthesis of zeolites is an efficient, low-cost, and green chemistry-based method that opens a new possibility in the field of material science and catalysis.

Data Availability

The data sets used and analyzed during the current study are available within the article only.

Conflicts of Interest

The authors declare that there is no conflict of interest.

Authors' Contributions

Virendra Kumar Yadav (V.K.Y.), G. Gnanamoorthy (G.G.), Nisha Choudhary (N.C.), Daoud Ali (D.A.), and Mohammed HA. Almarzoug (M.H.A.)Gokhlesh Kumar (G.K.) were responsible for conceptualization; V.K.Y., G.G., and N.C. were responsible for methodology; V.K.Y., D.A., and N.C. were responsible for software; V.K.Y., D.A., G.K., and N.C. were responsible for validation; V.K.Y., S.H.K., M.H.A., D.A., G.K., and N.C. were responsible for formal analysis; V.K.Y., G.G., and N.C. were responsible for investigation; V.K.Y., D.A., and N.C. were responsible for resources; G.K., D.A., M.H.A., G.G., and N.C. were responsible for data curation; D.A., V.K.Y., G.K., G.G., and N.C. were responsible for writing—original draft preparation; D.A. and V.K.Y. were responsible for writing—review and editing; V.K.Y., M.H.A., G.G., and N.C. were responsible for visualization; V.K.Y. and N.C. were responsible for supervision; V.K.Y., D.A., and N.C. were responsible for project administration; D.A. was responsible for funding acquisition. Reviewing, editing, and computational approach simulated by G.K.I. and S.H.K. and Mitesh B. Solanki. All authors have read and agree to the published version of the manuscript.

Acknowledgments

This work was funded by Researchers Supporting Project number RSP-2021/165, King Saud University, Riyadh, Saudi Arabia.

References

[1] J. Grand, H. Awala, and S. Mintova, "Mechanism of zeolites crystal growth: new findings and open questions," *CrystEngComm*, vol. 18, no. 5, pp. 650–664, 2016.

[2] S. Prodinger and M. A. Derewinski, "Recent progress to understand and improve zeolite stability in the aqueous medium," *Petroleum Chemistry*, vol. 60, no. 4, pp. 420–436, 2020.

[3] S. Guida, C. Potter, B. Jefferson, and A. Soares, "Preparation and evaluation of zeolites for ammonium removal from municipal wastewater through ion exchange process," *Scientific Reports*, vol. 10, no. 1, article 12426, 2020.

[4] W. Bao, L. Liu, H. Zou et al., "Removal of Cu^{2+} from aqueous solutions using Na-a zeolite from oil shale ash," *Chinese Journal of Chemical Engineering*, vol. 21, no. 9, pp. 974–982, 2013.

[5] J. Přech, P. Pizarro, D. P. Serrano, and J. Čejka, "From 3D to 2D zeolite catalytic materials," *Chemical Society Reviews*, vol. 47, pp. 8263–8306, 2018.

[6] S. Krause, N. Hosono, and S. Kitagawa, "Chemistry of soft porous crystals: structural dynamics and gas adsorption properties," *Angewandte Chemie International Edition*, vol. 59, pp. 15325–15341, 2020.

[7] N. Jiang, R. Shang, S. G. J. Heijman, and L. C. Rietveld, "High-silica zeolites for adsorption of organic micro-pollutants in water treatment: a review," *Water Research*, vol. 144, pp. 145–161, 2018.

[8] K. Mlekodaj, J. E. Olszowka, V. Tokarova et al., "Effect of alkali-free synthesis and post-synthetic treatment on acid sites in beta zeolites," *Molecules*, vol. 25, no. 15, p. 3434, 2020.

[9] P. J. Reeve and H. J. Fallowfield, "Natural and surfactant modified zeolites: a review of their applications for water remediation with a focus on surfactant desorption and toxicity towards microorganisms," *Journal of Environmental Management*, vol. 205, pp. 253–261, 2018.

[10] C. Belviso, "Zeolite for potential toxic metal uptake from contaminated soil: a brief review," *Processes*, vol. 8, no. 7, p. 820, 2020.

[11] Y. Li, L. Li, and J. Yu, "Applications of zeolites in sustainable chemistry," *Chem*, vol. 3, pp. 928–949, 2017.

[12] S. Sharma and A. Bhattacharya, "Drinking water contamination and treatment techniques," *Applied Water Science*, vol. 7, pp. 1043–1067, 2017.

[13] J. Byun, H. A. Patel, D. Thirion, and C. T. Yavuz, "Charge-specific size-dependent separation of water-soluble organic molecules by fluorinated nanoporous networks," *Nature Communications*, vol. 7, article 13377, 2016.

[14] A. Georgiadis, N. Charisiou, and M. Goula, "Removal of hydrogen sulfide from various industrial gases: a review of the most promising adsorbing materials," *Catalysts*, vol. 10, p. 36, 2020.

[15] W. Zou, H. Bai, L. Zhao, K. Li, and R. Han, "Characterization and properties of zeolite as adsorbent for removal of uranium(VI) from solution in fixed bed column," *Journal of Radioanalytical and Nuclear Chemistry*, vol. 288, pp. 779–788, 2011.

[16] N. Elboughdiri, "The use of natural zeolite to remove heavy metals Cu (II), Pb (II) and Cd (II), from industrial wastewater," *Cogent Engineering*, vol. 7, no. 1, p. 13, 2020.

[17] S. A. A. Nakhli, M. Delkash, B. E. Bakhshayesh, and H. Kazemian, "Application of zeolites for sustainable agriculture: a review on water and nutrient retention," *Water, Air, & Soil Pollution*, vol. 228, no. 12, p. 464, 2017.

[18] H. Deng and Y. Ge, "Formation of NaP zeolite from fused fly ash for the removal of Cu(ii) by an improved hydrothermal method," *RSC Advances*, vol. 5, pp. 9180–9188, 2015.

[19] D. Wu, B. Zhang, C. Li, Z. Zhang, and H. Kong, "Simultaneous removal of ammonium and phosphate by zeolite synthesized from fly ash as influenced by salt treatment," *Journal of Colloid and Interface Science*, vol. 304, pp. 300–306, 2006.

[20] Ž. Z. Tasić, G. D. Bogdanović, and M. M. Antonijević, "Application of natural zeolite in wastewater treatment: a review," *Journal of Mining and Metallurgy A: Mining*, vol. 55, no. 1, pp. 67–79, 2019.

[21] B. de Gennaro, P. Aprea, B. Liguori, B. Galzerano, A. Peluso, and D. Caputo, "Zeolite-rich composite materials for environmental remediation: arsenic removal from water," *Applied Sciences*, vol. 10, no. 19, p. 6939, 2020.

[22] H. Tang, X. Xu, B. Wang, C. Lv, and D. Shi, "Removal of ammonium from swine wastewater using synthesized zeolite from fly ash," *Sustainability*, vol. 12, p. 15, 2020.

[23] P. A. Dinis, M. M. S. Cabral Pinto, E. Garzanti, and F. T. Rocha, "Detrital record of the denudation of volcanic islands under sub-tropical climate (Cape Verde)," *Geochemistry*, vol. 79, pp. 235–246, 2019.

[24] M. M. S. Cabral-Pinto, M. Inácio, O. Neves et al., "Human health risk assessment due to agricultural activities and crop consumption in the surroundings of an industrial area," *Exposure and Health*, vol. 12, pp. 629–640, 2019.

[25] M. M. S. Cabral Pinto, P. A. Dinis, M. M. V. G. Silva, and E. A. Ferreira da Silva, "Sediment generation on a volcanic island with arid tropical climate: a perspective based on geochemical maps of topsoils and stream sediments from Santiago Island, Cape Verde," *Applied Geochemistry*, vol. 75, pp. 114–124, 2016.

[26] M. M. S. C. Pinto, E. Silva, M. Silva, P. Melo-Gonçalves, and C. Candeias, "Environmental risk assessment based on high-resolution spatial maps of potentially toxic elements sampled on stream sediments of Santiago, Cape Verde," *Geosciences*, vol. 4, no. 4, pp. 297–315, 2014.

[27] M. Król, "Natural vs. synthetic zeolites," *Crystals*, vol. 10, no. 7, p. 622, 2020.

[28] W. Franus, M. Wdowin, and M. Franus, "Synthesis and characterization of zeolites prepared from industrial fly ash," *Environmental Monitoring and Assessment*, vol. 186, no. 9, pp. 5721–5729, 2014.

[29] M. Gougazeh and J. C. Buhl, "Synthesis and characterization of zeolite A by hydrothermal transformation of natural Jordanian kaolin," *Journal of the Association of Arab Universities for Basic and Applied Sciences*, vol. 15, no. 1, pp. 35–42, 2014.

[30] A. Dussan, J. A. Calderón, and H. P. Quiroz, "Zeolites derived from natural minerals: solid rock and volcanic ash," *Materials Today*, vol. 34, pp. 148-149, 2020.

[31] N. Shiota, M. Togo, and A. Nakahira, "Synthesis of zeolites from volcanic ash and its evaluation," *Journal of the Japan Society of Powder and Powder Metallurgy*, vol. 64, pp. 601–605, 2017.

[32] M. Ç. Karakaya, N. Karakaya, and F. Yavuz, "Geology and conditions of formation of the zeolite-bearing deposits southeast of Ankara (Central Turkey)," *Clays and Clay Minerals*, vol. 63, pp. 85–109, 2015.

[33] P. Pereira, B. Ferreira, N. Oliveira et al., "Synthesis of zeolite a from metakaolin and its application in the adsorption of cationic dyes," *Applied Sciences*, vol. 8, no. 4, p. 608, 2018.

[34] X.-Y. Li, Y. Jiang, X.-Q. Liu, L.-Y. Shi, D.-Y. Zhang, and L.-B. Sun, "Direct synthesis of zeolites from a natural clay, attapulgite," *ACS Sustainable Chemistry & Engineering*, vol. 5, no. 7, pp. 6124–6130, 2017.

[35] V. K. Yadav, R. Suriyaprabha, G. K. Inwati et al., "A noble and economical method for the synthesis of low cost zeolites from coal fly ash waste," *Advances in Materials and Processing Technologies*, vol. 6, pp. 1–19, 2021.

[36] C. Wang, J. Zhou, Y. Wang, M. Yang, Y. Li, and C. Meng, "Synthesis of zeolite X from low-grade bauxite," *Journal of Chemical Technology & Biotechnology*, vol. 88, pp. 1350–1357, 2013.

[37] V. K. Yadav, N. Choudhary, V. Tirth et al., "A short review on the utilization of incense sticks ash as an emerging and overlooked material for the synthesis of zeolites," *Crystals*, vol. 11, no. 10, p. 1255, 2021.

[38] V. K. Yadav, K. K. Yadav, V. Tirth et al., "Extraction of value-added minerals from various Agricultural, Industrial and Domestic Wastes," *Industrial and Domestic Wastes Materials*, vol. 14, no. 21, p. 6333, 2021.

[39] V. K. Yadav, G. Gnanamoorthy, M. M. S. Cabral-Pinto et al., "Variations and similarities in structural, chemical, and elemental properties on the ashes derived from the coal due to their combustion in open and controlled manner," *Environmental Science and Pollution Research*, vol. 28, pp. 32609–32625, 2021.

[40] T.-C. Lin, G. Krishnaswamy, and D. S. Chi, "Incense smoke: clinical, structural and molecular effects on airway disease," *Clinical and Molecular Allergy*, vol. 6, no. 1, pp. 3–3, 2008.

[41] M. Waghmode, A. Gunjal, N. Nawani, and N. Patil, "Management of floral waste by conversion to value-added products and their other applications," *Waste and Biomass Valorization*, vol. 9, pp. 33–43, 2018.

[42] C.-R. Yang, T.-C. Lin, and F.-H. Chang, "Correlation between calcium carbonate content and emission characteristics of incense," *Journal of the Air & Waste Management Association*, vol. 56, no. 12, pp. 1726–1732, 2006.

[43] V. K. Yadav, B. Singh, and N. Choudhary, "Characterization of Indian incense stick powders for their physical, chemical and mineralogical properties," *World Journal of Environmental Biosciences*, vol. 9, pp. 39–43, 2020.

[44] V. K. Yadav, K. K. Yadav, G. Gnanamoorthy et al., "A novel synthesis and characterization of polyhedral shaped amorphous iron oxide nanoparticles from incense sticks ash waste," *Environmental Technology & Innovation*, vol. 20, article 101089, 2020.

[45] X. Ren, R. Qu, S. Liu et al., "Synthesis of zeolites from coal fly ash for removal of harmful gaseous pollutants: a review," *Aerosol and Air Quality Research*, vol. 20, pp. 1127–1144, 2020.

[46] N. Koshy, D. Singh, B. Jha, S. Kadali, and J. Patil, "Characterization of Na and Ca zeolites synthesized by various hydrothermal treatments of fly ash," *Advances in Civil Engineering Materials*, vol. 4, pp. 131–143, 2015.

[47] N. Tangboriboon, S. Wongkasemjit, R. Kunanuruksapong, and A. Sirivat, "An innovative synthesis of calcium zeolite type a catalysts from eggshells via the sol–gel process," *Journal of Inorganic and Organometallic Polymers and Materials*, vol. 21, pp. 50–60, 2011.

[48] R. A. Boulos, F. Zhang, E. S. Tjandra, A. D. Martin, D. Spagnoli, and C. L. Raston, "Spinning up the polymorphs of calcium carbonate," *Scientific Reports*, vol. 4, p. 3616, 2014.

[49] H. Isawi, "Using zeolite/polyvinyl alcohol/sodium alginate nanocomposite beads for removal of some heavy metals from wastewater," *Arabian Journal of Chemistry*, vol. 13, pp. 5691–5716, 2020.

[50] H. Smail, M. Rehan, K. Shareef, Z. Ramli, A.-S. Nizami, and J. Gardy, "Synthesis of uniform mesoporous zeolite ZSM-5

catalyst for Friedel-Crafts acylation," *ChemEngineering*, vol. 3, p. 35, 2019.

[51] P. Innocenzi, "Infrared spectroscopy of sol–gel derived silica-based films: a spectra-microstructure overview," *Journal of Non-Crystalline Solids*, vol. 316, pp. 309–319, 2003.

[52] N. M. Musyoka, L. F. Petrik, G. Balfour, W. M. Gitari, and E. Hums, "Synthesis of hydroxy sodalite from coal fly ash using waste industrial brine solution," *Journal of Environmental Science and Health, Part A*, vol. 46, pp. 1699–1707, 2011.

[53] W. Mozgawa, "The relation between structure and vibrational spectra of zeolites," *Journal of Molecular Structure*, vol. 596, pp. 129–137, 2001.

[54] M. Chigondo, U. Guyo, M. Shumba et al., "Synthesis and characterisation of zeolites from coal fly ash (CFA)," *Synthesis*, vol. 3, pp. 714–718, 2013.

[55] A. Fernández-Jiménez and A. Palomo, "Mid-infrared spectroscopic studies of alkali-activated fly ash structure," *Microporous and Mesoporous Materials*, vol. 86, pp. 207–214, 2005.

[56] M. Y. A. Mollah, S. Promreuk, R. Schennach, D. L. Cocke, and R. Güler, "Cristobalite formation from thermal treatment of Texas lignite fly ash," *Fuel*, vol. 78, pp. 1277–1282, 1999.

[57] M. Rokita, W. Mozgawa, and M. Handke, "The influence of Na^+ and Ca^{2+} ions on the SiO_2–$AlPO_4$ materials structure — IR and Raman studies," *Journal of Molecular Structure*, vol. 596, pp. 171–178, 2001.

[58] N. Kantiranis, A. Filippidis, T. Mouhtaris et al., "EPI-type zeolite synthesis from Greek sulphocalcic fly ashes promoted by H_2O_2 solutions," *Fuel*, vol. 85, pp. 360–366, 2006.

[59] G. K. Inwati, P. Kumar, W. D. Roos, H. C. Swart, and M. Singh, "UV-irradiation effects on tuning LSPR of Cu/Ag nanoclusters in ion exchanged glass matrix and its thermodynamic behaviour," *Journal of Alloys and Compounds*, vol. 823, article 153820, 2020.

[60] S. Mourdikoudis, R. M. Pallares, and N. T. K. Thanh, "Characterization techniques for nanoparticles: comparison and complementarity upon studying nanoparticle properties," *Nanoscale*, vol. 10, pp. 12871–12934, 2018.

[61] V. K. Yadav, D. Ali, S. H. Khan et al., "Synthesis and characterization of amorphous iron oxide nanoparticles by the sonochemical method and their application for the remediation of heavy metals from wastewater," *Nanomaterials*, vol. 10, p. 1551, 2020.

[62] D. Czarna-Juszkiewicz, P. Kunecki, R. Panek, J. Madej, and M. Wdowin, "Impact of fly ash fractionation on the zeolitization process," *Materials*, vol. 13, no. 5, article 1035, 2020.

[63] M. A. Klunk, S. B. Schröpfer, S. Dasgupta et al., "Synthesis and characterization of mordenite zeolite from metakaolin and rice husk ash as a source of aluminium and silicon," *Chemical Papers*, vol. 74, pp. 2481–2489, 2020.

[64] F. Stoppa, F. Scordari, E. Mesto, V. Sharygin, and G. Bortolozzi, "Calcium-aluminum-silicate-hydrate "cement" phases and rare Ca-zeolite association at Colle Fabbri, Central Italy," *Central European Journal of Geosciences*, vol. 2, pp. 175–187, 2010.

[65] G. Ferretti, G. Galamini, V. Medoro, M. Coltorti, D. Di Giuseppe, and B. Faccini, "Impact of sequential treatments with natural and Na-exchanged chabazite zeolite-rich tuff on pig-slurry chemical composition," *Water*, vol. 12, p. 20, 2020.

[66] T. Ennaert, J. Van Aelst, J. Dijkmans et al., "Potential and challenges of zeolite chemistry in the catalytic conversion of biomass," *Chemical Society Reviews*, vol. 45, pp. 584–611, 2016.

[67] G. Abbas, M. Saqib, J. Akhtar, G. Murtaza, M. Shahid, and A. Hussain, "Relationship between rhizosphere acidification and phytoremediation in two acacia species," *Journal of Soils and Sediments*, vol. 16, pp. 1392–1399, 2016.

[68] K. Li and D. Xue, "Estimation of electronegativity values of elements in different valence states," *The Journal of Physical Chemistry A*, vol. 110, no. 39, pp. 11332–11337, 2006.

[69] X. Zhao, F. Gu, Y. Wang, Z. Peng, and J. Liu, "Surface electronegativity as an activity descriptor to screen oxygen evolution reaction catalysts of Li–O_2 battery," *ACS Applied Materials & Interfaces*, vol. 12, pp. 27166–27175, 2020.

[70] V. Pandey, M. Ray, and V. Kumar, "Assessment of water-quality parameters of groundwater contaminated by fly ash leachate near Koradi Thermal Power Plant, Nagpur," *Environmental Science and Pollution Research*, vol. 27, pp. 27422–27434, 2020.

[71] S. Rajendran, G. K. Inwati, V. K. Yadav et al., "Enriched catalytic activity of TiO_2 nanoparticles supported by activated carbon for noxious pollutant elimination," *Nanomaterials*, vol. 11, no. 11, p. 2808, 2021.

[72] M. B. Solanki, P. Patel, S. Shinde, B. B. Parekh, and M. Joshi, "Growth and characterization of lithium chloride doped KDP crystals: a DFT and experimental approach," *Ferroelectrics*, vol. 571, no. 1, pp. 1–25, 2021.

[73] P. Giannozzi, S. Baroni, N. Bonini et al., "QUANTUM ESPRESSO: a modular and open-source software project for quantum simulations of materials," *Journal of Physics: Condensed Matter*, vol. 21, no. 39, article 395502, 2009.

[74] J. P. Perdew, K. Burke, and M. Ernzerhof, "Generalized gradient approximation made simple," *Physical Review Letters*, vol. 77, no. 18, pp. 3865–3868, 1996.

[75] G. Petretto, S. Dwaraknath, H. P. C. Miranda et al., "High-throughput density-functional perturbation theory phonons for inorganic materials," *Scientific Data*, vol. 5, no. 1, article 180065, 2018.

[76] W. Kohn and L. J. Sham, "Self-consistent equations including exchange and correlation effects," *Physical Review*, vol. 140, no. 4A, pp. A1133–A1138, 1965.

[77] M. Cococcioni, F. Mauri, G. Ceder, and N. Marzari, "Electronic-enthalpy functional for finite systems under pressure," *Physical Review Letters*, vol. 94, no. 14, article 145501, 2005.

[78] M. C. Payne, M. Hytha, I. Štich, J. D. Gale, and K. Terakura, "First principles calculation of the free energy barrier for the reaction of methanol in a zeolite catalyst," *Microporous and Mesoporous Materials*, vol. 48, no. 1-3, pp. 375–381, 2001.

[79] S. Yang, M. Lach-hab, I. I. Vaisman, E. Blaisten-Barojas, X. Li, and V. L. Karen, "Framework-type determination for zeolite structures in the inorganic crystal structure database," *Journal of Physical and Chemical Reference Data*, vol. 39, no. 3, article 033102, 2010.

[80] A. Khaleque, M. M. Alam, M. Hoque et al., "Zeolite synthesis from low-cost materials and environmental applications: a review," *Environmental Advances*, vol. 2, article 100019, 2020.